Dynamic Reduced Order Modeling of Entrained Flow Gasifiers

by

Rory F. D. Monaghan

B.E. (Honors), Mechanical Engineering (2002)
National University of Ireland, Galway

S.M., Mechanical Engineering (2005)
Massachusetts Institute of Technology

Submitted to the Department of Mechanical Engineering in Partial Fulfillment of
the Requirements for the Degree of

Doctor of Philosophy in Mechanical Engineering
at the
MASSACHUSETTS INSTITUTE OF TECHNOLOGY

FEBRUARY 2010

Signature of Autho ....

Department of Mechanical Engineering

December 16, 2009

Certified by..

Ahmed F. Ghoniem

Ronald C. Crane (1972) Professor

Thesis Supervisor

Accepted by..

David E. Hardt

Chairman, Department Committee on Graduate Students

1

Page left intentionally blank

Dynamic Reduced Order Modeling of Entrained Flow Gasifiers

by

Rory F. D. Monaghan

Submitted to the Department of Mechanical Engineering on December 16, 2009 in Partial Fulfillment of the Requirements for the Degree of Doctor of Philosophy in Mechanical Engineering

ABSTRACT

Gasification-based energy systems coupled with carbon dioxide capture and storage technologies have the potential to reduce greenhouse gas emissions from continued use of abundant and secure fossil fuels. Dynamic reduced order models (ROMs) that predict the operation of entrained flow gasifiers (EFGs) within IGCC (integrated gasification combined cycle) or polygeneration plants are essential for understanding the fundamental processes of importance. Such knowledge can be used to improve gasifier reliability, availability and maintainability, leading to greater commercialization of gasification technology.

A dynamic ROM, implemented in Aspen Custom Modeler, has been developed for a range of EFGs. The ROM incorporates multiple feedstocks, mixing and recirculation, particle properties, drying and devolatilization, chemical kinetics, fluid dynamics, heat transfer, pollutant formation, slag behavior and syngas cooling. The ROM employs a reactor network model (RNM) that approximates complex fluid mixing and recirculation using a series of idealized chemical reactors.

The ROM was successfully validated for steady-state simulation of four experimental gasifiers. The throughputs of these gasifiers range from 0.1 to 1000 metric tonnes per day (3 kW_{th} - 240 MW_{th}). Sensitivity analysis was performed to identify the parameters most important to ROM accuracy. The most important parameters are found to be those that determine RNM geometry, particle physical and kinetic properties, and slagging.

The ROM was used to simulate the steady-state and dynamic performance of a full-scale EFG system. In steady-state mode, the ROM was used to establish base case and fluxant requirements. The base case performance agreed with design specifications. Steady-state simulation was also used to determine important states for dynamic simulation. Six cases were examined in dynamic mode, including gasifier cold start. Dynamic results showed agreement with industrial experience for gasifier start-up times.

Thesis Supervisor: Ahmed F. Ghoniem
Title: Ronald C. Crane (1972) Professor

Page left intentionally blank

ACKNOWLEDGEMENTS

Page left intentionally blank

TABLE OF CONTENTS

LIST OF FIGURES

15

LIST OF TABLES

NOMENCLATURE

Capital Letters

A	Area (m^2) or Frequency factor ($kg/m^2/atm^n/s$)
$A^{\sim}$	Area per unit volume (m^2/m^3)
ACH	Stoichiometric ratio of air to char (kg/kg)
ACO	Stoichiometric ratio of air to coal (kg/kg)
B	Length scale for radiation heat transfer (m)
C	Particle conversion
C_D	Drag coefficient
D	Diffusivity (m^2/s)
E	Activation energy (kJ/kmol)
$F^{\sim}$	Viscous frictional force per unit volume (N/m^3)
K	Equilibrium constant or Absorption coefficient (m^{-1})
L	Length (m)
M	Reaction rate multiplier
N	Number density (m^{-3})
Nu	Nusselt number
P	Pressure (atm, bar, MPa or Pa)
Pe_h	Peclet number for heat transfer
Pe_m	Peclet number for mass transfer
$\dot{Q}'$	Heat transfer rate per unit axial length (kW/m)
$\dot{Q}''$	Heat transfer rate per unit area (kW/m^2)
R	Rate of chemical reaction ($kg/m^3/s$)
$\hat{R}$	Rate of chemical reaction ($kmol/m^3/s$)
$\mathfrak{R}$	Ideal gas constant (kJ/kmol/K)
Ra	Rayleigh number
Re	Reynolds number
S	Rate of species formation (kg/m^3) or Swirl number
$\tilde{S}_{\chi \to \phi}$	Sensitivity of output (ϕ) to input (χ)
Sh	Sherwood number
T	Temperature (K)
V	Volume (m^3)
X	Mass fraction (kg/kg)
$\hat{X}$	Mole fraction (kmol/kmol)
Y	Yield (kg/kg)
Z	CO-CO_2 ratio at particle surface

Lowercase Letters

a	Specific area (m^2/kg)
act	Actual
c_p	Specific heat capacity (kJ/kg/K)
d	Diameter (m)
f	Friction factor
f_{corr}	Correction factor
f_{JEZ}	Mass fraction of flow leaving ERZ to enter JEZ directly

f_N	Mass fraction of devolatilized nitrogen evolving as HCN
f_{slag}	Slag deposition factor
g	Gravitational acceleration (m/s^2)
h	Enthalpy (kJ/kg) or Heat transfer coefficient (kW/m^2/K)
$\hat{h}$	Enthalpy (kJ/kmol)
k	Conductivity (kW/m/K)
$k(T)$	Reaction rate constant ((kg/m^2/atm^n/s) for heterogeneous)
l	Length per unit mass (m/kg)
m	Mass (kg)
$\dot{m}$	Mass flow rate (kg/s)
$\dot{m}'$	Mass flow rate per unit axial length (kg/m/s)
$\dot{m}''$	Mass flow rate per unit area (mass flux) (kg/m^2/s)
n	Heterogeneous reaction order
$\dot{n}''$	Molar flux (kmol/m^2/s)
r	Radius (m)
$r^{\cdot}$	Resistivity (s/m)
$\bar{r}_{pore}$	Average pore radius (m)
s	Silica ratio
t	Time (s) or Thickness (m)
u	Internal energy (kJ/kg)
v	Velocity (m/s)
w	Mole weight (kg/kmol)
x	Axial position (m)

Greek Letters

α	Recirculation ratio (kg/kg) or switch
β	Particle density evolution parameter or Slag surface angle (deg) or Inverse film temperature (K^{-1})
χ	Chemical species
δ	Thickness (m)
Δ	Arbitrarily small number
ε	Volume fraction (m^3/m^3) or Porosity (m^3/m^3) or emissivity
ϕ	Mechanism factor or Thiele Modulus
η	Effectiveness factor
λ	Mass transfer coefficient (kmol/m^2/s)
λ_0	Air ratio (kg/kg)
λ_g	Gasifier air ratio (kg/kg)
μ	Dynamic viscosity (Pa.s)
θ	Jet expansion angle (deg)
ρ	Density (kg/m^3)
$\hat{\rho}$	Molar density (kmol/m^3)
σ	Stefan-Boltzmann constant (5.67×10^{-11} kW/m^2/K^4)
v	Stoichiometric coefficient or Kinematic viscosity (m^2/s)
Ω	Particle roughness (-) or Wall roughness (m)
ψ	Particle structural parameter

Subscripts

A	Molecular diffusion
act	Actual
amb	Ambient
c	Characteristic
C	Carbon or Concentration
CS	Cross section
cond	Conduction
conv	Convection
CV	Critical value (slag temperature)
dev	Devolatilization
d	Diameter
diff	Diffusion
dry	Drying
e	Electric
eff	Effective
ex	Extrinsic
exit	Gasifier exit
ext	External
f	Formation or Film
fus	Fusion (heat of)
g	Gas
H	Hydrogen (elemental)
HT	Heat transfer
i	Gas phase species
in	Intrinsic
int	Internal
j	Solid phase species (proximate)
k	Solid phase species (ultimate)
K	Knudsen diffusion
l	Wall layer (i.e. firebrick (refractory), insulating brick, steel wall)
liq	Liquid
m	Heterogeneous reaction
M	Moisture
n	Homogeneous reaction
p	Particle
pore	Intraparticle pore
r	Recirculated
rad	Radiation
ref	Refractory
rxn	Reaction
s	Particle surface
sens	Sensible
slag	Slag on wall
slagging	Slag transport to wall
sol	Solid
th	Thermal
w	Wall
x	Axial direction
0	Initial or reference state

Acronyms

ACM	Aspen Custom Modeler
ar	As received
ASU	Air Separation Unit
BYU	Brigham Young University
CCS	Carbon dioxide Capture and Storage (or Sequestration)
CCSD	Cooperative Research Centre for Coal in Sustainable Development
CCZ	Coal Combustion Zone
CFD	Computational Fluid Dynamics
CGE	Cold Gas Efficiency
CoP	ConocoPhillips
CRIEPI	Central Research Institute of the Electric Industry
CS	Cross Section
CSC	Convective Syngas Cooler
CSIRO	Commonwealth Scientific and Industrial Research Organization
CSTR	Continuously Stirred Tank Reactor (also WSR)
CWS	Coal-Water Slurry
daf	Dry, Ash-Free (also dmmf: "dry, mineral matter free")
DOE	United States Department of Energy
DSZ	Downstream Zone
ECBM	Enhanced Coal Bed Methane Recovery
ECUST	East China University of Science and Technology
EFG	Entrained Flow Gasifier
EGR	Enhanced Gas Recovery
EIA	Energy Information Administration
EOR	Enhanced Oil Recovery
ERZ	External Recirculation Zone
FC	Fixed Carbon
FB	Firebrick (refractory)
GE	General Electric
GHG	Greenhouse Gas
Gt	Gigatonne (one billion metric tonnes)
GW	Gigawatt
HHV	Higher Heating Value
HV	High-Volatile (for feedstock)
IB	Insulating brick
IGCC	Integrated Gasification Combined Cycle
IRZ	Internal Recirculation Zone
JEZ	Jet Expansion Zone
kW	Kilowatt
LCOE	Levelized Cost of Electricity
LHV	Lower Heating Value
MHI	Mitsubishi Heavy Industries
Mt	Megatonne (one million metric tonnes)
MW	Megawatt
NETL	National Energy Technology Laboratory
NG	Natural Gas
NGCC	Natural Gas Combined Cycle
OMB	Opposed Multi Burner
PC	Pulverized Coal
PFR	Plug Flow Reactor
ppm	Parts per million

PRENFLO	Pressurized Entrained Flow
PWR	Pratt and Whitney Rocketdyne
RAD	Radiation-as-diffusion
RNM	Reactor Network Model
ROM	Reduced Order Model
RPM	Random Pore Model
RSC	Radiant Syngas Cooler
SCPC	Supercritical Pulverized Coal
SCGP	Shell Coal Gasification Process
SFG	Solid Fuel Gasification
SUFCo	Southern Utah Fuel Company
TGA	Thermogravimetric analysis
tpd	Metric tonnes per day
VM	Volatile Matter
WGS	Water-Gas Shift
WGSR	Water-Gas Shift Reactor
WSR	Well-Stirred Reactor (also CSTR)

Chapter 1 INTRODUCTION

1.1 Chapter Overview

This chapter introduces the dual issues of increasing energy demand and greenhouse gas emissions. The potential role of carbon dioxide capture and storage in general, and gasification-based energy systems in particular are discussed. The various families of gasifiers are introduced and focus is given to entrained flow gasifiers. The various physical and chemical phenomena that occur during gasification are briefly described. Commercial entrained flow gasifier designs are discussed, as are the various problems associated with their operation. The role of computer-based modeling in general, and reduced order modeling in particular are presented with respect to better understanding gasification and improving reliability, availability and maintainability.

1.2 Energy and the Environment

The world currently consumes over 500 exajoules (EJ) of energy every year. That is the equivalent of over 220 million barrels of oil every day. As consumption increases in developed countries and as developing countries continue to industrialize, this figure is growing at an annual rate of over 2%. The Energy Information Administration (EIA) predicts that by 2030, the world will consume 45% more energy than it does at present [1]. Figure 1-1 shows EIA predictions of world energy demand to 2030.

Coupled with this rising demand is the threat of global climate change. There is near-universal consensus that human activities are contributing to a steady increase in the earth's average temperature [2]. The dominant cause of climate change is the increased level of carbon dioxide (CO_2) in the atmosphere. This is mostly due to fossil fuel combustion. Atmospheric CO_2 concentration has increased from a pre-industrial value of 280 ppm (parts per million) to 379 ppm in 2005. The world currently emits 26-29 gigatonnes (billion metric tonnes) of CO_2 ($GtCO_2$) every year, from [2] and [1], respectively. Increasing energy use means that this figure is growing at an annual rate of over 2%. Figure 1-2 shows EIA predictions of world CO_2 emissions to 2030.
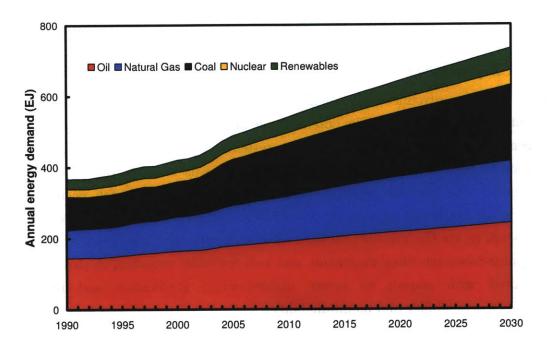
Figure 1-1: World energy demand to 2030
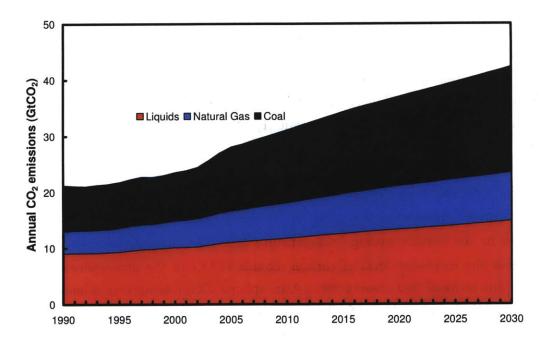
Figure 1-2: World CO$_2$ emissions to 2030

The key issue facing society is how to stabilize and eventually decrease CO_2 emissions while allowing economic growth, especially in the developing world. There are a number of technology-based options, which include: increased energy efficiency, switching to less carbon-intensive fuels, renewable forms of energy, nuclear energy, and CO_2 capture and storage (CCS) [3-5].

1.3 Carbon Dioxide Capture and Storage

CCS is a technology that involves the capture of CO_2 from combustion or industrial processes, its transport, and its long-term storage, so that it cannot be emitted to the atmosphere. Its component processes are summarized below.

1.3.1 Carbon Dioxide Capture

1.3.1.1 Post-Combustion Capture

Carbon dioxide is removed from the mix of CO_2, water vapor and nitrogen in the exhaust stream (flue gas) of the plant. For a coal-fired plant, CO_2 concentration in the flue gas is around 12-13% by volume. Post-combustion capture is the least capital-intensive option for retrofitting existing pulverized coal plants.

1.3.1.2 Oxy-Fuel Capture

Coal is burned in nearly-pure oxygen, as opposed to air, which produces a stream of CO_2 and water vapor. When the flue gas is cooled, the water vapor condenses, leaving a high-purity stream of CO_2. In this method, CO_2 capture is very simple, but the energy penalty and capital costs of generating high-purity oxygen are substantial.

1.3.1.3 Pre-Combustion Capture

Coal is gasified, not burned, in a mix of oxygen and steam, producing a synthesis gas (syngas) stream of carbon monoxide (CO), hydrogen (H_2), carbon dioxide (CO_2) and water vapor (H_2O). After a straightforward catalytic reaction downstream of the gasifier, which converts CO to CO_2 and H_2O to H_2, the syngas has a CO_2 concentration of 30-50%. This makes CO_2 removal from the syngas less

27

energy-intensive than post-combustion capture, at the cost of expensive equipment (air separation unit, gasifier, water-gas shift reactors) upstream of the power generation equipment (gas turbines, heat-recovery steam-generator, steam turbines). Applications of gasification-based energy systems include IGCC plants for the production of power, and polygeneration plants for the production of industrial chemicals, fuels, hydrogen, and potentially power. The gasification process will be discussed in greater detail in later sections.

1.3.2 Carbon Dioxide Transport and Storage

After capture, the CO_2 must be transported to its storage site. This is proposed to be done through the use of pipelines or liquefied tanker transport. Carbon dioxide storage for utility or industrial scale projects is typically assumed to imply storage in subterranean or sub-seabed geological formations. The most probable formations are described below and in Figure 1-3 [3].

1.3.2.1 Deep saline aquifers

These are large salt water (brine) bodies that lie thousands of meters below the surface of the earth. It is estimated 1000-10000 $GtCO_2$ could be stored in the world's saline aquifers [3].

1.3.2.2 Depleted oil and gas reservoirs

These formations have contained pressurized gases and liquids for millennia, so assuming they were not excessively damaged during exploitation, they should be able to contain pressurized CO_2.

1.3.2.3 Enhanced hydrocarbon recovery

As oil and gas fields are depleted, the pressure that drives production decreases. Fluids, including CO_2, can be pumped into the fields to maintain the pressure and flow. Oil viscosity is also reduced by the presence of CO_2. This is done on a large scale for enhanced oil recovery (EOR). It is also under investigation for enhanced gas recovery (EGR). Unmineable coal seams may be used for methane production, using a technique known as enhanced coalbed methane recovery (ECBM). This

28

involves a fluid, possibly CO_2, being injected into the coal seams and displacing methane, which is then recovered.
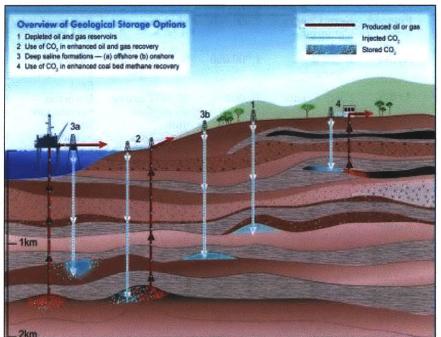
Figure 1-3: Geological storage options for CO_2 (from [3])

1.3.3 Application of CCS

The application of CCS technologies has been slow due to high costs and uncertainty with respect to CO_2 emissions regulations. There are however, a small number projects around the world that currently or plan to capture and store CO_2 from various industrial or energy processes. A sample of these projects is shown Table 1-1. For a full list of and information on current and planned worldwide CCS projects, refer to the interactive map on the website of the *Carbon Capture and Sequestration Technologies Program* at MIT (http://sequestration.mit.edu/). The first CCS project, Sleipner in Norway, was motivated by a national carbon tax of $40/tonne of CO_2. Most of the projects shown receive funding for research into CO_2 capture and storage techniques.

Table 1-1: Currently and planned CCS projects

Project	Status	Location	Capacity (tonnes CO_2/yr)	CO_2 source	CO_2 storage type	Comments
HECA (BP-Rio Tinto)	Planned	Kern County, California, USA	2,000,000	Coal and petcoke-fired IGCC	Enhanced oil recovery	Will be first IGCC-based CCS project
In Salah (BP)	Active	In Salah, Algeria	1,200,000	Stripped from natural gas	Depleted natural gas field	Largest CCS project by CO_2 capacity
Lacq (Total & others)	Active	Lacq, France	75,000	35 MW heavy oil oxyfuel unit	Depleted natural gas field	First oxyfuel CCS project
Mountaineer (AEP & Alstom)	Active	New Haven, West Virginia, USA	100,000	Slipstream from 1300 MW_e coal plant	Saline aquifer	First CCS project at US power plant
Schwarze Pumpe (Vattenfall)	Active	Spremberg, Germany	100,000	30 MW_{th} coal oxyfuel unit	Depleted natural gas field	First CCS project at a power plant
Sleipner (Statoil & others)	Active	Norwegian North Sea	1,000,000	Stripped from natural gas	Subsea saline aquifer	First CCS project of any kind. Motivated by carbon tax.
Snohvit (Statoil & others)	Active	Norwegian Barents Sea	700,000	Stripped from natural gas	Subsea saline aquifer	Facility located on the seabed
Weyburn (Pan Canadian & others)	Active	Weyburn, Saskatchewan, Canada	1,000,000	Great Plains Synfuel Plant, Beulah, North Dakota	Enhanced oil recovery	CO_2 source is a gasification-based coal-to-gas plant

In its study of fossil fuel electricity generation, the National Energy Technology Laboratory (NETL) compared the costs of applying CCS to bituminous coal plants (pre- and post-combustion capture) and natural gas plants (post-combustion capture only) [5]. No widely accepted cost figures are available for oxy-fuel CCS. The levelized cost of electricity (LCOE) produced by coal and gas plants with and without CCS is shown in Figure 1-4. In the figure, "NGCC" refers to natural gas combined cycle, "PC" refers to subcritical pulverized coal, "SCPC" refers to supercritical pulverized coal, and "GE", "CoP" and "Shell" refer to IGCC plants using GE, ConocoPhillips E-GAS and Shell SCGP gasifiers, respectively. The figure is reproduced from data presented in the NETL report on fossil-fuel-based energy options [5].
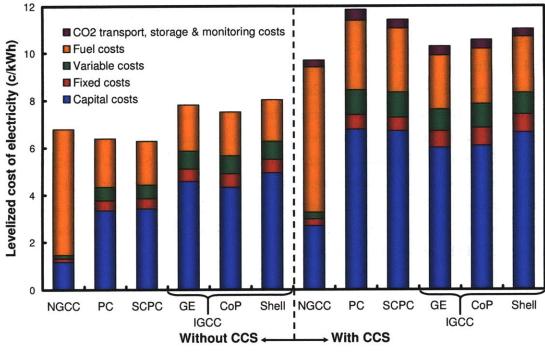
Figure 1-4: Levelized costs of electricity for fossil plants with and without CCS

From the point of view of baseload power generation, the main findings from the analysis are that without CO_2 capture, pulverized coal (PC) plants are cheaper sources of fossil fuel electricity than integrated gasification combined cycle (IGCC) plants. But when CO_2 is to be captured the picture changes. IGCC plants now have lower LCOE than pulverized-coal-based systems. Furthermore, it is apparent that capital cost is the major LCOE component for IGCC plants with and without CCS. For IGCC plants, the single largest capital expenditure is the gasifier itself. Gasification, its role in energy systems and gasifier designs are discussed in the next section.

1.4 Gasification

1.4.1 Overview

The gasification process can be defined as the process of reacting a carbonaceous feedstock with steam (H_2O) and oxygen (O_2) to form a synthesis gas (syngas) containing H_2 and CO. It can be viewed globally as incomplete combustion and usually refers to solid or liquid feedstocks. Gasification has been used in various

31

industrial and energy processes for centuries [6]. The first large-scale applications of gasification were for the production of town gas from coal for municipal lighting in the 18th and 19th centuries. Nazi Germany used coal gasification extensively for fuel production before and during the Second World War. The Apartheid government of South Africa also pursued large-scale coal gasification for transportation fuel production during the international oil embargo against that regime. The legacy of these courses of action is that South Africa has the most installed capacity of gasifiers of any country, mostly at SASOL's synthetic fuel plants at Secunda and Sasolburg. Furthermore, the technology used in South Africa is licensed by the German vendor, Lurgi. The United States has also made extensive use of gasification, constructing the Great Plain Synfuels plant in the aftermath of the oil shocks of the 1970s.

Figure 1-5 shows currently installed solid-feedstock-gasification-derived syngas capacity by product, according to the DOE/NETL 2007 Gasification Database [7]. It can be seen that chemicals and liquid fuels are the main products of gasification worldwide. China, South Africa and the United States are the main countries that employ gasification. Small plants in India, Finland Sweden, Serbia and Portugal are not shown in Figure 1-5. Solid-fuel-fired gasification-based power plants, in the form of IGCCs, have not been deployed globally at scale. At the time of publication of the database, only six utility-scale IGCC plants were in operation; Polk County and Wabash River in the United States, Schwarze Pumpe in Germany, Vresova in the Czech Republic, Puertollano in Spain, and Buggenum in the Netherlands. An additional coal-fired IGCC began operation in Nakoso, Japan in late 2007. Duke Energy are currently building a 630 MW$_e$ IGCC plant in Edwardsport, Indiana, which, when complete, will be the largest such plant in the world. Note the absence of gasification-based polygeneration plants in the currently installed capacity.
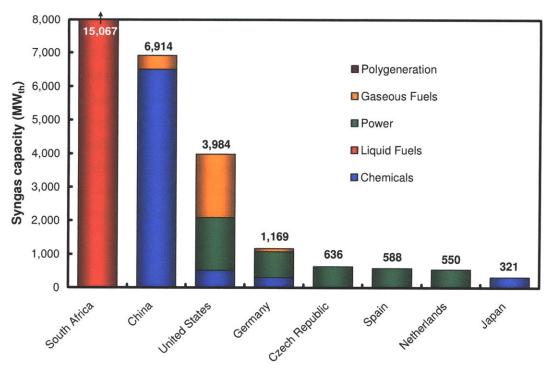
Figure 1-5: 2007 solid-feedstock-derived syngas capacity by product

1.4.2 The Role of the Gasifier

The role of the gasifier in energy systems is to convert solid carbonaceous feedstocks into syngas. Figure 1-6 shows the gasifier in a highly simplified IGCC/polygeneration plant schematic. Solid feedstock (coal, biomass, waste, petroleum coke, etc.) is supplied to the gasifier, along with an oxidant (O_2 or air) and steam or water. Devolatilization, combustion and gasification reactions occur in the gasifier, producing syngas, which consists mainly of CO and H_2. These, as well as other physical and chemical processes, will be discussed in detail in later sections. Upon leaving the gasifier at 1000-1400 °C, the syngas must be cooled prior to pollutant removal. Current commercial technologies for the removal of nitrogenous and sulfurous compounds and mercury operate at -50 to 100 °C; therefore the syngas passes through one or more coolers. Coolers may be in the form of heat exchangers (radiant or convective coolers) or quench vessels. These syngas cooling options will be discussed in detail later. After syngas cooling, particulates (fly ash and/or unconverted carbon) are removed by water washing or cyclone.

After cleaning, syngas can be used to produce chemicals, synthetic fuels or hydrogen. Syngas can also be supplied to a combined cycle gas turbine (CCGT) power plant for electricity generation. In cases where CO_2 is to be captured and stored (CCS), a water-gas shift reactor (WGSR) is used upstream of the gas turbine to produce high-purity H_2 for combustion. Chemical plants that employ gasification are particularly well suited to CCS as they already use WGSRs to change the $CO:H_2$ ratio of the syngas for chemical synthesis. Most such plants currently vent high-purity CO_2 directly to the atmosphere. The only on-site investments required to enable CCS at such chemical plants are a CO_2 compressor and a CO_2 off-take line. It should be noted that such investments are non-trivial.
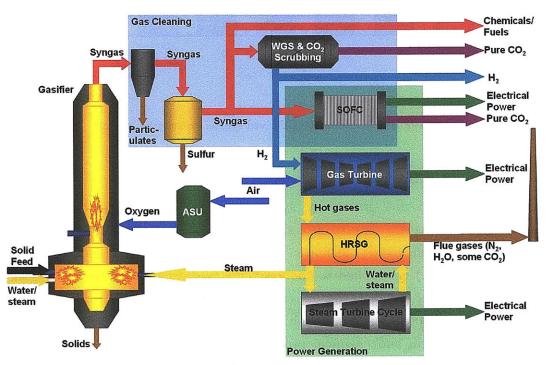
Figure 1-6: The gasifier in a highly simplified plant schematic

1.4.3 Types of Gasifiers

There are three general families of commercial gasifier designs: fixed bed, fluidized bed and entrained flow. The syngas composition of each family and design of gasifier is different because of the operating conditions associated with each. At a very basic level, the characteristics of the gasifier families are shown in Table 1-2. The most striking features of this table are the figures for current and planned

deployment. According to the DOE/NETL 2007 Gasification Database [7], all but one of the planned solid fuel gasification plants worldwide will be of the entrained flow design. The reasons for this are listed in the relative advantages row of the table: highest throughput, highest conversion and "cleanest" syngas. For most applications, a syngas free of hydrocarbons is desirable. The use of the word "relative" implies that improvements are still required in order to increase performance, reliability and efficiency of all gasifier families, not just fixed, fluidized or entrained designs. These points will be addressed later. Due to the preeminence of entrained flow gasifiers (EFGs), the remainder of this work focuses solely on that design.

Table 1-2: Characteristics of gasifier families

	Fixed bed	Fluidized bed	Entrained flow
Maximum temperature (K)	1420	1200	1640-1920
Pressure (atm)	1-27	1-68	1-82
Feedstock delivery	Dry crushed particles	Dry ground particles	Dry feed or slurry of pulverized particles
Feedstock particle size	5-50 mm	1-5 mm	<0.1 mm
Oxidant	Air or oxygen	Air or oxygen	Air or oxygen
Ash condition	Dry or slagging	Dry	Slagging
Residence time	>1 hour	0.5-1 hour (with recycle)	~1-5 seconds
Sulfur removal	Downstream at low temperature	In gasifier, using limestone or dolomite	Downstream at low temperature
Syngas HHV (MJ/m^3)	11-14	5.5 (air-blown)	11-13
Relative advantages	Widespread technology	High throughput Low hydrocarbons	Highest throughput Highest conversion Lowest hydrocarbons
Relative disadvantages	Lowest throughput Highest hydrocarbons Poor fuel flexibility	Complex recirculation equipment Trouble with caking coals	Trouble with low rank coals when using slurry-fed designs
Application	Synfuels and chemicals production	IGCC generation and chemicals production	IGCC generation, synfuels and chemicals production
Deployment Ref [7][1]	Current: 19.5 GWth mostly in South Africa & US Planned: 0 GWth	Current: 0.7 GWth mostly in Asia Planned: 0.3 GWth	Current: 8.9 GWth in Asia, Europe & US Planned: 29.0 GWth mostly in China & US

1.5 Entrained Flow Gasification

Entrained flow gasification consists of a number of physical and chemical sub-processes. Some of these sub-processes are similar to those that occur during

---

[1] These figures include all solid feedstocks: biomass/waste, coal and petroleum coke.

combustion of pulverized solid fuels. The sub-processes are introduced in this section, and are described in further detail in the section dealing with the submodels used in reduced order modeling.

1.5.1 Mixing and Recirculation

Inlet streams are brought into contact with each other and hot gases and particles in the gasifier by complex fluid flow fields. Vigorous mixing of inlet streams is important to ensure flame stability. To this end, various techniques are employed to mix inlet streams as quickly as possible. These approaches include the use of swirling inlet streams and opposed injection ports. Recirculation of hot combustion products to the injection ports also plays an important role in feedstock ignition.

1.5.2 Particle Heating, Drying and Devolatilization

Upon injection into the high temperature gasifier environment, the pulverized feedstock particles are exposed to heating rates of the order 10^5-10^6 K/s [8]. This rapid heating rate causes the moisture present in all solid fuels to rapidly vaporize. Volatile materials present in the feedstock also leave the particles under these conditions to form CO, H_2, CO_2, H_2O, aliphatics and aromatics of various sizes, and tar. This process is known as devolatilization or pyrolysis. The combustible gases that evolve during devolatilization are essential for establishing a stable flame near the fuel injector, and providing thermal energy necessary for later heterogeneous reactions. The solid residue remaining after devolatilization is referred to as char. Its primary constituents are carbon and ash. Devolatilization is an important mechanism in the initial stages of pollutant formation during gasification.

1.5.3 Homogeneous Reactions

Homogeneous oxidation of volatiles is responsible for providing the thermal energy needed to initiate heterogeneous char reactions. In the regions of the EFG near the oxidant inlet ports, excess O_2 is available for combustion. Away from the gasifier inlet, the equilibrium point of the water-gas shift (WGS) reaction ($CO + H_2O \Leftrightarrow CO_2 + H_2$) is one of the primary determinants of syngas composition. Under all steady-state EFG operating conditions, homogeneous reactions proceed much more rapidly than heterogeneous reactions [9].

1.5.4 Heterogeneous Reactions

Heterogeneous reactions are responsible for the conversion of char to syngas. The important heterogeneous reactions in a gasifier are:

Carbon partial combustion: $C + \frac{1}{2}O_2 \rightarrow CO$ (Eq. 1-1)

Carbon gasification: $C + H_2O \rightarrow CO + H_2$ (Eq. 1-2)

$C + CO_2 \rightarrow 2CO$ (Eq. 1-3)

$C + 2H_2 \rightarrow CH_4$ (Eq. 1-4)

These reactions are collectively known as the "char conversion reactions". Carbon combustion is exothermic and serves a similar purpose to volatiles combustion; namely to provide thermal energy for the endothermic gasification reactions. The reaction rates of C with H_2O (hydro-gasification) and C with CO_2 (Boudouard reaction) are roughly one tenth that of the oxidation reaction [6]. Under EFG conditions, the reaction rate of carbon with H_2 (methanation) is generally another 1-2 orders of magnitude lower [10]. Due to their importance and long reaction times, the overall rates of the hydro-gasification and Boudouard reactions are primary drivers for reactor size.

1.5.5 Char Particle Evolution

As devolatilization and char conversion occur, the structure of the particle changes. During devolatilization, voids of various sizes can form in the particle and radically alter the surface area available for reaction. The particle can also swell and deform during heating and devolatilization. As most solid feedstocks are highly porous in nature, there is a large amount of internal surface area available for reaction. How this internal area evolves with increasing levels of particle conversion has a large influence over heterogeneous reaction rates.

1.5.6 Heat Transfer

Conduction, convection and radiation play important roles in all EFG designs. At the high temperatures (1,000-1,800 °C) and particle loadings encountered in the gasifier, radiation is the primary mode of heat transfer. The role of convection is also important, particularly in syngas coolers and EFG designs that incorporate membrane-lined walls. Conduction heat transfer is critical as it is the only mechanism of heat loss and/or recovery through the gasifier walls.

1.5.7 Pollutant Formation

The pollutants profiles of gasifiers differ significantly from those of combustors due to the highly fuel-rich operation of the former. Gasifiers typically operate at equivalence ratios in the region 2-3, as opposed to values for combustors of 0.9-1.1. The nitrogenous compounds formed in a gasifier therefore include ammonia (NH_3) and hydrogen cyanide (HCN), in addition to nitrogen (N_2) and nitric oxide (NO). Similarly, the sulfurous compounds include hydrogen sulfide (H_2S) and carbonyl sulfide (COS) as well as sulfur dioxide (SO_2). More oxidized forms of nitrogen and sulfur, such as nitrogen dioxide (NO_2) and sulfur trioxide (SO_3), are typically not formed in gasifiers. Pollutants are released from the particle by two mechanisms: devolatilization and char conversion. Further reactions in the gas phase determine the final pollutant profile of the gasifier.

1.5.8 Ash and Slag Formation

A fraction of all solid feedstocks consists of mineral matter or ash which does not undergo conversion. Ash mass fractions range from 2% in petroleum coke to 40% in some biomass feedstocks. Mineral matter leaves the gasifier in two forms: fly ash and slag. Fly ash is formed when most or all of the organic constituent of the particle has been converted, leaving ash behind. These ash particles can fragment and form much smaller particles that are difficult to remove by cyclone. Slag is formed when an ash-bearing particle contacts a surface at a temperature above the ash fusion point. The ash melts, forming a viscous fluid that can flow on the surface. Unconverted carbon contained in the particle can be trapped in the slag layer, leading to losses in gasifier conversion efficiency. All commercial EFG designs operate in the slagging mode, meaning that they maintain surface

temperatures above the ash fusion point. This enables collection of molten slag at the bottom of the gasifier.

1.6 Commercial EFG Designs

There are a large number of commercial entrained flow gasifier (EFG) designs in use and development worldwide. Over 90% of planned solid-fuel-derived syngas capacity is accounted for by three EFG designs: General Electric (GE), Shell Coal Gasification Process (SCGP) and ConocoPhillips (CoP) E-GAS. The GE gasifier was originally developed by Texaco and acquired by GE in 2004. The CoP E-GAS gasifier was originally developed by Dow and its spin-off Destec and acquired during CoP's take-over of Destec in 2003. SCGP grew from the original Koppers-Totzek entrained flow gasifier of the 1930s. Important characteristics of these and other commercial EFG designs are shown in Table 1-3. Simplified schematics of these three designs are shown in Figure 1-7. Before proceeding further it is important to appreciate the major differences between the EFG designs highlighted in Table 1-3. These differences in design characteristics are discussed below.
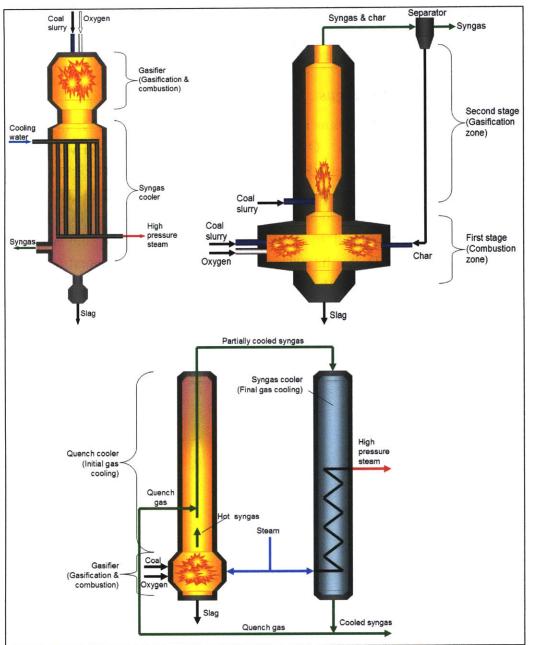
Figure 1-7: (a) GE (radiant), (b) CoP E-GAS and (c) SCGP gasifiers

Table 1-3: Commercial entrained flow gasifier characteristics

Process	Vendor	Flow	Feed	Injectors	Oxidant	Stages	Wall lining	Syngas cooling
E-GAS	CoP	Up	Slurry	Opposed	O_2	Two	Refractory	Quench
GE[1]	GE	Down	Slurry	Axial	O_2	One	Refractory	Quench or Radiant + Quench
MHI[2]	MHI	Up	Dry	Radial	Air	Two	Membrane	Quench
OMB[3]	ECUST[4]	Down	Slurry	Opposed	O_2	One	Refractory	Quench
PRENFLO[5]	Uhde	Up	Dry	Radial	O_2	One	Membrane	Radiant + Quench
SCGP[6]	Shell	Up	Dry	Radial	O_2	One	Membrane	Radiant + Quench
SFG[7]	Siemens	Down	Dry	Axial	O_2	One	Membrane	Quench

1.6.1 Feedstock Delivery

Pulverized feedstock may be delivered by either slurry or dry systems. In a slurry-fed system, pulverized feedstock is blended with water and surfactant to create a slurry. This slurry can be pumped to high pressures required for injection to the gasifier. The main drawback of this system is the fact that the solid mass fraction in the slurry is typically limited to 60-70% due to high slurry viscosity. Because of the high water content, gasification of high-moisture (low rank) coals is problematic with slurry-fed systems. In addition, the high heat of vaporization of water means that slurry-fed designs typically have lower thermal efficiencies than dry-fed gasifiers. Dry feed systems employ pressurized entraining gases, usually nitrogen (N_2), although Shell is investigated the use of recycled CO_2 for the SCGP design [11]. Dry feed systems typically operate in a batch process and suffer from poor reliability, but allow for the gasification of low rank coals. GE is investigating the use of a continuous-flow dry feed pump (Stamet) that it hopes will address these issues [12].

1.6.2 Injector Configuration

Injector configuration may be axial, opposed or radial. The choice of injector configuration has a major influence over the mixing and ignition processes at the gasifier inlet. Injectors may also employ swirl vanes and annular streams to

---

[1] GE: General Electric
[2] MHI: Mitsubishi Heavy Industries
[3] OMB: Opposed Multi Burner
[4] ECUST: East China University of Science and Technology
[5] PRENFLO: Pressurized Entrained Flow
[6] SCGP: Shell Coal Gasification Process
[7] SFG: Solid Fuel Gasification

improve mixing. The exact designs of commercial injectors are closely-guarded secrets.

1.6.3 Oxidant

The choice of oxidant depends on the required use of the syngas produced by the gasifier. Virtually all chemical processes require high purity O_2 (95-99% pure). Gasification for power generation in an IGCC may be fed by air or O_2. The only air-blown commercial EFG design is the MHI. The use of air means that the MHI gasifier does not require an air separation unit (ASU), but produces a syngas whose major constituent is N_2 (typically 50-55%). ASUs consume a significant amount of the power produced by an O_2-blown IGCC. Due to the high N_2 concentration in syngas, air-blown gasifiers are at a thermodynamic disadvantage relative to O_2-blown equivalents when CCS is required. MHI, however, claims that the additional energy requirement and cost for CO_2 separation is more than offset by the absence of an ASU [13].

1.6.4 Number of Stages

Two-stage gasifiers invariably employ a first stage for combustion and a second stage for gasification. Such gasifiers supply sufficient oxidant to the first stage (combustor or oxidizer) to fully oxidize the volatile materials that evolve from the feedstock at high temperatures. The solid particles are not fully consumed in this stage. The oxidizer can be viewed as providing heat, H_2O, CO_2 and char to the second stage (reductor). The second stage is typically operated under extremely fuel-rich conditions. In the absence of sufficient O_2, gasification occurs and syngas is produced. Gasification reactions typically proceed much slower than oxidation reactions, so solid particles are typically not fully converted upon leaving the gasifier. Therefore two-stage gasifiers must employ char recycling.

1.6.5 Wall Lining

The options for wall lining reflect two fundamentally different views of the role of slag in the gasifier. Refractory-lined EFGs use layers of high-chromium firebrick and insulating brick to protect the external steel pressure vessel from the high temperatures and corrosive slag present in the gasifier. The high thermal

resistance offered by the refractory-lined wall is intended to keep the internal wall temperature sufficiently high to allow easy flow of liquid slag down the walls. By contrast, membrane-lined EFGs run cooling water through the walls of the gasifier with the intention of keeping the internal wall (steel in this case) below the ash fusion temperature. The intention in these designs is to build up a protective layer of solid slag which would act in lieu of firebrick. Once the solid slag layer reaches a certain thickness (a few centimeters), the surface temperature rises above the ash fusion point and allows subsequent deposits of ash to flow on the wall as liquid slag. The main advantage of refractory-lined EFGs is the relative simplicity of the design. Refractory bricks, however, require frequent replacement, leading to gasifier downtime [14].

1.6.6 Syngas Cooling

As previously stated, hot syngas leaving the gasifier must be cooled prior to cleaning. Radiant syngas coolers (RSCs) are counter-flow heat exchangers in which syngas flows through a central orifice surrounded by tubes containing high pressure cooling water. This design is known as a waterwall. The main benefit of RSCs is the increase in overall plant thermal efficiency through heat recovery steam generation. RSCs, however, are very expensive due to their size and materials requirements. RSCs are so-called because the main mode of heat transfer from the syngas is radiation. Syngas coolers that operate in the lower-temperature convective regime (convective syngas coolers, or CSCs) have also been investigated, but most development has now ceased due to diminishing returns on heat recovery at lower temperatures and problems with slag blockages [15]. Quench coolers typically involve passing hot syngas through a vessel of water. This serves three main purposes: the syngas is cooled, solids drop out of the gas stream, and in plants where a water-gas shift reactor (WGSR) is used to increase H_2 and CO_2 concentrations, the quench cooler adds H_2O to the gas stream. Quench coolers are much less capital intensive than RSCs, but are not capable of recovering as much useful energy from the hot syngas, due to the highly irreversible nature of quenching. Some syngas coolers employ pre-cooling by gas quench. This involves recycling previously-cooled syngas back to the hot syngas.

1.7 Problems with Current EFG Designs

1.7.1 Lack of Dynamic Feedstock Flexibility

One of the selling points of gasification is its ability to handle a wide range of feedstocks. While it is true that gasifiers can be designed to handle one or more of many solid feedstocks, switching feeds once the gasifier is built is difficult. The three primary factors controlling feedstock flexibility are the ash fusion temperature, ash composition and feedstock moisture content. Since entrained flow gasifiers operate in slagging mode, operators must be sure that the gasifier can effectively operate at high enough temperatures to ensure adequately low slag viscosity for any feed. The third factor, feedstock moisture content, is an issue for slurry-fed designs. As stated above, slurries in water already add more H_2O than is required for gasification, and a moisture-rich feedstock can cause the gasifier temperature to drop low enough to (1) shift the chemical equilibrium points of the reactions, (2) slow the reaction rates, (3) reduce the thermal efficiency of the gasifier and (4) affect slag viscosity, leading to blockages.

1.7.2 Injector Failure

Solid feed and slurry feed injector nozzles frequently fail in entrained flow gasifiers. The extremely rapid devolatilization in the reactor, and subsequent volatiles combustion, leads to very high flame temperatures close to the injector. Abrasion by solid fuel particles is another possible failure mechanism. Evidence from operating gasifiers suggests that slurry-fed designs fail more frequently than those using dry feed.

1.7.3 Refractory Failure

Poor refractory performance is responsible for one outage per month on average [16]. There are two main modes of refractory failure: physical wear and chemical corrosion. Physical wear can be due to spalling (usually under high temperatures), creep, erosion by solid particles, or thermal shock. Temperatures in excess of the refractory design specification could be due to poor thermal management at the wall, poor design with a flame impinging on a small wall area, flow patterns within the gasifier that create hot-spots, or caking coal particles sticking to the wall and burning. Chemical corrosion means the wall itself takes part in chemical reactions.

This would most likely be with some of the ash component materials. Most commercial refractory materials are high in Cr_2O_3 (chromium oxide), which is susceptible to reaction with oxides of Si (silicon), Fe (iron), Al (aluminum) and Ca (calcium) in coal and petroleum coke ash. Coal ash also contains K (potassium), Na (sodium), and Mg (manganese), while petroleum coke ash contains Ni (nickel) and V (vanadium), all of which are corrosive to high-Cr_2O_3 materials. Cooled membranes like those employed by the Shell and Siemens gasifiers go some way towards addressing these problems, but at greater cost than refractory materials.

1.7.4 Slag Blockages

High pressure gasification requires complex slag removal equipment. A slag trap captures the molten slag that runs down the walls of the gasifier and depressurizes it in a lock, for batch removal. Unintended cooling of the slag or a change in the ash fusion temperature (caused by feedstock variability) can lead to partial or full solidification of the slag near the trap. A secondary issue is that of slag corroding the trap. Again, feedstock variability may introduce corrosive ash compounds for which the trap was not designed. In severe cases the trap becomes completely blocked or damaged and requires gasifier shut-down for cleaning and/or repair.

1.7.5 Poor Space Efficiency

Entrained flow gasifiers are enormous devices. Industrial scale units (comprising gasifier and syngas cooler) can reach heights of 80-90 m [11, 17]. They are typically larger than either fixed or fluidized bed devices. This issue is being address by the Pratt & Whitney Rocketdyne (PWR) gasifier, which uses temperatures and pressures in excess of 2,000 °C and 60 atm. The gasifier is claimed to be 90% smaller than conventional entrained flow devices of the same capacity [18]. It is unclear from the limited literature available on the PWR gasifier how wall material performance and adequate thermal management are achieved in this environment. Entrained flow gasifiers also suffer from the existence of internal "dead zones". These are volumes within the gasifier that, through a mismatch of physical design and the properties of the flow field, serve no useful purpose for fuel conversion.

1.7.6 Downstream Fouling and Poisoning

Three gasifier outputs are particularly detrimental to downstream plant operations: unburned char, fly ash particles, and sulfurous compounds. Char and fly ash cause physical fouling of heat exchange surfaces in syngas coolers and steam generators. Freezing of slag in piping can also result in jammed valves, etc. Sulfur compounds that leave the gasifier, such as H_2S and COS, can poison catalysts for conversion of syngas to fuels and chemicals. These sulfur compounds can also attack metal surfaces such as turbine blades. After combustion to SO_2 (sulfur dioxide) and SO_3 (sulfur trioxide) in the gas turbine and subsequent cooling in the heat recovery steam generation (HRSG) system, these sulfur components can form corrosive sulfuric acid on surfaces that are below the acid dew point temperature.

1.7.7 Poor Plant Integration

IGCC and polygeneration plants are extremely complex, and in many cases, individual plant components may not be optimized for overall plant configuration.

1.7.8 Example of Gasifier Operational Record

Information on the operational record of the two GE gasifiers at the Eastman Chemicals Plant in Kingsport, Tennessee is presented in the report "Update on Operations, Economic Improvement Opportunities" [19]. The Kingsport plant gasifies 1,300 metric tonnes per day (tpd) of bituminous coal to produce acetic anhydride, acetic acid, methyl acetate and methanol. The facility employs one operational GE gasifier and keeps a second on "hot standby". This means that natural gas is continuously burned in the standby gasifier to keep its internal temperature sufficiently high to allow fast switchover from one gasifier to the other in the event of an unplanned outage. Table 1-4 presents the reasons for gasifier shutdowns for the period January-September 2004. Note that these figures do not account for the need to switch from one gasifier to the other.

Table 1-4: Gasifier shutdowns for January-September 2004

Description	Quantity	Downtime (hours)
Coal quality related	4	15.2
Flange leak	1	0
Valve failure	1	36.1
Planned for tri-annual shutdown	1	241 (10 days)
Refractory	1	4.2
Slurry feed pump	1	4.4
Relief valve failure	1	0

Figure 1-8 is reproduced from the Eastman report [19] and shows the times between gasifier switches and shutdowns for the period 1984 to 2004. Note that the Kingsport gasifiers began operation in 1983. The data shows that even after 20 years of gasifier operational experience, the longest the plant has continuously run is roughly 40 days. The report also highlights the fact that the Kingsport gasification facility is one of the most reliable such facilities in the world.
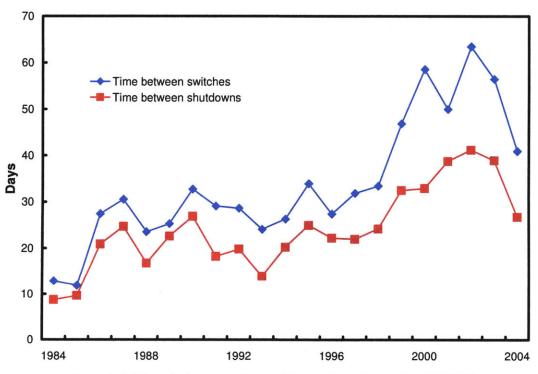
Figure 1-8: Times between gasifier switches and shutdowns for 1984-2004

1.8 Computer-Based Simulation as a Solution

1.8.1 The Need for Models

Computer-based simulation is one method whereby improved gasifier designs and plant layouts can be analyzed and compared. The U.S. Department of Energy recognizes simulations as one of the most important steps to greater commercialization of gasification [20]:

> *"The need for more sophisticated advanced gasifier and other process models ranks very high. Needs include: (1) defining what models are clearly needed to benefit the entire industry before developing them; (2) focusing model development on dynamic models that can be used not only to predict the steady-state performance of a gasifier, but also to simulate transient events; and (3) validating the models with actual plant data rather than using theoretical diagnostics or dynamic modeling as substitutes for actual operational experience."*

These models would ideally employ computational fluid dynamics (CFD) and extremely detailed submodels for the various physical, chemical and dynamic processes occurring inside the gasifier. Table 1-5 highlights the roles that computer-based simulation can play in addressing the problems encountered by current entrained flow gasifier designs.

Table 1-5: The roles of simulation in addressing current EFG problems

Current problem	Solutions	How they help
Lack of dynamic feedstock flexibility	Dynamic char modeling Char properties	Accurately models feedstock switching
Injector failure	Turbulence-chemistry-radiation interactions	Accurately models flow and temperature distribution
Refractory failure	Particle dispersion Turbulence-chemistry-radiation interactions Slag properties	Accurately models wall interactions, thermal stresses, pressure effects and abrasion
Slag blockages	Turbulence-chemistry-radiation interactions Slag properties	Accurately models slag flow, composition and temperature distribution
Poor space efficiency	Particle dispersion Turbulence-chemistry-radiation interactions	Accurately models flow and conversion
Downstream fouling and poisoning	Particle dispersion Particle ragmentation Nitrogen and sulfur chemistry	Accurately models flow, conversion, ash distribution and pollutant formation
Poor plant integration	Dynamic gasifier simulation	Increases understanding of the role of the gasifier as part of the IGCC/polygeneration plant

The detail required for CFD simulations, however, makes integration of these models with process flowsheet models of the overall IGCC or polygeneration plant difficult and impractical. For this reason, the work presented here focuses on the development of reduced order models (ROMs), which capture the most important processes of gasification, but without the computational expense of more detailed simulation. The ROM will primarily be used to simulate the interactions of the gasifier with the rest of the IGCC or polygeneration plant, i.e. we seek to address the issues of feedstock flexibility (Section 1.7.1), downstream fouling and poisoning (Section 1.7.6) and plant integration (Section 1.7.7).

1.8.2 Reduced Order Models

Reduced order modeling involves the representation of the gasifier by a reactor network model (RNM). The RNM consists of idealized chemical reactors, including 0-D well-stirred reactors (WSRs or CSTRs) and 1-D plug flow reactors (PFRs). The appropriate use of 0-D and 1-D components in the RNM drastically reduces the computational expense of simulation compared to CFD. RNMs have been used for modeling EFGs since the 1970s [21-33]. A review of the available literature on the use of RNMs in gasifier modeling yielded interesting results. Table 1-6 shows the important characteristics of existing gasifier models that incorporate RNMs. It should be noted that any of the works shown in Table 1-6 that were published before the 1990s should not be considered "reduced order models". One- or two-dimensional models that incorporated RNMs were the most sophisticated simulation tools widely available at the time. The following trends are observable when reviewing the models presented in Table 1-6:

- All of these studies use a combination of WSRs and PFRs in series, in essence assuming fully 1-D axial flow.
- With the exception of Smith [24, 25], no consideration is given to either mixing or recirculation.
- With the exception of Bockelie [30], none of the studies consider the fate of ash/slag in the gasifier.
- Many of the studies apply arbitrary or unknown temperature boundary conditions on the gasifier walls.

49

- While some of the studies track the formation of sulfurous pollutants, none do so for nitrogenous pollutants.

- With the exception of Robinson [33], none of the current models are capable of dynamic simulation.

- With the exception of Bockelie [30], all of the studies focus on one gasifier design. Some studies do not validate their models against experimental results.

- With the exception of Valero et al [31, 32], none of the studies allow for blending of different feedstocks, such as coal, petcoke, biomass and/or waste.

From this review of the state-of-the-art, it is clear that there is a need for ROMs that incorporate submodels for variable feedstock properties, mixing and recirculation, slag behavior, heat loss through gasifier walls and pollutant formation. These submodels are required in addition to those already used in the previous studies, i.e. devolatilization, char conversion, particle properties, and chemical reactions. It is also important that these models are dynamic and validated for use over a range of commercial EFG designs.

The objectives of this research are therefore to develop a flexible, robust and dynamic reduced order model for simulation of a wide-range of solid fuel entrained flow gasifiers, to validate the model with experimental data, and to integrate it into an IGCC or polygeneration system software simulation model.

Table 1-6: Important characteristics of gasifier models that incorporate RNMs

Work	Ref	Gasifier	RNM	Mixing & recirc.	Particle props.	Dry & devol.	Char kinetics	Wall heat transfer	Pollutants	Slag	Dynamic	Validated
Ubhayakar (1977)	[21]	Generic 1-stage	1x 1-D PFR	Mixing	Fixed	Rate & yield	Yes	Unknown	No	No	No	No
Stickler (1979)	[22]	Generic 1-stage	1x 1-D PFR	Mixing	Fixed	Rate & yield	Yes	No				Yes
Wen (1979)	[23]	Pilot-scale Texaco (GE)	2 x WSR 1 x 1-D PFR	No	Fixed	Yes	Yes	Arbitrary	H_2S only	No	No	Yes
Smith (1980)	[24, 25]	Generic 1-stage	1 x 1-D PFR	Yes	Fixed	Rate & yield	Yes	Yes	No	No	No	Yes
Govind (1984)	[26]	Pilot-scale Texaco (GE)	2 x WSR 1 x 1-D PFR	No	Fixed	Rate & yield	Yes	Arbitrary	H_2S only	No	No	Yes
Phuoc (1987)	[27]	Generic 1-stage	1 x 2-D PFR	No	Fixed	Rate & yield	Yes	Arbitrary	No	No	No	No
Vamvuka (1995)	[28, 29]	Generic 1-stage	1 x 1-D PFR	No	Fixed	Unknown	Yes	Yes	No	No	No	No
Bockelie (2003)	[30]	GE, SCGP, E-GAS	1 x WSR	No	Yes	Yes	Yes	Yes	H_2S & COS	Yes	No	Yes
Valero (2006)	[31, 32]	PRENFLO	2 x WSR	No	Unknown	Yes	Yes	Arbitrary	H_2S & COS	No	No	Yes
Robinson (2008)	[33]	GE	1 x WSR 3 x WSR for cooler	No	No	No	No	Yes	H_2S only	No	Yes	No

1.9 Chapter Summary

This chapter described the potential role of gasification in addressing global energy and greenhouse gas emission issues. The focus of the research on entrained flow gasifiers (EFGs) was justified. Commercial EFG designs were described and compared. Technical issues with these current designs were presented and discussed. The roles of computer-based simulations generally, and reduced order models (ROMs) specifically were described. The next chapter will describe in detail the structure of the ROM developed as part of this research.

1.10 References

1. Energy Information Administration, 2007: "International Energy Outlook 2007". http://www.eia.doe.gov/oiaf/ieo/index.html
2. Solomon, S. et al, 2007: Technical Summary. In: "Climate Change 2007: The Physical Basis. Contribution of Working Group I to the Fourth Assessment Report of the Intergovernmental Panel on Climate Change" [Solomon, S., D. Qin, M. Manning, Z. Chen, M. Marquis, K.B. Averyt, M. Tignor, H.L. Miller (eds.)]. Cambridge University Press, Cambridge, United Kingdom and New York, NY, USA. http://ipcc-wg1.ucar.edu/wg1/wg1-report.html
3. Intergovernmental Panel on Climate Change [IPCC]. IPCC Special Report on Carbon Dioxide Capture and Storage. Prepared by Working Group III of the Intergovernmental Panel on Climate Change Cambridge, UK & New York, NY, USA: Cambridge University Press; 2005.
4. Massachusetts Institute of Technology [MIT]. The Future of Coal: options for a carbon-constrained world Cambridge, MA: 2007.
5. National Energy Technology Laboratory [NETL]. Cost and Performance Baseline for Fossil Energy Plants: Volume 1: Bituminous Coal and Natural Gas to Electricity. Revision 1 2007. DOE/NETL-2007/1281
6. Shadle L J, Berry D A, Syamlal M. Coal Conversion Processes, Gasification. Kirk-Othmer Encyclopedia of Chemical Technology. Vol. 6. John Wiley & Sons, Inc.; 2002.
7. National Energy Technology Laboratory [NETL]. Gasification Database: Active and Planned Commercial Gasification Plants 2007.
8. Niksa S, Liu G s, Hurt R H. Coal conversion submodels for design applications at elevated pressures. Part 1. devolatilization and char oxidation, Progress in Energy and Combustion Science 2003; 29: 425-477.
9. Shi S P, Zitney S E, Shahnam M, Syamlal M, Rogers W A. Modelling coal gasification with CFD and discrete phase method, Journal of the Energy Institute 2006; 79: 217-221.
10. Soelberg N R, Smoot L D, Hedman P O. Entrained flow gasification of coal, Fuel 1985; 64: 776-781.
11. Holt N. IGCC & Gasification for a Changing marketplace. Gasification Technologies Council [GTC]: Gasification Technologies Conference; 2006 Oct.; Washington (DC).
12. GE Energy: 2007 Press Release [webpage on the Internet]. n.d. [cited 2009 Aug 29]. Available from: http://www.gepower.com/about/press/en/2007press/061507.htm

13. Sakamoto K. Deployment of Air-Blown IGCC Technology with Carbon Capture. Gasification Technologies Council [GTC]: Gasification Technologies Conference; 2007 Oct.; San Francisco (CA).

14. Electric Power Research Institute [EPRI]. Cool Water Coal Gasification Program: Final Report 1990 Dec. GS-6806

15. Tampa Electric Company [TECO]. Tampa Electric Polk Power Station Integrated Gasification Combined Cycle Project: Final Technical Report. August 2002. DE-FC-2191MC27363

16. Bennett J. Field test Results, Phosphate-Modified High Chrome Oxide Refractory for Slagging Gasifiers. Gasification Technologies Council [GTC]: Gasification Technologies Conference; 2007 Oct.; San Francisco (CA).

17. Chhoa T. Shell Clean Coal Energy in Asia-Pacific. Gasification Technologies Council [GTC]: Gasification Technologies Conference; 2006 Oct.; Washington (DC).

18. Hartung J. Pratt & Whitney Rocketdyne (PWR) Compact Gasification System. Gasification Technologies Council [GTC]: Gasification Technologies Conference; 2007 Oct.; San Francisco (CA).

19. Moock N. Update on Operations, Economic Improvement Opportunities. Gasification Technologies Council [GTC]: Gasification Technologies Conference; 2004 Oct.; Washington (DC).

20. United States Department of Energy [U.S. DOE]. Gasification Technologies: Gasification Markets and Technologies – Present and Future – An Industry Perspective 2002 July. DOE/FE-0447

21. Ubhayakar S K, Stickler D B, Gannon R E. Modelling of Entrained-Bed Pulverized Coal Gasifiers, Fuel 1977; 56 (3): 281-291.

22. Stickler D B, Becker F E, Ubhayakar S K. Combustion of Pulverized Coal in High Temperature Preheated Air. American Institute of Aeronautics and Astronautics [AIAA]: 17th Aerospace Sciences Meeting; 1979 Jan. 15; New Orleans (LA): 1979, 79-0298

23. Wen C Y, Chaung T Z. Entrainment Coal Gasification Modeling, Industrial and Engineering Chemistry Process Design and Development 1979; 18 (4): 684-695.

24. Smith P J, Smoot L D. One-Dimensional Model for Pulverized Coal Combustion and Gasification, Combustion Science and Technology 1980; 23: 17-31.

25. Smith P J. Theoretical modeling of coal and gas fired turbulent combustion and gasification processes [dissertation]. Provo (UT): Brigham Young University; 1979. PhD thesis

26. Govind R, Shah J. Modeling and Simulation of an Entrained Flow Coal Gasifier, AIChE Journal 1984; 30 (1): 79-92.

27. Phuoc T X, Durbetaki P. Pulverized Coal Conversion in Downflow Gasifier, International Journal for Numerical Methods in Engineering 1987; 24: 203-218.

28. Vamvuka D, Woodburn E T, Senior P R. Modeling of an entrained flow coal gasifier: 1. Development of the model and general predictions, Fuel 1995; 74 (10): 1452-1460.

29. Vamvuka D, Woodburn E T, Senior P R. Modeling of an entrained flow coal gasifier: 2. Effect of operating conditions on reactor performance, Fuel 1995; 74 (10): 1461-1465.

30. Bockelie M, Denison M, Chen Z, Senior C, Sarofim A. Using Models to Select Operating Conditions for Gasifiers. Pittsburgh Coal Conference; 2003 Sept. 15; Pittsburgh (PA): 2003

31. Uson S, Valero A, Correas L, Martinez A. Co-Gasification of Coal and Biomass in an IGCC Power Plant: Gasifier Modeling, International Journal of Thermodynamics 2004; 7 (4): 165-172.
32. Valero A, Uson S. Oxy-co-gasification of coal and biomass in an integrated gasification combined cycle (IGCC) power plant, Energy 2006; 31: 1643-1655.
33. Robinson P J, Luyben W L. Simple Dynamic Gasifier Model That Runs in Aspen Dynamics, Ind Eng Chem Res 2008; 47: 7784-7792.

Chapter 2 MODEL DESCRIPTION

2.1 Chapter Overview

This chapter describes in detail the structure of the reduced order model. The reactor network model for one- and two-stage gasifiers is described. The implementation of the model in Aspen Custom Modeler is detailed, with special attention paid to the roles of conservation equations and submodels. Each of the submodels used in the model is described in detail.

2.2 The Reactor Network Model

Reactor Network Models (RNMs) are used to reduce the computational expense of gasifier simulation, compared to CFD-based models. It is therefore important to recognize the necessary differences between RNMs suitable for EFGs of vastly different design. The main design variation to consider when choosing an RNM is the number of firing stages of the gasifier. The next section describes an RNM for a one-stage gasifier. The subsequent section describes the modification of the one-stage RNM for use in a two-stage gasifier. The RNMs described below represent the base case configurations. Later sections describe the results of sensitivity analysis performed for the RNM.

2.2.1 One-Stage RNM

For modeling a one-stage gasifier the reactor network model (RNM) developed by Pedersen et al. [1, 2] is chosen. Pedersen's RNM was developed to study nitrogenous pollutant formation in axially-fired coal combustors. Use of an RNM in this case allowed the incorporation of complex elementary chemistry without the computational expense of detailed CFD-based simulations. Pedersen et al took the following approach to constructing an RNM:

1. CFD simulation of the combustor, without elementary nitrogen chemistry, to establish fluid and particle trajectories and streamlines,
2. Determination of zero axial velocity boundaries and fluid and particle residence times based on CFD simulation results,

3. Selection of RNM configuration and geometry based on CFD simulation results,

4. Validation of the RNM using CFD simulation results and experimental data.

Figure 2-1 is reproduced from [1] and shows fluid and particle trajectories, streamlines and the zero axial velocity boundaries for an axially-fired coal combustor. The predicted streamlines, shown in Figure 2-1d show two recirculation zones; one at the inlet (on the left hand side) and another towards the center of the combustor, which resembles an eye. The locations of the zero axial velocity boundaries indicate the existence of four distinct zones in the combustor: the internal recirculation zone (IRZ), the jet expansion zone (JEZ), the external recirculation zone (ERZ) and the downstream zone (DSZ). The characteristics of these zones as well as their application to the ROM are discussed below.
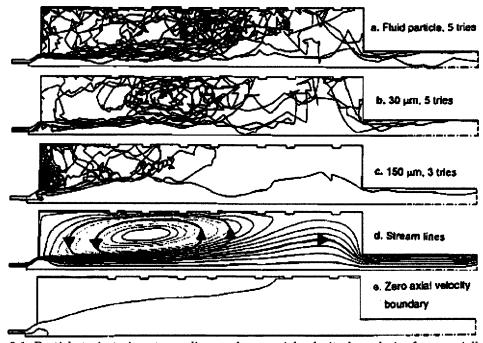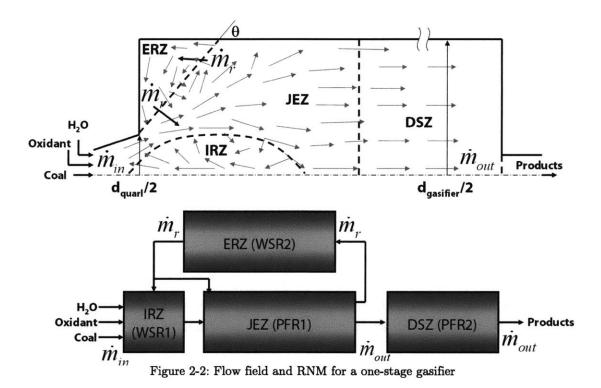
Figure 2-1: Particle trajectories, stream lines and zero axial velocity boundaries for an axially-fired coal combustor (reproduced from [1])

A schematic of the flow in an axially-fired swirling coal combustor and the RNM is shown in Figure 2-2. It consists of four reactors or zones; two WSRs and two PFRs. Feedstock, oxidant and H_2O (slurry or steam) enter at one end of the gasifier via swirl injectors. In the case of the slurry-fed GE gasifier for example,

coal slurry is introduced via an annular injector and oxygen enters via swirling central and annular injectors. In a reactor of this configuration, two recirculation zones are established; an internal recirculation zone (IRZ) and an external recirculation zone (ERZ). These recirculation zones correspond to those described above for Pedersen's work.

Figure 2-2: Flow field and RNM for a one-stage gasifier

The inlet streams mix vigorously with each other and with hot, recirculated gas and particles in the IRZ, which is represented by a WSR. To a first approximation, the structure of the IRZ may be considered to be governed primarily by the degree of swirl of the inlet streams. The precise inlet geometry and swirl conditions for most gasifiers are not known, so the assumption is made that the degree of swirl is sufficiently high to ensure full mixing of the inlet streams within a length of one quarl diameter (d_{quarl} in Figure 2-2) from the gasifier inlet. For axially-fired one-stage EFGs, such as the GE and Siemens designs, the IRZ is therefore modeled as a cylinder of diameter and length d_{quarl}, where d_{quarl} is the diameter of the quarl. For radially-fired one-stage EFGs, such as the SCGP and PRENFLO designs, the base case IRZ diameter and length are equal to the diameter of the gasifier, $d_{gasifier}$. All inlet streams are assumed to fully pass through the IRZ.

The two-phase flow leaves the IRZ fully mixed and enters the jet expansion zone (JEZ), where the sudden expansion at the inlet of the gasifier causes the flow to spread out. The JEZ is represented by a truncated conical PFR. As the flow approaches the walls of the gasifier, detrainment from the expanding jet occurs and the flow splits into two streams. The portion of the flow that detrains from the jet flows back towards the IRZ and the front-end of the JEZ through the external recirculation zone (ERZ), which is represented by a WSR.

To a first approximation, the structures of the JEZ and ERZ may be considered to be governed primarily by the geometry of the gasifier, and more specifically by the ratio of $d_{gasifier}$ to d_{quarl}. Since the precise inlet geometry of the gasifiers under consideration are not known, the assumption is made that the quarl diameter is sufficiently small compared to that of the gasifier, so that the JEZ can be modeled as expanding as if it were a free jet.

The remainder of the flow leaving the JEZ, which does not enter the ERZ, proceeds to the reactor exit via a fully 1-D flow in the downstream zone (DSZ). In the original work by Pedersen et al, the DSZ was represented using a WSR. The present work uses a PFR as it is better able to simulate the relatively slow gasification reactions.

Five parameters are needed to use this RNM: the length and diameter of the IRZ (L_{IRZ} and d_{IRZ}), the jet expansion angle (θ), the recirculation ratio ($\alpha = \dot{m}_r / \dot{m}_{in}$), and the fraction of flow entering the JEZ directly from the ERZ ($f_{JEZ} = \dot{m}_{ERZ \rightarrow JEZ} / (\dot{m}_{ERZ \rightarrow JEZ} + \dot{m}_{ERZ \rightarrow IRZ})$). In the expression for recirculation ratio, $\dot{m}_r$ and $\dot{m}_{in}$ refer to mass flow rates of the recirculating and inlet streams, respectively. The present work evaluates these parameters in the same manner as Pedersen et al. [1, 2]. Therefore, $L_{IRZ} = d_{IRZ}$ is chosen, as described above. The jet expansion angle is increased by swirl and decreased by combustion. As discussed above, the JEZ is assumed to expand as if it were a turbulent free jet, so a value of 9.7° is chosen for θ. This is the maximum observed jet expansion angle of a turbulent free jet (Chap. 2 in [3]). The recirculation ratio is evaluated using the method of Thring and Newby, where $\alpha = 0.47(d_{gasifier} / d_c) - 0.5$ (Chap. 2 in [3]), where d_c is the

characteristic diameter of the burner, which in this case is chosen as $d_c = d_{quarl}$ [4]. The Thring and Newby method assumes that $d_{gasifier}$ is significantly larger than d_c. It is not intended for use in cases where $d_{gasifier}$ approaches d_c. In these cases there will be no recirculation. The base case value for f_{JEZ} is set to zero, that is, all flow leaving the ERZ enters the IRZ. The length of the JEZ, L_{JEZ} is calculated by examination of the geometry of the RNM, so $L_{JEZ} = (d_{gasifier} - d_c)/2\tan\theta$. The length of the ERZ is $L_{ERZ} = L_{IRZ} + L_{JEZ}$.

It is very important to note that the ideal way to determine RNM structure is through CFD simulation, in a manner similar to the work of Pedersen et al. In the present work, at time of writing, no CFD simulation results are available for RNM construction. Therefore RNM parameters are chosen, as explained above, based on the observations of Pedersen et al. The impact of these assumptions on ROM results is examined in later sections using sensitivity analysis. Gasifier CFD simulations are currently under development in the Reacting Gas Dynamics Laboratory at MIT. When the results of this work become available, they should be used to refine RNM geometry in the ROM.

2.2.2 Flexible One- or Two-Stage RNM

The one-stage RNM described above is insufficient for modeling two-stage gasifiers, such as the CoP E-GAS or MHI gasifiers, which must also be considered. The one-stage RNM also does not include a zone for syngas cooling, which all commercial gasifiers employ. Therefore the one-stage RNM is modified by the addition of two extra reactors or zones, as shown in Figure 2-3.

In this flexible RNM, the first stage (combustor) of a two-stage gasifier is represented by a WSR, identified as the coal combustion zone (CCZ). In all two-stage designs, the first stage combustor is used to supply heat, CO_2, H_2O and char for the endothermic gasification reactions in the second stage (reductor). Oxygen is supplied in such quantities as to fully oxidize the volatile components of the coal, but not consume all of the resulting char. Therefore the stream exiting the CCZ is assumed to consist only of CO_2, H_2O, N_2, SO_2 and unconverted char. The RNM employs a switch that can be used to stop the material and energy flows from the

CCZ to the IRZ. This means that one-stage gasifiers, such as the GE, ECUST, PRENFLO, SCGP and Siemens designs can easily be modeled with this RNM.

The Cooler zone is represented by a PFR followed by a WSR. As described below in this section and in Section 2.5.9, the use of a PFR and WSR in series allows the user to examine all potential syngas cooling options: no cooling, radiant-only cooling, quench-only cooling, and radiant and quench cooling.
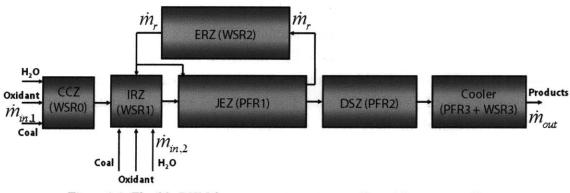
Figure 2-3: Flexible RNM for a one- or two-stage gasifier with syngas cooling

In addition to allowing the user to switch between one- and two-stage gasifiers, the flexible RNM uses other switches to allow simulation of a wide range of EFGs with different design characteristics. Refer to Table 1-6 for examples of design characteristics of commercial EFG designs. These switches are shown in Table 2-1. Flow direction in the ROM is determined by the sign of the gravitational acceleration constant used in the gas and particle momentum equations (see Table 2-2). A switch (FlowDirection) is used to control this. The method of feedstock delivery has a strong influence on the overall gasifier energy balance, and hence the exit temperature and compositions. Slurry-fed designs require sensible heat to vaporize liquid H_2O, while dry-fed designs do not. The ROM therefore includes a switch (α_{slurry}), which treats inlet H_2O streams as liquid or gas depending on its value.

Injector configuration is not directly dealt with in the ROM because this design characteristic manifests itself primarily through alterations to the fluid-particle flow field near the injector. These fields are simplified by the RNM and so are not truly predictable by the ROM. However, the base cases of axially-fired designs use RNM parameters similar to those of Pedersen et al [1, 2], i.e. $d_{IRZ} = d_{quarl}$, among other

60

expressions. The set of assumptions adopted from Pedersen's work is subject to sensitivity analysis, the results of which are presented in Chapter 3. For radial/opposed injector designs, it is assumed that $d_{IRZ} = d_{gasifier}$, as injection occurs at the gasifier walls.

Molar composition of the oxidant streams, while not strictly switches, can be varied to simulate O_2- or air-blown designs. The use of O_2-enriched air can also be examined. Composition of the ROM oxidant streams is also varied when simulating use of the gasifier with non-solid feeds, for example during gasifier preheat.

Heat transfer and hence temperature profiles in the gasifier are strongly affected by wall lining. Commercial designs may use refractory- or membrane-lined walls to achieve different slag behavior, as described in Section 1.6.5. Some experimental gasifiers, such as the CSIRO design, use electric heaters to maintain uniform wall temperature or a fixed temperature gradient for feedstock studies. The switch "CoolingSteam" is used to select the wall layer energy conservation equations appropriate for a particular design. For example, for designs that do not employ membrane-cooling, the stream of cooling water still exists in the ROM, but heat transfer to the cooling water is disabled.

The final switch in the ROM (CoolingMethod) allows the user to choose between the various syngas cooling options found in commercial gasifier designs. The type of syngas cooling system affects exit temperature and composition. The rate at which cooling occurs determines the extent to which reactions proceed during the cooling process. For example, high cooling rates found in quench vessels will likely freeze chemical composition. The switch performs the following functions:

- No cooling: CoolingMethod = 0. Outlet of syngas cooling submodel equals inlet.
- Radiant only: CoolingMethod = 1. Syngas cooling submodel uses 1-D PFR to simulate radiant syngas cooler.
- Quench only: CoolingMethod = 2. Syngas cooling submodel uses WSR to simulate quench cooler.

- Radiant and quench: CoolingMethod = 3. Syngas cooling submodel uses 1-D PFR to simulate radiant syngas cooler, followed by WSR to simulate quench cooler.

Table 2-1: Switches used in flexible one- or two-stage RNM

Characteristic	Switch	Description	Range of values
Flow direction	FlowDirection	Allows switch between down-flow and up-flow designs by changing the sign of the gravitational acceleration constant (g)	-1 or +1 -1 = Up-flow +1 = Down-flow
Feedstock delivery	α_{slurry}	Allows switch between slurry-fed and dry-fed (steam) designs by calculating properties for the H_2O inlet streams for liquid or gaseous H_2O, respectively. A mix of slurry and steam is also allowed.	0-1 0 = Dry-fed (steam) 1 = Slurry-fed
Injector configuration	d_{IRZ}	Allows switch between axial and opposed/radial injection by setting the IRZ diameter equal to that of the quarl or that of the gasifier, respectively.	d_{quarl}-$d_{gasifier}$ d_{quarl} = Axial $d_{gasifier}$ = Opposed/radial
Oxidant	$\hat{X}_{i,in}$	Allows switch between O_2- and air-blown designs by changing the molar composition of the oxidant inlet streams. Also allows any gaseous specie to be injected into the gasifier, e.g. CH_4 for preheat or N_2/CO_2 for feedstock pressurization.	0-1
Number of stages	α_{stage1}	Allows switch between one-stage and two-stage designs by excluding or including CCZ-to-IRZ connection, respectively.	0 or 1 0 = One-stage 1 = Two-stage
Wall lining	CoolingSteam	Allows switch between refractory-lined, membrane-lined and electrically-heated wall designs by changing the form of the mass and energy conservation equations used for the gasifier wall layers.	0, 1 or 2 0 = Refractory-lined 1 = Membrane-lined 2 = Electrically-heated
Syngas cooling	CoolingMethod	Allows switch between syngas cooling methods by changing the inlet and outlet values used in the syngas cooling submodel.	0, 1, 2 or 3 0 = No cooling 1 = Radiant only 2 = Quench only 3 = Radiant and quench

2.3 Conservation Equations

Within each reactor or zone of the RNM, the ROM expresses mass, energy and momentum conservation equations in a fixed reference frame, treating solid and gas phases as pseudo-fluids. In addition to the conservation equations for the gas-solid flow in the gasifier, mass and energy balances are performed on the walls of the gasifier, to establish the wall temperature profile and slag layer thickness. The conservation equations for a 1-D PFR, as well as a legend explaining the terms

used, are shown in Table 2-2. The same equations are applied to the WSRs, with $\partial/\partial x$ terms replaced by $1/L_{WSR}$, where L_{WSR} is the length of a WSR. The RNM and the conservation equations are solved in Aspen Custom Modeler (ACM). The conservation equations shown in Table 2-2 are one-dimensional in the axial direction. They are expressed in the ROM as dynamic equations, even for steady-state simulations. ACM allows easy switching between steady-state and dynamic simulation runs.

Mass conservation equations for gas-phase species, particle-phase species (both proximate and ultimate) and slag phases, which are shown below, include terms for accumulation $(\partial m/\partial t)$, advection $(\partial \dot{m}/\partial x)$ and mass addition/subtraction (S terms for chemical reactions and/or $\dot{m}'_{slagging}$ for migration of particles to wall). The gas-phase mass conservation equation also includes a diffusive term, which is dependent on $D_{g,eff,x}$, the effective gas phase diffusivity along the x-axis. The expression for $D_{g,eff,x}$ is shown further below, along with that for $k_{g,eff,x}$ (introduced below).

Gas-phase species mass conservation equation

$$\frac{\partial\left(A_{CS}X_i\rho_g\varepsilon_g\right)}{\partial t} = \frac{\partial}{\partial x}\left(A_{CS}D_{g,eff,x}\frac{\partial\left(X_i\rho_g\varepsilon_g\right)}{\partial x}\right) - \frac{\partial\left(A_{CS}v_g X_i\rho_g\varepsilon_g\right)}{\partial x} + A_{CS}S_i \quad \text{(Eq. 2-1)}$$

Solid-phase proximate species mass conservation equation

$$\frac{\partial\left(A_{CS}\rho_p\varepsilon_p X_j\right)}{\partial t} = -\frac{\partial\left(A_{CS}\rho_p\varepsilon_p X_j v_p\right)}{\partial x} + A_{CS}S_j - \dot{m}'_{slagging}X_j \quad \text{(Eq. 2-2)}$$

Solid-phase ultimate species mass conservation equation

$$\frac{\partial\left(A_{CS}\rho_p\varepsilon_p X_k\right)}{\partial t} = -\frac{\partial\left(A_{CS}\rho_p\varepsilon_p X_k v_p\right)}{\partial x} + A_{CS}S_k - \dot{m}'_{slagging}X_k \quad \text{(Eq. 2-3)}$$

Slag mass conservation equation

$$2\pi r_{gasifier}\rho_{slag}\frac{\partial \delta_{slag}}{\partial t} = -\frac{\partial \dot{m}_{slag}}{\partial x} + \dot{m}'_{slagging} \quad \text{(Eq. 2-4)}$$

Energy conservation equations for gas, particle and slag phases, which are shown below, include terms for accumulation $(\partial(mu)/\partial t)$, advection $(\partial(\dot{m}h)/\partial x)$, heat transfer (via radiation, convection and/or conduction) and enthalpy

63

addition/subtraction (S and R terms for chemical reactions and/or $\dot{m}'_{slagging}h_p$ for migration of particles to wall). In dealing with enthalpy transfers due to chemical reaction, the assumption is made that the heat of all reactions appears in the gas phase.

Gas-phase energy conservation equation

$$\frac{\partial\left(A_{CS}\rho_g\varepsilon_g u_g\right)}{\partial t} = \frac{\partial}{\partial x}\left(A_{CS}k_{g,eff,x}\frac{\partial T_g}{\partial x}\right) - \frac{\partial\left(A_{CS}\rho_g\varepsilon_g h_g v_g\right)}{\partial x}$$

$$+A_{CS}\left(\sum_i h_i\left(S_{dry,i}+S_{dev,i}\right)+\sum_m h_m R_m - h_C R_p\right)+\dot{Q}'_{conv,p\rightarrow g}-\dot{Q}'_{conv,g\rightarrow w}$$

(Eq. 2-5)

Solid-phase energy conservation equation

$$\frac{\partial\left(A_{CS}\rho_p\varepsilon_p u_p\right)}{\partial t} = -\frac{\partial\left(A_{CS}\rho_p\varepsilon_p h_p v_p\right)}{\partial x} - A_{CS}\left(\sum_i h_i\left(S_{dry,i}+S_{dev,i}\right)+\sum_m h_m R_m - h_C R_p\right)$$

$$-\dot{Q}'_{conv,p\rightarrow g}-\dot{Q}'_{rad,p\rightarrow w}-\dot{Q}'_{rad,p\rightarrow p}-\dot{m}'_{slagging}h_p$$

(Eq. 2-6)

Slag energy conservation equation

$$2\pi r_{gasifier}\rho_{slag}\frac{\partial\left(\delta_{slag}u_{slag}\right)}{\partial t} = 2\pi r_{gasifier}k_{slag}\frac{\partial}{\partial x}\left(\delta_{slag}\frac{\partial T_{slag}}{\partial x}\right) - \frac{\partial\left(\dot{m}_{slag}h_{slag}\right)}{\partial x}$$

$$+\dot{Q}'_{conv,g\rightarrow w}+\dot{Q}'_{rad,p\rightarrow w}-\dot{Q}'_{cond,slag\rightarrow w}+\dot{m}'_{slagging}h_p$$

(Eq. 2-7)

The gas-phase energy conservation equation also includes a diffusive term, which is dependent on $k_{g,eff,x}$, the effective gas phase conductivity along the x-axis. The expressions for $D_{g,eff,x}$ and $k_{g,eff,x}$ are shown below. The Peclet numbers for mass and heat transfer, Pe_m and Pe_h respectively, are fixed input parameters whose values are chosen by the user. They can be thought of as ratios of advective to diffusive terms for mass and heat transfer. Their relative importance to overall ROM results is examined using sensitivity analysis. Refer to Chapter 3 for more information.

$$D_{g,eff,x} = v_g r_p / 2Pe_m$$

(Eq. 2-8)

$$k_{g,eff,x} = c_{p,g}\rho_g v_g r_p / 2Pe_h$$

(Eq. 2-9)

Energy conservation equations for wall layers (firebrick (refractory, insulating brick and steel walls), which are shown below, allow for axial and radial heat conduction ($A_{CS} k \partial^2 T / \partial x^2$ and $\dot{Q}'_{cond}$ terms, respectively). Terms for radial conduction ($\dot{Q}'_{cond}$) are quantified in the section dealing with the heat transfer submodel, Section 2.5.6. The outermost wall layer includes terms for radiative and convective loss to the environment. Although not shown in Table 2-2, the ROM also includes mass and energy conservation equations for H_2O coolant flowing in the walls of the gasifier and/or radiant syngas cooler, in the event that such design characteristics are required.

L^{th} wall layer energy conservation equation

$$\frac{\partial \left(A_{CS,l} \rho_l u_l \right)}{\partial t} = A_{CS,l} k_l \frac{\partial^2 T_l}{\partial x^2} + \dot{Q}'_{cond,l-1 \rightarrow l} - \dot{Q}'_{cond,l \rightarrow l+1} \qquad \text{(Eq. 2-10)}$$

External wall layer energy conservation equation

$$\frac{\partial \left(A_{CS,ext} \rho_{ext} u_{ext} \right)}{\partial t} = A_{CS,ext} k_{ext} \frac{\partial^2 T_{ext}}{\partial x^2} + \dot{Q}'_{cond,ext-1 \rightarrow ext} - \dot{Q}'_{conv,ext \rightarrow amb} - \dot{Q}'_{rad,ext \rightarrow amb}$$

$$\text{(Eq. 2-11)}$$

Axial-direction momentum conservation equations for gas and solid phases, shown below, include terms for accumulation ($\partial(mv)/\partial t$), advection ($\partial(\dot{m}v)/\partial x$), momentum transfer ($F''_{g,w}$ and $F''_{g,p}$) and gravity (mg). The momentum transfer terms are evaluated in the fluid dynamics submodel, described in Section 2.5.5. The gas phase axial-direction momentum conservation equation also includes a pressure gradient term ($\partial P / \partial x$). The primary role of the momentum conservation equations in the ROM is to establish particle velocity profile in order to determine overall particle residence times. For the conditions encountered in EFG designs, it has been found that gas-solid momentum transfer strongly affect the solid phase, but have virtually no impact on the gas phase.

Gas-phase axial-direction momentum conservation equation

$$\frac{\partial \left(A_{CS} \rho_g \varepsilon_g v_g \right)}{\partial t} = -\frac{\partial \left(A_{CS} \rho_g \varepsilon_g v_g^2 \right)}{\partial x} + A_{CS} \left(-\frac{\partial P}{\partial x} + \rho_g \varepsilon_g g - F''_{g,w} - F''_{g,p} \right) \quad \text{(Eq. 2-12)}$$

Solid-phase axial-direction momentum conservation equation

$$\frac{\partial\left(A_{CS}\rho_p\varepsilon_p v_p\right)}{\partial t} = -\frac{\partial\left(A_{CS}\rho_p\varepsilon_p v_p^2\right)}{\partial x} + A_{CS}\left(\rho_p\varepsilon_p g + F_{g,p}'''\right)$$

(Eq. 2-13)

Although not shown in Table 2-2 an axial-direction momentum conservation equation is also used for the slag layer on the wall to express $\dot{m}_{slag}$ as a function of slag density, viscosity and thickness. The 1-D Navier-Stokes equation for the slag layer is resolved in a manner similar to lubrication theory. This is discussed in greater detail in the section describing the slag behavior submodel, Section 2.5.8.

The number of particles is conserved in order to determine the volume fraction of particles at each point in the gasifier. N_p refers to the number density of particles in units of m^{-3}. Particle volume fraction is found through the expression $\varepsilon_p = N_p V_p$. The particle conservation equation includes terms for accumulation ($\partial(A_{CS}N_p)/\partial t$), advection ($\partial(A_{CS}N_p v_p)/\partial x$) and migration of particles to wall ($\dot{m}_{slagging}/m_p$). As currently written, the particle conservation equation does not account for particle fragmentation, but could easily be modified if knowledge of fragmentation rates were known.

Particle number conservation equation

$$\frac{\partial\left(A_{CS}N_p\right)}{\partial t} = -\frac{\partial\left(A_{CS}N_p v_p\right)}{\partial x} - \frac{\dot{m}_{slagging}'}{m_p}$$

(Eq. 2-14)

Table 2-2: Conservation equations for 1-D PFR (part 1)

Conserved quantity	Expression	Variable solved for
Gas phase species mass	$$\frac{\partial\left(A_{CS}X_i\rho_g\varepsilon_g\right)}{\partial t} = \frac{\partial}{\partial x}\left(A_{CS}D_{g,eff,x}\frac{\partial\left(X_i\rho_g\varepsilon_g\right)}{\partial x}\right) - \frac{\partial\left(A_{CS}v_g X_i\rho_g\varepsilon_g\right)}{\partial x} + A_{CS}S_i$$	X_i (Gas phase mass fraction)
Solid phase species mass (proximate)	$$\frac{\partial\left(A_{CS}\rho_p\varepsilon_p X_j\right)}{\partial t} = -\frac{\partial\left(A_{CS}\rho_p\varepsilon_p X_j v_p\right)}{\partial x} + A_{CS}S_j - \dot{m}'_{slagging}X_j$$	X_j (Solid phase proximate mass fraction)
Solid phase species mass (ultimate)	$$\frac{\partial\left(A_{CS}\rho_p\varepsilon_p X_k\right)}{\partial t} = -\frac{\partial\left(A_{CS}\rho_p\varepsilon_p X_k v_p\right)}{\partial x} + A_{CS}S_k - \dot{m}'_{slagging}X_k$$	X_k (Solid phase ultimate mass fraction)
Gas phase energy	$$\frac{\partial\left(A_{CS}\rho_g\varepsilon_g u_g\right)}{\partial t} = \frac{\partial}{\partial x}\left(A_{CS}k_{g,eff,x}\frac{\partial T_g}{\partial x}\right) - \frac{\partial\left(A_{CS}\rho_g\varepsilon_g h_g v_g\right)}{\partial x}$$ $$+A_{CS}\left(\sum_i h_i\left(S_{dry,i}+S_{dev,i}\right)+\sum_m h_m R_m - h_C R_p\right) + \dot{Q}'_{conv,p\rightarrow g} - \dot{Q}'_{conv,g\rightarrow w}$$	T_g (Gas temperature)
Solid phase energy	$$\frac{\partial\left(A_{CS}\rho_p\varepsilon_p u_p\right)}{\partial t} = -\frac{\partial\left(A_{CS}\rho_p\varepsilon_p h_p v_p\right)}{\partial x} - A_{CS}\left(\sum_i h_i\left(S_{dry,i}+S_{dev,i}\right)+\sum_m h_m R_m - h_C R_p\right)$$ $$-\dot{Q}'_{conv,p\rightarrow g} - \dot{Q}'_{rad,p\rightarrow w} - \dot{Q}'_{rad,p\rightarrow p} - \dot{m}'_{slagging}h_p$$	T_p (Particle temperature)
Gas phase momentum	$$\frac{\partial\left(A_{CS}\rho_g\varepsilon_g v_g\right)}{\partial t} = -\frac{\partial\left(A_{CS}\rho_g\varepsilon_g v_g^2\right)}{\partial x} + A_{CS}\left(-\frac{\partial P}{\partial x}+\rho_g\varepsilon_g g - F''_{g,w} - F''_{g,p}\right)$$	v_g (Gas velocity)
Solid phase momentum	$$\frac{\partial\left(A_{CS}\rho_p\varepsilon_p v_p\right)}{\partial t} = -\frac{\partial\left(A_{CS}\rho_p\varepsilon_p v_p^2\right)}{\partial x} + A_{CS}\left(\rho_p\varepsilon_p g + F''_{g,p}\right)$$	v_p (Particle velocity)
Particle number	$$\frac{\partial\left(A_{CS}N_p\right)}{\partial t} = -\frac{\partial\left(A_{CS}N_p v_p\right)}{\partial x} - \frac{\dot{m}'_{slagging}}{m_p}$$	N_p (Particle number density)

Table 2-2: Conservation equations for 1-D PFR (part 2)

Conserved quantity	Expression	Variable solved for
Slag mass	$$2\pi r_{gasifier}\rho_{slag}\frac{\partial \delta_{slag}}{\partial t} = -\frac{\partial \dot{m}_{slag}}{\partial x} + \dot{m}'_{slagging}$$	δ_{slag} (Slag thickness)
Slag energy	$$2\pi r_{gasifier}\rho_{slag}\frac{\partial \left(\delta_{slag}u_{slag}\right)}{\partial t} = 2\pi r_{gasifier}k_{slag}\frac{\partial}{\partial x}\left(\delta_{slag}\frac{\partial T_{slag}}{\partial x}\right) - \frac{\partial \left(\dot{m}_{slag}h_{slag}\right)}{\partial x}$$ $$+\dot{Q}'_{conv,g\to w} + \dot{Q}'_{rad,p\to w} - \dot{Q}'_{cond,slag\to w} + \dot{m}'_{slagging}h_p$$	T_{slag} (Slag Temperature)
L^{th} wall layer energy	$$\frac{\partial \left(A_{CS,l}\rho_l u_l\right)}{\partial t} = A_{CS,l}k_l\frac{\partial^2 T_l}{\partial x^2} + \dot{Q}'_{cond,l-1\to l} - \dot{Q}'_{cond,l\to l+1}$$	T_l (Wall layer temperature)
External wall energy	$$\frac{\partial \left(A_{CS,ext}\rho_{ext}u_{ext}\right)}{\partial t} = A_{CS,ext}k_{ext}\frac{\partial^2 T_{ext}}{\partial x^2} + \dot{Q}'_{cond,ext-1\to ext} - \dot{Q}'_{conv,ext\to amb} - \dot{Q}'_{rad,ext\to amb}$$	T_{ext} (External wall temperature)

Legend:

A = Area	D = Diffusivity	$F^{''}$ = Volumetric force	g = Gravitational acceleration
h = Enthalpy	k = Conductivity	m = Mass	$\dot{m}$ = Mass flow
$\dot{m}'$ = Linear mass flux	N = Number density	P = Pressure	$\dot{Q}'$ = Linear heat flux
R = Rate of chemical reaction	S = Chemical reaction source terms	T = Temperature	u = Internal energy
v = Velocity	X = Mass fraction	ρ = Density	

Subscripts:

amb = Ambient	$cond$ = Conduction	$conv$ = Convection	CS = Cross section
dev = Devolatilization	dry = Drying	eff = Effective	ext = External
g = Gas	i = i^{th} gas phase specie	j = j^{th} proximate species	k = k^{th} ultimate specie
l = l^{th} wall layer	p = Particle	rad = Radiation	$slag$ = Slag on wall
$slagging$ = Slag transport to wall	w = Wall	x = Axial direction	

68

2.4 Model Implementation

As described above, mass, energy and momentum conservation equations are performed at every axial point in each of the PFRs, as well as for each WSR. In order to solve the equations presented in it is necessary to evaluate all of the unknown variables. This is achieved through the use of submodels, which interact with the conservation equations and with each other. Each submodel receives estimated input variables from the conservation equations and/or other submodels, evaluates the required terms for the conservation equations, and sends them to the conservation equations. The ROM evaluates the error for the conservation equations and compares it to the tolerance, or absolute residual, as defined by the ACM solver. For all conditions, the absolute residual is set to 10^{-8}. If the error exceeds the tolerance, the ROM solves the conservation equations and the submodel equations iteratively.

Figure 2-4 shows the role of the submodels in the ROM. Examples of submodels are shown on the left hand side of the figure. Variables that are passed between the conservation equations and submodels are shown by their symbols. The direction of information flow is indicated by the arrows. In addition to the variables evaluated by the submodels, fixed parameters, based on the design of the gasifier are provided. These parameters include information on the gasifier geometry, and physical and thermodynamic properties for the wall layers. Input parameters, which describe the RNM and are discussed above, are also input. The flux of particles to the wall ($\dot{m}'_{slagging}$) is not predictable by the ROM, due to the fact that particle deposition on the walls is highly dependent on the nature of the fluid flow field in the gasifier. For this reason, values for $\dot{m}'_{slagging}$ used in the ROM will either be assumed or taken from CFD simulations. It is apparent from Figure 2-4 that the submodels interact with each other in a highly complex manner. Therefore it is necessary that great care is used in their development. The individual submodels are discussed in detail in the next section.

L_{IRZ}

RNM Parameters

Inputs from x = x$_{n-1}$

θ, α, L_{IRZ}

Gasifier Design

$r_{quart}, r_{gasifier},$

$L_{gasifier}$

$x - position$

Reactor Network Model

A_{CS}

$r_{gasifier}, L_{gasifier},$

$r_{gasifier}$

Ω_{wall}

$\rho_l, k_l, u_l, A_{CS,l}$

N_p, T_p

Heat Transfer

$\dot{Q}'$ terms

$Re_{d,p}, Re_{d,w}, Pr, f$

v_g, v_p

Fluid Dynamics

$F''_{g,p}, F''_{g,w}$

$\rho_g, \varepsilon_g, \varepsilon_p, r_p$

$A''_{p,HT}, r_p$

$X_i, X_j, X_k, T_g, T_p, v_g, v_p, N_p$

$X_j, X_k, \varepsilon_p, \rho_p$

Physical and Thermodynamic Properties

$P, \rho_g, \rho_p, u_g, u_p, h_l, h_g,$

$h_p, h_C, D_{g,eff,x}, k_{g,eff,x}$

$P, \rho_p, h_l, h_p,$

$A''_{p,int}, A''_{p,ext}, A_m,$

h_C, a_{int}, a_{ext}

E_m, n_m, m_p, r_p

X_i, X_j, X_k, T_g, T_p

Chemical Reactions

S_i, S_j, S_k, R_m, R_p

v_p

Drying & Devolatilization

$S_{dry,i}, S_{dev,i}$

$\dot{m}_{slagging}$

Slag Behavior

T_{slag}, δ_{slag}

$\dot{m}_{slag}, k_{slag}, \rho_{slag}, u_{slag}, h_{slag}$

Simultaneous Solution of Conservation Equations at x = x$_n$

Gas phase species mass for X$_i$

Solid phase species mass (proximate) for X$_j$

Solid phase species mass (ultimate) for X$_k$

Gas phase energy for T$_g$

Solid phase energy for T$_p$

Gas phase momentum for v$_g$

Solid phase momentum for v$_p$

Particle number for N$_p$

Slag mass for δ_{slag}

Slag energy for T$_{slag}$

Lth wall layer energy for T$_l$

External wall energy for T$_{ext}$

Outputs to x = x$_{n+1}$

Figure 2-4: Model implementation using submodels

70

2.5 Submodels

2.5.1 Feedstock Properties

The ROM, as it is currently configured, allows for up to three different solid particle types to be injected into each of the stages. For a two-stage gasifier, this means that up to six different particle types can be introduced. Addition of extra particle types can be done easily. The solids can be combustible feedstocks, such as coal, recycled char, petroleum coke, biomass and/or waste, or non-combustible materials, such as fluxing agents (fluxants). Fluxants are used to reduce the viscosity of slag formed during high-temperature gasification and are discussed further in Chapter 4. Results of simulations involving the injection of two feedstocks (coal and petroleum coke or biomass) along with fluxant are also described in Chapter 4.

In determining the overall properties of solid feed streams entering the gasifier, the ROM calculates mass-flow-averaged values for physical, compositional, thermodynamic and kinetic parameters. Examples of these include: particle diameter, ultimate, proximate and ash composition analyses, and Arrhenius reaction rate parameters.

2.5.2 Physical and Thermodynamic Properties

Physical and thermodynamic properties for all gas phase species (with the exception of tar, which will be discussed later) are calculated using the Aspen Properties database. Solid phase properties are calculated according to the information in Table 2-3. Initial bulk particle density is assumed to be unknown and is calculated using Ergun and Menster's correlation based on dry, ash free hydrogen mole fraction ($\hat{X}_{H,daf}$) [5]. Particle bulk density, which is defined as the density of the entire particle including pore space, varies as char conversion occurs on internal and external particle surfaces. The particle density evolution parameter, β, is used to distinguish between particle conversion that takes place on external particle area (constant density) and internal particle area (constant radius) [12]. The density evolution parameter is described by $\beta = \eta r_p A_{p,\text{int}} / V_p$,

71

where η is the effectiveness factor, which will be discussed later, and r_p, $A_{p,int}$ and V_p are the particle radius, internal surface area, and volume, respectively.

Merrick's model [6] is used to predict heat capacity and enthalpy as functions of particle composition and temperature. This allows the thermodynamic properties of the particle to change as devolatilization occurs. Thermodynamic properties of ash are predicted by Kirov's linear heat capacity model [7]. Ash enthalpy of fusion ($\Delta h_{fus,ash}$) is chosen as 230 kJ/kg [8]. Particle internal energy (kJ/kg) is calculated by the thermodynamic relation $u_p = h_p - P/\rho_p$.

The random pore model (RPM) [9, 10] is used to model evolution of mass-specific internal particle area a_p, measured in units of m^2/kg, as a function of carbon conversion (C) and particle structural parameter (Ψ), while a fixed particle roughness ($\Omega=5$) is used to calculate external area. Particle roughness is defined as the ratio of actual particle external surface area to the external area of a smooth spherical particle of equal radius ($4\pi r^2$). Internal surface area evolution is tracked from the onset of devolatilization onwards. Liu's model is used to correlate post-devolatilization internal particle area as a function of initial proximate analysis [11]. The ROM submodels for chemical reaction and heat transfer require certain areas to be expressed as area per unit volume of reactor. These areas are the internal ($A_{p,int}^{"}$) and external ($A_{p,ext}^{"}$) particle areas, and the particle heat transfer area ($A_{p,HT}^{"}$), all measured in terms of m^2/m^3. They are evaluated as described in Table 2-3 using the particle volume fraction, $\varepsilon_p = N_p V_p$, where V_p is calculated at each point in the gasifier via the expression $V_p = 4\pi r_p^3/3$.

Table 2-3: Calculated solid phase properties

Property	Expression	Ref
Bulk density	$1/\rho_p = X_{daf}/\rho_{daf} + X_M/\rho_M + X_{ash}/\rho_{ash}$	
	$\rho_p = \rho_{p,0}\left(m_p/m_{p,0}\right)^{\beta/(3+\beta)}$; $\qquad \beta = \eta r_p A_{p,\mathrm{int}}/V_p$	[12]
	$\rho_{daf,0} = 1000/\left(0.44 + 0.84\hat{X}_{H,daf}\right)$; $\qquad r_p = r_{p,0}\left(\rho_p/\rho_{p,0}\right)^{-1/3}\left(m_p/m_{p,0}\right)^{1/3}$	[5]
	$m_p = \rho_p V_p$; $\qquad V_p = 4\pi r_p^3/3$	
Enthalpy	$h_p = X_{daf}h_{daf} + X_M h_M + X_{ash}h_{ash}$	
	$h_j(T) = h_{f,j} + \int_{T_0}^{T} c_{p,j}dT = h_{f,j} + h_{sens,j}$	
	$h_{sens,daf} = \Re/w_p\left(380/\left(\exp(380/T)-1\right) + 3600/\left(\exp(1800/T)-1\right) - 156\right)$	[6]
	$h_{sens,ash} = 0.594(T-298) + 0.293\times10^{-3}\left(T^2 - 298^2\right)$	[7]
Surface area	$a_p = a_{p,ext} + a_{p,\mathrm{int}}$; $\qquad a_{p,ext} = 4\pi r_p^2\Omega$	
	$a_{p,\mathrm{int}} = a_{p,\mathrm{int},0}(1-C)\sqrt{1-\psi\ln(1-C)}$; $\quad a_{p,\mathrm{int},0} = 10^3\left(218.4X_{VM}/X_{FC} + 98.4\right)$	[9] [10] [11]
	$\psi = 4\pi l_o(1-\varepsilon_0)/a_{p,\mathrm{int},0}^2$	
	$A_{p,\mathrm{int}}^{''} = a_{p,\mathrm{int}}\rho_p\varepsilon_p$; $\qquad A_{p,ext}^{''} = a_{p,ext}\rho_p\varepsilon_p$; $\qquad A_{p,HT}^{''} = a_{p,ext}\rho_p\varepsilon_p$	

Legend :	FC=Fixed carbon	V=Volume (m³)
a=Mass-specific area (m²/kg)	h=Enthalpy (kJ/kg)	VM=Volatile matter
A=Area (m²)	l=Volume-specific length (m/m³)	X=Mass fraction
A˝=Volume-specific area (m²/m³)	m=Mass (kg)	ρ=Density (kg/m³)
C=Conversion	M=Moisture	η=Effectiveness factor
c_p=Specific heat capacity (kJ/kgK)	r=Radius (m)	ψ=Structural parameter
daf=Dry, ash-free	T=Temperature (°C)	ε=Porosity or Volume fraction
		Ω=Roughness

2.5.3 Drying and Devolatilization

During particle drying, all moisture is assumed to leave the particle upon heating. Volatile composition and yield is modeled using the Merrick model [13]. One of the crucial factors leading to the choice of Merrick's model is the fact that it allows, in a simple manner, non-carbon organic species (H, O, N, S), in addition to carbon, to remain in the char after devolatilization, allowing for more realistic pollutant evolution simulation. This distinguishes it from a number of other popular devolatilization models, for example [14]. Rates of drying and devolatilization are

not calculated as these processes are sufficiently fast (~1 ms) compared to the residence time of the particles in the CCZ or IRZ (~20 ms)[1], where they are heated by volatiles combustion in excess O_2 (CCZ), or by recirculated gas and particles (IRZ). Therefore, all particles are assumed to be fully dried and devolatilized upon entering the JEZ. The products of devolatilization are: char, CH_4, C_2H_6, CO, CO_2, tar, H_2, H_2O, NH_3 and H_2S. Both char and tar products have compositions of the form $C_\alpha H_\beta O_\chi N_\delta S_\varepsilon$.

$$C_a H_b O_c N_d S_e \,(\text{daf coal}) \xrightarrow{\;dev\;} \alpha CO + \beta CO_2 + \chi H_2 + \delta H_2O + \varepsilon CH_4 + \phi C_2H_6$$
$$+ \gamma NH_3 + \eta H_2S + \iota \left(C_n H_o O_p N_q S_r \right) (\text{tar})$$
$$+ \varphi \left(C_i H_j O_k N_l S_m \right) (\text{char})$$

(Eq. 2-15)

All of the ash is assumed to remain in the char during devolatilization. In addition to five elemental balances for the global devolatilization process, the elemental compositions of char and tar are fixed, the yields of CH_4 and C_2H_6 are correlated to initial hydrogen content, and the yields of CO and CO_2 are correlated to initial oxygen content. The final constraint on devolatilization is the correlation relating the actual volatiles yield to initial volatile matter (VM) content obtained by proximate analysis (ASTM D3172): $Y_{daf,VM,act} = X_{daf,VM,0} - 0.36 X_{daf,VM,0}^2$. The overall mass balance for Merrick's devolatilization model is shown in matrix form in Figure 2-5.

_____

[1] Calculated by ROM

$$
\begin{bmatrix}
0.98 & 0.75 & 0.8 & 0.4286 & 0.2727 & 0.85 & 0 & 0 & 0 & 0 \\
0.002 & 0.25 & 0.2 & 0 & 0 & 0.0082 & 1 & 0.1111 & 0.1765 & 0.0588 \\
0.002 & 0 & 0 & 0.5714 & 0.7273 & 0.049 & 0 & 0.8889 & 0 & 0 \\
0.01 & 0 & 0 & 0 & 0 & 0.009 & 0 & 0 & 0.8235 & 0 \\
0.006 & 0 & 0 & 0 & 0 & 0.01 & 0 & 0 & 0 & 0.9412 \\
1 & 0 & 0 & 0 & 0 & 0 & 0 & 0 & 0 & 0 \\
0 & 1 & 0 & 0 & 0 & 0 & 0 & 0 & 0 & 0 \\
0 & 0 & 1 & 0 & 0 & 0 & 0 & 0 & 0 & 0 \\
0 & 0 & 0 & 1 & 0 & 0 & 0 & 0 & 0 & 0 \\
0 & 0 & 0 & 0 & 1 & 0 & 0 & 0 & 0 & 0
\end{bmatrix}
\begin{bmatrix}
X_{dev,Char} \\
X_{dev,CH_4} \\
X_{dev,C_2H_6} \\
X_{dev,CO} \\
X_{dev,CO_2} \\
X_{dev,Tar} \\
X_{dev,H_2} \\
X_{dev,H_2O} \\
X_{dev,NH_3} \\
X_{dev,H_2S}
\end{bmatrix}
=
\begin{bmatrix}
X_{daf,C,0} \\
X_{daf,H,0} \\
X_{daf,O,0} \\
X_{daf,N,0} \\
X_{daf,S,0} \\
1-Y_{VM,daf,act} \\
1.31X_{daf,H,0} \\
0.22X_{daf,H,0} \\
0.32X_{daf,O,0} \\
0.15X_{daf,O,0}
\end{bmatrix}
$$

Figure 2-5: Mass balance for devolatilization submodel

Since drying and devolatilization are assumed only to occur in the CCZ and/or IRZ, their source terms for the JEZ, ERZ and DSZ are all zero. Particles are fully dried and devolatilized upon leaving the IRZ, requiring the use of the following source terms in the CCZ and IRZ only.

Drying

Gas phase H_2O: $\quad S_{dry,H_2O} = \varepsilon_p \rho_p X_{M,0} v_p / L_{IRZ}$ \hfill (Eq. 2-16)

Particle-bound moisture (M): $\quad S_{dry,M} = -S_{dry,H_2O}$ \hfill (Eq. 2-17)

Devolatilization

Gas phase species: $\quad S_{dev,i} = \varepsilon_p \rho_p X_{daf,0} X_{dev,i} v_p / L_{IRZ}$ \hfill (Eq. 2-18)

Particle-bound volatile matter (VM): $\quad S_{dev,i} = -\sum_i S_{dev,i}$ \hfill (Eq. 2-19)

As previously stated, certain physical and thermodynamic properties for tar are calculated separately from the other gas phase species as tar does not exist in Aspen Properties. These include density, heat capacity and enthalpy. Tar is assumed to have similar properties, on a mass basis, to benzene (C_6H_6) [15]. Therefore, when calculating molar properties of tar, it is necessary to scale the relevant properties of benzene by the ratio of the molecular weights, e.g.

$\hat{h}_{tar} = \hat{h}_{C_6H_6} w_{tar} / w_{C_6H_6}$, where $w_{tar} = 1/\sum_k \hat{X}_k / w_k$.

75

2.5.4 Chemical Reactions

Chemical reactions appear in the mass conservation equations as source terms S_i, S_j and S_k for gas phase, solid phase (proximate) and solid phase (ultimate) species, respectively. These source terms have units of kg/m^3/s. For gas phase species, which can participate in both homogeneous and heterogeneous reactions, the source term is defined below:

$$S_i = w_i \left(\sum_n v_{i,n} \hat{R}_n + 1/w_C \sum_m v_{i,m} R_m \right)$$

(Eq. 2-20)

where $\hat{R}_n$ is the rate of the nth homogeneous reaction in units of kmol/m^3/s and R_m is the rate of the mth heterogeneous reaction, both of which are described further in this section. The source terms for solid phase proximate and ultimate species are shown in Table 2-4. Since the proximate species all participate in different reactions, each source term is unique. Source terms for ash and moisture are obviously identical for both proximate and ultimate analyses. The source terms for the elemental coal constituents, C, H, O, N and S, are all identical due to the fact that all of the these species undergo the same processes: devolatilization and heterogeneous chemical reaction.

Table 2-4: Source terms for solid phase proximate and ultimate species

Analysis	Solid phase specie	Source term
Proximate	Fixed carbon	$S_{FC} = -\sum_m R_m$
	Volatile matter	$S_{VM} = -\sum_i S_{dev,i} w_i$
	Ash	$S_{ash} = 0$
	Moisture	$S_M = -S_{dry}$
Ultimate	k = C, H, O, N, S	$S_k = S_{k,dev} w_k + X_{k,daf} S_{FC}$
	Ash	$S_{ash} = 0$
	Moisture	$S_M = -S_{dry}$

2.5.4.1 Homogeneous Reactions

The global kinetics of homogeneous reactions for major species are modeled using rate expressions derived from Westbrook [16] and Jones [17]. Homogeneous reaction rate expressions are of the form

$$\hat{R}_n = k_n [\chi_1]^{n_1} [\chi_2]^{n_2} \qquad \text{(Eq. 2-21)}$$

and have units of kmol/m^3/s, are shown in Table 2-5. Note that simulation convergence difficulties were frequently encountered in ACM when $k_n(T)$ was used for homogeneous reactions. For this reason, the values of k shown in Table 2-5 and used in the ROM are not functions of temperature for irreversible homogeneous reactions. For each irreversible homogeneous reaction, an average value of k_n was calculated over the expected temperature range inside the gasifier. Also, oxidation kinetics for C_2H_6 and tar were assumed to be of the same form as that for CH_4. These simplifications do not affect the accuracy of the model as heterogeneous, not homogeneous, reactions are rate limiting under all realistic conditions. Equilibrium coefficients for homogeneous reactions are determined from data presented in the NIST-JANAF Thermochemical Tables [18]. The rate expression for the water-gas shift reaction in the radiant syngas cooler is described in Section 2.5.9.

Table 2-5: Homogeneous reaction rate expressions

Reaction	Rate expression	Ref
$CO + \frac{1}{2}O_2 \xrightarrow{k_1} CO_2$	$R_1 = 10^5 [CO][O_2]^{0.25} [H_2O]^{0.5}$	[16]
$H_2 + \frac{1}{2}O_2 \underset{k_{-2}}{\overset{k_2}{\rightleftharpoons}} H_2O$	$R_2 = 6.8 \times 10^{15} \exp(-20141/T) \times$ $\left([H_2]^{0.25}[O_2]^{1.5} - [H_2O]/K_2 \right)$	[17]
$CH_4 + \frac{1}{2}O_2 \xrightarrow{k_3} CO + 2H_2$	$R_3 = 10^8 [CH_4][O_2]^{1.25}$	[17]
$CO + H_2O \underset{k_{-4}}{\overset{k_4}{\rightleftharpoons}} CO_2 + H_2$	$R_4 = 2.75 \times 10^9 \exp(-10072/T) \times$ $\left([CO][H_2O] - [CO_2][H_2]/K_4 \right)$	[17]
$CH_4 + H_2O \xrightarrow{k_5} CO + 3H_2$	$R_5 = 10^5 [CH_4][H_2O]$	[17]
$C_2H_6 + O_2 \xrightarrow{k_6} 2CO + 3H_2$	$R_6 = 10^8 [C_2H_6][O_2]^{1.25}$	
$Tar + O_2 \xrightarrow{k_7} CO + H_2 + SO_2 + N_2$	$R_7 = 10^8 [Tar][O_2]^{1.25}$	

2.5.4.2 Heterogeneous Reactions

The ROM considers the four heterogeneous reactions presented below. They are similar in overall structure to the reactions presented in Chapter 1. In these reactions, however, allowance is made for the presence of non-carbon organic char elements. As mentioned in Section 2.5.3 above, this allows for more accurate prediction of pollutant evolution via devolatilization and char conversion. The choices of NH_3 and H_2S as the nitrogenous and sulfurous products are described in the section dealing with pollutant formation. For the char oxidation reaction, a mechanism factor (Φ) is used to account for direct conversion of carbon to CO_2 at low temperatures. It is evaluated as shown below [15].

$$C_\alpha H_\beta O_\chi N_\delta S_\varepsilon + \left(\tfrac{\alpha}{\phi} + \tfrac{\beta}{4} - \tfrac{\chi}{2} - \tfrac{3\delta}{4} - \tfrac{\varepsilon}{2}\right)O_2 \rightarrow 2\alpha\left(1 - \tfrac{1}{\phi}\right)CO$$
$$+ \alpha\left(\tfrac{2}{\phi} - 1\right)CO_2 + \left(\tfrac{\beta - 3\delta - 2\varepsilon}{2}\right)H_2O + \delta NH_3 + \varepsilon H_2S \tag{Eq. 2-22}$$

$$C_\alpha H_\beta O_\chi N_\delta S_\varepsilon + (\alpha - \chi)H_2O \rightarrow \alpha CO + \left(\tfrac{2\alpha + \beta - 2\chi - 3\delta - 2\varepsilon}{2}\right)H_2 + \delta NH_3 + \varepsilon H_2S \tag{Eq.2-23}$$

$$C_\alpha H_\beta O_\chi N_\delta S_\varepsilon + \alpha CO_2 \rightarrow 2\alpha CO + \chi H_2O + \left(\tfrac{\beta - 2\chi - 3\delta - 2\varepsilon}{2}\right)H_2 + \delta NH_3 + \varepsilon H_2S \tag{Eq.2-24}$$

$$C_\alpha H_\beta O_\chi N_\delta S_\varepsilon + \left(\tfrac{4\alpha - \beta + 2\chi + 3\delta + 2\varepsilon}{2}\right)H_2 \rightarrow \chi H_2O + \alpha CH_4 + \delta NH_3 + \varepsilon H_2S \tag{Eq. 2-25}$$

For $r_p < 25 \times 10^{-6} m$; $\qquad \phi = (2Z + 2)/(Z + 2)$

For $25 \times 10^{-6} m \le r_p \le 0.5 \times 10^{-3} m$; $\qquad \phi = \dfrac{(2Z + 2) - Z(200 r_p - 0.005)/0.095}{Z + 2}$ $\qquad$ (Eq.2-26)

For $r_p > 0.5 \times 10^{-3} m$; $\qquad \phi = 1.0$

Where: $Z = [CO]/[CO_2] = 2500 \exp(-6249/T_f)$

The kinetics of high-temperature and high-pressure heterogeneous reactions can be modeled using a variety of assumed mechanisms; the most applicable to reduced order modeling being (1) semi-global mechanisms incorporating adsorption-reaction-desorption expressions, and (2) global mechanisms incorporating n^{th}-order expressions. Semi-global mechanisms that incorporate adsorption-reaction-desorption steps would ideally be used in modeling solid fuel gasification, because they more accurately reflect the physiochemical processes that occur during heterogeneous chemical reactions. An extensive literature review was conducted to identify potentially suitable semi-global mechanisms. These mechanisms and their

rate expressions at zero char conversion (R_0) are presented in Table 2-6. The main conclusion of the review is that semi-global mechanisms are not yet at the required level of maturity for gasifier simulation. Most mechanisms are not validated over wide enough ranges of temperature, pressure and gas composition to be applicable for entrained flow gasification. For this reason, the ROM accepts heterogeneous kinetic data for global reactions incorporating n^{th}-order expressions only.

Table 2-6: Semi-global mechanisms for heterogeneous gasification reactions (part 1)

Work	Reaction	Mechanism	Expression
Gadsby (1946) [19]	$C+H_2O$	$H_2O \rightleftharpoons (H_2O)$ $H_2 \rightleftharpoons (H_2)$ $C+(H_2O) \longrightarrow CO+H_2$	$R_0 = k_1 P_{H_2O} / \left(1 + k_2 P_{H_2} + k_3 P_{H_2O}\right)$ This expression was developed for atmospheric pressure and has not been found accurate at high pressures.
Gadsby (1948) [20]	$C+CO_2$	$CO_2 \longrightarrow (O) + CO$ $C+(O) \longrightarrow (CO)$ $CO \rightleftharpoons (CO)$	$R_0 = k_1 P_{CO_2} / \left(1 + k_2 P_{CO} + k_3 P_{CO_2}\right)$ This expression was developed for atmospheric pressure and has not been found accurate at high pressures.
Blackwood (1958) [21]	$C+H_2O$	$H_2O \rightleftharpoons (H)(OH) \longrightarrow (O)(H_2)$ $H_2 \rightleftharpoons (H_2)$ $C+(O) \longrightarrow CO$ one of $\begin{cases} -CH_2 + H_2 \longrightarrow CH_4 \\ -CH_2 + H_2O \longrightarrow CH_4 + (O) \end{cases}$	$R_0 = \dfrac{k_1 P_{H_2O} + k_4 P_{H_2} P_{H_2O} + k_5 P_{H_2O}^2}{1 + k_2 P_{H_2} + k_3 P_{H_2O}}$
Blackwood (1959) [22]	$C+H_2$	Not stated.	$R_0 = k P_{H_2}$
Blackwood (1960) [23]	$C+CO_2$	$CO_2 \longrightarrow CO + (O)$ $CO \rightleftharpoons (CO)$ $C+(O) \longrightarrow CO$ $CO_2 + (CO) \longrightarrow 2CO + (O)$ $CO+(CO) \longrightarrow CO_2 + C$	$R_0 = \dfrac{k_1 P_{CO_2} + k_5 P_{CO_2}^2}{1 + k_2 P_{CO} + k_3 P_{CO_2}}$
Muhlen (1985) [24]	$C+CO$, H_2, CO_2, H_2O	Blackwood (1958 & 1960) for H_2O & CO_2, respectively.	$R_0 = \dfrac{k_1 P_{CO_2} + k_8 P_{CO_2}^2 + k_9 P_{H_2O} + k_{11} P_{H_2O}^2 + k_{12} P_{H_2} P_{H_2O} + k_4 P_{H_2}^2}{1 + k_2 P_{CO_2} + k_3 P_{CO} + k_{10} P_{H_2O} + k_5 P_{H_2}}$ This is a summation of the Blackwood H_2O & CO_2 expressions and $R_{H_2} = k_4 P_{H_2}^2 / \left(1 + k_5 P_{H_2}\right)$, neglecting most higher order terms.
Adanez (1985) [25]	$C+CO_2$	$C+CO_2 \rightleftharpoons CO + C(O)$ $C(O) \longrightarrow CO + C$	$R_0 = k_1 P_{CO_2} / \left(1 + k_2 P_{CO_2} + k_3 P_{CO}\right)$ Similar to Blackwood with the omission of the squared term.

Table 2-6: Semi-global mechanisms for heterogeneous gasification reactions (part 2)

Work	Reaction	Mechanism	Expression
Goyal (1989) [26]	C+H$_2$O (with CO present)	None, empirical correlation used.	$R_0 = \exp\left(A - \dfrac{B}{T}\right) \Bigg/ \left[1 + \exp\left(C - \dfrac{D}{T}\right)\left\{F\left(\dfrac{P_{H_2}}{P_{H_2O}}\right) + G\left(\dfrac{P_{CO}}{P_{H_2O}}\right)\right\}\right]^2$
Sha (1990) [27]	C+H$_2$O (with CO present) C+CO$_2$	Not stated.	$R_{0,H_2O} = \dfrac{k_1 P_{H_2O}}{1 + k_2 P_{H_2O} + k_3 P_{H_2} + k_4 P_{CO}}$ $\qquad$ $R_{0,CO_2} = \dfrac{k_1 P_{CO_2}}{1 + k_2 P_{CO} + k_3 P_{CO_2}}$ Expression for CO$_2$ is similar to Blackwood with the omission of the squared term.
Nozaki (1992) [28]	C+CO$_2$	$C + CO_2 \rightleftharpoons CO + C(O)$ $C(O) \longrightarrow CO$ $C(O) + CO_2 \longrightarrow CO + CO_2$ or $C + CO_2 \rightleftharpoons CO + C(O)$ $C(O) \longrightarrow CO$	$R_0 = \dfrac{P_{CO_2} + k_1 P_{CO_2}^2}{k_2 P_{CO_2} + k_3}$ Both proposed mechanisms results in the same expression.
Weeda (1993) [29]	C+H$_2$O	Not stated.	$R_{0,H_2O} = k_1 P_{H_2O} \Big/ \left(1 + k_2 P_{H_2O} + k_3 \sqrt{P_{H_2}}\right)$
Roberts (2006) [30]	C+H$_2$O C+CO$_2$	$C + H_2O \underset{k_2}{\overset{k_1}{\rightleftharpoons}} H_2 + C(O)$ $C(O) \overset{k_3}{\longrightarrow} CO$ one of $\begin{cases} C + H_2 \overset{k_4}{\longrightarrow} C(H_2) \\ C + \frac{1}{2}H_2 \overset{k_5}{\longrightarrow} C(H) \end{cases}$ $C + CO_2 \underset{k_2}{\overset{k_1}{\rightleftharpoons}} CO + C(O)$ $C(O) \overset{k_3}{\longrightarrow} CO$	$R_{0,H_2O} = \dfrac{k_1 P_{H_2O}}{1 + k_1/k_3 P_{H_2O}}$ $\qquad$ $R_{0,CO_2} = \dfrac{k_1 P_{CO_2}}{1 + k_1/k_3 P_{CO_2}}$ These expressions do not account for inhibition due to CO and H$_2$.
Roberts (2007) [31]	C+CO$_2$, H$_2$O	Same as Roberts (2006)	$R_0 = R_{0,CO_2} + R_{0,H_2O}\left(1 - k_1/k_3 P_{CO_2}\Big/\left(1 + k_1/k_3 P_{CO_2}\right)\right)$ Rate constants and expressions same as Roberts (2006). Again, these expressions do not account for inhibition due to CO and H$_2$.
CCSD (2008) [32]	C+CO$_2$	Same as Roberts (2006)	This work does not explicitly give a reaction rate expression, but it makes similar arguments to Roberts (2007). An expression would look something like: $R_0 = R_{0,NoCO} \times (\text{Effect of CO})$

81

2.5.4.2.1 Intrinsic Kinetic Data

Due to the variety of ways to express n^{th}-order rate expressions, the ROM can accept kinetic data in one of two forms; intrinsic (area-specific) or extrinsic (mass-specific). Intrinsic kinetic data results in the calculation of an intrinsic reaction rate constant for the mth reaction:

$$k_{in,m} = A_{in,m} \exp(-E_{in,m} / \Re T) \qquad \text{(Eq. 2-27)}$$

which has units of $kg/m^2/bar^n/s$. The area over which this reaction occurs is either the total particle area available for reaction, or the external particle area, depending on the source of the nth-order data. The reaction rate ($kg/m^3/s$) is expressed as:

$$R_m = k_{in,m}(A_{p,ext}^{"} + \eta_m A_{p,int}^{"})P_{s,m}^{n_{in,m}} \qquad \text{(Eq. 2-28)}$$

Expressions for the evaluation of the internal and external surface are presented in Table 2-3. The partial pressure of each reactant at the particle surface ($P_{s,m}$) is found by estimating its diffusion through a boundary layer around the particle:

$$\dot{n}_i^{"} = \lambda_i \frac{\left(P_i - P_{s,i}\right)}{P} + \frac{P_{s,i}}{P}\sum_i \dot{n}_i^{"} \qquad \text{(Eq. 2-29)}$$

where the molar flux of each gas phase specie to the particle surface is given by $\dot{n}_i^{"} = -a_p / \left(A_p^{"} w_i\right)\sum_m v_{i,m} R_m$ [37], and λ_i is the mass transfer coefficient ($kmol/m^2/s$) for species i through the boundary layer, given by $\lambda_i = Sh\rho_g D_{i,A} /(\overline{w}_g r_p^2)$. In this expression, Sh is the Sherwood number, which for particles of this size is ~2, and $\overline{w}_g$ is the average molecular weight of the gas phase. The heterogeneous reaction and particle boundary layer diffusion equations must be solved simultaneously.

Since the ROM does not solve the intra-particle reaction-diffusion equation, a method for calculating the bulk reactivity of the particle is required; namely the

effectiveness factor (η_m). The effectiveness factor accounts for the fact that concentration gradients of gaseous reactants exist within the particle. It is calculated from the Thiele Modulus (Φ_m) for each heterogeneous reaction using the equations below [33]. Kinetic-limited reactions result in effectiveness factors close to unity, while diffusion-limited reactions give values near zero. When reaction rate data is based on the particle external area only, η_m is set to zero.

$$\eta_m = \frac{3}{\phi_m}\left(\frac{1}{\tanh\phi_m} - \frac{1}{\phi_m}\right) \qquad \text{(Eq. 2-30)}$$

$$\phi_m = \frac{r_p}{3}\left(\frac{10^{-2}(n_m+1)k_{m,in}\rho_p V_{i,m}a_{p,\text{int}}\Re T_g P_{s,m}^{(n_m-1)}}{2w_C D_{i,\text{eff},p}}\right)^{0.5} \qquad \text{(Eq. 2-31)}$$

$D_{i,\text{eff},p}$ is the effective diffusivity of the ith gaseous reactant in the particle. The Thiele Modulus for a heterogeneous reaction is the ratio of reaction rate to pore diffusion rate of the reactant. The use of 10^{-2} in the expression is to ensure proper dimensionality with the units of measurement used in the ROM. $D_{i,\text{eff},p}$ is approximated as a combination of the molecular ($D_{i,A}$) and Knudsen ($D_{i,K}$) diffusivities [33, 34].

$$D_{i,\text{eff},p} = \frac{\varepsilon}{2}\left(\frac{1}{D_{i,A}} + \frac{1}{D_{i,K}}\right)^{-1} \qquad \text{(Eq. 2-32)}$$

$$D_{i,K} = 9.70\times10^5 \bar{r}_{pore}\left(T_p/w_i\right)^{0.5} \qquad \text{(Eq. 2-33)}$$

Evaluation of the intraparticle Knudsen diffusivity of the reactants is difficult as it requires knowledge of the internal structure of the particle. Assuming knowledge of particle porosity (ε) in a similar manner to [35], solution of the following two simultaneous equations yields a first order estimate of the average pore radius ($\bar{r}_{pore}$) of a particle modeled by the random pore model (RPM) [9, 10].

$$a_{\text{int}} = \pi\bar{r}_{pore}l_{pore}\left(1 - \bar{r}_{pore}\sqrt{\pi l_{pore}\rho_p/3}\right) \qquad \text{(Eq. 2-34)}$$

$$\varepsilon = \pi\bar{r}_{pore}^2 l_{pore}\rho_p\left(1 - 2\bar{r}_{pore}/3\sqrt{\pi l_{pore}\rho_p/3}\right) \qquad \text{(Eq. 2-35)}$$

83

2.5.4.2.2 Extrinsic Kinetic Data

Relatively few sources of high pressure intrinsic (area-based) kinetic data exist for the gasification reactions. An example of this type of data is the work of the Cooperative Research Centre for Coal in Sustainable Development (CCSD), Australia [35]. Due to the lack of intrinsic data, extrinsic data, which lump the effects of film diffusion, pore diffusion and chemical kinetics into a single expression, can also be used in the ROM. Extrinsic data results in the calculation of an extrinsic reaction rate constant for the mth reaction:

$$k_{ex,m} = A_{ex,m} \exp(-E_{ex,m} / \Re T) \qquad \text{(Eq. 2-36)}$$

which has units of $1/\text{bar}^n/\text{s}$. The reaction rate $(\text{kg/m}^3/\text{s})$ is therefore expressed as:

$$R_m = k_{ex,m} \left(\rho_{p,0} \varepsilon_{p,0} \frac{a_{p,\text{int}}}{a_{p,\text{int},0}} \right) P_m^{n_{ex,m}} \qquad \text{(Eq. 2-37)}$$

Note that P_m is the partial pressure of the reactant in the bulk fluid, not the film boundary layer. Recall from Table 2-3 that $a_{p,\text{int}} / a_{p,\text{int},0} = (1-C)\sqrt{1 - \psi \ln(1-C)}$, meaning that knowledge of the particle internal surface area is not required when using extrinsic rate expressions. However, extrinsic expressions are more limited to specific temperature and pressure ranges than intrinsic ones due to the additional approximations involved in their development. For full descriptions of the intrinsic and extrinsic n^{th}-order rate expressions used in the ROM, refer to Chapter 3.

2.5.5 Fluid Dynamics

As described in Section 2.2 above, macro-scale inlet stream mixing and flow recirculation are modeled using the Reactor Network Model (RNM) developed by Pedersen [1, 2]. One-dimensional gas-particle and gas-wall viscous interactions are approximated using drag coefficient (C_D) and friction factor (f) methods, respectively. Table 2-7 shows the expressions used to evaluate the viscous interaction terms. The gas-particle friction interaction $(F_{g,p}''$ $(\text{N/m}^3))$ can be

positive or negative, depending on the relative velocities of gas and particle, hence the $v_{slip}/|v_{slip}|$ term in the force expression. The gas-wall friction interaction ($F_{g,w}^{"}$ (N/m³)) is positive under all conditions.

Table 2-7: Viscous interactions

Viscous interaction	Force per unit volume (N/m³)	Ref
Gas-particle	$F_{g,p}^{"} = 3\varepsilon_p C_D \rho_g \varepsilon_g^{-2.65} v_{slip}^2 / (8r_p) v_{slip}/|v_{slip}|$	[38]
	$C_D = 24/\text{Re}_{d,p}\left(1 + 0.15\text{Re}_{d,p}^{0.687}\right)$	[39]
Gas-wall	$F_{g,w}^{"} = f\rho_g \varepsilon_g v_g^2 / (16r_{gasifier})$	
	$1/f^{0.5} = -2\log_{10}\left(\Omega_{wall}/7.4r_{gasifier} + 2.51/\text{Re}_{d,w} f^{0.5}\right)$	[40]

2.5.6 Heat Transfer

The heat transfer terms evaluated in the ROM are shown in Figure 2-6. The ROM is capable of simulating gasifiers with wall cooling (membrane-lined) and without (refractory-lined). Conduction through the wall layers of the gasifier is modeled in the axial and radial directions. Intraparticle conduction is not considered due to the small particle sizes involved. Three forced convection terms (gas-to-particle, gas-to-wall and wall-to-coolant in membrane-lined gasifiers), and one natural convection term (external wall-to-atmosphere) are considered. The Nusselt number for gas-to-particle convection is calculated using Eq. 4.75 in [41].

$$Nu_{d,p} = 1.32 \, \text{Re}_{d,p}^{1/2} \, \text{Pr}^{1/3}$$
(Eq. 2-38)

Nusselt numbers for gas-to-wall and wall-to-coolant convection are calculated using the Petukhov equation (Eq. 8.62 in [42]).

$$Nu_{d,w} = (f/8)\,\text{Re}_{d,w}\,\text{Pr}/(1.07 + 12.7(f/8)^{1/2}(\text{Pr}^{2/3} - 1))$$
(Eq. 2-39)

The Nusselt number for external convection is evaluated using the Churchill and Chu equation (Eq. 9.26 in [42]).

$$Nu_{ext} = \{0.825 + 0.387Ra_{ext}^{1/6}/[1 + (0.492/\text{Pr}_{ext})^{9/16}]^{8/27}\}^2$$
(Eq. 3-40)

Reynolds numbers (Re$_d$), Prandtl numbers (Pr), friction factors (f) and Rayleigh (Ra$_L$) used in the above equations are defined below.

$$\text{Re}_{d,p} = \rho_g \left| v_{slip} \right| d_p / \mu_g$$

(Eq. 3-41)

$$\text{Re}_{d,w} = \rho_g v_g d_{gasifier} / \mu_g$$

(Eq. 3-42)

$$\text{Pr} = c_p \mu / k$$

(Eq. 3-43)

$$1/f^{0.5} = -2.0 \log_{10} \left(\Omega / 3.7 d_{gasifier} + 2.51 / \left(\text{Re}_{d,w} f^{0.5} \right) \right)$$

(Eq. 3-44)

$$Ra_L = g\beta \left(T_s - T_{amb} \right) L^3 / v\alpha$$

(Eq. 3-45)

where

Ω=Wall roughness (m)

g=Gravitational acceleration (m/s^2)

$\beta = 2 / \left(T_s + T_{amb} \right)$

T_s=Average external wall temperature (K)

T_{amb}=Ambient temperature (K)

L=Gasifier length (m)

$v = \mu / \rho$

$\alpha = k / \rho c_p$

Radiative heat transfer between particles is modeled using the radiation-as-diffusion (RAD) approximation [43, 44]. The Rosseland equation is used to express radiation throughout the particle cloud as a function of particle radius, temperature and temperature gradient, as well as the absorption coefficient (K) of the particle cloud.

$$\dot{Q}_{rad}^{"} = -\frac{64\pi r_{gasifier}^2 \sigma T_p^3}{3K} \frac{\partial T_p}{\partial x}$$

(Eq. 2-46)

The use of the RAD approximation requires KB > 3, where B is the characteristic dimension of the gasifier. For clouds of particles of the size of pulverized coal $K = \pi r_p^2 N_p$, where r$_p$ and N$_p$ are the particle radius and number density (1/m^3),

respectively. The emissivity of a particle cloud is $\varepsilon_p = 1 - \exp(-KB)$. This means that the particle cloud must be of sufficient optical thickness. Radiation in the gas phase is neglected as preliminary analysis indicates the absorption coefficient for the gas phase is significantly lower than that for the particle cloud.

Under all pilot- and commercial-scale EFG conditions and under most lab-scale EFG conditions, the requirement of KB > 3 is met. It is not met, however, for experimental gasifiers that (1) have very narrow diameter (small B), or (2) operate at very low pressure, (low N_p and K). For cases in which KB < 3, a correction factor, $f_{corr,rad}$ = KB/3, is used to gradually toggle particle radiation on and off. Therefore, at KB << 3, $f_{corr,rad}$ << 1, while at KB = 3, $f_{corr,rad}$ = 1. These cases for which KB < 3 are discussed further in the sections on validation of the CSIRO and BYU gasifiers, in the section on gasifier cold start simulation.

Radiation between particles and wall assumes no reflection from the wall [45]. The ROM allows radiation heat transfer between adjacent zones of the RNM. Radiation from the external wall of the gasifier treats the environment as a black body. For use in the energy conservation equations shown in Table 2-2, heat transfer terms must be evaluated in terms of heat transfer rates per unit axial length, with units of (kW/m). The expressions for these terms are shown below.

$$\dot{Q}'_{conv,p \to g} = A''_{p,HT} A_{CS} h_{p,g} \left(T_p - T_g \right) \qquad \text{(Eq. 2-47)}$$

$$\dot{Q}'_{conv,g \to w} = 2\pi r_{gasifier} h_{g,w} \left(T_g - T_w \right) \qquad \text{(Eq. 2-48)}$$

$$\dot{Q}'_{rad,p \to w} = 2\pi r_{gasifier} \sigma \varepsilon_w \varepsilon_p \left(T_p^4 - T_w^4 \right) \qquad \text{(Eq. 2-49)}$$

$$\dot{Q}'_{rad,p \to p} = -\frac{\partial}{\partial x} \left(\dot{Q}''_{rad} A_{CS} \right) \qquad \text{(Eq. 2-50)}$$

$$\dot{Q}'_{cond,l \to l+1} = \frac{2\pi k_l \left(T_l - T_{l+1} \right)}{\ln \left(r_{l+1} / r_l \right)} \qquad \text{(Eq. 2-51)}$$

$$\dot{Q}'_{conv,ext \to amb} = 2\pi r_{ext} h_{ext} \left(T_{ext} - T_{amb} \right) \qquad \text{(Eq. 2-52)}$$

$$\dot{Q}'_{rad,ext \to amb} = 2\pi r_{ext} \sigma \varepsilon_{ext} \left(T_{ext}^4 - T_{amb}^4 \right) \qquad \text{(Eq. 2-53)}$$
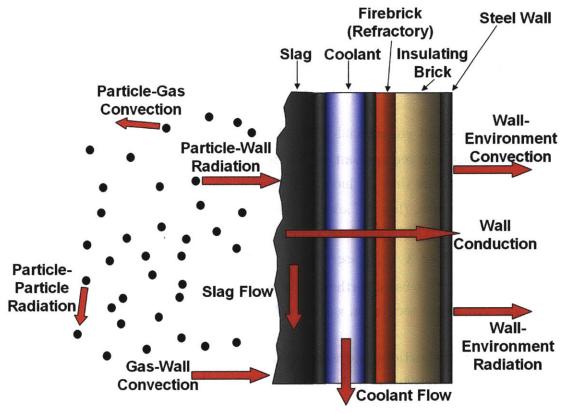
Figure 2-6: Heat transfer terms evaluated

2.5.7 Pollutant Formation

The evolution of two types of pollutants is modeled in the ROM: nitrogenous and sulfurous compounds. As previously stated, the reducing conditions in the gasifier mean that NH_3, HCN, H_2S and COS are formed in significant quantities, in addition to N_2, NO and SO_2, which are formed during coal combustion. Because of this, widely-used global chemistry submodels for nitrogenous compound formation during combustion [46, 47], which do not track NH_3 and HCN, are not suitable for use. See the extensive reviews carried out by Hill and Smoot [48] and Glarborg et al [49] for further details. Likewise, the commonly-used assumption that all sulfur evolves as SO_2 during combustion is not applicable. Submodels for nitrogen and sulfur chemistry are described below.

2.5.7.1 Nitrogenous Pollutants

Nitric oxide (NO) is the most important nitrogenous pollutant for combustion systems. There are three pathways to its creation, which are known as fuel NO,

88

thermal NO and prompt NO. Fuel NO is formed by the release of nitrogen from the fuel. Thermal NO is formed by the oxidation of atmospheric nitrogen at high temperature in fuel-lean conditions (the Zeldovich mechanism). Prompt NO is formed by the reaction of atmospheric nitrogen with hydrocarbon radicals in fuel-rich flame regions. In coal-fired combustion systems, fuel NO is recognized as the most important pathway for pollutant formation [48]. For gasification, which is a fuel-rich process usually occurring in high-purity oxygen, fuel-bound nitrogen is of even greater importance.

Nitrogen is present in all solid feedstocks. Mass fractions of nitrogen are in the range 0.5-2.5% for wood, peat and coal [50]. Nitrogen is released from solid feedstocks by two primary processes: devolatilization and char conversion. Nitrogenous compounds released by devolatilization have been observed to include NH_3, HCN and tar. The ratio of these compounds has been observed to depend on feedstock, particle heating rate and maximum temperature. Char conversion in reducing conditions primarily produces NH_3. Once in the gas phase, NO is formed by oxidation near the inlet streams, while NH_3, HCN and N_2 are formed in the oxygen-lean gasification environment. Kilpinen and Leppalahti have proposed and validated a detailed gas phase nitrogen chemistry submodel for gasification environments [51]. This submodel involves over 250 elementary homogeneous reactions between about 50 species. Aspen Custom Modeler (ACM) does not contain thermodynamic properties for free radicals, so the use of Kilpinen and Leppalahti's submodel in the ROM would be impractical. Liu and Gibbs have developed a global nitrogen chemistry submodel for fluidized bed biomass gasification conditions [52, 53]. In this submodel, devolatilization produces NH_3 and HCN, while char conversion produces NH_3. The following global gas phase nitrogen reactions are included: 7 homogeneous reactions and 16 reactions that are catalyzed by char, bed material or limestone particles. The submodel was not validated by the authors, but subsequent work by a different group found good agreement between experimental results and the submodel [54]. Therefore the Liu and Gibbs submodel is used in the ROM. Since particle loadings for entrained flow systems are approximately 10^{-2}-10^{-3} times those for fluidized bed systems, reactions catalyzed by the solid phase are not included in the ROM.

Table 2-8 shows the reactions, rate expressions and rate parameters used in the nitrogen submodel. Note that rate expressions are in units of $mol/m^3/s$ and molar

concentrations are in units of mol/m^3. It is apparent from examining the reactions in Table 2-8 that there are two distinct reaction pathways: one for NH_3 and one for HCN, which are illustrated in Figure 2-7. Because the reactions are irreversible, there is no mechanism for conversion of NH_3 to HCN and vice versa. This means that the choice of NH_3:HCN ratio for devolatilization is important. Recall from Section 2.5.3 that the original Merrick devolatilization submodel does not allow for the evolution of HCN. Therefore the option to distribute evolved nitrogen between NH_3 and HCN with the parameter f_N was added. The effect of this parameter will be examined later in sensitivity analysis.

Table 2-8: Reactions, expression and parameters for nitrogen submodel

Reaction	Rate expression	Parameters
NH_3 reaction mechanism		
$NH_3 \rightarrow \frac{1}{2}N_2 + \frac{3}{2}H_2$	$k[NH_3]^{1.25}$	$k = 3.288 \times 10^{-2} T^{1.25} \exp\left(-\frac{8304}{T}\right)$
$NO + NH_3 + \frac{1}{4}O_2 \rightarrow N_2 + \frac{3}{2}H_2O$	$k[NH_3]^{0.5}[NO]^{0.5}[O_2]^{0.5}$	$k = 1.07 \times 10^{12} \exp\left(-\frac{29400}{T}\right)$
$NH_3 + \frac{3}{4}O_2 \rightarrow \frac{1}{2}N_2 + \frac{3}{2}H_2O$	$k[NH_3][O_2]^{0.75}$	$k = 313.425 T^{1.75} \exp\left(-\frac{20131}{T}\right)$
$NH_3 + \frac{5}{4}O_2 \rightarrow NO + \frac{3}{2}H_2O$	$k[NH_3][O_2]$	$k = 2.3 \times 10^{14} \exp\left(-\frac{38160}{T}\right)$
HCN reaction mechanism		
$HCN + \frac{1}{2}O_2 \rightarrow CNO$	$k[HCN][O_2]$	$k = 2.14 \times 10^5 \exp\left(-\frac{10000}{T}\right)$
$CNO + \frac{1}{2}O_2 \rightarrow NO + CO$	$\dfrac{k[HCN][O_2]}{1 + \frac{k_2}{k_1}[NO]}$	$k = 2.14 \times 10^5 \exp\left(-\frac{10000}{T}\right)$
		$\dfrac{k_1}{k_2} = 1.02 \times 10^9 \exp\left(-\frac{25460}{T}\right)$
$CNO + NO \rightarrow N_2 + \frac{1}{2}O_2 + CO$	$\dfrac{k[HCN][O_2][NO]}{\frac{k_2}{k_1} + [NO]}$	$k = 2.14 \times 10^5 \exp\left(-\frac{10000}{T}\right)$
		$\dfrac{k_1}{k_2} = 1.02 \times 10^9 \exp\left(-\frac{25460}{T}\right)$
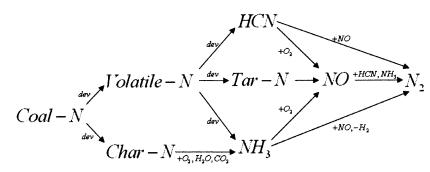
Figure 2-7: Nitrogen global reaction mechanism

2.5.7.2 Sulfurous Compounds

Most solid feedstocks contain some quantity of sulfur. Coal in general contains 0.5-4% sulfur by weight. Bituminous coals from the eastern United States have particularly high sulfur content, leading to their blending with lower-sulfur western sub-bituminous coals[1] for power generation. Use of blends with sub-bituminous coal lowers the thermal efficiency of plants, but drastically reduces SO_2 emissions. Similarly to nitrogen, sulfur is released during devolatilization and char conversion. Unlike nitrogen however, significant amounts of fuel-bound sulfur may be remain in the ash content of the feedstock, eventually becoming trapped in slag. In the reducing environment of gasifiers, sulfur appears in the gas phase in the form of H_2S. Devolatilization also produces sulfur-containing tar. Tar combustion near the injectors produces SO_2. Further reactions lead to the production of H_2S and COS.

Sulfur emissions in solid fuel combustion consist almost totally of SO_2 [55]. For this reason, there are much fewer kinetic submodels available for sulfurous compounds than there are for nitrogenous ones. Literature review found that existing sulfur reaction submodels of two types exist: equilibrium-based submodels [56] and detailed kinetic submodels [57, 58]. The detailed submodels developed by Gerasimov and Bogacheva [57] and Savel'ev et al [58] consists of 18 reactions of 14 species, and 61 reactions of over 50 species, respectively, making them unsuitable for use in the ROM. Detailed chemistry submodels also exist for Claus reactors, where H_2S is converted to elemental sulfur (see [59] and the references therein).

Since no global kinetic mechanisms for sulfur chemistry currently exist for combustion or gasification environments, we used Savel'ev's submodel [58] in conjunction with GRI-Mech 3.0 [60] and CHEMKIN [61] to determine the overall trends of sulfur chemistry under gasification conditions. The reaction of a syngas mixture, consisting of 38.6% CO, 19.8% H_2, 13.9% CO_2, 27.6% H_2O and 0.1% SO_2, in a well-stirred reactor (WSR) was simulated at temperatures and pressures in the range 1,300-1,900 K and 1-40 bar, respectively. Mole fraction profiles for the major sulfur species, SO_2, COS and H_2S, are shown in Figure 2-8. Our analysis of the Savel'ev submodel in CHEMKIN suggests that SO_2, which is produced by tar combustion near the injector, is first converted to COS, and then to H_2S. High pressure has the effect of increasing the rate of SO_2-to-COS conversion. At low

---

[1] Low sulfur sub-bituminous coals include Powder River Basin (PRB) from Wyoming.

temperature, high pressure slows the rate of COS-to-H_2S conversion, while at high temperature, high pressure appears to speed the rate of COS-to-H_2S conversion. In the presence of O_2, H_2S is rapidly converted to SO_2.
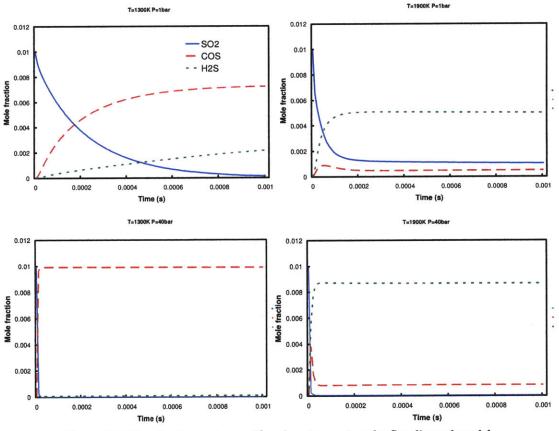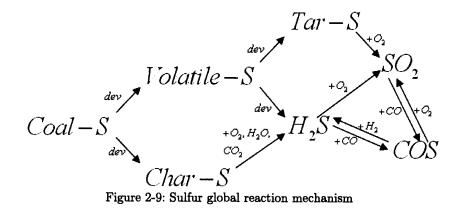
Figure 2-8: Trends of gas phase sulfur chemistry using the Savel'ev submodel

Using the results of the CHEMKIN analysis above, the ROM uses a three-step gas-phase sulfur chemistry submodel, consisting of the reactions shown below. As no global kinetic expressions were found for these reactions, they are assumed to proceed to equilibrium. In practice in the ACM code, rate expressions with extremely high rate constants are used for these reactions. Sensitivity analysis, discussed in later sections, will be used to determine the effect of these rate parameters on ROM accuracy. The overall sulfur global reaction mechanism is shown in Figure 2-9.

92

$$H_2S + \tfrac{3}{2}O_2 \rightarrow SO_2 + H_2O \qquad\qquad\qquad \text{(Eq.2-54)}$$

$$SO_2 + CO \rightleftarrows COS + O_2 \qquad\qquad\qquad\quad \text{(Eq.2-55)}$$

$$COS + H_2 \rightleftarrows H_2S + CO \qquad\qquad\qquad\quad \text{(Eq.2-56)}$$

Figure 2-9: Sulfur global reaction mechanism

2.5.8 Slag Behavior

Entrained flow gasifiers, which always operate in slagging mode, require slag viscosity no greater than 25 Pa.s (250 poise) for ease of removal [66, 67]. Slag can be modeled as a single or double layer on the gasifier wall. Figure 2-10 presents the mass and energy flows for one- and two-layer slag submodels. Two-layer submodels use separate control volumes for liquid and solid slag layers. In these models, the boundary between solid and liquid slag is located at the point where the temperature is the slag fusion temperature (or temperature of critical viscosity, T_{cv}). Typical values of T_{cv} for coals suitable for entrained flow gasification are in the range 1300-1400 °C. At this temperature the slag transitions from a fluid with temperature-dependent viscosity to a solid with infinite viscosity. This is a more accurate depiction of wall slagging behavior than one-layer submodels, which lump solid and liquid layers together as one solid-liquid phase with temperature-dependent viscosity.
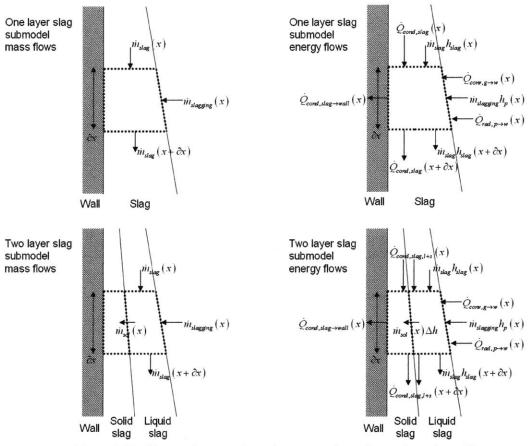
Figure 2-10: Mass and energy flows for one- and two-layer slag submodels

A two-layer slag submodel was initially developed for the ROM, but it proved extremely numerically unstable. The node-spacing on the gasifier wall was too coarse to allow smooth transition of slag from liquid to solid in the axial direction. Addition of extra nodes improved the situation somewhat, but the two-layer slag submodel was only adequately stable with such node-spacing as to render reduced order modeling pointless. Therefore, the slag submodel employed in the ROM is of the one-layer variety.

The one-dimensional Navier-Stokes equation in Cartesian coordinates is applied to the layer of slag on the gasifier wall. The Navier-Stokes equation is simplified to the form shown below by using the following assumptions: (1) very thin slag layer ($\delta_{slag} \ll r_{gasifier}$), (2) steady-state, fully-developed, axisymmetric flow, (3) no momentum flux due to particle addition at slag surface, and (4) uniform slag properties in the radial direction.

$$0 = \rho g_x + \frac{\partial}{\partial r}\left(\mu \frac{\partial v_{slag,x}}{\partial r}\right)$$

(Eq. 2-57)

Integrating this expression across the thickness of the slag layer results in the following expression for slag mass flow rate, which depends on the angle of the wall from the vertical (β), as well as slag thickness (δ_{slag}), density (ρ_{slag}) and viscosity (μ_{slag}).

$$\dot{m}_{slag} = \frac{2\pi r_{gasifier}\rho_{slag}^2 \delta_{slag}^3 g \cos \beta}{3\mu_{slag}}$$

(Eq. 2-58)

Slag viscosity (μ_{slag}) is evaluated as a function of slag composition and temperature using the semi-empirically-based Urbain model [62]. In a review of slag viscosity models, the Urbain model, which is shown below, was recognized as one of the most suitable models for the reducing conditions encountered in gasifiers [63]. This model groups the slag's constituent oxides into three mole fractions: glass formers ($\hat{x}_g$), glass modifiers ($\hat{x}_m$) and amphoterics ($\hat{x}_a$). Glass formers are acidic oxides, which raise viscosity, while glass modifiers are basic oxides, which lower viscosity. Amphoterics may act either as formers or modifiers, depending on their position within the slag structure.

$$\mu_{slag} = aT \exp\left(b10^3 / T\right) \qquad \text{(Eq. 2-59)}$$

where

$$-\ln a = 0.2693b + 13.9751$$

$$b = b_0 + b_1 \hat{X}_{SiO_2} + b_2 \hat{X}^2_{SiO_2} + b_3 \hat{X}^3_{SiO_2}$$

$$b_0 = 13.8 + 39.9355\alpha - 44.049\alpha^2$$

$$b_1 = 30.481 - 117.1505\alpha + 129.9978\alpha^2$$

$$b_2 = -40.9429 + 234.0486\alpha - 300.04\alpha^2$$

$$b_3 = 60.7619 + 153.9276\alpha + 211.1616\alpha^2$$

$$\alpha = \hat{X}_m / \left(\hat{X}_m + \hat{X}_a\right)$$

$$\hat{X}_g = \hat{X}_{SiO_2} + \hat{X}_{P_2O_5}$$

$$\hat{X}_m = \hat{X}_{FeO} + \hat{X}_{CaO} + \hat{X}_{MgO} + \hat{X}_{Na_2O} + \hat{X}_{K_2O} + \hat{X}_{MnO} + \hat{X}_{NiO}$$

$$\hat{X}_a = \hat{X}_{Al_2O_3} + \hat{X}_{Fe_2O_3} + \hat{X}_{B_2O_3}$$

The slag mass conservation equation provides an estimate of $\dot{m}_{slag}$, which is used to calculate a value for δ_{slag}. The energy conservation equation provides an estimate of T_{slag}, which is used to calculate a value for μ_{slag}. Both of these conservation equations are shown below. The flux of particles to the wall $\left(\dot{m}'_{slagging}\right)$ is not predictable by the ROM, due to the fact that particle deposition on the walls is highly dependent on the nature of the fluid flow field in the gasifier. For this reason, values for $\dot{m}'_{slagging}$ used in the ROM will either be assumed or taken from CFD simulations.

Slag mass conservation equation
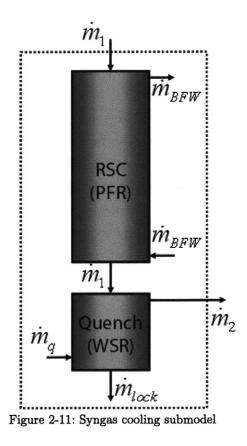
$$2\pi r_{gasifier}\rho_{slag}\frac{\partial \delta_{slag}}{\partial t} = -\frac{\partial \dot{m}_{slag}}{\partial x} + \dot{m}'_{slagging} \qquad \text{(Eq. 2-60)}$$

Slag energy conservation equation

$$2\pi r_{gasifier}\rho_{slag}\frac{\partial\left(\delta_{slag}u_{slag}\right)}{\partial t} = 2\pi r_{gasifier}k_{slag}\frac{\partial}{\partial x}\left(\delta_{slag}\frac{\partial T_{slag}}{\partial x}\right) - \frac{\partial\left(\dot{m}_{slag}h_{slag}\right)}{\partial x}$$
$$+\dot{Q}'_{conv,g\rightarrow w} + \dot{Q}'_{rad,p\rightarrow w} - \dot{Q}'_{cond,slag\rightarrow w} + \dot{m}'_{slagging}h_p \qquad \text{(Eq. 2-61)}$$

2.5.9 Syngas Cooling

A significant portion of the available experimental data for gasifiers gives syngas composition for cooled, dry, sulfur-free (sweet) syngas. In order to compare the predicted composition of hot, raw syngas from the gasifier to the measured composition of sweet syngas, it is necessary to consider the method of syngas cooling employed. Syngas cooling is modeled using a 1-D PFR, with an integrated WSR, downstream of the downstream zone (DSZ) in the reactor network model (RNM). The syngas cooling submodel is shown schematically in Figure 2-11.

Figure 2-11: Syngas cooling submodel

A switch in the cooler zone allows the simulation of all possible syngas cooling options: radiant cooling only (PFR only), quench cooling only (WSR only), radiant and quench cooling (PFR and WSR in series), and no cooling (no PFR or WSR). The cooler zone allows the same physical and chemical processes to occur as the RNM does in the gasifier. Therefore all of the conservation equations identified in Table 2-2 are solved in the cooler zone. The ROM models a radiant syngas cooler (RSC) as a 1-D counter-flow heat exchanger. Saturated liquid water (boiler feed water or BFW) enters the cold end of the cooling tubes (water wall) at a

prescribed pressure. The flow rate of cooling water is such that it is assumed to leave the water wall as a saturated vapor at the same pressure and temperature. The relatively slow cooling rate of syngas in commercial-scale operating RSCs (around 100 K/s) allows the water-gas shift reaction to occur. This is in contrast to the rapid cooling rates associated with quench coolers (around 30,000 K/s). Operational experience suggests that very little or no reaction occurs in quench coolers [64]. The ROM models a quench cooler as a vessel containing saturated H_2O at the syngas pressure. Heat transfer between syngas and quench water is assumed to be sufficiently high to allow them to reach the same exit temperature. Energy conservation determines the quality of the quench water. The vapor fraction of H_2O is assumed to leave the cooler with the syngas. The liquid water fraction leaves with solidified slag particles via the lock hopper.

Initial simulations of the RSC showed very rapid progression of the water-gas shift reaction. This is most likely due to the fact that the kinetic parameters for the water-gas shift shown in Table 2-5 were originally developed as part of an overall hydrocarbon oxidation scheme by Westbrook [16] and Jones [17]. As no combustion occurs in the RSC, the global rate of the water-gas shift is expected to be much slower. Therefore, the kinetic expression and parameters developed by Bustamante et al [65] are used for the water-gas shift in the RSC. The parameters, whose use resulted in more realistic RSC exit compositions, are shown below.

$$\hat{R}_{WGS,RSC} = 7.40 \times 10^{14} \exp\left(-\frac{34674}{T}\right)\left(\left(\frac{[CO]}{10^3}\right)^{0.5}\left(\frac{[H_2O]}{10^3}\right) - \frac{1}{K_{C,WGS}}\left(\frac{[CO_2]}{10^3}\right)\left(\frac{[H_2]}{10^3}\right)\right)$$

(Eq. 2-62)

2.6 Convergence Considerations

A number of calculations performed in the ROM require alteration from their original form to ensure simulation stability over a range of gasifier operating conditions. Two examples of this have been discussed above: the use of temperature-independent rate constants for all gas-phase reactions, except the water-gas shift, and the use of a single-layer slag submodel. Other convergence considerations are discussed below.

98

2.6.1 Non-Uniform Node-Spacing in JEZ and DSZ

Unlike some detailed CFD simulation codes, node-spacing in ACM cannot be changed or optimized during ROM operation. Therefore a generally-applicable node-spacing scheme must be applied to the plug flow reactors (PFRs) in the ROM. Fine node-spacing is required where gradients in calculated properties are steepest. In combustion and gasification systems, the steepest gradients are present where oxidation reactions occur. The following species oxidize to produce CO_2, H_2O and thermal energy in the ROM: CO, H_2, CH_4, C_2H_6, char and tar. The only region in the gasifier where fuel and O_2 are present is near the feedstock injectors. It can therefore be assumed that the steepest gradients in temperature and concentration are to be found near the front end of the JEZ. Recall that the CCZ and IRZ are treated as WSRs and all quantities are therefore spatially uniform within them. The node-spacings within the PFRs used in the ROM (i.e. JEZ, DSZ and Cooler) are shown in Figure 2-12. Note that all lengths shown in Figure 2-12 are dimensionless. The actual lengths of each of the PFRs are determined by the geometry of the gasifier. The DSZ is zoned in a similar manner to the JEZ because temperatures generally decrease towards the end of the gasifier.

Section 1: Node spacing: 0.0025 (4 nodes)

Section 2: Node spacing: 0.0125 (8 nodes)

JEZ: 20
nodes total

Section 3: Node spacing: 0.11125 (8 nodes)

L=0.01

L=0.10

L=1.00

Section 1: Node spacing: 0.005 (2 nodes)

Section 2: Node spacing: 0.025 (4 nodes)

DSZ: 10
nodes total

Section 3: Node spacing: 0.2225 (4 nodes)

L=0.01

L=0.10

L=1.00

Cooler: 10
nodes total

Node spacing: 0.1 (10 nodes)

L=1.00
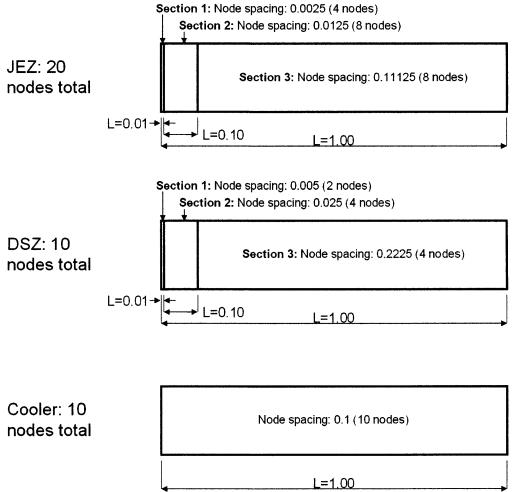
Figure 2-12: Node-spacings for PFRs used in the ROM

2.6.2 No Chemical Reactions in IRZ

As previously stated, particle drying and devolatilization occurs in the IRZ. Homogeneous and heterogeneous chemical reactions are not allowed to occur in that zone. This is because concentrations of combustible species re-enter the IRZ from the ERZ and oxidize rapidly. If the concentrations of the species entering from the ERZ are low enough, their high rate of oxidation can result in their concentrations in the IRZ being negative. Switching off all chemical reactions in the IRZ eliminates this problem. As the problem only occurs in certain situations, sensitivity analysis will be performed, where possible, on allowing reactions in the IRZ.

100

2.6.3 Near-Zero Species Concentration

A combination of rapid chemical kinetics and coarse node-spacing raises the possibility of zero or negative species concentrations. To avoid this, the reaction rate for the nth homogeneous reaction is computed as follows.

$$\hat{R}_n = k_n \left[\chi_{corr,1} \right]^{n_1} \left[\chi_{corr,2} \right]^{n_2}$$

where

$$\left[\chi_{corr,i} \right]^{n_i} = \left[\chi_i \right] \times \left[\left[\chi_i + \Delta_g \right]\right]^{(n_i-1)}$$

(Eq. 2-63)

In this expression, $[\chi_i]$ is the molar concentration of the ith gas-phase specie in $kmol/m^3$ and Δ_g is an arbitrarily small number, which is set to 10^{-7} for all simulation runs. The reaction rate for the mth heterogeneous reaction rate is computed in a similar manner. Refer to Section 2.5.4.2 for explanations of the nomenclature for the rate expression. X_{FC} is the mass fraction of fixed carbon (proximate analysis) of the solid phase, $\hat{X}_{s,m}$ is the mole fraction at the particle surface of the gas-phase specie consumed by the mth heterogeneous reaction, and Δ_g is identical to that used homogeneous reactions. Under operating conditions in which char conversion approaches 100%, char conversion occurs before H_2O and CO_2 reactants are exhausted. Therefore to ensure ROM stability, Δ_p is set to a much larger number than Δ_g so that fixed carbon mass fraction can approach zero smoothly. The value of Δ_p is set to 10^{-4} for all simulation runs.

$$R_m = f_{corr} k_{in,m} \left(A_{p,ext}'' + \eta_m A_{p,int}'' \right) P_{s,m}^{n_{in,m}}$$

where

$$f_{corr} = \left(X_{FC} / \left(X_{FC} + \Delta_p \right) \right) \times \left(\hat{X}_{s,m} / \left(\hat{X}_{s,m} + \Delta_g \right) \right)$$

(Eq. 2-64)

2.6.4 Char Composition Calculation

In order to calculate physical and thermodynamic properties of char, it is necessary to compute the dry, ash-free (DAF) particle elemental composition (ultimate analysis). This can be done for the kth element using the following expression.

$$X_{k,daf} = X_k / \left(1 - X_M - X_{Ash}\right)$$ (Eq. 2-65)

In practice in the ROM, however, this expression breaks down as carbon conversion approaches rises above 90%. At these high conversions, ash mass fraction (X_{Ash}) approaches unity, making the denominator very small. Slight numerical inaccuracies, such as those introduced by the use of Δ_p to avoid negative concentrations can result in values of $X_{k,daf}$ in excess of unity or less than zero. In the IRZ, particle composition will reflect the fact that some of the particles will be newly-injected, while others, entering from the ERZ, will be partially or fully converted. In all zones outside the IRZ, char should have a dry, ash-free composition identical to that prescribed by Merrick's devolatilization submodel, $C_\alpha H_\beta O_\chi N_\delta S_\varepsilon$ [13]. Therefore, the following expression is used across the entire range of carbon conversions. At low levels of carbon conversion (C) (i.e. in the IRZ), the standard DAF elemental expression (shown above) dominates the expression, while at high conversions, the value from the devolatilization submodel ($X_{k,dev}$) is dominant.

$$X_{k,daf} = \left(1 - C\right) \frac{X_k}{1 - X_M - X_{Ash}} + \left(C\right) X_{k,dev}$$ (Eq. 2-66)

2.7 Chapter Summary

A reduced order model (ROM) capable of simulating the steady-state and dynamic operation of a range of entrained flow gasifiers has been presented. The ROM employs a reactor network model (RNM) consisting of three well-stirred reactors (WSRs), two plug flow reactors (PFRs) and one integrated PFR-WSR. The RNM employs five user-defined, adjustable parameters that approximate the complex mixing and recirculation processes that take place inside gasifiers. This greatly reduces computational expense when compared to more detailed CFD-based models. Determination of these five RNM parameters is difficult and ultimately requires the use of detailed CFD simulation in order to visualize the fluid flow field. The results of such simulations are not yet available, so base case values for RNM parameters are chosen based on the original findings of Pedersen. These

values are subjected to sensitivity analysis to determine their importance in overall ROM accuracy. The results of this analysis are presented in the next chapter.

The ROM also employs user-defined switches that account for design and operational characteristics such as flow direction (up or down), feedstock delivery (slurry or dry), injector configuration (axial or opposed/radial), oxidant (air or oxygen), number of stages (one or two), wall lining (refractory, membrane or heated), and syngas cooling (radiant, quench, both or none). These switches enable simulation of any commercial or experimental entrained flow gasifier design with one model. This is the first gasifier model to have such a range of simulation flexibility.

At every point within the reactor network model, one- or two-dimensional conservation equations for mass, energy, momentum and particle loading are solved. These conservation equations calculate profiles of mass fractions, temperatures and velocities for gas and solid species. In addition, mass and energy conservation equations for slag layers and energy conservation equations for wall layers allow determination of accurate temperature boundary conditions. Physical, thermodynamic and transport properties, source terms and chemical reaction mechanisms are supplied to the conservation equations by highly-detailed submodels. The ROM employs submodels for the simulation of multiple feedstock physical and thermodynamic properties, drying and devolatilization, homogeneous and heterogeneous chemical reactions, viscous fluid-solid interactions, nitrogenous and sulfurous pollutant formation, slag behavior, and syngas cooling. No other simulation tool for gasification accounts for such a range of physical and chemical phenomena in such detail. It is important to remember that the key enabler for such detail in simulation submodels in the ROM is the reactor network model. The RNM frees up computational effort from solving for the fluid flow field and allows it to be used for solving detailed submodels in very short times.

Now that the ROM has been fully described, the next chapter deals with its validation for use over a range of entrained flow gasifier designs. Sensitivity analysis is also performed to identify input variables and parameters critical to simulation results.

2.8 References

1. Pedersen L S, Breithauptb P, Dam-Johansen K, Weber R. Residence Time Distibutions in Confined Swirling Flames, Combustion Science and Technology 1997; 127 (1): 251-273.
2. Pedersen L S, Glarborg P, Dam-Johansen K, Hepburn P W, Hesselmann G. A Chemical Engineering Model for Predicting NO Emissions and Burnout from Pulverized Coal Flames, Combustion Science and Technology 1998; 132 (1): 251-314.
3. Beer J M, Chigier N A. Combustion Aerodynamics. London (UK): Applied Science Publishers, Ltd; 1972.
4. Smart J P, Woycenko, D M, Morgan, D J, van de Kamp, W L. Studies on Scale-Up of Swirl-Stabilised Pulverised-Coal Burners in the Thermal Range 2.5 – 12 MW, Journal of the Institute of Energy 1996; 69: 131-144.
5. Ergun S, Menster M. A Correlation between Helium Density and Hydrogen Content of Coals, Fuel 1960; 39: 509-510.
6. Merrick D. Mathematical models of the thermal decomposition of coal: 2. Specific heats and heats of reaction, Fuel 1983; 62: 540-546.
7. Kirov N Y. BCURA Monthly Bulletin 1965; 29: 33.
8. Seggiani M. Modelling and simulation of time varying slag flow in a Prenflo entrained-flow gasifier, Fuel 1998; 77 (14): 1611-1621.
9. Bhatia S K, Perlmutter D D. A Random Pore Model for Fluid-Solid Reactions: 1. Isothermal, Kinetic Control, AIChE Journal 1980; 26 (3): 379-386.
10. Bhatia S K, Perlmutter D D. A Random Pore Model for Fluid-Solid Reactions: 2. Diffusion and Transport Effects, AIChE Journal 1981; 27 (2): 247-254.
11. Liu G s, Tate A G, Bryant G W, Wall T F. Mathematical modeling of coal char reactivity with CO_2 at high pressures and temperatures, Fuel 2000; 79: 1145-1154.
12. Liu G s, Niksa S. Coal conversion submodels for design applications at elevated pressures. Part 2. Char gasification, Progress in Energy and Combustion Science 2004; 30: 679-717.
13. Merrick D. Mathematical models of the thermal decomposition of coal: 1. The evolution of volatile matter, Fuel 1983; 62: 534-539.
14. Kobayashi H, Howard J B, Sarofim A F. Coal devolatilization at high temperatures, Proceedings of the Combustion Institute 1976; 411-425.
15. Wen C Y, Chaung T Z. Entrainment Coal Gasification Modeling, Industrial and Engineering Chemistry Process Design and Development 1979; 18 (4): 684-695.
16. Westbrook C K, Dryer F L. Simplified Reaction Mechanisms for the Oxidation of Hydrocarbon Fuels in Flames, Combustion Science and Technology 1981; 27: 31-43.
17. Jones W P, Lindstedt R P. Global Reaction Schemes for Hydrocarbon Combustion, Combustion and Flame 1988; 73: 233-249.
18. Chase M W. NIST-JANAF Thermochemical Tables Fourth Edition. National Institute of Standards and Technology, Gaithersburg (MD): 1998.
19. Gadsby J, Hinshelwood C N, Sykes K W. The kinetics of the reactions of the steam-carbon system, Proc R Soc 1946; 187A: 129-151.
20. Gadsby J, Long F J, Sleightholm, P, Sykes K W. The mechanism of the carbon dioxide-carbon reaction, Proc R Soc 1948; 193A: 357-376.
21. Blackwood J D, McGrory F. The carbon-steam reaction at high pressures, Aust J Chem 1958; 11: 16-33.
22. Blackwood J D. The reaction of carbon with hydrogen at high pressures, Aust J Chem 1959; 12: 14-28.

23. Blackwood J D, McGrory F. The reaction of carbon with carbon dioxide at high pressures, Aust J Chem 1960; 13: 194-209.
24. Muhlen H-J, van Heek K H, Juntgen H. Kinetic studies of steam gasification of char in the presence of H_2, CO_2 and CO, Fuel 1985; 64: 944-949.
25. Adanez J, Miranda J L, Gavilan J M. Kinetics of lignite-char gasification by CO_2, Fuel 1985; 64: 801-804.
26. Goyal A, Zabransky R F, Rehmat A. Gasification Kinetics of Western Kentucky Bituminous Coal Char, Ind Eng Chem Res 1989; 28: 1767-1778.
27. Sha X Z, Chen Y G, Cao J, Yang Y M, Ren D Q. Effects of operating pressure on coal gasification, Fuel 1990; 69: 656-659.
28. Nozaki T, Adschiri T, Fujimoto K. Coal char gasification under pressurized CO_2 atmosphere, Fuel 1992; 71: 349-350.
29. Weeda M, Abcouwer H H, Kapteijn F, Moulijn J A. Steam gasification kinetics and burn-off behaviour for a bituminous coal derived char in the presence of H_2, Fuel Processing Technology 1993; 36: 235-242.
30. Roberts D G, Harris D J. A kinetic Analysis of Coal Char Gasification Reactions at High Pressures, Energy & Fuels 2006; 20: 2314-2320.
31. Roberts D G, Harris D J. Char gasification in mixtures of CO_2 and H_2O: Competition and inhibition, Fuel 2007; 86: 2672-2678.
32. Cooperative Research Centre for Coal in Sustainable Development [CCSD]. Char reactivity in gas mixtures: towards an understanding of the C-CO-CO_2 reaction system: Technical Note 35 2008 May.
33. Laurendeau N M. Heterogeneous kinetics of coal char gasification and combustion, Progress in Energy and Combustion Science 1978; 4: 221-270.
34. Hong J, Hecker W C, Fletcher T H. Modeling high-pressure char oxidation using Langmuir kinetics with an effectiveness factor, Proceedings of the Combustion Institute 2000; 28: 2215-2223.
35. Cooperative Research Centre for Coal in Sustainable Development [CCSD]. Gasification Conversion Model - PEFR: Research Report 80 2007 Dec.
36. Kajitani S, Hara S, Matsuda H. Gasification rate analysis of coal char with a pressurized drop tube furnace, Fuel 2002; 81: 539-546.
37. Hong J. Modeling char oxidation as a function of pressure using an intrinsic Langmuir rate equation [dissertation]. Provo (UT): Brigham Young University; 2000 Apr. PhD thesis
38. Arastoopour H, Gidaspow D. Vertical Pneumatic Conveying Using Four Hydrodynamic Models, Industrial and Engineering Chemistry Fundamentals 1970; 18 (2): 123.
39. Rowe P N, Henwood G A. Drag Forces in Hydraulic Model of Fluidized Bed, Transactions of the Institution of Chemical Engineers 1961; 39: 43.
40. White F M. Fluid Mechanics, Second Edition. New York (NY): McGraw-Hill; 1986.
41. Mills A F. Heat Transfer, Second Edition. Upper Saddle River (NJ): Prentice Hall Inc.; 1999.
42. Incropera F P, DeWitt D P. Fundamentals of Heat and Mass Transfer, Fifth Edition. New York (NY): John Wiley & Sons, Inc.; 2002.
43. Hottel H C, Sarofim A F. Radiative Transfer. New York (NY): McGraw-Hill; 1967.
44. Smoot L D, Smith P J. Coal Combustion and Gasification. New York (NY): Plenum Press; 1985.
45. Smith P J, Smoot L D. One-Dimensional Model for Pulverized Coal Combustion and Gasification, Combustion Science and Technology 1980; 23: 17-31.

46. De Soete G G. Overall reaction rates of NO and N_2 formation from fuel nitrogen, Fifteenth Symposium (International) on Combustion. The Combustion Institute, 1975: 1093-1102.
47. Hill S C, Smoot L D, Smith P J. Prediction of nitrogen oxide formation in turbulent coal flames, Twentieth Symposium (International) on Combustion. The Combustion Institute, 1984; 1391-1400.
48. Hill S C, Smoot L D. Modeling of nitrogen oxides formation and destruction in combustion systems, Progress in Energy and Combustion Science 2000; 26: 417-458.
49. Glarborg P, Jensen A D, Johnsson J E. Fuel nitrogen conversion in solid fuel fired systems, Progress in Energy and Combustion Science 2003; 29: 89-113.
50. Leppalahti J, Koljonen T. Nitrogen evolution from coal, peat and wood gasification: Literature review, Fuel Processing Technology 1995; 43: 1-45.
51. Kilpinen P, Leppalahti J. Gas-phase conversion of NH_3 to N_2 in gasification product gases – A kinetic modeling study, 1992. Report 92-2, Abo Akademi, Turku, Finland.
52. Liu H, Gibbs B M. Modelling of NO and N_2O emissions from biomass-fired circulating fluidized bed combustors, Fuel 2002; 81: 271-280.
53. Liu H, Gibbs B M. Modelling NH_3 and HCN emissions from biomass circulating fluidized bed gasifiers, Fuel 2003; 82: 1591-1604.
54. Pinto F, Andre R N, Lopes H, Dias M, Gulyurtlu I, Cabrita I. Effect of Experimental Conditions on Gas Quality and Solids Produced by Sewage Sludge Gasification. 2. Sewage Sudge Mixed with Biomass, Energy & Fuels, 2008; 22: 2314-2325.
55. Flagan R C, Seinfeld J H. Fundamentals of Air Pollution Engineering. Englewood Cliffs (NJ): Prentice Hall; 1988.
56. Jazbec M, Sendt K, Haynes B S. Kinetic and thermodynamic analysis of the fate of sulphur compounds in gasification products, Fuel 2004; 83: 2133-2138.
57. Gerasimov G Ya, Bogacheva T M. Modeling of the Transformation of Sulfur Compounds in Oxygen Gasification of Coal Dust, Combustion, Explosion & Shock Waves 2001; 37: 406-412.
58. Savel'ev A M, Starik A M, Titova N S. Formation Kinetics of Sulfur-Bearing Compounds in Combustion of Hydrocarbon Fuels In Air, Combustion, Explosion & Shock Waves 2002; 38: 609-621.
59. Monnery W D, Hawboldt K A, Pollock A, Svrcek W Y. New experimental data and kinetic rate expression for the Claus reaction, Chemical Engineering Science 2000; 55: 5141-5148.
60. GRI-Mech Home Page [webpage on the internet]. n.d. [cited 2009 Sep 8]. Available from: http://www.me.berkeley.edu/gri˙mech/
61. Reaction Design: Products – CHEMKIN [webpage on the internet]. n.d. [cited 2009 Sep 8]. Available from: http://www.reactiondesign.com/products/open/chemkin.html
62. Urbain G, Cambier F, Deletter M, Anseau M R. Viscosity of Silicate Melts, Transactions of the Journal of the British Ceramics Society 1981; 80: 139.
63. Vargas S, Frandsen F J, Dam-Johansen K. Rheological properties of high-temperature melts of coal ashes and other silicates, Progress in Energy and Combustion Science 2001; 27: 237-429.
64. Bockelie M, Denison M, Chen Z, Senior C, Sarofim A. Using Models to Select Operating Conditions for Gasifiers. Pittsburgh Coal Conference; 2003 Sept. 15; Pittsburgh (PA): 2003
65. Bustamante F, Enick R M, Killmeyer R P, Howard B H, Rothenberger K S, Cugini A V, Morreale B D, Ciocco M V. Uncatalyzed and Wall-Catalyzed

Forward Water-Gas Shift Reaction Kinetics, AIChE Journal 2005; 51: 1440-1454.

66. Song W, Tang L, Zhu X, Wu Y, Rong Y, Zhu Z, Koyama S. Fusibility and flow properties of coal ash and slag, Fuel 2009 ; 88 : 297-304.

67. Email communication between the author and Mr. Jerry Schlather, Senior Development Associate, Eastman Chemical Company, Kingsport (TN).

Chapter 3 VALIDATION AND SENSITIVITY ANALYSIS

3.1 Chapter Overview

This chapter describes the steady-state validation results of the ROM. Experimental data is presented for one pilot-scale and three laboratory-scale entrained flow gasifiers. The methods for sensitivity analyses are described. Gasifier geometry and operating conditions are presented and their implementation in the ROM is discussed. ROM simulation results are compared to the experimental data to assess the accuracy of the ROM. The results of sensitivity analysis are also presented and discussed in detail.

3.2 Experimental Data for EFGs

In order to assess the accuracy of the ROM in simulating gasifier performance, it is necessary to validate the ROM. This is done by comparing experimental data from operational gasifiers to ROM simulation results. Examples of experimental data useful for this purpose, i.e. validation data, include: exit temperatures, carbon conversions, syngas compositions and temperature profiles. In addition to experimental data, gasifier geometry, operating conditions (i.e. pressure, inlet flow rates, etc.) and feedstock description must be known. With very few exceptions, such data is typically not publically available for commercial-scale gasifiers, those in which we are most interested in modeling. There are however, numerous research groups in academia, industry and government laboratories that publish experimental results in publically available literature. The results of literature review for experimental data for entrained flow gasifiers are shown in Table 3-1.

The decision not to use certain experimental data presented in Table 3-1 was taken in cases where there was simply not enough information to adequately describe the gasifier in question in the ROM. The studies that are not used in the present research are shown in Table 3-1 to aid future work in this field. The work of Zhong et al [13] is particularly interesting as it is one of the few papers that deals with pollutant formation in the gasifier.

Table 3-1: Experimental data for entrained flow gasifiers

Work	Gasifier	Operating conditions	Feedstock data	Geometry	Validation data	Number of tests	Suitable for use?
Watanabe [1] & Hara [2]	2 tpd lab-scale MHI	Yes	Yes	Yes	Experimental and CFD results for temperature profiles, exit gas composition, exit carbon conversion, exit char flow rate, exit gas HHV[1], CGE[2]	7	Yes
CCSD [3]	0.1 tpd lab-scale CSIRO[3]	Yes	Yes	Yes	Experimental and CFD results for carbon conversion and gas composition profiles	4	Yes
Soelberg [4] & Highsmith [5]	1 tpd lab-scale BYU[4]	Yes	No kinetics	Yes	Experimental results for exit carbon conversion, and gas composition and pollutant profiles	1	Yes
EPRI[5] [6]	1000 tpd pilot-scale Texaco	Yes	No kinetics	Inferable	Design specification for exit gas composition	1	Yes
EPRI [7]	1000 tpd pilot-scale Texaco	Yes	No kinetics	Inferable	Experimental results for exit carbon conversion, and cooled, cleaned gas composition	6	Yes
TECO[6] [8]	2300 tpd full-scale Texaco	Yes	No kinetics	Inferable	Experimental results for cooler temperatures	n/a	Supports [6, 7]
NETL [9]	2700 tpd full-scale GE	Yes	No kinetics	Inferable	Design specification for cooled gas composition, gas temperatures, cooler temperatures	1	Supports [6, 7]
Chen [10-12]	200 tpd pilot-scale MHI	Yes	Yes	Yes	Incomplete data for temperature and exit gas composition	n/a	No
Zhong [13]	Lab-scale ECUST	No	No kinetics	Yes	Experimental data for nitrogen pollutant profiles	5	No
WRE[7] [14] & NETL [15]	Full-scale E-GAS	Partial	No kinetics	No	Experimental data for exit syngas composition	1	No
Eurlings [16]	Full-scale SCGP	Yes	No kinetics	No	Experimental data for exit CO_2 fraction, exit carbon conversion, CGE	10+	No

[1] HHV: Higher heating value
[2] CGE: Cold gas efficiency
[3] CCSD: Cooperative Research Centre for Coal in Sustainable Development
[4] BYU: Brigham Young University
[5] EPRI: Electric Power Research Institute
[6] TECO: Tampa Electric Company
[7] WRE: Wabash River Energy Ltd.

The term "No kinetics" in reference to feedstock data means that although the feedstock composition is known, no kinetic data is given. The term "Inferable" in reference to gasifier geometry means that although the specific details of the geometry are not specified, it has been possible to infer them with further literature review. This is discussed further in the section on the Texaco (GE) gasifier. Due to the results of this literature review, the ROM is validated using experimental data for the gasifier designs listed below.

- 2 tpd MHI lab-scale gasifier
- 0.1 tpd CSIRO lab-scale gasifier
- 1 tpd BYU lab-scale gasifier
- 1,000 tpd Texaco (GE) pilot-scale gasifier

Note that the feed rates of the selected gasifiers are over the range 0.1-1,000 tpd, four orders of magnitude. In the presentation of validation results that follows, ROM predictions for non-validated simulation outputs are shown in addition to validated simulation outputs. Non-validated ROM predictions, while not fully reliable, can be useful in explaining observed phenomena and ROM strengths and weaknesses. Examples of non-validated simulation outputs include profiles of char properties, profiles of wall heat flux, and profiles of heterogeneous reaction rates.

3.3 Overview of Sensitivity Analysis

Sensitivity analysis is important when certain parameters are unknown or assumed, as is the case with most practical simulations. It is used to identify the input parameters or variables that have the greatest influence on simulation results. Important input parameters or variables identified by sensitivity analysis, whose values are unknown, can then be investigated in order to improve simulation accuracy. The sensitivity ($\tilde{S}_{\chi \to \phi}$) of a simulation output (ϕ) to an input (χ) is defined as follows.

$$\tilde{S}_{\chi \to \phi} = \frac{\partial \ln \phi}{\partial \ln \chi} \approx \frac{\chi}{\phi} \frac{\Delta \phi}{\Delta \chi} \qquad \text{(Eq. 3-1)}$$

Sensitivity analysis is performed for the ROM in the manner described below. The most important ROM outputs for each simulation are identified. These ROM outputs are chosen because they best describe the operation of the particular gasifier in question. Examples of such outputs include exit carbon conversion (C_{exit}), gasifier exit temperature[1] ($T_{exit} - T_{amb}$), RSC exit temperature ($T_{RSC,exit} - T_{amb}$), and ratios of important species that indicate gas compositions such as H_2:CO ratio, NH_3:HCN ratio and H_2S:SO_2 ratio. Input parameters whose values are potentially important to these ROM outputs are then identified. Realistic base case values for these input parameters are chosen. The ROM is then run allowing one input parameter at a time to be varied over a range of ±10% around its base case value. The change of the ROM outputs for a given change in an individual input parameter can then be observed and compared to those for other input parameters for a particular gasifier design.

The potentially important input parameters for the gasifiers simulated by the ROM, as well as their base case values, are shown in Table 3-2. Input parameters are classified as one of four types: gasifier design parameters, reactor network model parameters, particle parameters and heat transfer parameters.

Gasifier design parameters are concerned with the design and operation of the gasifier. The wall temperature parameter (T_{wall}) is only relevant for designs whose walls are heated or cooled to a prescribed temperature. This is discussed further in the sections describing the CSIRO and BYU gasifiers.

Reactor network model (RNM) parameters describe the structure of the RNM. Sensitivity analysis of the RNM structure is of particular interest in designs that are likely to include significant recirculation in the main volume of the gasifier, i.e. the BYU and GE designs.

Particle parameters describe the structure and properties of the char particles. The particle parameters relevant to a particular ROM simulation depend on the type of heterogeneous kinetic data used for the feedstock in question. Intrinsic kinetic data requires knowledge of the internal particle structure, while extrinsic kinetic data does not. The only ROM simulation that uses intrinsic kinetic data is that for the

---

[1] Ambient temperature is used as a reference for comparison of exit tmperatures. Failure to use a reference temperature would result in different results depending on what temperature scale is employed.

CSIRO gasifier. Refer to Section 2.5.4.2 for more details on heterogeneous reaction expressions.

Heat transfer parameters are used to describe heat transfer in the simulation. Peclet numbers for mass and heat are used to compare advective to diffusive transport of mass and energy. Diffusive effects are expected to be small in the gasifier. The base case values of wall emissivity (ε_{wall} = 0.83) and slag conductivity (k_{slag} = 1.89 W/m/K) are values used by Seggiani [19] for a slag layer. For the laboratory-scale gasifiers simulated, i.e. the MHI, CSIRO and BYU designs, only a very thin slag layer is assumed to be present. There are two reasons for this:

1. Laboratory-scale gasifiers are not run continuously and are therefore not designed for full slagging operation. It is likely that in practice the slag layer formed on the walls of these designs during experiments is quite thin.
2. When the slag submodel is activated for the laboratory-scale gasifiers, slag layers that can approach the length-scales of the gasifier diameters are predicted by the ROM. This issue arises because of the narrow diameters of the laboratory-scale gasifiers.

For simulation of the Texaco (GE) pilot-scale gasifier, full slagging is assumed and therefore a slag thickness is not specified. In this case the slag submodel is activated and predicts slag behavior in the manner described in Section 2.4.7. The slag deposition factor (f_{slag}) refers to the assumed mass fraction of solids entering the gasifier that is eventually deposited on the wall. Therefore f_{slag} = 0.1 means that 10% of the solid mass entering the gasifier contacts the wall and forms a slag layer. The slag deposition factor is used as the ROM is not capable of simulating the movement of particles to the gasifier walls, which is strongly controlled by the turbulent flow field [20].

Table 3-2: Input parameters and base case values for the ROM

Parameter	Description	Units	MHI 2 tpd	CSIRO 0.1 tpd	BYU 1 tpd	GE 1,000 tpd
Base case			M-4	CRC252	n/a	Test 4
Gasifier design parameters						
$m_{O2}{:}m_C$	Inlet ratio of O_2 to C	-	1.06	1.37	1.30	1.20
$m_{H2O}{:}m_C$	Inlet ratio of H_2O to C	-	0	0	0.39	0.87
P	Operating pressure	bar	20	20	1	42
T_{wall}	Wall temperature	°C	n/a	1400	677-1127	n/a
$t_{FB}/(t_{FB}+t_{IB})$	Firebrick fraction of wall	-	0.727	n/a	n/a	0.727
Reactor network model parameters						
d_{IRZ}	IRZ diameter	m	0.24	0.07	0.1	0.5
L_{IRZ}	IRZ length	m	0.24	0.07	0.1	0.5
α	Recirculation ratio	-	0	0	0.44	1.54
θ	Jet expansion angle	deg	0	0	9.7	9.7
f_{JEZ}	Fraction of flow directly from ERZ to JEZ	-	0	0	0	0
Particle parameters						
$\varepsilon_{p,0}$	Post-devolatilization porosity	%	n/a	15	n/a	n/a
$a_{p,int,0}$	Post-devolatilization internal area	m^2/g	n/a	315	n/a	n/a
$Y_{VM,daf,act}$	DAF volatile yield	-	0.309	0.409	0.416	0.375
ψ	Structural parameter	-	3	n/a	5	3
M_m	Multiplier for rate of mth heterogeneous reaction	-	1	1	1	1
Heat transfer parameters						
Pe_m	Peclet number for mass transfer	-	1000	1000	1000	1000
Pe_h	Peclet number for heat transfer	-	1000	1000	1000	1000
ε_w	Wall emissivity	-	0.83	0.83	0.83	0.83
δ_{slag}	Slag layer thickness	m	10^{-4}	10^{-4}	10^{-4}	n/a
f_{slag}	Slag deposition factor	-	n/a	n/a	n/a	0.1
k_{slag}	Slag conductivity	W/m/K	1.89	1.89	1.89	1.89

The results of sensitivity analysis are shown both graphically and in tables. An example of graphical sensitivity analysis results is shown in Figure 3-1. In this case, the ROM output chosen for analysis is $T_{exit} - T_{amb}$. The x-axis shows the percentage change of each parameter from its base case value and the y-axis shows the percentage change in $T_{exit} - T_{amb}$ due to changes in each parameter. The absolute value of the slope of a line on the plot represents the sensitivity of the output to a particular parameter. It is therefore apparent that for this example case, T_{exit} is most sensitive to changes in the inlet ratios of O_2 and H_2O to C. Other important parameters include f_{JEZ}, d_{IRZ}, recirculation ratio and pressure. Parameters that result in changes of $T_{exit} - T_{amb}$ less than 0.01% are omitted for the sake of clarity.
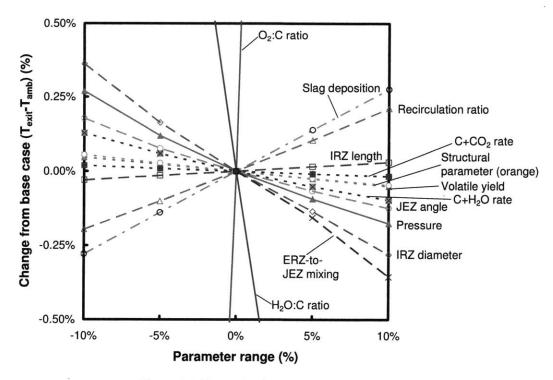
Figure 3-1: Example of sensitivity analysis results

The next sections give detailed descriptions of the gasifier designs and experiments used for validation, the assumptions used in implementing them in the ROM, the results of ROM validation, and the findings of sensitivity analysis on the results. Specific sensitivity analyses are conducted for pollutant formation and syngas cooling submodels. These are detailed in the sections on the BYU and Texaco (GE) results, respectively.

115

3.4 MHI Lab-Scale Gasifier

3.4.1 Experimental Description

The commercial-scale MHI gasifier design is discussed in Chapter 1. The lab-scale MHI gasifier differs in terms of some design aspects, the most important of which are physical size and the use of refractory-line walls in the second stage (reductor), as opposed to membrane-lined walls. Figure 3-2 gives a description of the 2 tpd lab-scale MHI gasifier. The gasifier is up-flow, dry-fed, air-blown, radially/tangentially-fired and two-stage, with a membrane-lined combustor and a refractory-lined reductor. It is assumed that as this is a lab-scale gasifier, it does not operate for sufficiently long periods of time to warrant full slagging and slag removal. The first stage is fed with coal, recycled char and air, while the second stage is fed with coal and air.

$D_1 = 0.24$ m
$D_2 = 0.3$ m
$H = 5.85$ m
$t_{FB} = 0.16$ m
$t_{IB} = 0.06$ m
$t_{st} = 0.02$ m

Characteristic	2 tpd MHI lab-scale
Flow direction	Up
Feedstock delivery	Dry (no H_2O at all)
Injector configuration	Radial & tangential
Oxidant	Air
Number of stages	2
Wall lining	Membrane in combustor Refractory in reductor
Syngas cooling	Quench
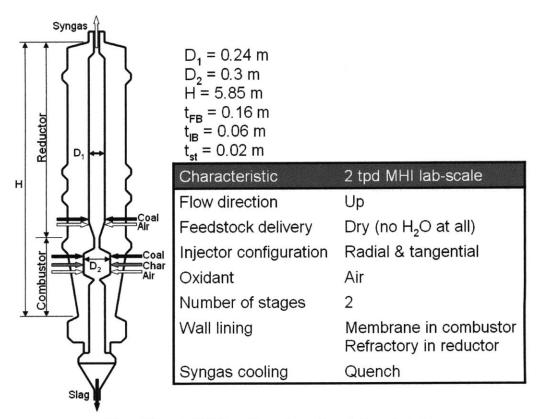
Figure 3-2: 2 tpd MHI gasifier schematic and characteristics

The experimental work on the MHI gasifier [1, 2] does not make reference to the composition of the refractory-lined walls in the reductor. The overall wall thickness is known from the diagrams provided, but thicknesses, conductivities, densities and heat capacities for firebrick (refractory) and insulating brick layers are not known. Therefore the wall is assumed to have the same ratio of layer thicknesses as that of the GE gasifier. The total wall thickness of the GE gasifier $(t_{FB} + t_{IB} + t_{st})$ is 0.82 m, while of the MHI gasifier is 0.24 m [1, 2]. Thicknesses of refractory, insulating brick and steel layers $(t_{FB}, t_{IB}$ and t_{st}, respectively) for the GE gasifier are 0.55 m, 0.21 m and 0.06 m, respectively. Refer to Section 3.7.1 for information on these dimensions. The thickness values are scaled to the total wall thickness of the MHI gasifier, giving the values shown in Figure 3-2. Sensitivity analysis will be performed to determine the influence of t_{FB} and t_{IB} on overall ROM performance.

Table 3-3 shows the test conditions used for experiments using the MHI gasifier. The coal types used in the tests, Coal M (for Moura) and Coal T (for Taiheiyo), are Australian and Japanese bituminous coals, respectively. Their ultimate and proximate analyses are given in Table 3-4. All tests are conducted at a pressure of 2 MPa (20 bar). Air ratio and gasifier air ratio are two methods used by Watanabe [1] to specify the stoichiometry of the gasifier, with respect to coal flow and total coal and char flow, respectively. Their expressions are given below. ACO and ACH refer to the stoichiometric flow rates of air with respect to (1) coal and (2) coal and char flow rates, respectively. All flow rates for these tests are expressed in units of kg/hr.

Air ratio:

$$\lambda_0 = \frac{\dot{m}_{air,total}}{\left(\dot{m}_{coal,combustor} + \dot{m}_{coal,reductor}\right)ACO}$$ (Eq. 3-2)

Gasifier air ratio:

$$\lambda_g = \frac{\dot{m}_{air,total}}{\left(\dot{m}_{coal,combustor} + \dot{m}_{coal,reductor}\right)ACO + \dot{m}_{char}ACH}$$ (Eq. 3-3)

Table 3-3: Test conditions for 2 tpd MHI gasifier

Test		M-1	M-2	M-3	M-4	T-1	T-2	T-3
Input data								
Coal type		M	M	M	M	T	T	T
Pressure	MPa	2	2	2	2	2	2	2
Air ratio		0.469	0.495	0.525	0.476	0.463	0.488	0.525
Gasifier air ratio		0.358	0.381	0.409	0.367	0.392	0.463	0.506
Combustor coal	kg/hr	40.7	41.4	40.6	41.2	50.1	51.9	50.7
Reductor coal	kg/hr	60.3	59.3	58.3	61.3	52.2	49.6	50.5
Recycled char	kg/hr	38.1	36.3	34.8	37.8	33.6	9.8	7.7
Combustor air	kg/hr	391.7	418.4	436.6	409.7	342.0	365.4	371.8
Reductor air	kg/hr	66.96	66.58	66.49	66.68	61.9	65.1	66.3

Table 3-4 shows the ultimate and proximate analyses of the coals tested in the 2 tpd MHI gasifier. Data for a third coal, Coal NL, another Australian bituminous coal is also given. Coal NL is included in Table 3-4 for the following reason. Extrinsic (mass-based) n^{th}-order kinetic expressions for Coal M and Coal T were developed by Kajitani et al [17]. In their experiments, coal samples were tested in a pressurized drop tube furnace. Full extrinsic n^{th}-order kinetic expressions were developed for Coal NL only. The kinetic rates of Coal M and Coal T were then expressed with respect to the rate of Coal NL using scaling factors. The values of the scaling factors for Coal M and Coal T, 1.06 and 1.45, respectively, are shown in Table 3-4. Kajitani found that under entrained flow gasifier conditions this approach yielded satisfactory accuracy.

Table 3-4: Specifications of coal tested in 2 tpd MHI gasifier

Analysis			Coal M	Coal T	Coal NL
Proximate	Fixed carbon	wt%	56.20	35.80	55.60
	Volatile matter	wt%	30.90	46.80	27.80
	Ash	wt%	8.70	12.10	13.40
	Moisture	wt%	4.20	5.30	3.20
Ultimate	C	wt%	73.10	64.59	68.80
	H	wt%	5.09	5.41	4.26
	O	wt%	7.00	11.61	8.87
	N	wt%	1.48	0.94	1.13
	S	wt%	0.44	0.18	0.35
	Ash	wt%	8.70	12.10	13.40
	Moisture	wt%	4.20	5.30	3.20
Scaling factor for $A_{ex,m}$			1.06	1.45	1.00

Table 3-5 shows the kinetic rate parameters for Coal NL. In order to use these parameters for Coal M and Coal T, frequency factors for Coal NL ($A_{ex,m}$) are multiplied by the scaling factors shown in Table 3-4. At this point it is useful to recall that for extrinsic kinetic data, such as Kajitani's, the reaction rate expression computed by the ROM has the form shown below. Note that the parameters presented in Table 3-5 are applicable only over certain temperature ranges. This highlights the fact that extrinsic kinetic expressions are of a more empirical nature

118

than intrinsic data, because they lump the effects of film diffusion, pore diffusion and chemical reaction together.

$$R_m = k_{ex,m} \left(\rho_{p,0} \varepsilon_{p,0} \frac{a_{p,int}}{a_{p,int,0}} \right) P_m^{n_{ex,m}}$$

(Eq. 3-4)

where

$$k_{ex,m} = A_{ex,m} \exp(-E_{ex,m} / \Re T)$$

$$a_{p,int} / a_{p,int,0} = (1 - C)\sqrt{1 - \psi \ln(1 - C)} \quad \rightarrow \text{Random pore model}$$

$$C = \text{Conversion}$$

Table 3-5: Kinetic rate parameters for Coal NL

Reactant		O_2	H_2O		CO_2	
Temp. range	°C		< 1260	>1260	< 1200	> 1200
ψ		14	3	3	3	3
$A_{ex,m}$	$10^6/MPa^n/s$	136	289	0.0855	334	0.0678
$E_{ex,m}$	MJ/kmol	130	252	140	271	163
$n_{ex,m}$		0.68	0.64	0.84	0.54	0.73

3.4.2 Implementation in the ROM

The Reactor Network Model, which was introduced in Chapter 2, must be adapted for simulation of the 2 tpd MHI gasifier. Figure 3-3 shows the dimensions and characteristics of the RNM for this case. The most important feature of the RNM is that it does not consider external recirculation from the JEZ, through the ERZ, back to the IRZ. The validity of this assumption will be examined in the section on sensitivity analysis. The main reasons for using this assumption are:

1. External recirculation can be considered to be governed primarily by the presence of a sudden expansion. Since there is no sudden expansion downstream of the second-stage injectors, external recirculation is not expected.[1]

2. The aspect ratio (length-to-diameter ratio) of the reductor is very large (roughly 15). It is therefore likely that any external recirculation occurs over a short distance with respect to the entire reductor length

---

[1] Note that there is a throat (a contraction followed by an expansion) between the combustor and reductor, which would cause external recirculation. In this RNM configuration, the throat region is modeled as part of the CCZ, which is a well-stirred reactor.

119

The CCZ models the combustor and throat regions of the gasifier as a simple cylinder of dimensions L_{CCZ} = 0.68 m, d_{CCZ} = 0.3 m. These are the dimensions of the first stage combustor and throat as specified by [1, 2]. The IRZ models the region near the second-stage injectors and is represented by a cylinder of length and diameter equal to the reductor diameter (i.e. L_{IRZ} = 0.24 m, d_{IRZ} = 0.24 m). These dimensions are estimates and are subject to sensitivity analysis (see following sections). As explained above, external recirculation is not considered, so flow to the ERZ is zero and its dimensions are unimportant. Since external recirculation is not considered, the relative lengths of the JEZ and DSZ are not important, as long as their lengths plus that of the IRZ add up the total length of the reductor (3.64 m). Therefore the JEZ and DSZ are modeled as cylinders of equal length (L_{JEZ} = L_{DSZ} = 1.7 m) and diameter (d_{JEZ} = d_{DSZ} = 0.24 m). All of the RNM dimensions are shown in Figure 3-3.
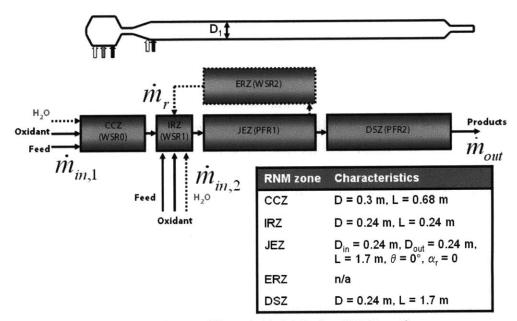
Figure 3-3: Reactor Network Model for 2 tpd MHI gasifier

Up to three feedstock types at each injector stage can be supplied to the ROM, allowing the injection of coal and recycled char in the first stage. Proximate and ultimate analyses of recycled char are calculated using the expressions shown in Table 3-6. Carbon conversion at the gasifier exit (C_{exit}) is known from the experiments performed by Watanabe et al [1]. Dry, ash-free char composition ($X_{k,daf}$) is known from the char composition calculation shown in Chapter 2. For exit carbon conversion values in the experimental range of 64-87%, mass fractions

120

of ash in char are calculated to be in the range 19-43%. This is consistent with the findings of Watanabe et al [18].

Table 3-6: Calculations for recycled char proximate and ultimate analyses

Analysis	Solid phase specie	Mass fraction in recycled char
Proximate	Fixed carbon	$X_{FC,char} = \dfrac{1 - C_{exit}}{1 - C_{exit} + X_{C,daf} X_{Ash,0}}$
	Ash	$X_{Ash,char} = 1 - X_{FC,char}$
	Volatile matter	$X_{VM,char} = 0$
	Moisture	$X_{M,char} = 0$
Ultimate	k = C, H, O, N, S	$X_{k,char} = X_{k,daf} X_{FC,char}$
	Ash	$X_{VM,char} = 0$
	Moisture	$X_{M,char} = 0$

3.4.3 Results of Validation

The ROM was validated by using it to simulate seven experiments that are described in detail by Watanabe [1]. The conditions for the seven tests are shown in Table 3-3. The model results were validated against the following experimental results and CFD simulations from Watanabe [1]: syngas temperature profiles, syngas composition, carbon conversion efficiency, char flow rate, syngas heating value and cold gas efficiency.

The validation results of reduced order modeling are shown in Figure 3-4 to Figure 3-10. Plots of additional non-validated ROM predictions are shown in Figure 3-11 to Figure 3-18. Although the latter set of plots is not strictly validated, they offer useful insight into the trends seen in the former set. Figure 3-4 and Figure 3-5 compare the experimentally recorded syngas temperature profiles for Coal M and Coal T, respectively, with Watanabe's CFD predictions and the ROM predictions. The flat sections of the ROM temperature profiles (a-b and c-d) indicate the location of the CCZ and IRZ, which are both WSRs. The steep drop in temperature (b-c) is the boundary between the CCZ, where combustion occurs, and the IRZ, where endothermic drying and devolatilization occur. The steep rise in temperature (d-e) is the result of rapid volatiles oxidation at the front end of the JEZ. The comparisons show satisfactory model accuracy in predicting syngas temperature profiles in the reductor of the gasifier (e-f), especially for Coal M. ROM accuracy in this region appears to be similar to that of the CFD model. For

121

tests performed with Coal T, neither ROM nor CFD simulations predict the full extent of the flattening of the temperature profile. The ROM however, predicts the gasifier exit temperature to within 60 °C (point f) for all Coal T tests.
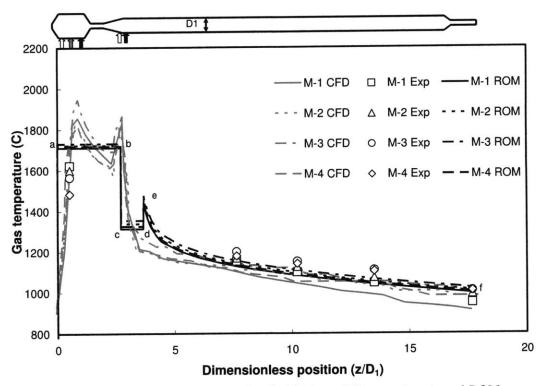
Figure 3-4: Temperature profiles for Coal M from CFD, experiments and ROM
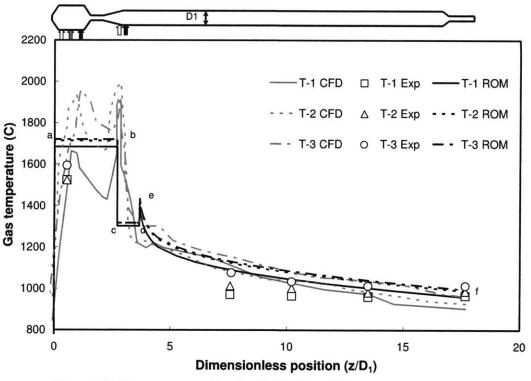
Figure 3-5: Temperature profiles for Coal T from CFD, experiments and ROM

Figure 3-6 compares the experimentally recorded syngas composition for all tests at the gasifier exit with the Watanabe's CFD predictions and the ROM predictions. The primary syngas constituent in all cases is N_2 due to the fact that the MHI gasifier is air-blown. Nitrogen mole fraction at the exit for all cases is 55-60% and is not shown in Figure 3-6. The comparison shows ROM accuracy to be similar to that of the CFD model. It is important to note that for all tests, the gas phase exiting the gasifier is at local chemical equilibrium. Differences between experiments and ROM and CFD predictions are due to differences in the predicted exit temperature as well as differences in stoichiometry due to predicted char reaction rates. Refer to Figure 3-13 for a profile plot of major gas phase species for Test M-1.
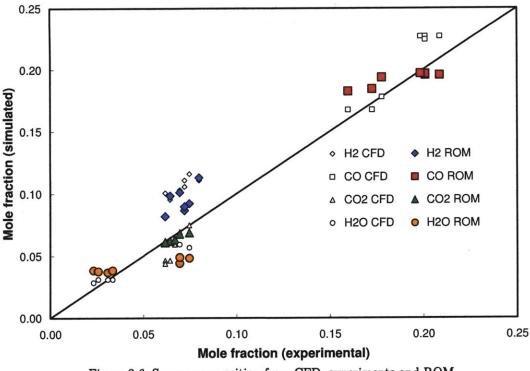
Figure 3-6: Syngas composition from CFD, experiments and ROM

Figure 3-7 compares the experimentally recorded carbon conversion for all tests at the gasifier exit with the Watanabe's CFD predictions and the ROM. Because char recycle is employed in the MHI gasifier, carbon conversion for the MHI is defined below. In the equation, $\dot{m}_{C,gas,out}$ represents the mass flow rate of carbon contained in the gas phase at the gasifier exit. Since char is recycled, the value calculated here should be regarded as the carbon conversion "per pass". Figure 3-7 shows that while the ROM slightly under-predicts carbon conversion, its accuracy appears to be similar to that of the CFD model.

$$C_{exit} = \frac{\dot{m}_{C,gas,out}}{\left(\dot{m}_{coal,combustor} + \dot{m}_{coal,reductor}\right)X_{C,in,coal} + \dot{m}_{char}X_{C,in,char}} \qquad \text{(Eq. 3-5)}$$

Figure 3-8 compares the experimentally recorded char mass flow rate for all tests at the gasifier exit with the Watanabe's CFD predictions and the ROM predictions. The ROM over-predicts char flow rate, which stands to reason as it also under-predicts carbon conversion (see Figure 3-7). Again, a level of accuracy similar to that for CFD analysis was achieved by the ROM. The relatively low carbon

conversions and high char flow rates are further illustrated in Figure 3-11 and Figure 3-12, which show that carbon is the dominant solid species in particles leaving the gasifier.
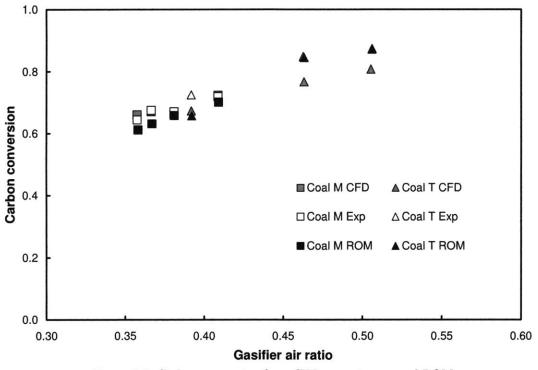
Figure 3-7: Carbon conversion from CFD, experiments and ROM
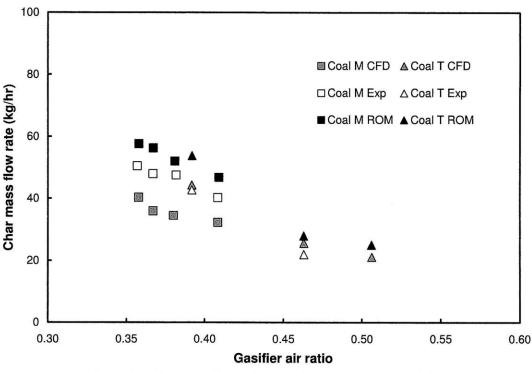
Figure 3-8: Char mass flow rate from CFD, experiments and ROM

Figure 3-9 compares the experimentally recorded syngas higher heating value (HHV) for all tests with the Watanabe's CFD predictions and the ROM predictions. HHV is calculated on a dry, volumetric basis. The comparison shows that the ROM under-predicts syngas HHV, but is more accurate than the CFD model.

Figure 3-10 compares the experimentally recorded gasifier cold gas efficiency (CGE_{HHV}) for all tests with the Watanabe's CFD predictions and the ROM predictions. CGE_{HHV} is defined below. The comparison shows that the ROM slightly over-predicts CGE_{HHV} for all tests. Its accuracy, however, appears to be similar to that of the CFD model.

$$CGE_{HHV} = \frac{\dot{m}_{syngas} HHV_{syngas}}{\left(\dot{m}_{coal,combustor} + \dot{m}_{coal,reductor} \right) HHV_{coal}} \qquad \text{(Eq. 3-6)}$$

126
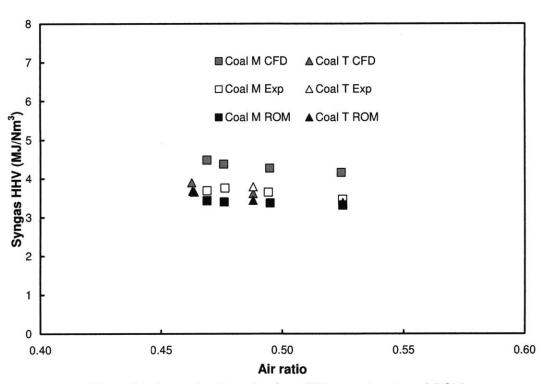
Figure 3-9: Syngas heating value from CFD, experiments and ROM
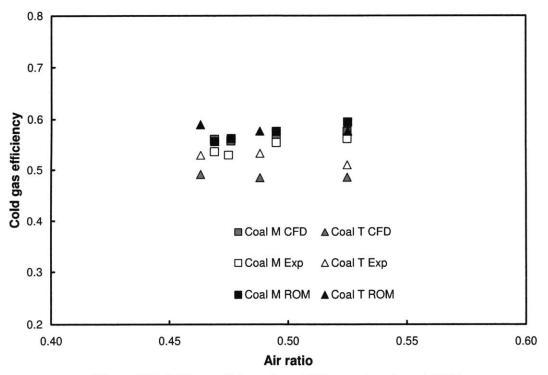
Figure 3-10: Cold gas efficiency from CFD, experiments and ROM

127

The ROM shows generally satisfactory agreement with experiments and CFD simulations for the 2 tpd MHI gasifier. It should be noted that the time required for ROM simulation is on the order of 1-5 minutes, while detailed CFD simulation requires days.

3.4.4 Additional ROM Predictions

Profiles of non-validated ROM predictions along the gasifier length are shown in Figure 3-11 to Figure 3-18. Figure 3-11 and Figure 3-12 show predicted ultimate and proximate analysis profiles. For clarity the only ultimate analysis profile shown is for Test 1. The profiles for other tests have similar shapes. Also, the plots for proximate analysis omit data sets for volatiles and moisture, as their mass fractions are negligible for most of the gasifier length. The plots indicate that due to the low conversion of the MHI design, particles leave the gasifier with fixed carbon mass fractions of 35-75%. This illustrates the need for char recycling, which is employed in the MHI design. The effect of raw coal injection in the second stage is seen in the sudden jump in carbon mass fraction at $z/D_1 \sim 3$. Mass fractions of non-carbon char species are very low as a result of devolatilization.
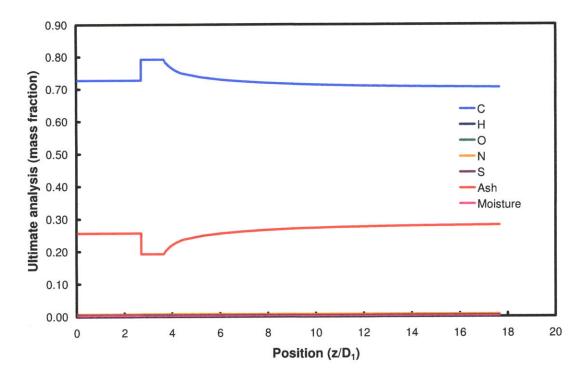
Figure 3-11: Ultimate analysis profile for Test M-1 for MHI lab-scale gasifier
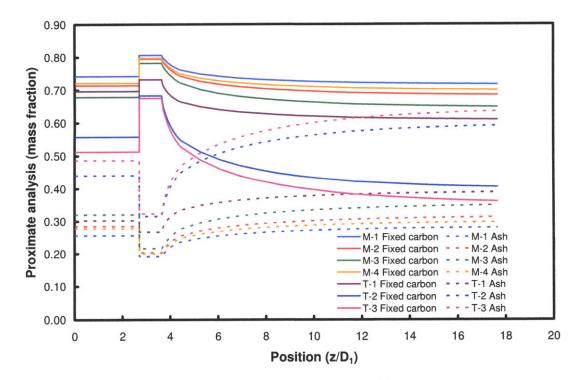
Figure 3-12: Proximate analysis profiles for MHI lab-scale gasifier

Figure 3-13 shows the predicted gas composition profile for Test M-1. Profiles for other tests are omitted for clarity. As expected, N_2 is the dominant specie in the air-blown MHI gasifier, having an exit mole fraction of 61%. The positions of the first stage combustor, where CO_2 and H_2O dominate, and second stage reductor, where CO and H_2 dominate, are clearly seen on the plot. The fact that mole fractions of H_2O and CO_2 are greater than zero at the exit mean that low conversion appears to be governed more by low temperatures in the reductor than by lack of reactants.
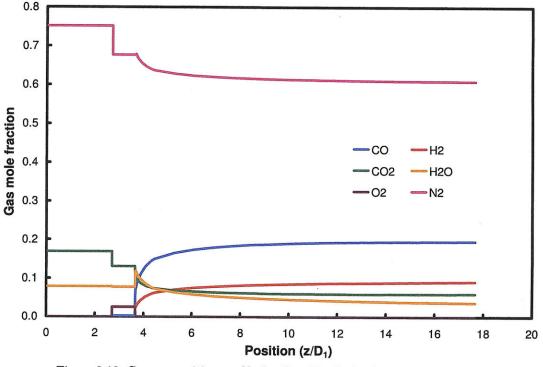
Figure 3-13: Gas composition profile for Test M-1 for MHI lab-scale gasifier

Figure 3-14 and Figure 3-15 show predicted particle bulk density and mass profiles, respectively. Predictions for particle diameter are omitted as they show virtually no change in particle diameter along the gasifier length. This indicates that most char conversion occurs on the internal surface area of the particle (decreasing bulk density) as opposed to the external area (decreasing diameter). The effect of raw coal injection in the second stage is again seen in the sudden jumps in the profiles. Recall that particles enter the gasifier with diameter 40 microns and initial density calculated by the char properties submodel of the ROM (see Section 2.5.2).
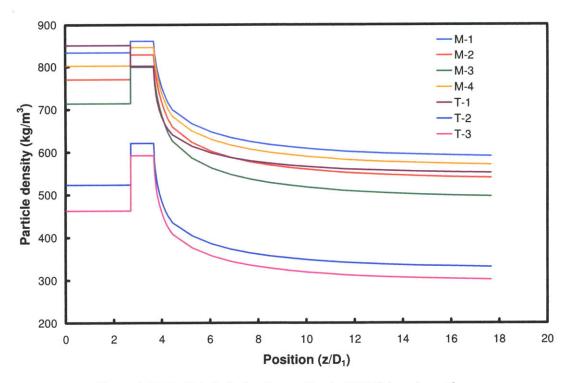
Figure 3-14: Particle bulk density profiles for MHI lab-scale gasifier
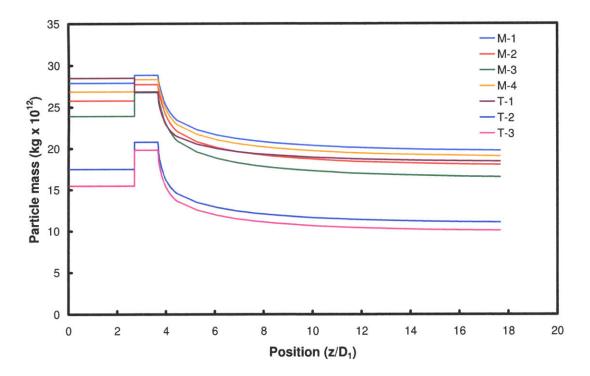
Figure 3-15: Particle mass profiles for MHI lab-scale gasifier

Figure 3-16 shows predicted particle volume fraction profiles. Particle volume fraction is predicted to increase along the gasifier length, which first appears to be counter-intuitive as particles are being consumed. This prediction is explained by two factors: (1) as explained above, virtually all char conversion occurs on the internal particle area, meaning that particle diameter and bulk volume $(4/3\rho\pi r^3)$ do not change significantly, and (2) as temperature decreases along gasifier length, so does gas density, meaning that higher particle loading occurs near the gasifier exit. The jump in particle volume fraction at the start of the second stage is due to the drop in temperature due to drying and devolatilization of raw coal. See the temperature profiles in Figure 3-4 and Figure 3-5 for further illustration.
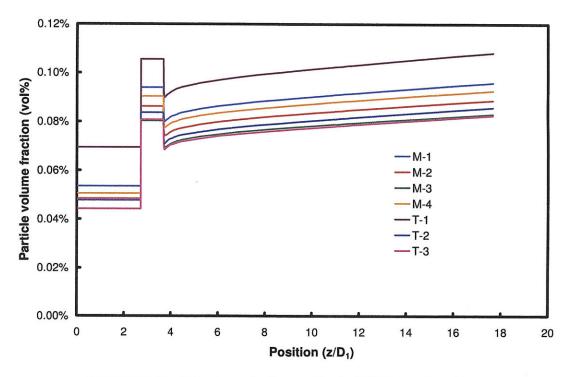
Figure 3-16: Particle volume fraction profiles for MHI lab-scale gasifier

Figure 3-17 shows predicted particle heterogeneous reaction rate profiles. Since the heterogeneous rate expressions used in simulating the MHI gasifier are extrinsic (mass-based) in form, reaction rates are given in units of 1/s. Predictions of reaction rates follow expected trends. Air is supplied to the second stage in just enough quantities to oxidize volatiles, while minimizing char oxidation. The char-O_2 reaction is briefly the fastest, but once O_2 is exhausted, $C+H_2O$ is the dominant heterogeneous reaction. Its rate and that of $C+CO_2$ decrease as do temperatures.

132
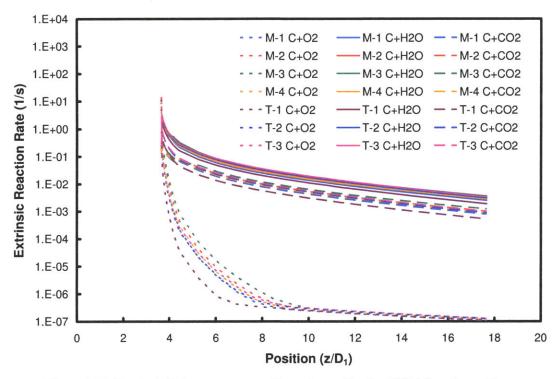
Figure 3-17: Extrinsic heterogeneous reaction rate profiles for MHI lab-scale gasifier

Figure 3-18 shows predicted radiative and convective wall heat flux profiles. As expected, particle-wall radiation is the dominant heat transfer mode. Heat fluxes in the first stage (combustor) are about an order of magnitude higher due to (1) very high temperatures caused by volatiles and char oxidation, and (2) use of membrane-cooling in that stage. Recall that radiative heat transfer scales with T^4. Particle enthalpy flux to the wall is not shown as the ROM does not simulate slagging for the MHI lab-scale gasifier. The next section describes the results of sensitivity analysis for the 2 tpd MHI gasifier.
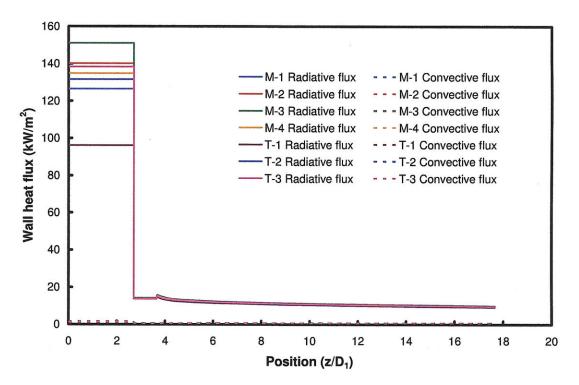
Figure 3-18: Wall heat flux profiles for MHI lab-scale gasifier

3.4.5 Sensitivity Analysis

Sensitivity analysis is performed to identify the modeling parameters and variables that are of greatest importance in determining the ROM outputs. The parameters considered in sensitivity analysis for the MHI design, as well as their base case values, are shown in Table 3-2. Recall that all parameters are varied over the range ±10% of their base case values.

Figure 3-19 and Table 3-7 present the results of sensitivity analysis for the 2 tpd MHI gasifier. The test case chosen for sensitivity analysis is test M-4, described in Table 3-2. Exit carbon conversion (C_{exit}) is the ROM output used in sensitivity analysis. It is clear from Figure 3-19 that C_{exit} is most sensitive to O_2:C ratio and pressure. Other important parameters include d_{IRZ}, ε_{wall}, $t_{FB}/(t_{FB}+t_{IB})$ and the rate of the C+H_2O reaction.

Increasing the inlet O_2:C ratio increases C_{exit} because higher temperatures and hence faster kinetics are achieved with more O_2. This however comes at the cost of additional CO_2 in the product syngas, leading to reduced heating value. Increasing

134

operating pressure also increases conversion by raising gas phase reactant partial pressures in the gasifier.

Decreasing wall emissivity decreases heat loss through the reductor wall, increases the temperature in the reductor and hence increases reaction rate and carbon conversion. The same effect is achieved by increasing the insulating brick thickness fraction in the gasifier wall, i.e. decreasing $t_{FB}/(t_{FB}+t_{IB})$. Increasing the rates of gasification reactions obviously has an effect on C_{exit}. As expected, the effect of the $C+H_2O$ reaction is more pronounced than that of the $C+CO_2$ reaction, due to former's higher rate under most EFG operating conditions. Having identified the sensitivity of the ROM predictions to these input parameters, it is very important to ensure they are as accurate as possible in order to reduce simulation errors.
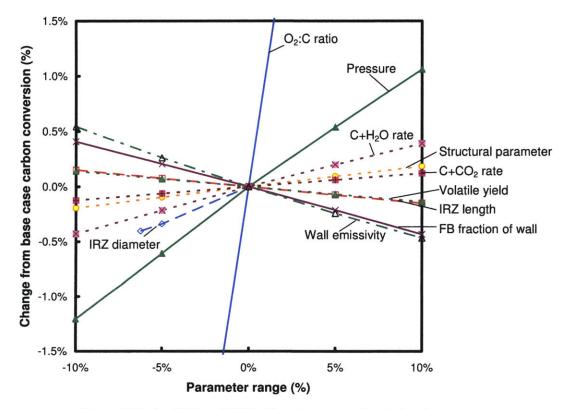
Figure 3-19: Sensitivity of MHI exit carbon conversion to input parameters

135

Table 3-7: Sensitivity of MHI exit carbon conversion to input parameters

Parameter (χ)	Description	Sensitivity ($S_{\chi \to \phi}$)	Comments
Gasifier design parameters			
m_{O2}:m_C	Inlet ratio of O_2 to C	1.043	This is the most important parameter
m_{H2O}:m_C	Inlet ratio of H_2O to C	n/a	No H_2O is added to gasifier
P	Operating pressure	0.114	This is the second most important parameter
T_{wall}	Wall temperature	n/a	T_{wall} is not fixed
$t_{FB}/(t_{FB}+t_{IB})$	Firebrick fraction of wall	-0.042	
Reactor network model parameters			
d_{IRZ}	IRZ diameter	0.066	
L_{IRZ}	IRZ length	-0.015	
α	Recirculation ratio	n/a	In the base case, recirculation cannot occur
θ	Jet expansion angle	n/a	In the base case, recirculation cannot occur
f_{JEZ}	Fraction of flow directly from ERZ to JEZ	n/a	In the base case, recirculation cannot occur
Particle parameters			
$\varepsilon_{p,0}$	Post-devolatilization porosity	n/a	Extrinsic kinetics do not require this
$a_{p,int,0}$	Post-devolatilization internal area	n/a	Extrinsic kinetics do not require this
$Y_{VM,daf,act}$	DAF volatile yield	-0.014	
ψ	Structural parameter	0.019	
M_{C+H2O}	Multiplier for rate of $C+H_2O$ reaction	0.041	
M_{C+CO2}	Multiplier for rate of $C+CO_2$ reaction	0.012	
Heat transfer parameters			
Pe_m	Peclet number for mass transfer	0.000	
Pe_h	Peclet number for heat transfer	0.000	
ε_w	Wall emissivity	-0.050	
δ_{slag}	Slag layer thickness	0.000	Fixed slag thickness used as input
f_{slag}	Slag deposition factor	n/a	Slagging is not simulated
k_{slag}	Slag conductivity	0.000	

In order to investigate to investigate to role of recirculation in the reductor of the gasifier, the sensitivity of gas temperature profiles to large changes in selected RNM parameters is considered. Figure 3-20 shows the sensitivity of the temperature profile predicted by the ROM to changes to the RNM. Experimental and CFD results for test M-4 [1] are also shown for comparison. Decreasing the IRZ diameter to a very small value (0.08 m), which has the effect of increasing the jet expansion angle (θ), and introducing external recirculation, results in a much different temperature profile. A markedly different temperature profile in the reductor (line e-g-f in Figure 3-20) is now observed. The effect of recirculation is to ensure more mixing and hence more uniform temperature distribution. The experimental results suggest that this does not occur and therefore the assumption of no external recirculation appears to be valid. Decreasing the IRZ length

eliminates the spike in temperature at the front end of the JEZ (d-e), producing profiles that closely match the CFD simulations.
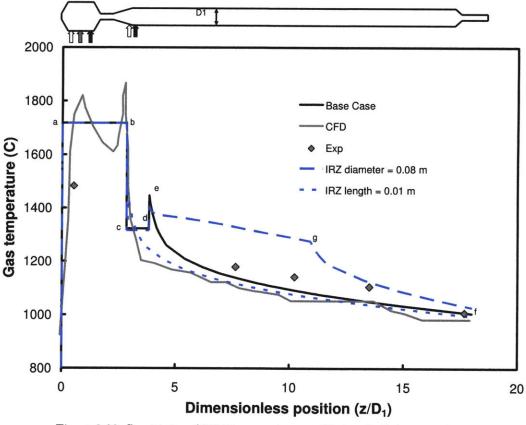
Figure 3-20: Sensitivity of MHI temperature profile to selected parameters

3.4.6 Summary

The ROM has been validated using experimental data for seven tests using two types of bituminous coal performed in a 2 tpd (metric-tonne-per-day) MHI lab-scale gasifier. The MHI gasifier is up-flow, dry-fed, air-blown, radially/tangentially-fired and two-stage, with a membrane-lined combustor and a refractory-lined reductor. Lumped extrinsic (mass-based) parameters were provided for the coals used. Experimental data used for validation includes temperature profiles, exit gas composition, exit carbon conversion, exit char mass flow rate, exit gas higher heating value, and overall gasifier cold gas efficiency. Comparison of ROM predictions to experimental data and CFD predictions carried out by others shows satisfactory ROM accuracy.

137

The temperature profiles, shown in Figure 3-4 and Figure 3-5, clearly show the difference in temperatures between the first stage combustor and the second stage reductor. This difference is also seen in Figure 3-18, which presents predictions of wall heat flux profiles. Radiation is everywhere the dominant mode of heat transfer due to high temperatures and high particle loading. Radiation in the combustor, which has cooled walls, and where temperatures are highest, is much greater than in the reductor. The largest predicted error in exit temperature is 60 °C. Note that exit temperatures are experimentally recorded in the range 950-1013 °C.

The gasifier is predicted to produce syngas of the following composition: 18.3-19.7% CO, 8.2-11.3% H_2, 6.1-6.9% CO_2 and 3.7-4.9% H_2O. The bulk of the remainder of the gas consists of N_2 due to the fact that the MHI gasifier is air-blown. Figure 3-13 shows that CO_2 and H_2O are consumed by char gasification reactions to produce CO and H_2.

The maximum error in carbon conversion is 65.7% predicted vs. 72.5% experimentally recorded. This 6.8 percentage point difference corresponds to an error of -9.3%. The dominant heterogeneous reaction is shown by Figure 3-17 to be the hydro-gasification reaction ($C+H_2O$). The reaction of $C+CO_2$ proceeds at a rate roughly an order of magnitude less than that of $C+H_2O$. Char oxidation is important only in the early stages of the gasifier, before O_2 is exhausted.

Sensitivity analysis has also been performed to determine the input parameters and variables of highest importance to ROM predictions. Each of the selected important ROM inputs is varied ±10% around their base case value and the effect of this on exit carbon conversion is observed. Figure 3-19 and Table 3-7 show that increases in inlet O_2:C ratio, pressure, IRZ diameter and $C+H_2O$ reaction rate have important positive impacts on carbon conversion. Wall emissivity and firebrick fraction of wall thickness have important negative impacts on carbon conversion. Increased pressure and $C+H_2O$ reaction rate lead to faster char conversion, as does the higher temperatures produced by more oxygen. By increasing wall emissivity and firebrick thickness (in effect reducing insulating brick thickness), more heat is lost through the gasifier walls, which reduces temperature and char gasification rates.

The effect of reducing IRZ diameter (in effect increasing external recirculation, see Section 2.2.1) on conversion is further examined. It is found that for the MHI gasifier, inclusion of external recirculation leads to distortion of the temperature profiles. See Figure 3-20 for an illustration of this. Recirculation causes flattening of the temperature profile, which is not seen experimentally. Therefore the most appropriate reactor network model for the lab-scale MHI gasifier is one that consists of the CCZ for the first stage, and the IRZ, JEZ and DSZ for the second stage. The ERZ is unimportant when no external recirculation occurs.

Note that the steady-state simulations presented in this section were all performed in a matter of 1-5 minutes on a desktop personal computer. CFD simulations of similar systems are known to take 1-5 days to reach a converged solution, depending on the treatment of turbulence.

3.5 CSIRO Lab-Scale Gasifier

3.5.1 Experimental Description

The CSIRO gasifier is a purely experimental design and is not intended to be developed for commercial use, hence its exclusion from the review of commercial EFG designs in Chapter 1. At a fundamental level it is a continuous flow chemical reactor used to assess the gasification characteristics of Australian coals. The fact that it is a purely experimental gasifier in no way detracts from the utility of its results in validating the ROM. Figure 3-2 gives a description of the 0.1 tpd lab-scale CSIRO gasifier. The gasifier is down-flow, dry-fed, air-blown, axially-fired and one-stage, with electrically heated walls to ensure a uniform temperature of 1400 °C. It is assumed that as this is a lab-scale gasifier, it does not operate for sufficiently long periods of time to warrant full slagging and slag removal. Inlet streams are heavily diluted by nitrogen (N_2) to control reaction rates. The CSIRO gasifier attempts to approximate plug flow as closely as possible, by employing a very high aspect ratio (~30) and a specially-designed injector (see Figure 2 in [3]). Due to the lack of recirculation it uses inlet streams that are preheated to 900-1000 °C in order to ignite the feedstock. Note that as the walls are electrically heated to a uniform temperature, the compositions of the insulating walls are not important for the ROM.

Coal feed

Gas feed

Electrical
pre-heaters

Reaction zone
(gasifier)

Electrical
heaters

Insulation

Quench bath

Gas sampling
probe

L

D

$D = 0.07$ m
$L = 2.1$ m
t_{FB} = n/a
t_{IB} = n/a
t_{st} = n/a

Characteristic	0.1 tpd CSIRO lab-scale
Flow direction	Down
Feedstock delivery	Dry (no H_2O at all)
Injector configuration	Axial
Oxidant	Air (+N_2 diluent)
Number of stages	1
Wall lining	Electrically heated
Syngas cooling	Quench

Figure 3-21: 0.1 tpd CSIRO gasifier schematic and characteristics

Table 3-8 shows the test conditions imposed for experiments using the CSIRO gasifier. The coal types are identified by codes given by CCSD [3]. The coal types used in the tests are all Australian bituminous coals. Their ultimate and proximate analyses are given in Table 3-8. All tests are conducted at a pressure of 2 MPa (20 bar). All flow rates for these tests are expressed in units of kg/hr.

Table 3-8: Test conditions and coal specification for 0.1 tpd CSIRO gasifier

Test		1	2	3	4
Input data					
Pressure	MPa	2	2	2	2
Coal flow rate	kg/hr	2.07	1.75	2	1.84
Air flow rate	kg/hr	3.08	6.67	8.39	6.61
N_2 flow rate	kg/hr	51.58	49.47	25.79	49.34
Gas inlet temperature	°C	917	1000	1000	1000
Coal type		CRC299	CRC358	CRC274	CRC252
Inlet particle diameter	μm	118	100	110	128
Initial particle density	kg/m^3	1571	1396	1410	1429
Post-devolatilization particle porosity	-	0.25	0.10	0.07	0.15
Proximate analysis					
Fixed carbon	wt%	39.7	59.4	58.0	39.1
Volatile matter	wt%	24.3	19.2	28.0	38.8
Ash	wt%	25.0	20.2	9.3	11.3
Moisture	wt%	10.9	1.2	4.7	10.7
Ultimate Analysis					
C	wt%	52.1	69.6	72.0	60.9
H	wt%	2.8	3.7	4.1	4.6
O	wt%	8.1	3.3	7.8	11.2
N	wt%	0.8	1.4	1.7	0.9
S	wt%	0.3	0.7	0.4	0.4
Ash	wt%	25.0	20.2	9.3	11.3
Moisture	wt%	10.9	1.2	4.7	10.7

Table 3-9 shows the intrinsic (area-specific) kinetic rate parameters for the test coals used in the CSIRO gasifier. These parameters were originally obtained through testing done in the CSIRO gasifier [3]. At this point it is useful to recall that for intrinsic kinetic data, such as CCSD's, the reaction rate expression computed by the ROM has the form shown below. Refer to Section 2.5.4.2.1 for more details on the application of these types of kinetic data into the ROM.

$$R_m = k_{in,m}(A^{"}_{p,ext} + \eta_m A^{"}_{p,\text{int}})P^{n_{in,m}}_{s,m}$$

where

$$k_{in,m} = A_{in,m}\exp(-E_{in,m}/\Re T)$$

(Eq. 3-7)

Table 3-9: Kinetic rate parameters for CSIRO gasifier test coals from [3]

Reaction	Parameter	Units	CRC299	CRC358	CRC274	CRC252
$C+O_2$	$A_{in,1}$	$kg/m^2/s/atm^n$	601	319	13.8	0.00125
	$E_{in,1}$	$GJ/kmol$	0.1565	0.1605	0.138	0.102
	$n_{in,1}$		0.8	0.8	0.8	0.8
$C+H_2O$	$A_{in,2}$	$kg/m^2/s/atm^n$	10400	226	600	1960
	$E_{in,2}$	$GJ/kmol$	0.2679	0.2382	0.228	0.253
	$n_{in,2}$		0.4	0.4	0.4	0.4
$C+CO_2$	$A_{in,3}$	$kg/m^2/s/atm^n$	83200	202	20000	4100
	$E_{in,3}$	$GJ/kmol$	0.2905	0.2432	0.289	0.261
	$n_{in,3}$		0.3	0.4	0.4	0.4
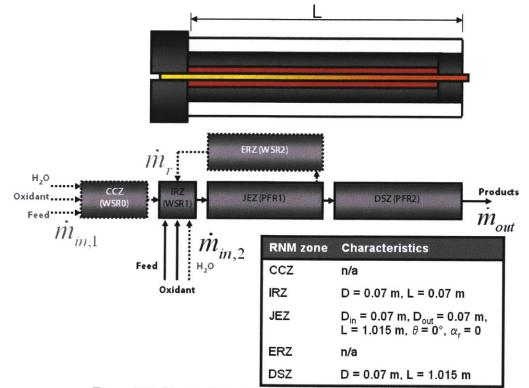
3.5.2 Implementation in the ROM

Figure 3-22 shows the dimensions and characteristics of the RNM for this case. The most important features of the RNM are that (1) it does not employ a CCZ because the CSIRO gasifier is single-stage and (2) it does not consider external recirculation from the JEZ, through the ERZ, back to the IRZ and to the front of the JEZ. External recirculation is not considered for similar reasons as those described in Section 3.4.2; namely no sudden expansions exist, and the aspect ratio (~30) is sufficiently high to render any external recirculation insignificant.

The IRZ models the region near the injectors and is modeled as a cylinder of length and diameter equal to the gasifier diameter (i.e. L_{IRZ} = 0.07 m, d_{IRZ} = 0.07 m). These dimensions are estimations and are subject to sensitivity analysis (see following sections). As explained above, external recirculation is not considered, so flow to the ERZ is zero and its dimensions are unimportant. Since external recirculation is not considered, the relative lengths of the JEZ and DSZ are not important, as long as their lengths plus that of the IRZ add up the total length of the reductor (2.1 m). Therefore the JEZ and DSZ are modeled as right cylinders of equal length (L_{JEZ} = L_{DSZ} = 1.015 m) and diameter (d_{JEZ} = d_{DSZ} = 0.07 m). All of the RNM dimensions are shown in Figure 3-22.

One piece of information is missing from the CCSD report: the post-devolatilization porosity of particles ($\varepsilon_{p,0}$). The simulation work carried out by CCSD makes the assumption that most of the char formed by devolatilization is dense with a porosity of less than 40% [3]. Therefore values of $\varepsilon_{p,0}$ in the range 0-40% are chosen for each coal type such that the exit carbon conversion (C_{exit}) is near the value

142

recorded by CCSD. The chosen values of $\varepsilon_{p,0}$ are shown in Table 3-8. The influence of $\varepsilon_{p,0}$ on ROM results will be examined by sensitivity analysis.

Figure 3-22: Reactor Network Model for 0.1 tpd CSIRO gasifier
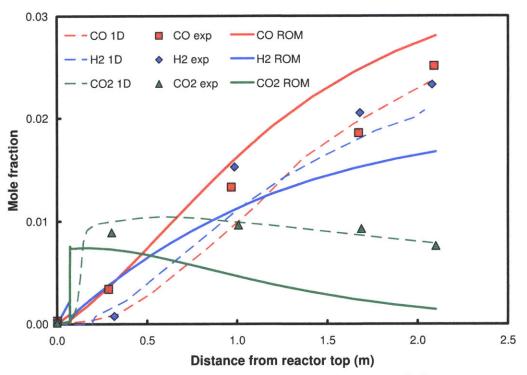
3.5.3 Results of Validation
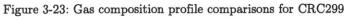
The ROM was validated by using it to simulate the four experimental tests that are described in detail by CCSD [3]. The conditions for the four tests are shown in Table 3-8. The model results were validated against the experimental data for syngas composition profiles and carbon conversion profiles, as well as against 1-D and 2-D simulations from CCSD [3].

The results of reduced order modeling are shown in Figure 3-23 to Figure 3-30. Plots of additional non-validated ROM predictions are shown in Figure 3-30 to Figure 3-43. Although the latter set of plots is not strictly validated, they offer useful insight into the trends seen in the former set. Figure 3-23 and Figure 3-24 show the gas composition and carbon conversion profiles, respectively, for coal type CRC299. Figure 3-25 and Figure 3-26, Figure 3-27 and Figure 3-28, and Figure

143

3-29 and Figure 3-30 show the same information for coal types CRC358, CRC274 and CRC252, respectively. Note that for all tests the dominant gas phase specie is N_2, with mole fractions always around 90%.

It is observed that the gas composition profiles of all tests follow the same trend; rapid formation of CO_2 due to volatile and char combustion, followed by slower destruction of CO_2 and formation of CO and H_2 via the gasification reactions. The point at which CO and H_2 formation commences can be assumed to represent the point where all O_2 has been consumed. The results of reduced order modeling show that if $\varepsilon_{p,0}$ is chosen such that C_{exit} is close to the experimental value, satisfactory accuracy in predicting gas composition profiles can be obtained. The prediction for CRC299 is the least satisfactory, while those for CRC358, CRC274 and CRC252 appear to be as accurate as those of the simulation work performed by CCSD.

The highest carbon conversion is seen for CRC274, which is also the test which shows the highest temperatures (see Figure 3-42). The opposite is true for CRC299; low conversion coincides with low temperatures. The test conditions used in CRC299 results in the lowest inlet O_2:C ratio of any of the tests; 0.67 compared to 1.28-1.37 for the other tests. A possible explanation for the low carbon conversion seen for CRC358 (Figure 3-26) is the fact that the volatile content of that coal is much lower than that of the others (19% vs. 28% and 39% for coals CRC274 and CRC 252, respectively). This means that a greater proportion of the carbon in CRC358 is in the form of fixed carbon, as opposed to volatiles. Carbon conversion due to devolatilization is much easier and faster to achieve than that due to char conversion. So despite reasonably high temperatures present for CRC358, more time is needed for slow gasification reactions to obtain similar carbon conversions to the other tests.

Figure 3-23: Gas composition profile comparisons for CRC299
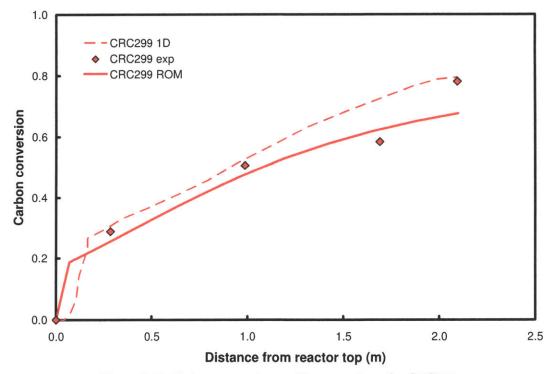
Figure 3-24: Carbon conversion profile comparisons for CRC299
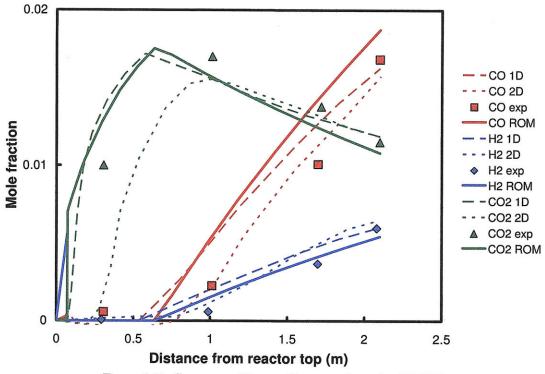
Figure 3-25: Gas composition profile comparisons for CRC358
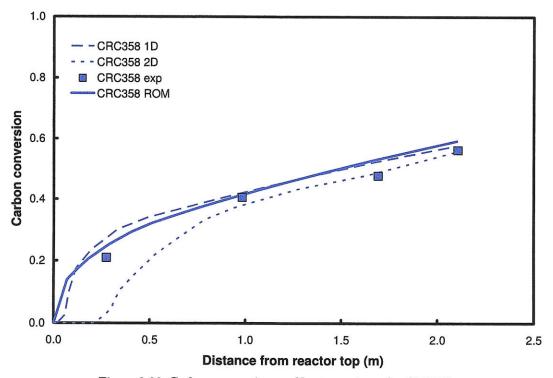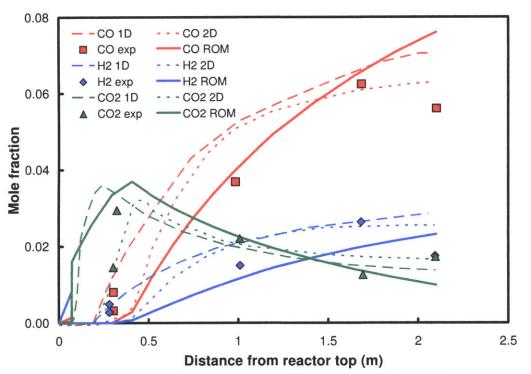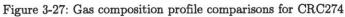
Figure 3-26: Carbon conversion profile comparisons for CRC358

146

Figure 3-27: Gas composition profile comparisons for CRC274
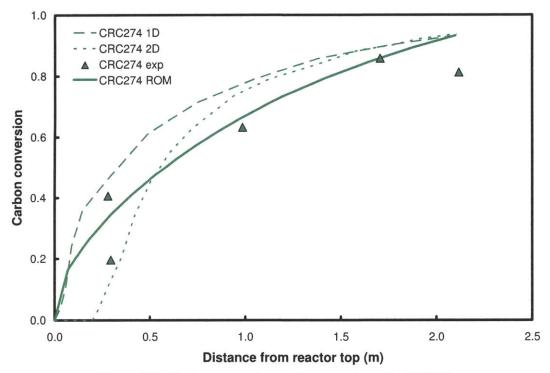
Figure 3-28: Carbon conversion profile comparisons for CRC274

147
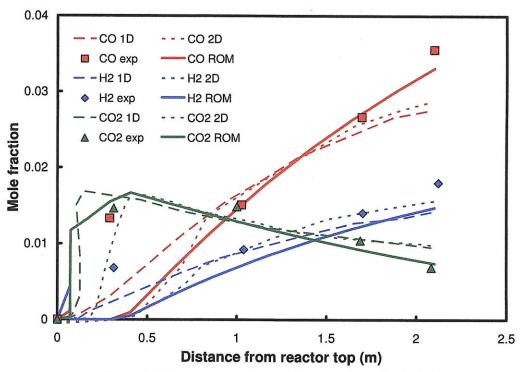
Figure 3-29: Gas composition profile comparisons for CRC252
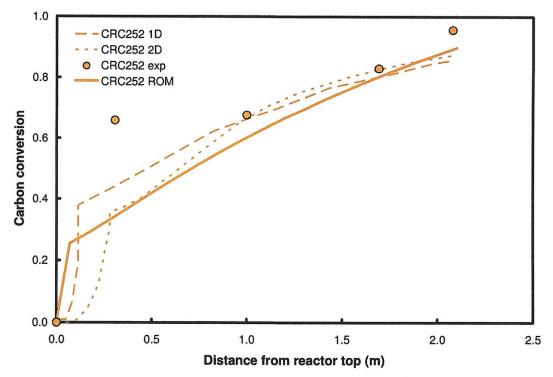
Figure 3-30: Carbon conversion profile comparisons for CRC252

3.5.4 Additional ROM Predictions

Profiles of non-validated ROM predictions along the gasifier length are shown in Figure 3-31 to Figure 3-43. Figure 3-31 and Figure 3-32 show predicted ultimate and proximate analysis profiles. For clarity the only ultimate analysis profile shown is for test CRC252. The profiles for other tests have similar shapes. Also, the plots for proximate analysis omit data sets for volatiles and moisture, as their mass fractions are negligible for most of the gasifier length. The plots indicate that particles leave the CSIRO gasifier with carbon mass fractions of 35-65%.
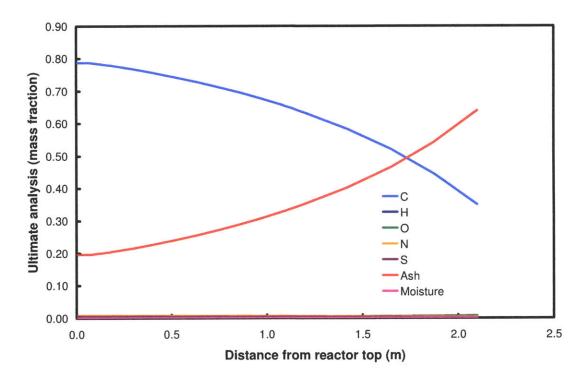
Figure 3-31: Ultimate analysis profile for test CRC252 for CSIRO lab-scale gasifier
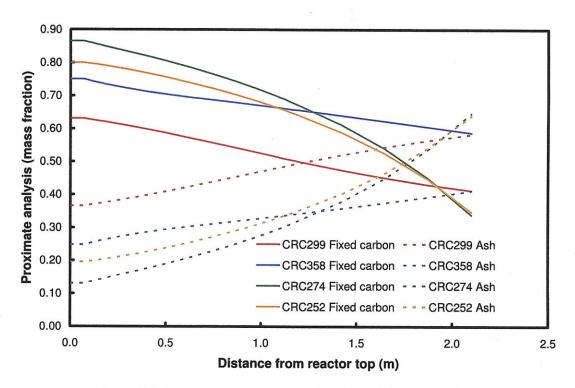
Figure 3-32: Proximate analysis profiles for CSIRO lab-scale gasifier

Figure 3-33 and Figure 3-34 show predicted particle bulk density and mass profiles, respectively. Predictions for particle diameter are omitted as they show virtually no change in particle diameter along the gasifier length. This indicates that most char conversion occurs on the internal surface area of the particle (decreasing bulk density) as opposed to the external area (decreasing diameter). Recall that particles enter the gasifier with the diameters and densities shown in Table 3-8 (i.e. 100-128 microns and 1369-1571 kg/m^3).
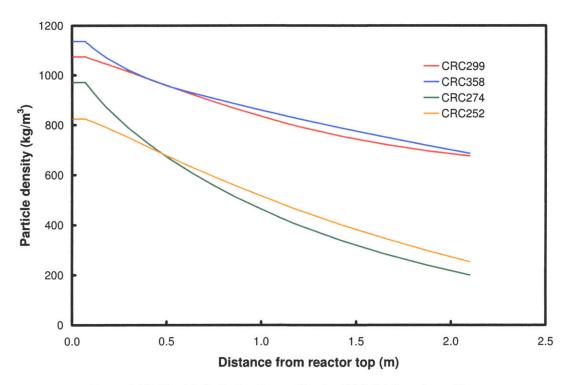
Figure 3-33: Particle bulk density profiles for CSIRO lab-scale gasifier
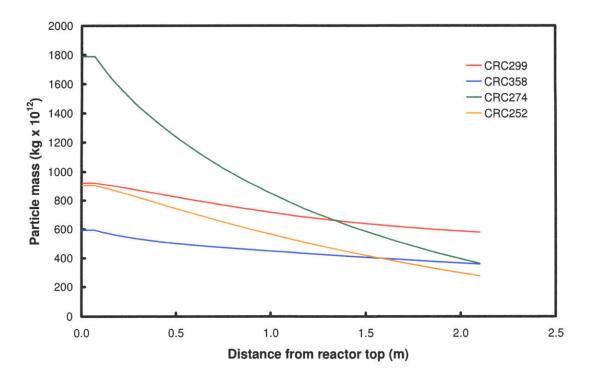
Figure 3-34: Particle mass profiles for CSIRO lab-scale gasifier

151

Figure 3-16 shows predicted particle volume fraction profiles. Particle volume fraction is predicted to stay roughly uniform along the gasifier length. This prediction is explained by two factors: (1) as explained above, virtually all char conversion occurs on the internal particle area, meaning that particle diameter and bulk volume $(4/3\rho\pi r^3)$ do not change significantly, and (2) as wall temperature is uniform at 1400 °C along gasifier length, gas and particle temperatures approach that value. See the temperature profiles in Figure 3-42 for further illustration. Particle volume fractions are extremely low for all CSIRO gasifier tests because the gas flow is heavily-diluted with nitrogen. The mole fraction of N_2 for all tests is around 95%. In order to maintain desirable stoichiometry, particle loading must be reduced.
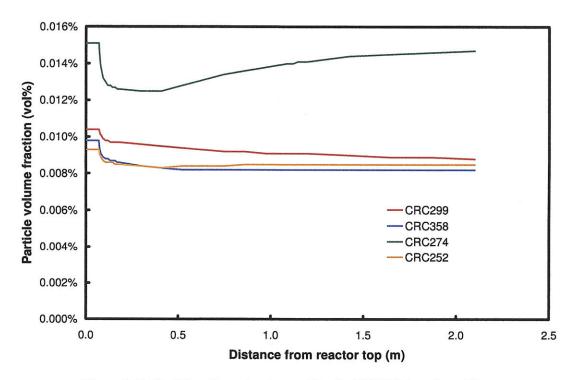
Figure 3-35: Particle volume fraction profiles for CSIRO lab-scale gasifier

Figure 3-36 and Figure 3-37 show predicted particle internal surface area and heterogeneous intrinsic reaction rate profiles. For the CSIRO gasifier, it is possible to examine surface area and reaction rate profiles separately because the heterogeneous rate data provided by CSIRO is intrinsic (area-based) in nature. The internal surface areas of all coals are predicted to rise due to particle

152

evolution. In the cases of CRC252 and CRC274, internal areas reach maxima of around 900 m^2/g and 800 m^2/g, respectively. The exit carbon conversions for these two tests are much higher than they are for the other two tests. The different shapes of these profiles reflect the fact that heterogeneous kinetic data for CSIRO tests are intrinsic in nature. Predictions of reaction rates follow expected trends, and are similar to those observed for the MHI gasifier. Air is supplied to gasifier in just enough quantities to oxidize volatiles, while minimizing char oxidation. The char-O_2 reaction is briefly the fastest, but once O_2 is exhausted, C+H_2O is the dominant heterogeneous reaction. Its rate and that of C+CO_2 decrease as do temperatures.

Figure 3-38 shows predicted heterogeneous extrinsic reaction rate profiles. Extrinsic rates can be found by multiplying the particle internal surface area, shown in Figure 3-36, by the intrinsic reaction rate, shown Figure 3-37. A noticeable feature of the intrinsic rate profiles for coals CRC274 and CRC252 is the increase towards the end of the gasifier. This is despite the fact that temperature decreases or stays roughly uniform in these cases. This explained by the fact that the high levels of particle conversion for coals CRC274 and CRC252 (refer to Figure 3-28 and Figure 3-30, respectively) allow easier diffusion of reactants into the particle structure, thus increasing intrinsic rate. Figure 3-39 shows that the effectiveness factors of both gasification reactions increase in the latter stages of the gasifier for coals CRC274 and CRC252.

While the shapes of extrinsic reaction rate profiles are similar to those of intrinsic profiles, the effect of surface area reduction for coals CRC274 and CRC252 are seen towards the end of the gasifier in Figure 3-38. While extrinsic rates are of little interest when intrinsic data is available, they are useful when compared to results from other gasifier designs used for ROM validation, which use extrinsic rate data.
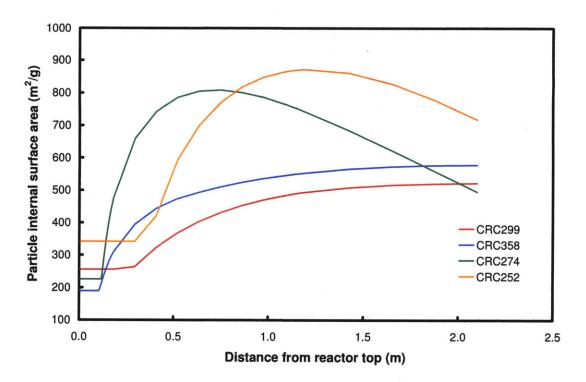
Figure 3-36: Particle internal surface area profiles for CSIRO lab-scale gasifier
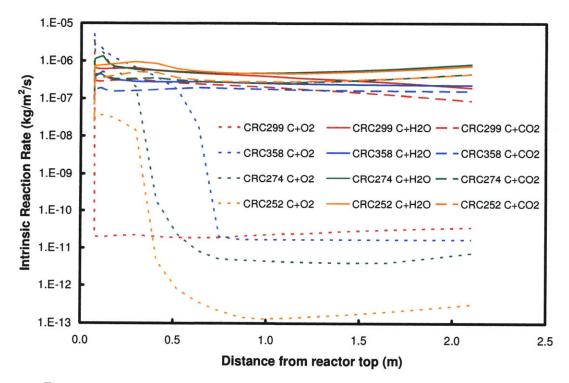
Figure 3-37: Heterogeneous intrinsic reaction rate profiles for CSIRO lab-scale gasifier

154
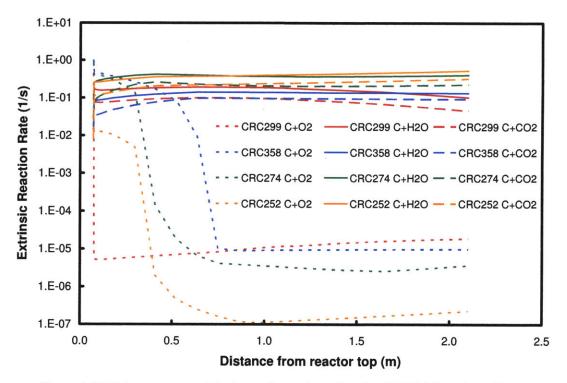
Figure 3-38: Heterogeneous extrinsic reaction rate profiles for CSIRO lab-scale gasifier
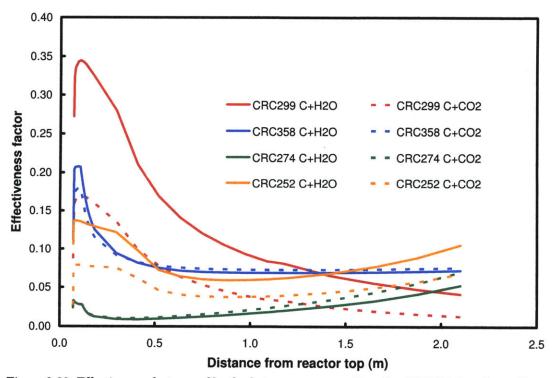
Figure 3-39: Effectiveness factor profiles for heterogeneous reactions for CSIRO lab-scale gasifier

155

A further advantage of intrinsic rate expressions is that they allow one to examine the roles played by film diffusion and pore diffusion-reaction in heterogeneous reactions. Figure 3-40 and Figure 3-41 shows predicted resistivities to reaction caused by film diffusion and pore diffusion-reaction for coals CRC358 and CRC252, respectively. Using the effectiveness factor method does not allow one to distinguish between pore diffusion and reaction within the pores as they are intimately linked. To distinguish between pore diffusion and pore reaction, one must solve reaction-diffusion equations within the particle. This approach is extremely computationally-expensive and is not used here. Resistivities to film diffusion ($r''_{diff,m}$) and pore diffusion-reaction ($r''_{rxn,m}$) for the mth heterogeneous reaction are calculated as follows.

$$r''_{diff,m} = \hat{\rho}_g \left(\hat{X}_i - \hat{X}_{s,i} \right) / \dot{n}''_{i,m} \qquad \text{(Eq. 3-8)}$$

$$r''_{rxn,m} = \hat{\rho}_g \hat{X}_{s,i} / \dot{n}''_{i,m} \qquad \text{(Eq. 3-9)}$$

where

$\hat{\rho}_g$ =Molar gas density (kmol/m^3)

$\hat{X}_i$ = Bulk mole fraction of ith gas-phase reactant

$\hat{X}_{s,i}$ =Surface mole fraction of ith gas-phase reactant

$\dot{n}''_{i,m}$ =Molar flux of ith gas-phase reactant for mth heterogeneous reaction (kmol/m^2/s)

The molar flux of each gas-phase reactant, O_2, H_2O and CO_2, is calculated from the diffusion-reaction equations presented in Section 2.5.4.2.1. The profiles shown in Figure 3-40 and Figure 3-41 show that both gasification reactions ($C+H_2O$ and $C+CO_2$) are limited by the kinetics of reaction, while char oxidation is film-diffusion-limited. Figure 3-41 does not show resistivities for the $C+O_2$ reaction as O_2 concentration after volatiles oxidation is negligible.

It is important to note that in the case of CRC252 for both gasification reactions resistivity due to film diffusion is of the same order of magnitude as that due to pore diffusion-reaction. It is also apparent that as the particles approach the end of the reactor, where temperatures are higher for test CRC252 (see Figure 3-42), the kinetic limitation of both reactions becomes less obvious. In fact the profiles show that near the end of the reactor, resistivities due to film diffusion and pore

diffusion-reaction for $C+CO_2$ are identical. This shows the strong effect temperature has on reaction kinetics, compared to diffusion kinetics. Another factor that acts to decrease resistivities due to pore reaction-diffusion is the increase in effectiveness factors for CRC252 seen in Figure 3-39. CRC358 shows a much higher degree of kinetic-control for gasification, with resistivities due to pore diffusion-reaction roughly one order of magnitude higher than those for film diffusion. Char oxidation ceases for test CRC358 after about 0.7 m because O_2 is exhausted at this point.
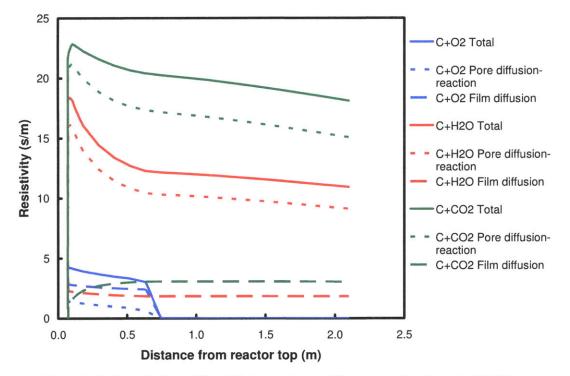
Figure 3-40: Resistivities of film diffusion and pore diffusion-reaction for test CRC358
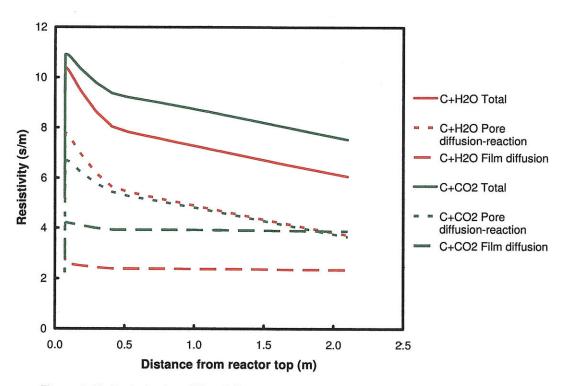
Figure 3-41: Resistivities of film diffusion and pore diffusion-reaction for test CRC252

Figure 3-42 and Figure 3-43 show predicted temperature and wall heat flux profiles. As expected, all gas and particle temperatures approach the uniform wall value of 1400 °C. Test CRC274 shows a significant temperature rise due to char combustion. Refer to Figure 3-27 to see that CO_2 mole fraction reaches a peak in this test of 4%, much higher than values encountered in other tests. Endothermic gasification reactions then reduce temperatures. The other tests show similar behavior; temperatures initially rise rapidly due to oxidation, later rising at slower rates due to the combined effects of gasification and heat transfer from the walls.

The effect of these temperature profiles are seen in Figure 3-43. Negative wall heat fluxes are seen where gas and particle temperatures are lower than that of the wall. Note that radiative and convective fluxes are of the same order for the CSIRO gasifier. This is primarily due to the low particle volume fraction encountered in this design (see Figure 3-35). It should also be noted that the small diameter of the CSIRO gasifier means that KB ~ 0.1, much lower than the minimum required value of 3 (see Section 2.5.6). Recall that K is the absorption coefficient of the particle cloud, while B is the characteristic length of the gasifier, which is very thin in this case. This means that the ROM is likely to over-predict the role of particle-

wall radiation. The fact that the radiation submodel does not include gas-wall radiation is also likely to introduce error into the predictions due to low particle loading in the CSIRO gasifier.
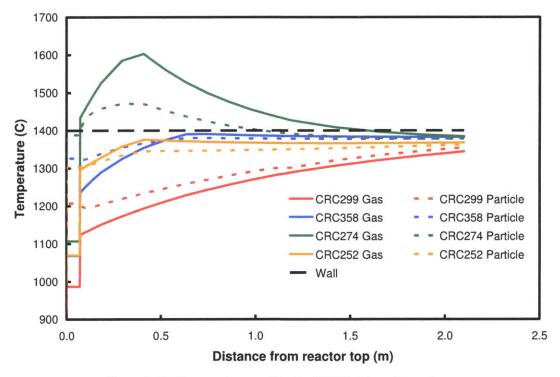
Figure 3-42: Temperature profiles for CSIRO lab-scale gasifier
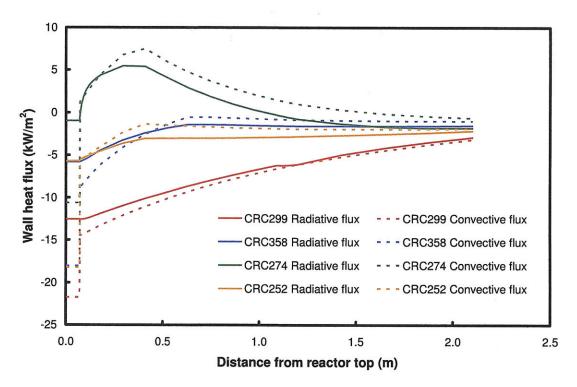
Figure 3-43: Wall heat flux profiles for CSIRO lab-scale gasifier

3.5.5 Sensitivity Analysis

Sensitivity analysis is performed to identify the modeling parameters and variables that are of greatest importance in determining the ROM outputs. The parameters considered in sensitivity analysis for the CSIRO design, as well as their base case values, are shown in Table 3-2. Recall that all parameters are varied over the range ±10% of their base case values.

Note that as the oxidant stream for the CSIRO design is heavily diluted with N_2, the method used to vary O_2:C ratio used for the other designs cannot be used here. For the other designs, O_2:C ratio is changed simply by changing the flow rate of oxidant while maintaining steady feedstock flow rate. In the case of the CSIRO gasifier, this approach leads to the addition of more N_2, which more than counters the effects of more O_2, leading to erroneous sensitivity analysis. Therefore for the CSIRO design, oxidant flow rate is held steady while O_2 mass fraction in the stream is increased.

160

Figure 3-44 and Table 3-10 present the results of sensitivity analysis for the 0.1 tpd CSIRO gasifier. The test case chosen for sensitivity analysis is CRC252, described in Table 3-2. Exit carbon conversion (C_{exit}) is the ROM output used in sensitivity analysis. It is clear from Figure 3-19 that C_{exit} is most sensitive to wall temperature[1]. Other important parameters include inlet O_2:C ratio, pressure and volatile yield.

Increasing the wall temperature increases overall reaction rates and carbon conversion. Increasing the inlet O_2:C ratio and gasifier operating pressure have the same effect on conversion, similar to the other gasifier designs.

The relatively minor effect of increasing the heterogeneous reaction rates in the CSIRO design indicates that the char conversion reactions are diffusion-limited. This is supported by the fact that the effectiveness factors for the $C+H_2O$ and $C+CO_2$ reactions in the base case are calculated in the ranges 0.06-0.13 and 0.03-0.07, respectively. The weak effect of heterogeneous reaction rates is only seen for the CSIRO tests as for all other ROM simulations, extrinsic (lumped) reaction expressions are used.

Volatile yield is important for this case as the volatile matter composition of the raw coal is 38%, a high value. Increasing wall emissivity has a small positive effect indicating there is a net heat addition from the walls.

---

[1] Recall that the CSIRO gasifier is the only design considered that uses electrical heaters to maintain a uniform wall temperature.
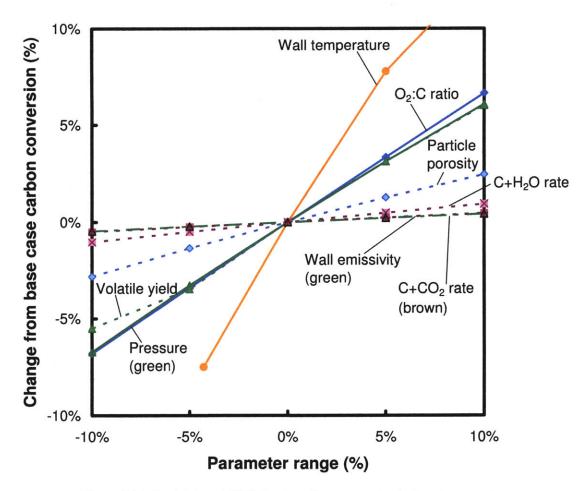
Figure 3-44: Sensitivity of CSIRO exit carbon conversion to input parameters

Table 3-10: Sensitivity of CSIRO exit carbon conversion to input parameters

Parameter (χ)	Description	Sensitivity ($S_{\chi \to \phi}$)	Comments
Gasifier design parameters			
$m_{O2}:m_C$	Inlet ratio of O_2 to C	0.672	
$m_{H2O}:m_C$	Inlet ratio of H_2O to C	n/a	No H_2O is added to gasifier
P	Operating pressure	0.639	
T_{wall}	Wall temperature	1.557	This is the most important parameter
$t_{FB}/(t_{FB}+t_{IB})$	Firebrick fraction of wall	n/a	Walls are electrically-heated
Reactor network model parameters			
d_{IRZ}	IRZ diameter	n/a	In the base case, recirculation cannot occur
L_{IRZ}	IRZ length	n/a	In the base case, recirculation cannot occur
α	Recirculation ratio	n/a	In the base case, recirculation cannot occur
θ	Jet expansion angle	n/a	In the base case, recirculation cannot occur
f_{JEZ}	Fraction of flow directly from ERZ to JEZ	n/a	In the base case, recirculation cannot occur
Particle parameters			
$\varepsilon_{p,0}$	Post-devolatilization porosity	0.262	
$a_{p,int,0}$	Post-devolatilization internal area	0.010	
$Y_{VM,daf,act}$	DAF volatile yield	0.618	
ψ	Structural parameter	n/a	For intrinsic kinetics, this is calculated
M_{C+H2O}	Multiplier for rate of $C+H_2O$ reaction	0.098	
M_{C+CO2}	Multiplier for rate of $C+CO_2$ reaction	0.048	
Heat transfer parameters			
Pe_m	Peclet number for mass transfer	0.000	
Pe_h	Peclet number for heat transfer	0.000	
ε_w	Wall emissivity	0.044	
δ_{slag}	Slag layer thickness	0.000	Fixed slag thickness used as input
f_{slag}	Slag deposition factor	n/a	Slagging is not simulated
k_{slag}	Slag conductivity	0.000	

3.5.6 Summary

The ROM has been validated using experimental data for tests of four types of Australian bituminous coal performed in the 0.1 tpd (metric-tonne-per-day) CSIRO lab-scale gasifier. The CSIRO gasifier is down-flow, dry-fed, air-blown, axially-fired and one-stage, with electrically heated walls to ensure a uniform temperature of 1400 °C. The inlet streams are heavily diluted with nitrogen to control reaction rates. Experimental data used for validation consists of gas composition profiles and carbon conversion profiles. Detailed intrinsic (area-based) heterogeneous reaction rate parameters were provided by CSIRO. One missing piece of information was the post-devolatilization particle porosity. Porosity for each coal type is estimated by matching predicted exit carbon conversion values to

experimental values. Comparison of ROM predictions of carbon conversion profiles (not just exit values) and gas composition to experimental data and CFD predictions carried out by others shows satisfactory ROM accuracy. Accuracy is best for coals CRC252 and CRC358 and worst for coal CRC299. See Figure 3-23 to Figure 3-30 for illustration of this. The trends of very rapid volatiles combustion, followed by slower char oxidation, and finally char gasification are clearly seen in all of the gas composition profile plots. These processes are also seen in the temperature profiles shown in Figure 3-42.

The fact that intrinsic kinetic rate expressions were provided for the coals in questions allows one to examine the char conversion processes present in the CSIRO gasifier in more detail than those present in the other designs. Figure 3-33 and Figure 3-34 show particle bulk density and mass profiles decrease proportional to each other. This means that particle conversion primarily occurs on the particle internal surface area, decreasing density, as opposed to on the external surface, where reactions decrease diameter. The results of pore growth and coalescence are seen in Figure 3-36, with increases in particle internal areas, followed by decreases in some cases. Figure 3-40 and Figure 3-41 clearly show that the $C+O_2$ reaction is film-diffusion-limited, while the $C+H_2O$ and $C+CO_2$ reactions are pore-diffusion-reaction-limited. The profiles show the stronger effect of temperature on reaction kinetics than on diffusion. These findings mirror those of other work in this area.

The dominant heterogeneous reaction is shown by Figure 3-37 to be the hydro-gasification reaction $(C+H_2O)$. The reaction of $C+CO_2$ proceeds at roughly 20-30% of the rate of $C+H_2O$. Char oxidation is important only in the early stages of the gasifier, before O_2 is exhausted. The predicted wall heat flux profiles, shown in Figure 3-43, show a potential limitation of the radiation submodel employed in the ROM. Because of very low particle loading, due to heavy N_2 dilution, and the very narrow diameter of the CSIRO gasifier, KB < 3. This means that the particle cloud inside the gasifier is not sufficiently optically thick to use the radiation-as-diffusion approximation described in Section 2.5.6. Therefore, particle-to-wall radiative flux is likely to be over-estimated. In addition, since particle cloud radiation will be very small, gas-phase radiation, which is not considered in the radiation submodel, is likely to be important.

164

Sensitivity analysis has also been performed to determine the input parameters and variables of highest importance to ROM predictions. Each of the selected important ROM inputs is varied ±10% around their base case value and the effect of this on exit carbon conversion is observed. Figure 3-44 and Table 3-10 show that increases in wall temperature, inlet O_2:C ratio, pressure and volatile yield have important positive impacts on carbon conversion. Increased pressure, temperature and O_2 levels rate lead to faster char conversion. Increased volatile yield also increases conversion by allowing an easier route to carbon conversion through faster devolatilization as opposed to slower gasification. It appears that the exponential term in the heterogeneous reaction expressions is of greater importance than the frequency factor, due to the lack of strong dependence on the $C+H_2O$ rate multiplier.

The effects of RNM geometry on simulation of the CSIRO gasifier are not examined as it is strongly suspected that the very long and narrow dimensions of the gasifier render any recirculation zones negligible. It should be noted that the gasifier was specifically designed to approximate plug flow. Therefore the most appropriate reactor network model for the lab-scale CSIRO gasifier is one that consists of the IRZ, JEZ and DSZ. The CCZ is unimportant as this is a single-stage design and the ERZ is unimportant when no external recirculation occurs.

Note that the steady-state simulations presented in this section were all performed in a matter of 1-5 minutes on a desktop personal computer. CFD simulations of similar systems are known to take 1-5 days to reach a converged solution, depending on the treatment of turbulence.

3.6 BYU Lab-Scale Gasifier

3.6.1 Experimental Description

The Brigham Young University (BYU) gasifier is a purely experimental design and is not intended to be developed for commercial use, hence its exclusion from the review of commercial EFG designs in Chapter 1. The BYU gasifier bears many resemblances to commercial designs such as GE and Siemens. Figure 3-45 gives a description of the 1 tpd lab-scale BYU gasifier. The gasifier is down-flow, dry-fed, O_2-blown, axially-fired and one-stage, with refractory-lined and water-cooled walls.

165

It is assumed that as this is a lab-scale gasifier, it does not operate for sufficiently long periods of time to warrant full slagging and slag removal.

The gasifier operates at atmospheric pressure and therefore does not employ a steel pressure wall outside the insulation layers. It is constructed of five cylindrical modules, one of which incorporates a radially-adjustable gas sample probe. This feature, coupled with changing the order of the cylindrical modules allows sampling of gas composition at different points in the radial and axial directions. The BYU data is unique as it is the only experimental work that measures the profiles of nitrogenous and sulfurous pollutants. See references [4, 5] for full descriptions of the BYU gasifier and experimental methods.

$D = 0.20$ m
$L = 1.24$ m
$t_{FB} = 0.037$ m
$t_{IB} = 0.014$ m
$t_{st} = n/a$

Characteristic	1 tpd BYU lab-scale
Flow direction	Down
Feedstock delivery	Dry
Injector configuration	Axial
Oxidant	O_2
Number of stages	1
Wall lining	Refractory with cooling
Syngas cooling	Quench
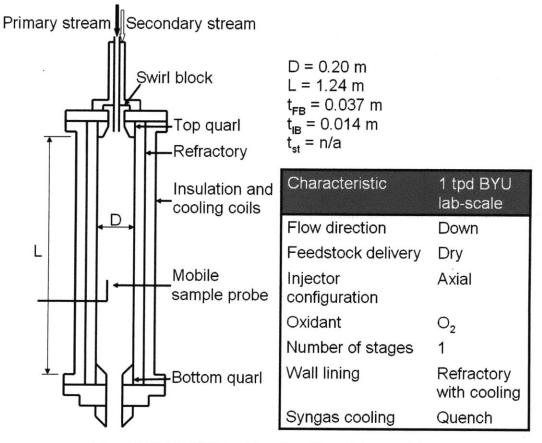
Figure 3-45: 1 tpd BYU gasifier schematic and characteristics

Table 3-11 shows the test conditions used for experiments using the BYU gasifier. The coal type used in the tests is a Utah high-volatile (HV) bituminous coal. All tests are conducted at atmospheric pressure (0.1 MPa or 1 bar). All flow rates for

166

these tests are expressed in units of kg/hr. No kinetic data was given for the coal used in the BYU test, so the kinetic data for Coal NL from Kajitani [17] is used for reduced order modeling. Refer to Table 3-4 and Table 3-5 for information on Coal NL. The conditions and properties of coolant are not stated, but internal wall temperatures at the gasifier inlet and outlet were measured. The inlet and outlet wall temperatures inside the gasifier were recorded as 1400 K (1127 °C) and 950 K (677 °C), respectively. These values are used in the ROM to impose a linear temperature profile along the gasifier wall. Refer to the "Refractory" data set in the temperature profile plot shown in Figure 3-56.

Table 3-11: Test conditions and coal composition for 1 tpd BYU gasifier

Parameters	Units	Values
Pressure	MPa	0.1
Coal flow rate	kg/hr	24.5
O_2 flow rate	kg/hr	22.295
H_2O (steam) flow rate	kg/hr	6.615
Coal, O_2 inlet temperature	°C	93
H_2O (steam) inlet temperature	°C	157
Coal type		Utah HV bituminous
Inlet particle diameter	µm	41.5
Coal LHV	kJ/kg	29,400
Proximate analysis		
Fixed carbon	wt%	45.0
Volatile matter	wt%	44.0
Ash	wt%	8.5
Moisture	wt%	2.5
Ultimate Analysis		
C	wt%	72.0
H	wt%	5.5
O	wt%	12.0
N	wt%	1.4
S	wt%	0.6
Ash	wt%	8.5
Moisture	wt%	2.5

3.6.2 Implementation in the ROM

Figure 3-46 shows the dimensions and characteristics of the RNM for this case. The most important features of the RNM are that (a) it does not employ a CCZ because the BYU gasifier is single-stage and (b) it considers external recirculation from the JEZ, through the ERZ, back to the IRZ and to the front of the JEZ. External recirculation is considered as there is a sudden expansion at the gasifier inlet. Internal recirculation is also considered as swirl is used to stabilize the flame.

The IRZ models the region near the injectors and is modeled as a cylinder of length and diameter equal to the quarl diameter (i.e. L_{IRZ} = 0.1 m, d_{IRZ} = 0.1 m). These dimensions are estimates and are chosen as they are the dimensions used by Pedersen et al. Since external recirculation is to be considered, the expansion angle of the JEZ (θ) is chosen as 9.7°. This is an estimate and is chosen as it is the jet expansion angle used by Pedersen et al in developing the RNM. The length of the JEZ (L_{JEZ}) is determined from the trigonometric expression $L_{JEZ} = (d_{gasifier} - d_{IRZ})/2\tan\theta$. ERZ length is L_{ERZ} = L_{IRZ} + L_{JEZ}. Using the dimensions of the BYU gasifier and the assumption that θ = 9.7°, L_{JEZ} = 0.2925 m and L_{ERZ} = 0.3925 m. The length of the DSZ is simply the remainder of the gasifier length, L_{DSZ} = $L_{gasifier}$ − L_{IRZ} − L_{JEZ} = 0.8475 m. The diameter of the DSZ is equal to that of the gasifier, so d_{DSZ} = 0.2 m. This is also the exit diameter of the JEZ. All of the RNM dimensions are shown in Figure 3-46. They are estimates and are subject to sensitivity analysis (see following sections).

As previously stated, no kinetic data is presented in the reports on the BYU tests [4, 5], so in implementing the model in the ROM, the "Scaling factor for $A_{ex,m}$", as defined in Table 3-4, is adjusted so that exit carbon conversion (C_{exit}) matches the experimentally-recorded value of 79%.

RNM zone	Characteristics
CCZ	n/a
IRZ	D = 0.1 m, L = 0.1 m
JEZ	D_{in} = 0.1 m, D_{out} = 0.2 m, L = 0.2925 m, θ = 9.7°, α_r = 0.44
ERZ	A_{in} = 0.0031 m², A_{out} = 0.0237 m², L = 0.3925
DSZ	D = 0.2 m, L = 0.8475 m
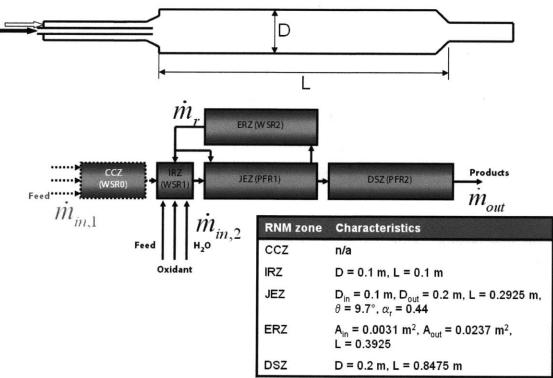
Figure 3-46: Reactor Network Model for 1 tpd BYU gasifier

3.6.3 Results of Validation

The ROM was validated by using it to simulate one experimental test that is described in detail in references [4, 5]. The conditions for the test are shown in Table 3-11. The model results were validated against the experimental data for dry syngas composition profiles. In addition to this, experimental data for concentration profiles of nitrogenous (NH_3, HCN, NO) and sulfurous (H_2S, COS, SO_2) compounds are used to tune the pollutant formation submodel described in Section 2.4.8. Gas composition data was obtained at 6 radial positions and 6 axial positions [4, 5]. At each axial position, the average across the radial positions was calculated and compared to ROM results.

The results of reduced order modeling are shown in Figure 3-47. As stated above, the scaling factor for $A_{ex,m}$ was adjusted to obtain C_{exit} = 79%. A scaling factor of 0.125 was found to be satisfactory. The ROM predicts the correct trends in gas composition profiles, although it appears to over-predict CO and H_2, while under-predicting CO_2. The rate of O_2 consumption is predicted with reasonable accuracy, most likely due to the fact that the $C+O_2$ reaction is diffusion-limited, so

169

discrepancies between actual and simulated kinetics have little bearing on the overall reaction rate. Despite the lack of kinetic data for the coal used in the BYU test, and the fact that only one set of test results are available, Figure 3-47 appears to show satisfactory ROM validation. A likely explanation for the inaccuracies seen in Figure 3-47 is the fact that the ROM predicts extremely high temperatures near the top of the reactor. Refer to the temperature profiles presented in Figure 3-56 for illustration of this. Predicted peak gas temperatures in the area where volatiles and char oxidation occur exceed 2500 °C. There are two possible causes of this, which are discussed below.

The first possible cause is the high volatile matter content of the coal, 44%. The ROM assumes near-instant devolatilization, meaning that a large of amount of combustible matter is introduced to the ROM in the presence of O_2. Higher-volatile feedstocks results in more volatiles being released. Since homogeneous oxidation reactions occur so rapidly, a large amount of thermal energy is released in a small volume, causing the large temperature increase. In reality, devolatilization is likely to occur over a longer time, thereby allowing dissipation of thermal energy. The assumption of near-instantaneous devolatilization is more accurate at high pressures, which increase the rate of volatiles release, than at atmospheric pressure, which is used in the BYU gasifier.

The second possible cause is inaccuracies in the radiation submodel at the operating conditions of the BYU gasifier. This is discussed in further detail in the following section, and specifically in the description of Figure 3-57, the predicted wall heat flux profiles.
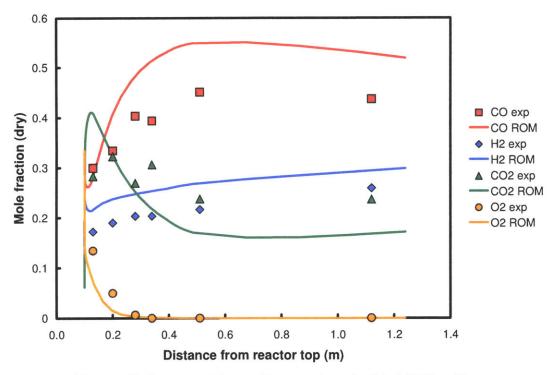
Figure 3-47: Gas composition profile comparisons for 1 tpd BYU gasifier

Figure 3-48 and Figure 3-49 show comparisons of measured and predicted profiles for nitrogenous and sulfurous pollutants, respectively. Note that in the case of nitrogenous pollutants, the frequency factors (A_n) of the reaction rate expressions described in Section 2.4.6 were tuned to match the experimental profiles as closely as possible. In the case of sulfurous pollutants, most reactions were originally assumed to proceed either to completion or to equilibrium. Table 3-12 shows the original and tuned frequency factors obtained for the pollutant formation submodel.

Figure 3-48 shows that the tuned pollutants submodel is capable of replicating the trends, if not the exact profiles, of nitrogen compound evolution. Tuning for nitrogenous species involved reducing all frequency factors to 0.1% of their original values. Additionally, the devolatilization parameter $f_N = X_{dev,HCN}/(X_{dev,HCN} + X_{dev,HCN})$ was tuned to a value of 0.3 from an original value of 0.

Near the inlet, HCN and NH_3 are formed by devolatilization. Initially NO is rapidly formed by oxidation of volatiles. Once O_2 has been exhausted, NO begins to be consumed. Char conversion by gasification leads to the production of NH_3.

171

The submodel shows rates and formation and destruction of NO that appear to be much higher than experiments indicate. This is likely to be caused by the very high oxidation-zone temperatures predicted by the ROM, which are shown in Figure 3-56. Furthermore the submodel appears to under-predict the formation of NH_3 under these gasification conditions.
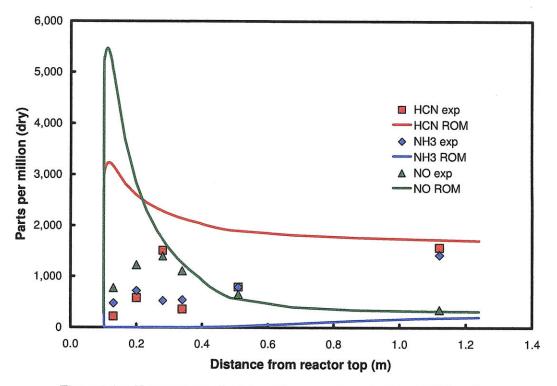
Figure 3-48 : Nitrogenous pollutant profile comparisons for 1 tpd BYU gasifier

Figure 3-49 shows that the pollutant submodel is again able to replicate the trends but not the exact profiles of sulfurous pollutant formation and destruction. Frequency factors for sulfurous pollutants were tuned to the values shown in Table 3-12. Devolatilization forms H_2S, which is rapidly oxidized to SO_2 near the inlet. After all O_2 is consumed, SO_2 reconverts to H_2S, forming small amounts of COS. The peak SO_2 fraction predicted by the ROM is about double that observed in experiments and the conversion of SO_2 to H_2S is predicted to occur more rapidly than is observed. The ROM appears to predict COS fraction more accurately than the other sulfurous species.

172
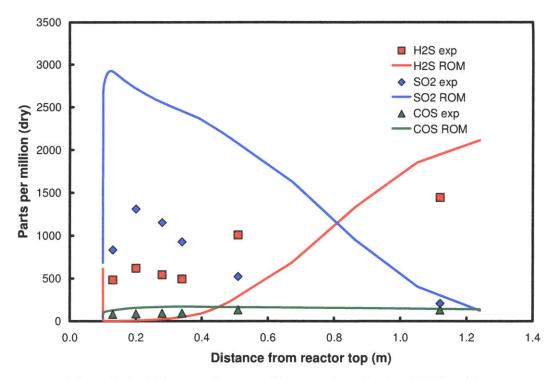
Figure 3-49 : Sulfurous pollutant profile comparisons for 1 tpd BYU gasifier

Table 3-12: Original and tuned pollutant reaction frequency factors

Reaction	Units	Frequency factors	
		Original	Tuned
Nitrogenous pollutants			
$NH_3 \rightarrow \frac{1}{2}N_2 + \frac{3}{2}H_2$	$(\mathrm{mol/m^3})^{-0.25}\mathrm{K}^{-1.25}\mathrm{s}^{-1}$	$A = 3.288 \times 10^{-2}$	$A = 10^{-3}A_{original}$
$NO + NH_3 + \frac{1}{4}O_2 \rightarrow N_2 + \frac{3}{2}H_2O$	$(\mathrm{mol/m^3})^{-0.5}\mathrm{s}^{-1}$	$A = 1.07 \times 10^{12}$	$A = 10^{-3}A_{original}$
$NH_3 + \frac{3}{4}O_2 \rightarrow \frac{1}{2}N_2 + \frac{3}{2}H_2O$	$(\mathrm{mol/m^3})^{-0.75}\mathrm{K}^{-1.75}\mathrm{s}^{-1}$	$A = 313.425$	$A = 10^{-3}A_{original}$
$NH_3 + \frac{5}{4}O_2 \rightarrow NO + \frac{3}{2}H_2O$	$(\mathrm{mol/m^3})^{-1}\mathrm{s}^{-1}$	$A = 2.3 \times 10^{14}$	$A = 10^{-3}A_{original}$
$HCN + \frac{1}{2}O_2 \rightarrow CNO$	$(\mathrm{mol/m^3})^{-1}\mathrm{s}^{-1}$	$A = 2.14 \times 10^5$	$A = 10^{-3}A_{original}$
$CNO + \frac{1}{2}O_2 \rightarrow NO + CO$	$(\mathrm{mol/m^3})^{-1}\mathrm{s}^{-1}$	$A = 2.14 \times 10^5$	$A = 10^{-3}A_{original}$
$CNO + NO \rightarrow N_2 + \frac{1}{2}O_2 + CO$	$(\mathrm{mol/m^3})^{-1}\mathrm{s}^{-1}$	$A = 2.14 \times 10^5$	$A = 10^{-3}A_{original}$
$f_N = X_{dev,HCN}/(X_{dev,HCN} + X_{dev,NH_3})$	-	0	0.3
Sulfurous pollutants			
$H_2S + \frac{3}{2}O_2 \rightarrow SO_2 + H_2O$	$(\mathrm{kmol/m^3})^{-1}\mathrm{s}^{-1}$	n/a	$A = 10^{10}$
$SO_2 + CO \rightleftarrows COS + O_2$	$(\mathrm{kmol/m^3})^{-1}\mathrm{s}^{-1}$	n/a	$A = 5 \times 10^5$
$COS + H_2 \rightleftarrows H_2S + CO$	$(\mathrm{kmol/m^3})^{-1}\mathrm{s}^{-1}$	n/a	$A = 5 \times 10^5$

173

3.6.4 Additional ROM Predictions

Profiles of non-validated ROM predictions along the gasifier length are shown in Figure 3-50 to Figure 3-57. Figure 3-50 and Figure 3-51 show predicted ultimate and proximate analysis profiles. The plots show that particles leave the gasifier with carbon fractions of about 63%. This corresponds to carbon conversion of 79%, as previous mentioned.
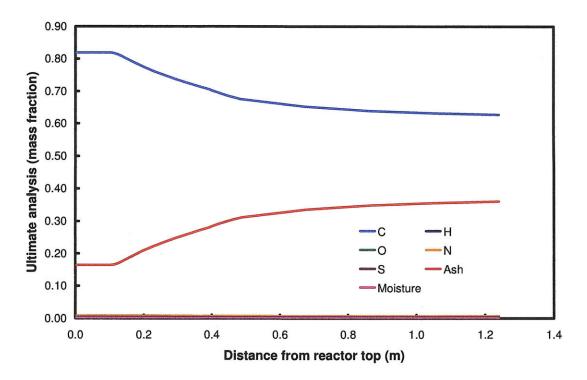
Figure 3-50: Particle ultimate analysis profile for BYU lab-scale gasifier
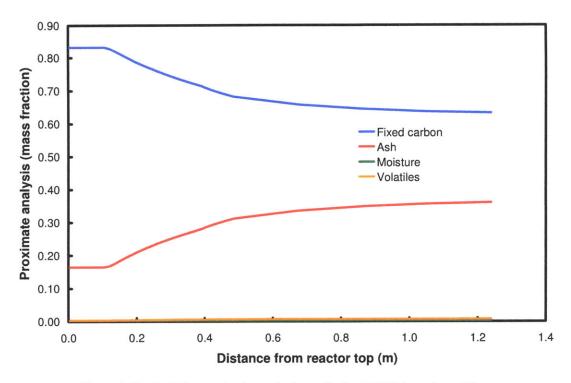
Figure 3-51: Particle proximate analysis profile for BYU lab-scale gasifier

Figure 3-52 and Figure 3-53 show predicted particle bulk density and mass profiles, respectively. Predictions for particle diameter are omitted as they show virtually no change in particle diameter along the gasifier length. This indicates that most char conversion occurs on the internal surface area of the particle (decreasing bulk density) as opposed to the external area (decreasing diameter). Recall that particles enter the gasifier with diameter 41.5 microns.
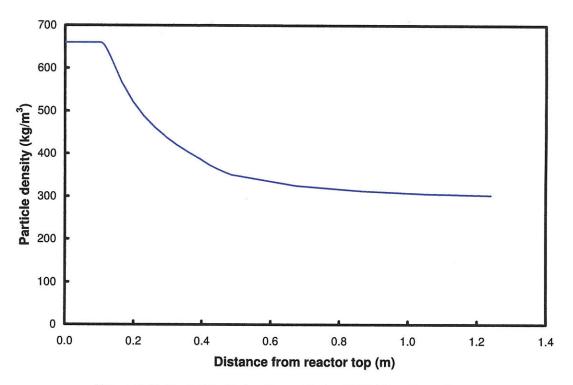
Figure 3-52: Particle bulk density profile for BYU lab-scale gasifier
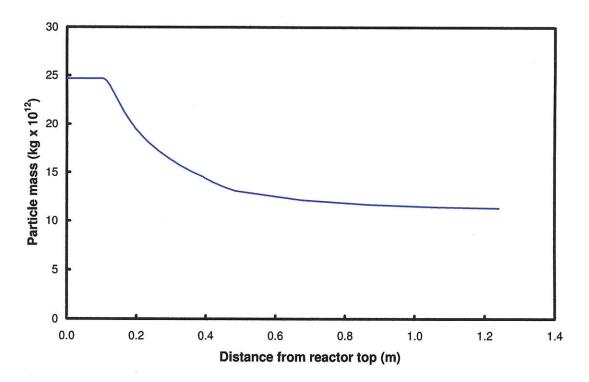
Figure 3-53: Particle mass profile for BYU lab-scale gasifier

176

Figure 3-54 shows the predicted particle volume fraction profile. Particle volume fraction is predicted to drop rapidly and then gradually rise along the gasifier length. This prediction is explained by two factors: (1) as explained above, virtually all char conversion occurs on the internal particle area, meaning that particle diameter and bulk volume $(4/3\rho\pi r^3)$ do not change significantly, and (2) as gas and particle temperatures spike and gradually decrease, so does gas density. Therefore particle loading initially drops and then rises. See the temperature profiles in Figure 3-56 for further illustration. Absolute values for particle volume fraction are low compared to commercial gasifier designs due to the low operating pressure (1 bar) of the BYU gasifier.
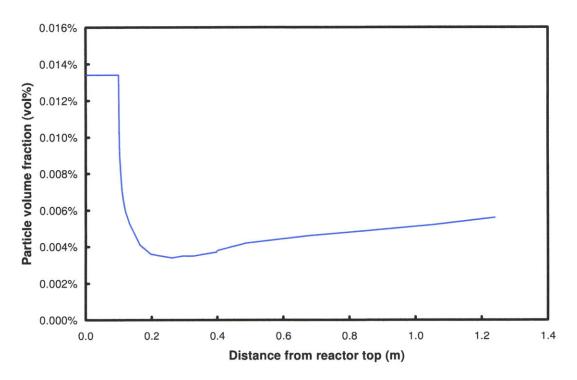
Figure 3-54: Particle volume fraction profile for BYU lab-scale gasifier

Figure 3-55 shows predicted particle heterogeneous reaction rate profiles. Since the heterogeneous rate expressions used in simulating the BYU gasifier are extrinsic (mass-based) in form, reaction rates are given in units of 1/s. As has been observed for the other gasifier simulations, the rate of the $C+O_2$ reaction dominates at early stages but approaches zero as O_2 becomes exhausted. Char gasification reactions are predicted to continue until the particles leave the gasifier.

177
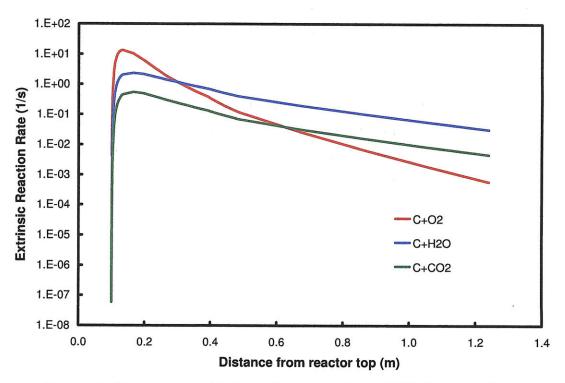
Figure 3-55: Heterogeneous extrinsic reaction rate profiles for BYU lab-scale gasifier

Figure 3-56 shows predicted temperature profiles. Note the linear wall temperature profile ("Refractory") as specified in previous sections and by Soelberg et al [4]. As previously discussed, a likely explanation for the extremely high temperatures seen in the first half of the gasifier, is that the large volatile matter fraction (44%) released by the coal during devolatilization leads to more volatiles oxidation than is seen in other designs. The fact that (a) the ROM assumes virtually instantaneous devolatilization, and (b) volatiles oxidation reactions proceed extremely rapidly to completion mean that a large amount of thermal energy is released in a relatively small volume and is not easily dissipated. A second possible explanation for the high temperature is inaccuracies in the radiation submodel when used under the conditions present in the BYU gasifier. This is discussed in greater detail in the following paragraph.

178
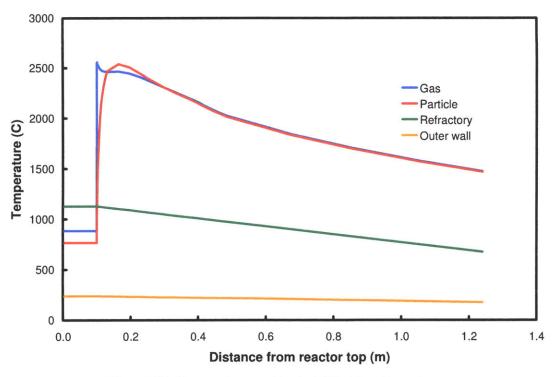
Figure 3-56: Temperature profiles for BYU lab-scale gasifier

Figure 3-57 shows predicted wall heat flux profiles. Two features are immediately apparent upon examination of the heat flux profiles: (1) convection is more important than radiation in the highest-temperature portion of the gasifier, which appears to be counter-intuitive, and (2) there are two peaks of maximum radiative flux.

Two important variables in the determination of particle-to-wall radiative flux are (a) particle number density, which is proportional to volume fraction shown in Figure 3-54 and is used to calculate particle cloud absorption coefficient and emissivity, and (b) particle temperature. In the region of highest particle temperature (see Figure 3-56), the lowest values of particle volume fraction are present (see Figure 3-54). Low particle volume fraction causes the ROM to calculate low radiative flux in this region. The second peak is caused by the rise of particle volume fraction as temperatures drop. This leads one to conclude that the radiation submodel used in the ROM is unsuitable for use at low particle volume fractions (i.e. low pressures). At low pressure and particle loading, the role of gas-phase radiation, which is not accounted for in the current submodel, is of greater

179

relative importance. It is possible that this would lead to higher radiative flux in the volatiles oxidation region, thus reducing the value of the peak temperature.

The step seen in the convective flux profile at about 0.4 m indicates the JEZ-DSZ boundary. Since a fraction of mass flow in the JEZ is modeled as being recirculated through the ERZ and back to the IRZ, the mass flow rate and velocity of gas flow in the DSZ is lower than in the JEZ. The reduced velocity leads to reduced Reynolds and Nusselt numbers, and therefore to reduced heat transfer coefficient and convective flux.
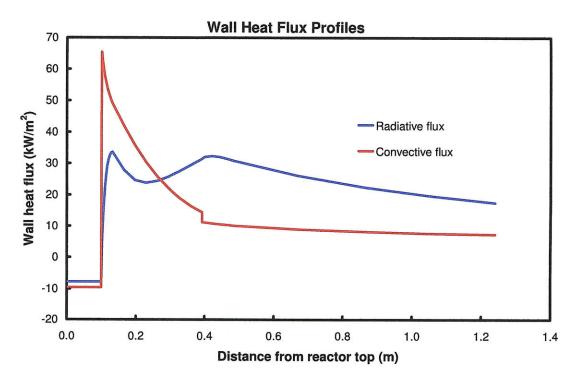
Figure 3-57: Wall heat flux profiles for BYU lab-scale gasifier

3.6.5 Sensitivity Analysis

Sensitivity analysis is performed to identify the modeling parameters and variables that are of greatest importance in determining the ROM outputs. The parameters considered in sensitivity analysis for the BYU design, as well as their base case values, are shown in Table 3-2. Recall that all parameters are varied over the range ±10% of their base case values. In addition to sensitivity analysis for overall

180

ROM performance, sensitivity analysis was performed specifically for the pollutant formation submodels.

Figure 3-58 and Table 3-13 present the results of sensitivity analysis for the 1 tpd BYU gasifier. Exit carbon conversion (C_{exit}) is the ROM output used in sensitivity analysis. It is clear from Figure 3-19 that C_{exit} is most sensitive to inlet O_2:C ratio. Other important parameters include d_{IRZ}, T_{wall}, $C+H_2O$ rate, ε_{wall}, H_2O:C ratio and α, all of which are of roughly equal importance.

Because internal and external recirculation are considered to be important in the BYU gasifier, all RNM parameters are subjected to sensitivity analysis. They are listed here in order of descending sensitivity of C_{exit} to their value: d_{IRZ}, α, θ, f_{JEZ} and L_{IRZ}. The fact that C_{exit} is much more sensitive to d_{IRZ} than it is to L_{IRZ} leads one to conclude that the size of IRZ is of secondary importance compared to effect that d_{IRZ} exerts on recirculation ratio α through the correlation $\alpha = 0.47(d_{gasifier}/d) - 0.5$ where $d = d_{IRZ}$. Refer to Section 2.2 and references [3 & 4].

Increasing the flow directly from the ERZ to the JEZ, bypassing the IRZ, (i.e. increasing f_{JEZ}) has a negative effect on conversion. This is possibly due to the fact that direct flow from the ERZ to the IRZ allows hot reacting gases (H_2O and CO_2) to preheat the cold inlet streams in the IRZ. The rates of the char conversion reactions are therefore higher when $f_{JEZ} = 0$.
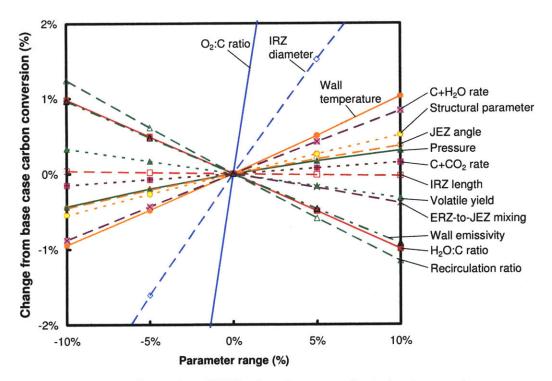
Figure 3-58: Sensitivity of BYU exit carbon conversion to input parameters

Table 3-13: Sensitivity of BYU exit carbon conversion to input parameters

Parameter (χ)	Description	Sensitivity ($S_{\chi \to \bullet}$)	Comments
Gasifier design parameters			
$m_{O2}{:}m_C$	Inlet ratio of O_2 to C	1.412	This is the most important parameter
$m_{H2O}{:}m_C$	Inlet ratio of H_2O to C	-0.099	
P	Operating pressure	0.037	
T_{wall}	Wall temperature	0.098	
$t_{FB}/(t_{FB}+t_{IB})$	Firebrick fraction of wall	n/a	Wall temperature profile is imposed
Reactor network model parameters			
d_{IRZ}	IRZ diameter	0.313	
L_{IRZ}	IRZ length	-0.003	
α	Recirculation ratio	-0.120	
θ	Jet expansion angle	0.041	
f_{JEZ}	Fraction of flow directly from ERZ to JEZ	-0.038	
Particle parameters			
$\varepsilon_{p,0}$	Post-devolatilization porosity	n/a	Extrinsic kinetics do not require this
$a_{p,int,0}$	Post-devolatilization internal area	n/a	Extrinsic kinetics do not require this
$Y_{VM,daf,act}$	DAF volatile yield	-0.033	
ψ	Structural parameter	0.053	
M_{C+H2O}	Multiplier for rate of $C+H_2O$ reaction	0.085	
M_{C+CO2}	Multiplier for rate of $C+CO_2$ reaction	0.015	
Heat transfer parameters			
Pe_m	Peclet number for mass transfer	0.000	
Pe_h	Peclet number for heat transfer	0.000	
ε_w	Wall emissivity	-0.094	
δ_{slag}	Slag layer thickness	0.000	Fixed slag thickness used as input
f_{slag}	Slag deposition factor	n/a	Slagging is not simulated
k_{slag}	Slag conductivity	0.000	

Figure 3-59, Figure 3-60 and Table 3-14 present the results of sensitivity analysis for the nitrogenous and sulfurous pollutant submodels, respectively. The ROM output used for nitrogenous pollutants is exit $NH_3{:}HCN$ ratio, while for sulfurous pollutants it is exit $H_2S{:}SO_2$ ratio. Figure 3-59 shows that the parameters of the nitrogenous pollutants submodel to which exit $NH_3{:}HCN$ ratio is most sensitive are: the fraction of devolatilized nitrogen that evolves as HCN (f_N), and the rates of the reactions shown below. This should not be taken to mean that the reactions presented below are the most important nitrogen reaction. It simply means that the chosen nitrogen reaction pathway, which is likely to be inaccurate, is most sensitive to perturbation in the identified parameters.

$$NO + NH3 + \tfrac{1}{4}O_2 \to N_2 + \tfrac{3}{2}H_2O \qquad \text{(Eq. 3-10)}$$

$$NH_3 + \tfrac{5}{4}O_2 \rightarrow NO + \tfrac{3}{2}H_2O \qquad \text{(Eq. 3-11)}$$

Figure 3-60 shows that the parameters of the sulfurous pollutants submodel to which exit $H_2S{:}SO_2$ ratio is most sensitive are the rates of the reactions below.

$$H_2S + \tfrac{3}{2}O_2 \rightarrow SO_2 + H_2O \qquad \text{(Eq. 3-12)}$$

$$SO_2 + CO \rightarrow COS + O_2 \qquad \text{(Eq. 3-13)}$$

It should be recalled that the pollutant submodels were tuned specifically for the conditions present in the BYU lab-scale gasifier. They should not be considered predictive over a range of gasifier designs and operating conditions.
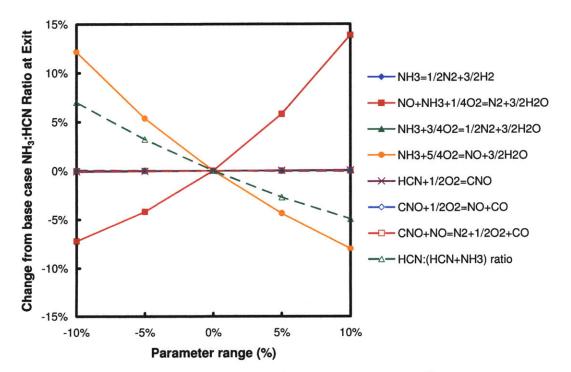
Figure 3-59: Sensitivity of BYU exit $NH_3{:}HCN$ ratio to nitrogenous pollutant parameters
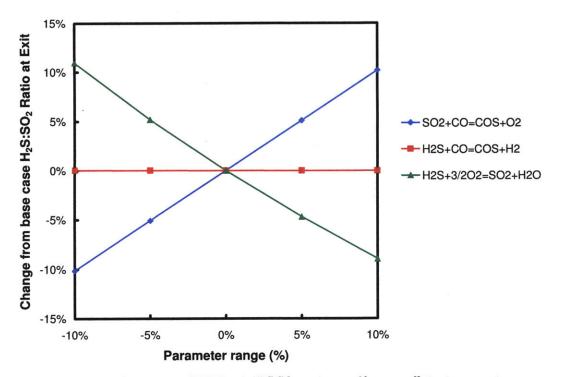
Figure 3-60: Sensitivity of BYU exit H_2S:SO_2 ratio to sulfurous pollutant parameters

Table 3-14: Sensitivity of BYU exit NH_3:HCN and H_2S:SO_2 ratios to pollutant parameters

Reaction rate or parameter (χ)	Sensitivity ($S_{\chi \to \phi}$)
Nitrogenous pollutants	
$NH_3 \to \frac{1}{2}N_2 + \frac{3}{2}H_2$	0.000
$NO + NH_3 + \frac{1}{4}O_2 \to N_2 + \frac{3}{2}H_2O$	1.026
$NH_3 + \frac{3}{4}O_2 \to \frac{1}{2}N_2 + \frac{3}{2}H_2O$	0.000
$NH_3 + \frac{5}{4}O_2 \to NO + \frac{3}{2}H_2O$	-0.990
$HCN + \frac{1}{2}O_2 \to CNO$	0.007
$CNO + \frac{1}{2}O_2 \to NO + CO$	-0.007
$CNO + NO \to N_2 + \frac{1}{2}O_2 + CO$	0.000
$f_N = X_{dev,HCN} / (X_{dev,HCN} + X_{dev,NH_3})$	-0.595
Sulfurous pollutants	
$H_2S + \frac{3}{2}O_2 \to SO_2 + H_2O$	1.016
$SO_2 + CO \rightleftarrows COS + O_2$	-0.003
$COS + H_2 \rightleftarrows H_2S + CO$	-0.992

3.6.6 Summary

The ROM has been validated using experimental data for one test using bituminous coal performed in a 1 tpd (metric-tonne-per-day) BYU lab-scale

185

gasifier. The BYU gasifier is down-flow, dry-fed, O_2-blown, axially-fired and one-stage, with refractory-lined and water-cooled walls. No kinetic parameters were provided for the feedstock, so lumped extrinsic (mass-based) parameters, similar to those used for MHI validation, were used. Experimental data used for validation includes dry-basis profiles of major gas-phase species (CO, H_2, CO_2 and O_2), nitrogen compounds (HCN, NH_3 and NO), and sulfur compounds (SO_2, COS and H_2S). Information was also provided for exit carbon conversion and inlet and outlet refractory temperatures, but these were used as inputs in order to tune heterogeneous kinetics and to determine temperature boundary conditions, respectively. Comparison of ROM predictions to experimental data shows reasonable ROM accuracy.

The main trend observed in validation results is the very high temperature predicted near the gasifier inlet, as seen in Figure 3-56. The ROM predicts peak gas and particle temperatures of about 2500 °C, which are much higher than values predicted for other gasifier designs. This causes the ROM to over-predict reaction rates in high-temperature regions, leading to the errors in gas-phase composition prediction seen in Figure 3-47. The likely cause of temperature over-prediction is the fact that the radiation submodel is unsuitable for simulating gasifier operation at low particle loading, when KB < 3. The BYU gasifier operates at atmospheric pressure, meaning that particle volume fractions are lower than those for other designs. Refer to the predicted profile of particle volume fraction in Figure 3-54 for an illustration of this. Low particle loading, which leads to low particle cloud emissivity, increases the relative importance of gas-phase radiative heat transfer, which is not accounted for in the radiation submodel. For these reasons, it is likely that the ROM under-predicts the total radiative wall flux (see Figure 3-57) and thus over-predicts temperature.

The effects of this error are exacerbated by the fact that the coal in question has a very high volatile matter mass fraction of 44%. This means that a larger-than-usual amount of devolatilized gases undergo exothermic oxidation in a very small volume near the gasifier inlet, leading to a temperature spike.

Experimental profiles of pollutant composition have been used to tune the pollutant formation submodel, described in Section 2.5.7. Results for nitrogenous

pollutants, which are presented in Figure 3-48, show the tuned submodel is capable of replicating the trends of pollutant formation. Predicted exit values for HCN and NO are close to experimentally-recorded values, while that for NH_3 is mush less than the recorded-value. Similarly, results for sulfurous pollutants, which are presented in Figure 3-49, show the submodel is capable of broad trend-following. Predicted exit values for all sulfurous compounds are reasonably close to experimentally-recorded values.

Sensitivity analysis has also been performed to determine the input parameters and variables of highest importance to ROM predictions. Each of the selected important ROM inputs is varied ±10% around their base case value and the effect of this on exit carbon conversion is observed. Figure 3-58 and Table 3-13 show that increases in inlet O_2:C ratio, wall temperature, C+H_2O rate and IRZ diameter have important positive impacts on carbon conversion. Increased temperature, O_2 levels and reaction rates lead to faster char conversion. Increases in wall emissivity, inlet H_2O:C ratio and recirculation ratio have strong negative impacts on carbon conversion. While the effects of increased H_2O levels and wall emissivity are obvious, it is less clear why increased recirculation, caused by higher recirculation ratio and/or small IRZ diameter, leads to lower carbon conversion. The sensitivity of ROM results to reactor network model (RNM) parameters, such as IRZ diameter and recirculation ratio, indicates the important potential role of CFD simulations in supplying such parameters to the ROM.

Note that the steady-state simulations presented in this section were all performed in a matter of 1-5 minutes on a desktop personal computer. CFD simulations of similar systems are known to take 1-5 days to reach a converged solution, depending on the treatment of turbulence.

3.7 Texaco (GE) Pilot-Scale Gasifier

3.7.1 Experimental Description

The GE (formerly Texaco) gasifier design is discussed in Chapter 1 and is available in a range of commercial sizes as shown in Table 3-15 [21]. Experimental gasifier data gathered at the Cool Water IGCC project over the period 1980-1990 is used to validate the ROM for the GE design. Despite the fact that the Cool Water

project is referred to as "pilot-scale", the gasifier is in reality commercial-scale and since the mid-1990s has been in commercial operation at the Coffeyville Resources plant in Coffeyville, Kansas. It, along with a second GE gasifier, is used to produce ammonia from petroleum coke feedstock. See the next chapter for information on the GE-Bechtel Reference Plant.

Table 3-15: GE gasifier sizes

Plant	Pressure (bar)	Reactor size (m³)	Syngas cooling	Coal throughput (tpd)	Syngas production (MW$_{th}$)
Eastman Chemical, Kingsport, TN	70	13	Quench	1300	293
Cool Water IGCC, CA / Coffeyville Resources, KA	42	26	Radiant or quench	1000	264
Polk IGCC, Tampa Electric Co., FL	28	51	Radiant & convective	2000	484
GE-Bechtel Reference Plant (see next chapter)	56	51	Radiant & quench	2700	650

Figure 3-61 gives a description of the 1000 tpd pilot-scale GE gasifier. The gasifier is down-flow, slurry-fed, O_2-blown, axially-fired, one-stage, refractory-lined, slagging and radiant-cooled. The dimensions of the GE gasifier were obtained by comparing reactor size data and plant dimensions from Holt [21] to the gasifier schematic on the website of refractory manufacturer Saint-Gobain [22], which is shown in Figure 3-62[1]. Figure 3-62 also allows the determination of the wall layer thicknesses, densities and thermal conductivities. Wall layer thicknesses are shown in Figure 3-61 and the following thermal properties are used: ρ_{FB} = 4200 kg/m³, ρ_{IB} = 1600 kg/m³, k_{FB} = 2.4 W/m/K, k_{IB} = 0.81 W/m/K [22]. The wall layer properties (densities, conductivities and ratios of thicknesses) of the GE design are used for other designs where such properties are unknown (i.e. the MHI and BYU designs).

Table 3-16 shows the test conditions used for experiments using the GE gasifier as described by [7]. All of the coal types used in the tests are bituminous coals. All are from the United States, except Lemington, which is Australian. Their ultimate and proximate analyses are given in Table 3-16. No kinetic data was given for the coal used in the GE tests, so the kinetic data for Coal T from Kajitani [17] is used for reduced order modeling. Refer to Table 3-4 and Table 3-5 for information on Coal NL and Coal T.

---

[1] The image shown in Figure 3-62 no longer appears to be available on line.
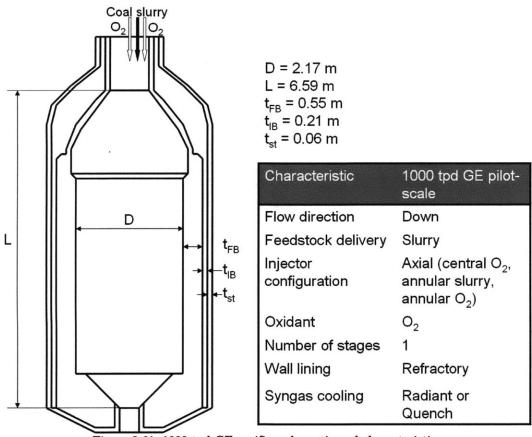
Figure 3-61: 1000 tpd GE gasifier schematic and characteristics
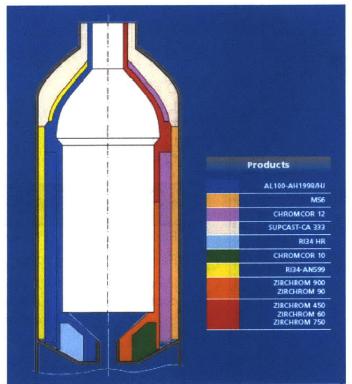
Figure 3-62: GE gasifier schematic from Saint-Gobain website [12]

All tests are conducted at a pressure of 4.2 MPa (42 bar). Carbon conversion data (C_{exit}) is taken at the exit of the gasifier and syngas composition data is taken at some point downstream of sulfur removal. It is therefore necessary to include the effect of syngas cooling in the ROM. Five of the six tests employ radiant syngas cooling while one employs quench cooling. In addition to the six tests described in Table 3-16, the ROM was validated by using it to replicate the gasifier exit syngas composition and temperature calculated by a process flowsheet model of the Cool Water plant design [6]. This dataset is referred to as the "design case" and is shown in the last column of Table 3-16.

Table 3-16: Test conditions and results for Cool Water gasifier

Test run		1	2	3	4	5	6	Design case
Coal type		Illinois #6	Pittsburgh #8	SUFCo	SUFCo	SUFCo	Lemington	SUFCo
Syngas cooling		Radiant	Radiant	Radiant	Radiant	Quench	Radiant	Radiant
Feed rate	kg/hr, ar	42871	35901	41999	46199	41999	39049	44330
Composition								
Ultimate	wt%, dry							
C		72.21	77.74	71.85	71.45	72.20	69.82	70.22
H		4.94	5.32	4.94	4.88	5.04	4.49	4.78
O		6.92	5.46	12.74	11.94	12.59	8.32	12.83
N		1.57	1.45	1.22	1.21	1.13	1.55	1.17
S		3.08	2.66	0.43	0.47	0.36	0.42	0.50
Ash		11.28	7.37	8.82	10.05	8.68	15.40	10.50
Proximate	wt%, ar							
Fixed carbon		42.58	55.44	45.34	44.72	45.40	52.04	44.50
Volatiles		35.65	35.66	36.73	36.23	36.78	29.86	36.05
Ash		9.95	7.25	7.94	9.05	7.81	14.91	9.45
Moisture		11.83	1.66	10.00	10.00	10.00	3.20	10.00
HHV	kJ/kg, dry	29871	32853	28799	28992	29195	28501	28817
H_2O feed rate	kg/hr	21821	24231	24576	25810	25516	22295	25990
O_2 feed rate	kg/hr	33483	34142	32495	35789	33191	33374	38456
Recycled slag feed rate	kg/hr	-	-	-	-	-	-	3892
Slurry concentration	wt%	63.4	59.3	60.6	61.7	59.7	62.9	60.5
RSC coolant flow rate	kg/hr	112037	106594	113398	138799	-	131088	-
Cooled clean syngas Composition	mol%, dry							See[1]
CO		44.88	44.27	42.97	43.66	42.77	44.20	0.309[1]
H_2		38.46	39.42	38.13	38.14	37.90	36.86	0.250[1]
CO_2		15.48	15.47	18.07	17.33	18.89	17.95	0.145[1]
H_2O		-	-	-	-	-	-	0.279[1]
Carbon conversion	%	96.5	96.4	98.5	98.1	96.2	98.0	-

3.7.2 Implementation in the ROM

Figure 3-63 shows the dimensions and characteristics of the RNM for this case. The most important features of the RNM are that (a) it does not employ a CCZ because the GE gasifier is single-stage and (b) it considers external recirculation from the JEZ, through the ERZ, back to the IRZ and to the front of the JEZ. External recirculation is considered as there is a sudden expansion at the gasifier inlet. Internal recirculation is also considered as swirling annular streams are used to stabilize the flame.

---

[1] Syngas composition for the design case is for the gasifier exit and is expressed as actual mole percentage, not dry mole percentage.

The IRZ models the region near the injectors and is modeled as a cylinder of length and diameter equal to the quarl diameter. Since the quarl diameter is not known, its value is estimated at 0.5 m (i.e. L_{IRZ} = 0.5 m, d_{IRZ} = 0.5 m). Since external recirculation is to be considered, the expansion angle of the JEZ (θ) is chosen as 9.7°. This is an estimate and is chosen as it is the jet expansion angle used by Pedersen et al in developing the RNM. The length of the JEZ (L_{JEZ}) is determined from the trigonometric expression $L_{JEZ} = (d_{gasifier} - d_{IRZ})/2\tan\theta$. ERZ length is L_{ERZ} = L_{IRZ} + L_{JEZ}. Using the dimensions of the Cool Water gasifier and the assumption that θ = 9.7°, L_{JEZ} = 4.88 m and L_{ERZ} = 5.38 m. The length of the DSZ is simply the remainder of the gasifier length, L_{DSZ} = $L_{gasifier}$ − L_{IRZ} − L_{JEZ} = 1.21 m. The diameter of the DSZ is equal to that of the gasifier, so d_{DSZ} = 2.17 m. This is also the exit diameter of the JEZ. All of the RNM dimensions are shown in Figure 3-63. They are estimates and are subject to sensitivity analysis (see following sections).

RNM zone	Characteristics
CCZ	n/a
IRZ	D = 0.5 m, L = 0.5 m
JEZ	D_{in} = 0.5 m, D_{out} = 2.17 m, L = 4.88 m, θ = 9.7°, α_r = 1.54
ERZ	A_{in} = 0.370 m^2, A_{out} = 3.50 m^2, L = 5.38 m
DSZ	D = 2.17 m, L = 1.21 m
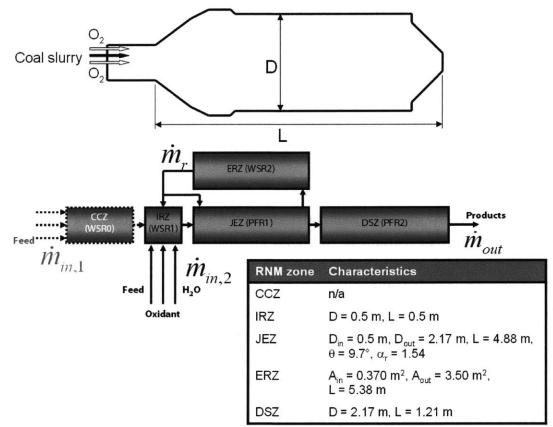
Figure 3-63: Reactor Network Model for 1000 tpd GE gasifier

3.7.3 Results of Validation

The ROM was validated by using it to simulate the six experimental tests described in detail in reference [7]. The conditions for the test are shown in Table 3-16. The model results were validated against the experimental data for exit carbon conversion (C_{exit}) and cooled, clean (sweet) syngas composition. These two separate pieces of validation data allow the performance of the radiant syngas cooler (RSC) submodel to be examined. Additionally, the ROM was validated by using it to replicate the gasifier exit syngas composition and temperature calculated by a process flowsheet model of the Cool Water plant design [6]. This set of data is referred to as the "design case".

Figure 3-64 shows the results of ROM simulation of the design case detailed in Table 3-16. The validation results show high ROM accuracy in predicting gasifier exit temperature, shown by point e on the plot (1261 °C predicted vs. 1247 °C expected). A similar level of accuracy in predicting exit temperature could be obtained by the use of a simplified non-recirculating ROM, in which the entire gasifier is modeled as a PFR, as evidenced by the data set "Refractory Face (Old RNM)" in Figure 3-64. However, use of the RNM shown in Figure 3-63 allows prediction of temperature profiles that fall within the operating conditions of the gasifier refractory and external walls. As seen in Figure 3-64, the non-recirculating ROM predicts a maximum internal temperature (point f, 1800 °C [22]), over 2100 °C, which exceeds the refractory failure temperature by over 300 °C. The maximum predicted external temperature (point g) falls well below the maximum allowable external wall temperature of 287 °C [23]. This appears to at least allow qualitative validation of the ROM.

The temperature step predicted by the recirculating ROM at about 700 °C, (a-b), is due to the IRZ, where the inlet streams, which enter at 25 °C, mix with the recirculated gas and particles, which are at about 1300 °C. In the JEZ, temperature first rises sharply as O_2 is rapidly consumed (b-c) primarily by volatiles, but also by char, before gradually decreasing as a result of the slower endothermic gasification reactions (c-d).

The ROM predicts that temperature remains almost constant for a significant portion of the gasifier length (d and e). This is because simulated char conversion approaches 100% before point e. Refer to the particle composition profiles in Figure 3-67 and Figure 3-68, and to the gas-phase composition profile in Figure 3-69. Once the heterogeneous reactions cease, homogeneous reactions equilibrate very quickly. In addition, the refractory walls of the GE gasifier ensure almost adiabatic conditions inside the reactor. Heat loss through the walls is calculated at less than 1% of coal higher heating value. Since syngas exiting the gasifier is at or very near local chemical equilibrium [24] ROM predictions of gas composition match extremely closely with those of the design case.

Figure 3-64: Temperature profiles for 1000 tpd GE gasifier design case
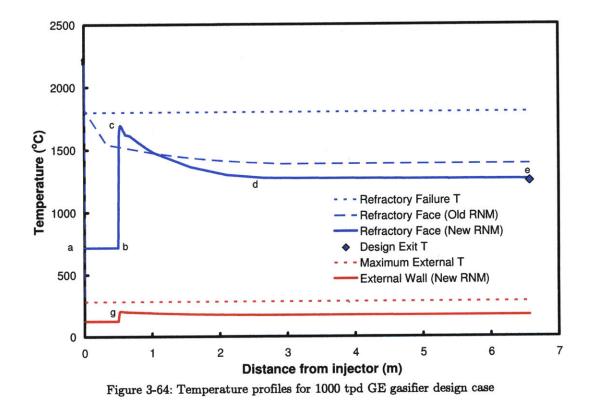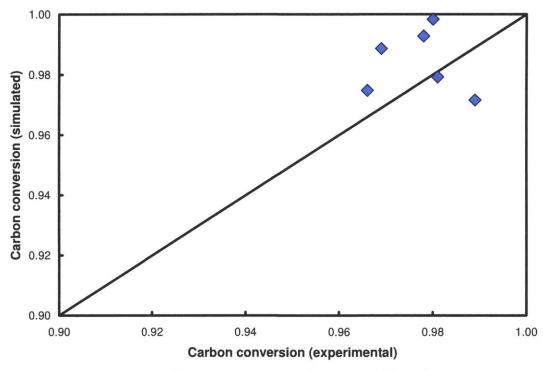
Figure 3-65 and Figure 3-66 shows the results of ROM simulation for the six tests detailed in Table 3-16. Plots of additional non-validated ROM predictions are shown in Figure 3-67 to Figure 3-74. Although the latter set of plots is not strictly validated, they offer useful insight into the trends seen in the former set. Figure 3-65 compares actual and simulated values for carbon conversion at the gasifier exit (C_{exit}). The ROM predicts that the primary means by which carbon

conversion is less than 100% is the effect of carbon-trapping in the slag layer. The slow rates of heterogeneous kinetics do not affect C_{exit}. The solid particles that leave the gasifier consist of almost 100% ash. The sensitivity of C_{exit} and T_{exit} to ROM input parameters is discussed in the next section.

Figure 3-65: Exit carbon conversions for 1000 tpd GE gasifier
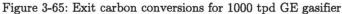
Figure 3-66 compares actual and simulated values for cooled, cleaned syngas composition. The x-axis shows the actual syngas composition found through experiment [7]. The y-axis shows two sets of ROM simulation outputs: syngas composition with (colored points) and without (black points) the effect of the water-gas shift (WGS) reaction in the RSC. Note that for the results that account for the WGS, the rate of that reaction in the RSC is tuned for the best fit of data. For all cases, the rate of the WGS reaction was tuned to 0-8% of the rate calculated by Bustamante's expression. See [25] and Section 2.4.8 for more details.

From Figure 3-66 it is clear that the WGS reaction in the RSC does not have a major effect on the final syngas composition. This is probably because the temperature in the RSC is sufficiently low to stop the kinetics of the reaction. Results for Test 2 are highlighted in Figure 3-66. When the WGS reaction is

195

allowed in the RSC for Test 2, its rate is tuned to 8% of its calculated value. For the quench-cooled test (Test 5), the rate of the WGS reaction in the quench cooler is set to zero, as is the case for all quench-cooled gasifiers simulated by the ROM. The ROM predicts that the syngas is at or very close to its final composition by the time it leaves the gasifier. The RSC submodel is still useful, however, as it required to predict the temperature of the syngas leaving the RSC. The Final Technical Report of the Polk Power Station IGCC states that in normal operation, gas leaving the RSC is consistently below 732 °C [8]. The ROM predicts RSC exit temperatures in the range 679-714 °C, which again validates the ROM. Note that in all test cases, coolant is modeled as entering the RSC as saturated liquid water at 111 bar [7].
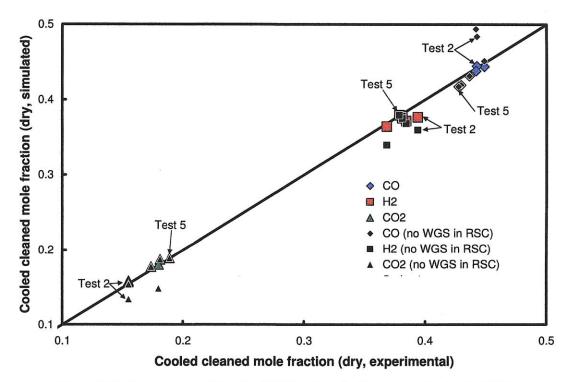
Figure 3-66: Syngas compositions for ROM with and without reaction in the RSC

3.7.4 Additional ROM Predictions

Profiles of non-validated ROM predictions along the gasifier length are shown in Figure 3-67 to Figure 3-74. Figure 3-67 and Figure 3-68 show predicted ultimate and proximate analysis profiles. The plots show that particles leave the gasifier with ash fractions very close to 100%. Under no conditions does ash fraction reach

100%. This is because minute amounts of volatiles and moisture are constrained to remain in the particle phase to maintain ROM stability. Due to the fact that slagging is simulated in the ROM, carbon conversion predicted to be below 100%. This indicates that carbon-trapping in the slag layer is an important mechanism of reducing overall gasifier carbon conversion.
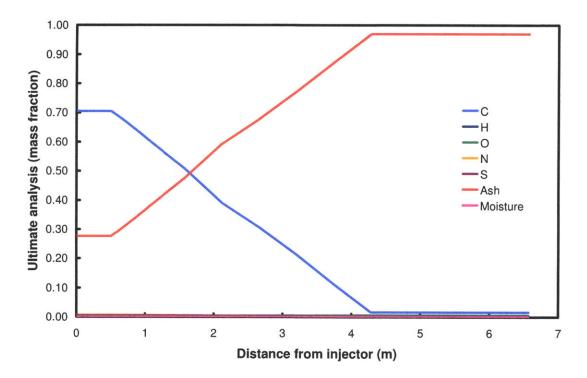
Figure 3-67: Ultimate analysis profile for Test 1 for GE pilot-scale gasifier
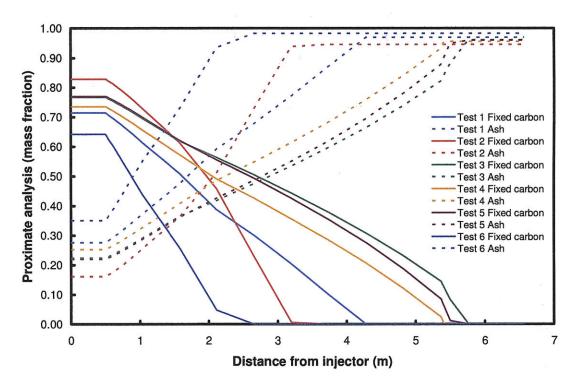
Figure 3-68: Proximate analysis profiles for GE pilot-scale gasifier

Figure 3-69 shows the predicted gas composition profile for Test 1. Profiles for other tests are omitted for clarity. Once again, the location of the IRZ is identified by the flat portions of the profiles seen up to 0.5 m. The results of volatiles oxidation are clearly seen with rapid rises of H_2O and CO_2. Char gasification reactions between 0.5 m and 4 m, lead to increases in CO and H_2, and decreases in CO_2 and H_2O. The flattening of the species profiles is due to the total conversion of char particles to ash. For Test 1, this occurs at around 4 m from the injector.
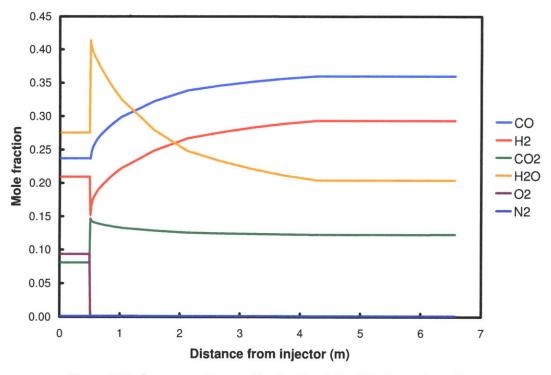
Figure 3-69: Gas composition profiles for Test 1 for GE pilot-scale gasifier

Figure 3-70 and Figure 3-71 show predicted particle bulk density and mass profiles, respectively. Predictions for particle diameter are omitted as they show virtually no change in particle diameter along the gasifier length. This indicates that most char conversion occurs on the internal surface area of the particle (decreasing bulk density) as opposed to the external area (decreasing diameter). Particles are assumed to enter the gasifier with diameter 100 microns. Initial densities are calculated by the particle properties submodel, which is described in Chapter 2. The flattening of the mass profiles seen in Figure 3-71 clearly indicates the cessation of heterogeneous reactions.
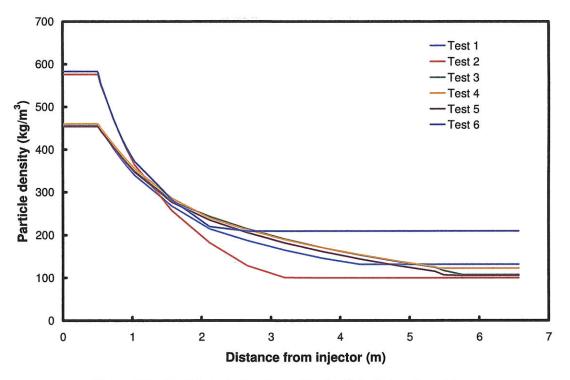
Figure 3-70: Particle bulk density profiles for GE pilot-scale gasifier
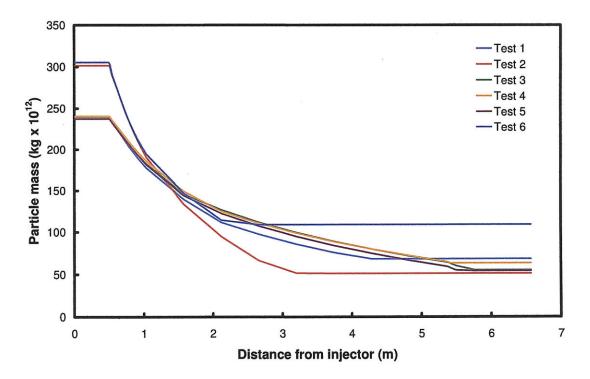
Figure 3-71: Particle mass profiles for GE pilot-scale gasifier

Figure 3-72 shows predicted particle volume fraction profiles. Particle volume fraction is predicted to drop rapidly as temperature rises (see Figure 3-64 for an illustration of this), which decreases gas density. Subsequent temperature decreases cause particle volume fraction to rise. This trend is mitigated by the effects of slagging. The migration of particles to the wall reduces volume fraction.
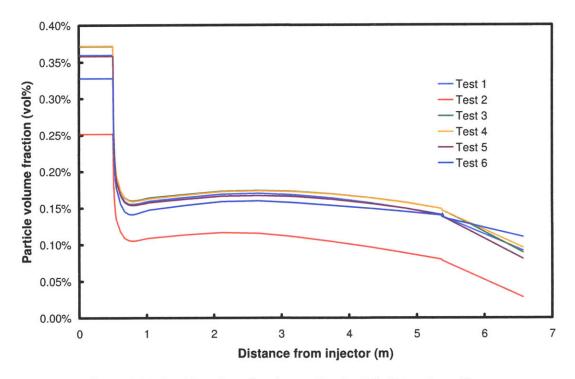
Figure 3-72: Particle volume fraction profiles for GE pilot-scale gasifier

Figure 3-73 shows predicted particle heterogeneous reaction rate profiles. Since the heterogeneous rate expressions used in simulating the BYU gasifier are extrinsic (mass-based) in form, reaction rates are given in units of 1/s. As has been observed for the other gasifier simulations, the rate of the $C+O_2$ reaction dominates in the very early stages but approaches zero quickly. Char gasification reactions are predicted to continue until the particles are fully converted to ash.
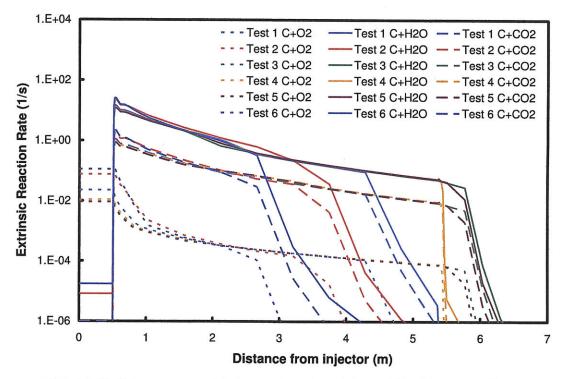
Figure 3-73: Heterogeneous extrinsic reaction rate profiles for GE pilot-scale gasifier

Figure 3-74 shows predicted wall heat flux profiles. Unlike the other gasifier designs used in ROM validation, slagging is simulated for the GE gasifier. Therefore, the enthalpy flux of particles that migrate to the wall is shown in the plot. Radiation and convection are of greatest importance in the highest-temperature regions of the gasifier, i.e. in the early stages. The plot shows that gas-to-wall convective flux is positive, while particle-to-wall radiative flux is negative. This means that in the early stages of the gasifier, $T_{gas} > T_{wall} > T_{particle}$. The large negative spike in radiative flux at about 5.4 m marks the location of the JEZ-DSZ boundary. It is not clear what causes this spike, but it appears to be a simulation numerical issue, as opposed to an issue with the radiation submodel itself. Outside the highest-temperature regions of the gasifier, particle enthalpy flux is predicted to be the dominant mode of heat transfer to the walls.
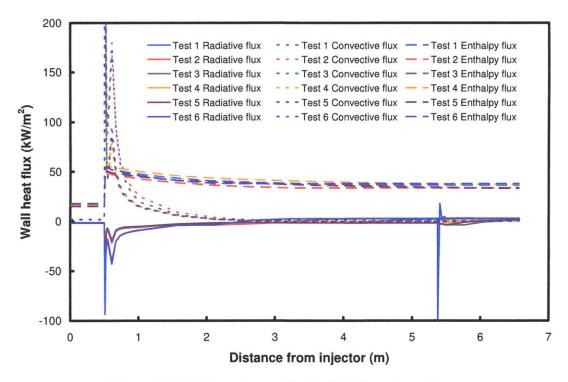
Figure 3-74: Wall heat flux profiles for GE pilot-scale gasifier

3.7.5 Sensitivity Analysis

Sensitivity analysis is performed to identify the modeling parameters and variables that are of greatest importance in determining the ROM outputs. The parameters considered in sensitivity analysis for the GE design, as well as their base case values, are shown in Table 3-2. Recall that all parameters are varied over the range ±10% of their base case values. In addition to sensitivity analysis for overall ROM performance, sensitivity analysis was performed specifically for the radiant syngas cooler (RSC) submodel.

Figure 3-75, Figure 3-76 and Table 3-17 present the results of sensitivity analysis for the GE design. The test case chosen for sensitivity analysis is Test 4, described in Table 3-2 and Table 3-16. Exit carbon conversion (C_{exit}) and gasifier exit temperature ($T_{exit} - T_{amb}$) are the ROM outputs used in sensitivity analysis. Carbon conversion and exit temperature are most sensitive to inlet O_2:C and H_2O:C ratios. More O_2 leads to higher temperatures and greater conversion, while more H_2O leads to lower temperatures and less conversion. This illustrates the main problem encountered with slurry-fed gasifier designs.

203

Slag deposition is an important factor in GE gasifier operation. Increased deposition lowers conversion as carbon becomes trapped in the slag layer, while raising temperature due to the additional thermal insulation it provides. RNM parameters f_{JEZ}, d_{IRZ} and α are important to both conversion and temperature. Increased values for f_{JEZ} and d_{IRZ} lead to better overall mixing of the flow in the gasifier and increased residence times. This is a possible explanation for the increased conversion and decreased temperature (caused by more endothermic char conversion). However, it is not immediately clear why increased recirculation ratio has the opposite effect. Other ROM inputs are of less importance to conversion and exit temperature.
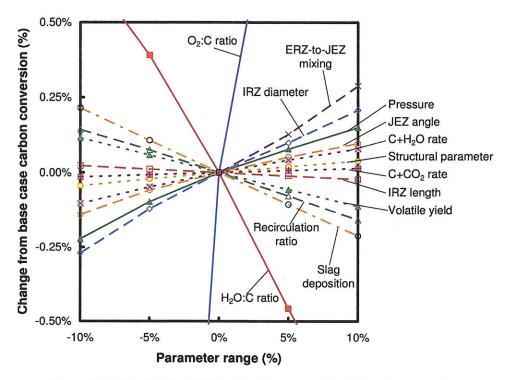
Figure 3-75: Sensitivity of GE exit carbon conversion to input parameters
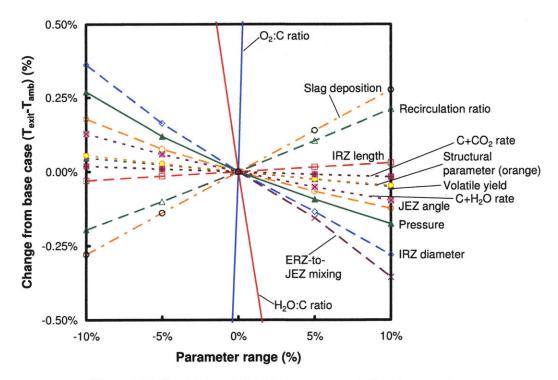
Figure 3-76: Sensitivity of GE exit temperature to input parameters

Table 3-17: Sensitivity of GE carbon conversion and exit temperature to input parameters

Parameter (χ)	Description	Sensitivity ($S_{\chi \to \phi}$)		Comments
		Carbon conv.	Exit temp.	
Gasifier design parameters				
$m_{O2}{:}m_C$	Inlet ratio of O_2 to C	0.522	1.419	This is the most important parameter
$m_{H2O}{:}m_C$	Inlet ratio of H_2O to C	-0.082	-0.341	This is the second most important parameter
P	Operating pressure	0.018	-0.022	
T_{wall}	Wall temperature	n/a	n/a	T_{wall} is not fixed
$t_{FB}/(t_{FB}+t_{IB})$	Firebrick fraction of wall	0.000	-0.001	
Reactor network model parameters				
d_{IRZ}	IRZ diameter	0.023	-0.031	
L_{IRZ}	IRZ length	-0.002	0.003	
α	Recirculation ratio	-0.015	0.020	
θ	Jet expansion angle	0.011	-0.015	
f_{JEZ}	Fraction of flow directly from ERZ to JEZ	0.027	-0.033	
Particle parameters				
$\varepsilon_{p,0}$	Post-devolatilization porosity	n/a	n/a	Extrinsic kinetics do not require this
$a_{p,int,0}$	Post-devolatilization internal area	n/a	n/a	Extrinsic kinetics do not require this
$Y_{VM,daf,act}$	DAF volatile yield	-0.011	-0.005	
ψ	Structural parameter	0.004	-0.005	
M_{C+H2O}	Multiplier for rate of $C+H_2O$ reaction	0.009	-0.011	
M_{C+CO2}	Multiplier for rate of $C+CO_2$ reaction	0.001	-0.002	
Heat transfer parameters				
Pe_m	Peclet number for mass transfer	0.000	0.000	
Pe_h	Peclet number for heat transfer	0.000	0.000	
ε_w	Wall emissivity	0.000	0.000	
δ_{slag}	Slag layer thickness	n/a	n/a	Slagging is simulated
f_{slag}	Slag deposition factor	-0.021	0.028	Slagging is simulated
k_{slag}	Slag conductivity	0.000	0.000	

Figure 3-77 and Figure 3-78 present the results of sensitivity analysis for the RSC submodel. The test case chosen for RSC sensitivity analysis is Test 2, not Test 4 as is employed for overall ROM sensitivity analysis. The main reason for this is the fact that for Test 2, the best match for cooled cleaned gas composition is when the rate of the WGS reaction in the RSC is non-zero, allowing more meaningful sensitivity analysis. The conditions for Test 2 are described in Table 3-16. RSC exit temperature ($T_{RSC,exit}$ - T_{amb}) and exit $H_2{:}CO$ ratio are the ROM outputs used in sensitivity analysis.
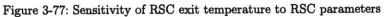
Figure 3-77 shows that exit temperature is most sensitive to the emissivity of the RSC wall (i.e. heat exchange tubes or "water wall"). The heat exchange tubes in

the RSC are assumed to have a thin coating of slag. The throat at the bottom of the gasifier (the inverted conical shape in Figure 3-61) ensures that the slag layer on the wall drops straight down to a pool of liquid water at the bottom of the RSC. The inner wall of the RSC has a greater diameter than the throat so it is assumed that the slag layer in the gasifier does not reach the RSC wall. There are, however, fly ash particles present in the RSC, which can stick to the wall. The wall temperatures are too low for slag flow, so slag thickness in the RSC ($\delta_{slag,RSC}$) is set to 1 mm.

The overall thermal resistance of the slag layer, due to $\delta_{slag,RSC}$ and k_{slag}, is of secondary importance as are the coolant pressure (and temperature, since coolant is assumed to be a saturated vapor-liquid mixture) and the rate of the WGS reaction, as stated above. This would suggest that the largest thermal resistance in the RSC is convective-radiative heat transfer in from the gas-particle stream to the wall.

Figure 3-78 shows that exit H_2:CO ratio has similar sensitivities to exit temperature, with the exception of WGS rate, which is obviously important in determining gas composition. As discussed above however, conditions in the gasifier appear to have greater influence over final syngas composition than kinetics in the RSC.

Figure 3-77: Sensitivity of RSC exit temperature to RSC parameters
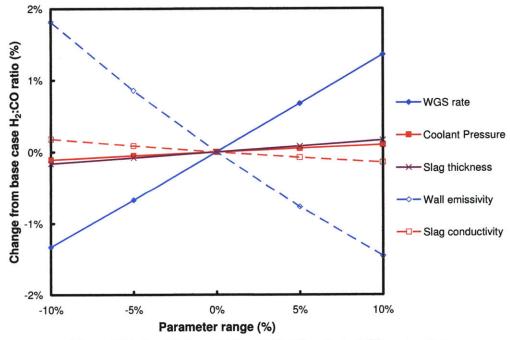
Figure 3-78: Sensitivity of RSC exit H$_2$:CO ratio to RSC parameters

Table 3-18: Sensitivity of RSC exit temperatures and H_2:CO ratio to RSC parameters

Parameter (χ)	Description	Sensitivity ($S_{\chi \to \phi}$)		Comments
		Exit temp.	H_2:CO ratio	
M_{WGS}	Multiplier for rate of WGS reaction	0.007	0.134	This is very important for exit H_2:CO ratio
P	Operating pressure	0.030	0.010	
Pe_m	Peclet number for mass transfer	0.000	0.000	
Pe_h	Peclet number for heat transfer	0.000	0.000	
ε_w	Wall emissivity	-0.256	-0.163	This is the most important parameter
δ_{slag}	Slag layer thickness	0.020	0.016	
k_{slag}	Slag conductivity	-0.021	-0.016	

3.7.6 Summary

The ROM has been validated using experimental data for six tests using four types bituminous coal performed in the 1000 tpd (metric-tonne-per-day) Texaco (GE) pilot-scale gasifier at the Cool Water IGCC power plant. In addition, the Cool Water gasifier design case has been used for validation. The Cool Water gasifier is down-flow, slurry-fed, O_2-blown, axially-fired, one-stage, refractory-lined, slagging and radiant-cooled. Gasifier dimensions were not provided but these have been constructed using information from a number of sources detailed above. No kinetic parameters were provided for the feedstocks, so lumped extrinsic (mass-based) parameters, similar to those used for MHI validation, were used. Experimental data used for validation includes gasifier exit temperature, exit carbon conversion values, and dry-basis composition of cooled, cleaned syngas. The temperature of gas leaving the radiant syngas cooler under normal operating conditions is also known. Unfortunately no profiles of any measurable variable or parameter inside the gasifier or cooler are available. Comparison of ROM predictions to experimental data shows satisfactory ROM accuracy. Unlike the other validation cases described, slagging is simulated for the GE gasifier.

The ROM predicts rapid temperature rise, as seen in Figure 3-64, in the early stages of the gasifier due to volatiles oxidation. Analysis of the extrinsic rates of the heterogeneous reactions in Figure 3-73 shows that char oxidation does not occur to any reasonable extent. This means that char conversion is achieved almost entirely through gasification. The fact that Figure 3-73 shows heterogeneous reactions ceasing before the outlet of the gasifier means that full particle conversion is achieved. Refer to Figure 3-67 and Figure 3-68 for further

illustration of this. Note that full particle carbon conversion does not equate to full gasifier carbon conversion. Figure 3-65 shows that the ROM simulates gasifier carbon conversion in the range 97.1% - 99.8%. While these values are in general higher than those recorded experimentally, they indicate that carbon-trapping in the slag layer plays an important role in limiting conversion.

Figure 3-66 implies that under the operating conditions encountered in the Cool Water gasifier, the role of the water-gas shift reaction in changing syngas composition in the RSC is rather small. Syngas is predicted to exit the gasifier at or very near its final cooled, cleaned composition. The ROM accurately predicts RSC exit temperature, which is important for the overall plant energy balance. Although unconfirmed by experimental results, the ROM predicts that the most important heat loss mode in the gasifier is through the flux of enthalpy to the gasifier wall carried by slagging particles. Radiation and convection are of lesser importance and are roughly equal to each other.

Sensitivity analysis has also been performed to determine the input parameters and variables of highest importance to ROM predictions. Each of the selected important ROM inputs is varied ±10% around their base case value and the effect of this on exit carbon conversion is observed. Figure 3-75, Figure 3-76 and Table 3-17 show that increases in inlet O_2:C ratio, ERZ-to-JEZ mixing and IRZ diameter have important positive impacts on carbon conversion. Increases in inlet H_2O:C ratio, slag deposition and recirculation ratio have strong negative impacts on carbon conversion. While the effects of increased H_2O levels and slag deposition, leading to enthalpy loss, are obvious, it is less clear why increased recirculation, caused by higher recirculation ratio and/or small IRZ diameter, and decreased ERZ-to-JEZ mixing leads to lower carbon conversion.

Sensitivity analysis has also been performed to establish the most important parameters to RSC exit temperature and gas composition. Figure 3-77 and Figure 3-78 show that wall emissivity and water-gas shift reaction rate are important determinants. The analysis assumes that slag layers on the heat transfers tubes are very thin. The sensitivity of overall ROM results to reactor network model (RNM) parameters, such as IRZ diameter and recirculation ratio, indicates the important potential role of CFD simulations in supplying such parameters to the ROM. Another role of critical importance for CFD simulations is to supply

estimates for the flux slag particles to gasifier walls. This flux is not predictable by the ROM.

Note that the steady-state simulations presented in this section were all performed in a matter of 1-5 minutes on a desktop personal computer. CFD simulations of similar systems are known to take 1-5 days to reach a converged solution, depending on the treatment of turbulence.

3.8 Chapter Summary

The ROM has been validated using experimental data for three laboratory-scale gasifiers (MHI, CSIRO and BYU) and one pilot-scale gasifier (Cool Water Texaco (GE)). Validation for the 2 tpd MHI gasifier uses seven sets of experimental data that include temperature profiles, exit gas composition, exit carbon conversion, exit char mass flow rate, exit gas higher heating value, and overall gasifier cold gas efficiency. Lumped extrinsic (mass-based) parameters were provided for the coals used. Comparison of ROM predictions to experimental data and CFD predictions carried out by others shows satisfactory ROM accuracy. The predicted profiles for the MHI design show differences in temperature, gas composition, wall heat flux and particle loading between the first stage combustor and the second stage reductor. Radiation is everywhere the dominant mode of heat transfer due to high temperatures and high particle loading. Radiation in the combustor, which has cooled walls, and where temperatures are highest, is much greater than in the reductor. The dominant heterogeneous reaction is $C+H_2O$, with $C+CO_2$ proceeding at a rate roughly an order of magnitude slower. Char oxidation is important only in the early stages of the gasifier, before O_2 is exhausted. Sensitivity analysis indicates that inlet O_2:C ratio, pressure, IRZ diameter, $C+H_2O$ reaction rate, wall emissivity and firebrick fraction of wall thickness are the most important factors affecting carbon conversion. It is found that for the MHI gasifier, inclusion of external recirculation leads to distortion of the temperature profiles. Therefore the most appropriate reactor network model for the lab-scale MHI gasifier is one that consists of the CCZ for the first stage, and the IRZ, JEZ and DSZ for the second stage.

Validation of the 0.1 tpd CSIRO gasifier uses four sets of experimental data that include gas composition profiles and carbon conversion profiles. Detailed intrinsic

211

(area-based) heterogeneous reaction rate parameters were provided by CSIRO. One missing piece of information was the post-devolatilization particle porosity. Porosity for each coal type is estimated by matching predicted exit carbon conversion values to experimental values. Comparison of ROM predictions of carbon conversion profiles (not just exit values) and gas composition to experimental data and CFD predictions carried out by others shows satisfactory ROM accuracy. The trends of very rapid volatiles combustion, followed by slower char oxidation, and finally char gasification are clearly seen the gas composition and temperature profile plots. Use of intrinsic kinetic rate expressions allows one to examine the char conversion processes present in the CSIRO gasifier in great detail. Particle bulk density and mass profiles decrease proportional to each other, meaning that particle conversion primarily occurs on the particle internal surface area. The results show increases in particle internal areas, followed by decreases in some cases. The $C+O_2$ reaction is predicted to be film-diffusion-limited, while the gasification reactions are pore-diffusion-reaction-limited. The dominant char reaction is $C+H_2O$. The reaction of $C+CO_2$ proceeds at roughly 20-30% of the rate of $C+H_2O$. Char oxidation is important only in the early stages of the gasifier, before O_2 is exhausted. The predicted wall heat flux profiles show a potential limitation of the radiation submodel at low particle loading and small gasifier diameter. Since particle cloud radiation will be very small, gas-phase radiation, which is not considered in the radiation submodel, is likely to be important. Sensitivity analysis indicates that wall temperature, inlet O_2:C ratio, pressure and volatile yield are the most important factors affecting char conversion. It appears that the exponential term in the heterogeneous reaction expressions is of greater importance than the frequency factor, due to the lack of strong dependence on the $C+H_2O$ rate multiplier. The effects of RNM geometry on simulation of the CSIRO gasifier are not examined as it is strongly suspected that the very long and narrow dimensions of the gasifier render any recirculation zones negligible. Therefore the most appropriate reactor network model for the lab-scale CSIRO gasifier is one that consists of the IRZ, JEZ and DSZ.

Validation of the 1 tpd BYU gasifier uses one set of experimental data that includes dry-basis profiles of major gas-phase species and pollutants, exit carbon conversion and inlet and outlet refractory temperatures. No kinetic parameters were provided for the feedstock, so lumped extrinsic parameters, similar to those used for MHI validation, were used. The kinetic parameters are tuned to match

212

exit carbon conversion and refractory temperatures. Comparison of ROM predictions of species profiles to experimental data shows reasonable ROM accuracy. The main trend observed in validation results is the very high temperature, 2500 °C, predicted near the gasifier inlet. This causes the ROM to over-predict reaction rates, leading to the errors in gas-phase composition prediction. The likely cause of temperature over-prediction is the fact that the radiation submodel is unsuitable for simulating gasifier operation at the low pressure and particle loading used in the BYU gasifier. Such conditions increase the relative importance of gas-phase radiative heat transfer, which is not accounted for in the radiation submodel. This error is exacerbated by the fact that the coal in question has a very high volatile matter mass fraction of 44%, leading to larger-than-usual volatiles oxidation in a very small volume near the gasifier inlet. Tuning the pollutant submodel enables reasonably accurate replication of NO, HCN, SO_2 and COS profile trends. Experimental NH_3 profiles, however, cannot be reproduced. Sensitivity analysis indicates inlet O_2:C and H_2O:C ratios, wall temperature, C+H_2O rate, IRZ diameter, wall emissivity and recirculation ratio are the most important factors affecting char conversion. The sensitivity of ROM results to reactor network model (RNM) parameters, such as IRZ diameter and recirculation ratio, indicates the important potential role of CFD simulations in supplying such parameters to the ROM.

Validation of the 1000 tpd Texaco (GE) gasifier uses four sets of experimental data that include exit temperatures, exit carbon conversion values, and dry-basis composition of cooled, cleaned syngas. No kinetic parameters were provided for the feedstock, so lumped extrinsic parameters, similar to those used for MHI validation, were used. No profiles of any measurable variable or parameter inside the gasifier or cooler are available. Comparison of ROM predictions to experimental data shows satisfactory ROM accuracy. Slagging is simulated for the GE gasifier. The ROM predicts rapid temperature rise in the early stages of the gasifier due to volatiles oxidation. Analysis of the extrinsic rates of the heterogeneous reactions shows that char oxidation does not occur to any reasonable extent, meaning that char conversion is achieved almost entirely through gasification. Full particle conversion is predicted to be achieved before the exit. The ROM simulates gasifier carbon conversion in the range 97.1% - 99.8%. The results indicate that carbon-trapping in the slag layer plays an important role in limiting conversion. Syngas is predicted to exit the gasifier very near its final

cooled, cleaned composition. The ROM accurately predicts RSC exit temperature. Although unconfirmed by experimental results, the ROM predicts that the most important heat loss mode in the gasifier is through the flux of enthalpy to the gasifier wall carried by slagging particles. Radiation and convection are of lesser importance and are roughly equal to each other. Sensitivity analysis for the gasifier indicates that inlet O_2:C and H_2O:C ratios, ERZ-to-JEZ mixing, IRZ diameter, slag deposition and recirculation ratio are the most important factors affecting char conversion. Sensitivity analysis for the RSC indicates that wall emissivity and water-gas shift reaction rate are important factors affecting RSC exit composition and temperature. The sensitivity of overall ROM results to reactor network model (RNM) parameters indicates the important potential role of CFD simulations in supplying such parameters to the ROM. Another role of critical importance for CFD simulations is to supply estimates for the flux slag particles to gasifier walls.

Note that the steady-state simulations presented in this chapter were all performed in a matter of 1-5 minutes on a desktop personal computer. CFD simulations of similar systems are known to take 1-5 days to reach a converged solution, depending on the treatment of turbulence. Now that the ROM has been validated for a wide variety of entrained flow gasifier designs, it will be used to simulate the steady-state and dynamic performance of a full-scale GE gasifier.

3.9 References

1. Watanabe H, Otaka M. Numerical simulation of coal gasification in entrained flow coal gasifier, Fuel 2006; 85: 1935-1943.
2. Hara S, Ichikawa K, Inumaru J, Ashizawa, M. Examination of Gasification Characteristics of Pressurized Two-Stage Entrained Flow Coal Gasifier, JSME International Journal, Series B 2001; 44: 337-343.
3. Cooperative Research Centre for Coal in Sustainable Development [CCSD]. Gasification Conversion Model - PEFR: Research Report 80 2007 Dec.
4. Soelberg N R, Smoot L D, Hedman P O. Entrained flow gasification of coal 1. Evaluation of mixing and reaction processes from local measurements, Fuel 1985; 64: 776-781.
5. Highsmith J R, Soelberg N R, Hedman P O, Smoot L D, Blackman A U. Entrained flow gasification of coal 2. Fate of nitrogen and sulfur pollutants as assess from local measurements, Fuel 1985; 64: 782-788.
6. Electric Power Research Institute [EPRI]. Cool Water Coal Gasification Program: First Annual Progress Report. EPRI AP-2487: 1982.
7. Electric Power Research Institute [EPRI]. Cool Water Coal Gasification Program: Final Report. EPRI GS-6806: 1990.

8. Tampa Electric Company [TECO]. Tampa Electric Polk Power Station Integrated Gasification Combined Cycle Project: Final Technical Report. DE-FC21-91MC27363: 2002.

9. National Energy Technology Laboratory [NETL]. Cost and Performance Baseline for Fossil Energy Plants: Volume 1: Bituminous Coal and Natural Gas to Electricity. Revision 1 2007. DOE/NETL-2007/1281

10. Chen C, Horio M, Kojima T. Numerical simulation of entrained flow coal gasifier. Part 1: modeling of coal gasification in an entrained flow gasifier, Chemical Engineering Science 2000; 55: 3861-3874.

11. Chen C, Horio M, Kojima T. Numerical simulation of entrained flow coal gasifier. Part 2: effects of operating conditions on gasifier performance, Chemical Engineering Science 2000; 55: 3875-3883.

12. Chen C, Horio M, Kojima T. Use of numerical modeling in the design and scale-up of entrained flow coal gasifiers, Fuel 2001; 80: 1513-1523.

13. Zhong C, Shuai Y, Qinfeng W, Zunhong Y. Distribution of HCN, NH_3, NO and N_2 in an entrained flow gasifier, Chemical Engineering Journal 2009; 148: 312-318.

14. Wabash River Energy Ltd. [WRE]. Wabash River Coal Gasification Repowering Project: Final Technical Report. DE-FC21-92MC29310: 2000.

15. National Energy Technology Laboratory [NETL]. Wabash River Coal Gasification Repowering Project: A DOE Assessment. DOE/NETL-2002/1164: 2002.

16. Eurlings J Th G M, Ploeg J E G. Process Performance of the SCGP at Buggenum IGCC. Gasification Technologies Council [GTC]: Gasification Technologies Conference; 1999 Oct.; San Francisco (CA).

17. Kajitani S, Hara S, Matsuda H. Gasification rate analysis of coal char with a pressurized drop tube furnace, Fuel 2002; 81: 539-546.

18. Email correspondence between Hiroaki Watanabe, CRIEPI and Dr. Cheng Zhang, MIT, July 3, 2008.

19. Seggiani M. Modelling and simulation of time varying slag flow in a Prenflo entrained-flow gasifier, Fuel 1998; 77 (14): 1611-1621.

20. Barta L E, Beer J M, Sarofim A F, Teare J D. Coal Fouling Tendency Model. The Impact of Ash Deposition on Coal Fired Plants, Proc. Engineering Found. Conf.; 1993; Solihull, UK: 177-188.

21. Holt N. IGCC & Gasification for a Changing marketplace. Gasification Technologies Council [GTC]: Gasification Technologies Conference; 2006 Oct.; Washington (DC).

22. Gasification High Performance Refractories Saint-Gobain - [homepage on the Internet]. n.d. [cited 2009 Oct 19]. Available from: http://www.refractories.saint-gobain.com/Gasification.aspx

23. Coffeyville Resources Nitrogen Fertilizers, LLC Petroleum Coke Gasification Based Ammonia Plant Coffeyville (KA): n.d.

24. Watkinson A P, Lucas J P, Lim C J. A prediction of performance of commercial coal gasifiers, Fuel 1991; 70: 519-527.

25. Bustamante F, Enick R M, Killmeyer R P, Howard B H, Rothenberger K S, Cugini A V, Morreale B D, Ciocco M V. Uncatalyzed and Wall-Catalyzed Forward Water-Gas Shift Reaction Kinetics, AIChE Journal 2005; 51: 1440-1454.

Chapter 4 FULL-SCALE GASIFIER SIMULATION RESULTS

4.1 Chapter Overview

This chapter presents the steady-state and dynamic simulation of a full-scale 2700 tpd GE gasifier. The GE-Bechtel Reference IGCC Plant is introduced, with particular attention paid to the gasifier and syngas cooling systems. A base case for steady-state gasifier operation is established and justified. The important role of slag viscosity in the gasifier is given special attention. Steady-state simulations are used to determine realistic initial, intermediate and final states for dynamic simulations. Finally, the results of six dynamic gasifier simulations, including a gasifier cold-start, are presented in detail.

4.2 GE-Bechtel Reference IGCC Plant

The GE-Bechtel Reference IGCC Plant (henceforth referred to as the "Reference Plant") is a 630 MW_e IGCC plant design offered by a partnership of General Electric (GE) and Bechtel Corporation [1-3]. The option of CO_2 capture is offered as an additional "Carbon Island" [3]. The Reference Plant employs two parallel 51 m^3 GE gasifiers that operate at a pressure of 56 bar. This very high pressure allows each gasifier to process about 2700 metric tonnes per day (tpd) of bituminous coal with almost 98% conversion efficiency. As previously described in Chapters 1 and 2, the GE gasifier is down-flow, slurry-fed, O_2-blown, axially-fired, one-stage, refractory-lined and slagging. The standard syngas cooling system offered for the Reference Plant consists of a radiant syngas cooler (RSC) followed by a quench cooler.

The Reference Plant is chosen as the base case for full-scale gasifier simulation for the following reasons: it employs a widely-used gasification technology (GE), it is the highest-throughput entrained flow gasifier configuration, it is the subject of detailed study by NETL [4] (henceforth referred to as the "NETL report"), and a Reference Plant is currently under construction in Edwardsport, Indiana.

217

A schematic of the gasifier and syngas cooling system is shown in Figure 4-1. Dimensions for the gasifier and RSC were obtained by comparing reactor size data and plant dimensions from Holt [1] to the gasifier schematic on the website of refractory manufacturer Saint-Gobain [5]. Refer to the section on Texaco (GE) pilot-scale gasifier validation in Chapter 3 for more information on how gasifier dimensions were determined. The RSC is assumed to be a cylinder of internal diameter equal to that of the gasifier. Its length of 40 m is approximate and was obtained from the scaled drawing provided by Holt [1]. Coolant, entering as saturated liquid water and leaving as saturated steam is assumed to flow up the RSC in an annular configuration of pipes. The pipes are assumed to have internal diameters of 0.05 m (50 mm) and thicknesses of 0.01 m (10 mm) [6]. No dimensions for the quench cooler were found in the literature, so it is modeled[1] as a water-filled cylinder of length and diameter 2 m.

The flow rates and conditions of the important streams for the gasifier and syngas cooler in a Reference Plant are shown in Table 4-1. The stream numbers in Table 4-1 correspond to those in Figure 4-1. All of this data was obtained directly or calculated from Case 2 (IGCC plant with CCS) in the NETL report [4]. It is important to note that the flow rates presented in Table 4-1 are for one gasifier only, while those presented in the NETL report are for two gasifiers. The liquid flow rate leaving the quench cooler with slag was calculated using a mass balance for the gasifier and syngas cooler from the NETL report. Temperatures and pressures of the dry milled coal and slurry water streams are not known, but since the conditions of the coal-water slurry (CWS) are known, conditions for the former two streams are unnecessary. The NETL report assumes coolant enters the RSC as subcooled liquid at 313 °C and 138 bar and leaves as saturated vapor at the same pressure (i.e. T = 336 °C). As mentioned above, the ROM assumes the coolant is always saturated at a specified temperature. Therefore, RSC coolant is assumed to both enter and leave at 336 °C and 138 bar. The error this introduces into the energy balance can be reasonably assumed to be negligible due to the large latent heat of vaporization of water. The temperature at which quench water enters the cooler is unknown, but by using the ROM to match the quenched gas

---

[1] The author visited the Eastman Chemical gasification facility at Kingsport, Tennessee during the summer of 2009. The quench coolers used at this facility were observed to be roughly this size.

outlet conditions, it was found to be around 135 °C. At the pressure inside the quench cooler (roughly 56 bar) this means the water enters as a subcooled liquid.
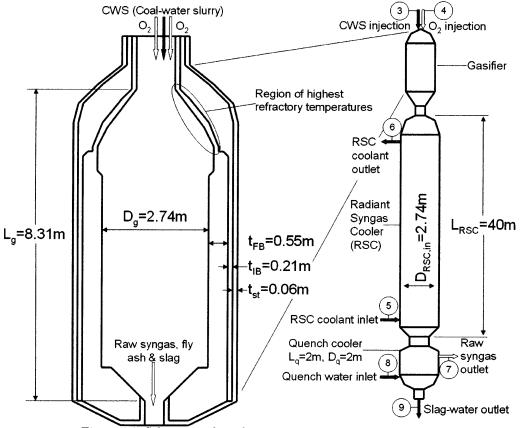
Figure 4-1: Schematic of gasifier and syngas cooler for Reference Plant

Table 4-1: Flow rates and conditions for Reference Plant gasifier and syngas cooler

Stream number	Stream name	Solids flow rate	Liquid & gas flow rate	Total flow rate	Temperature	Pressure
		kg/hr	kg/hr	kg/hr	°C	bar
1	Milled coal	113586	0	113586	-	-
2	Slurry water	0	46661	46661	-	-
3	Coal-water slurry	113586	46661	160247	60.8	72.3
4	Oxidant	0	95078	95078	96.8	67.5
5	RSC coolant in	0	274301	274301	313.2	137.8
6	RSC coolant out	0	274301	274301	335.9	137.8
7	Quenched gas	0	305065	305065	210.4	55.0
8	Quench water in	0	323059	323059	-	-
9	Slag-water out	12468	260852	273320	-	-

Table 4-2 shows the ultimate and proximate analyses of coal used in the NETL report. It is a widely-used high-sulfur bituminous coal, Illinois No. 6. The oxidant stream to the gasifier consists of 95% O_2, 3.2% Ar (argon), and 1.8% N_2, all expressed as mole percentages. The inlet flow rates of the gasifier in the Reference

219

Plant result in inlet ratios of O_2:C and H_2O:C of 1.24 and 0.64, respectively. For the Cool Water pilot-scale gasifier tests described in Chapter 3 the inlet O_2:C ratio was 1.20-1.27, while the inlet H_2O:C ratio was 0.80-0.94. The fact that the inlet H_2O:C ratio of the Reference Plant is 20-30% lower that that of the Cool Water plant means that much higher temperatures can be expected in the Reference Plant.

Table 4-2: Feedstock description

	Units	Values
Coal type		Illinois No. 6 bituminous
Higher heating value	kJ/kg	27113
Proximate analysis		
Fixed carbon	wt%	44.19
Volatile matter	wt%	34.99
Ash	wt%	9.7
Moisture	wt%	11.12
Ultimate Analysis		
C	wt%	63.75
H	wt%	4.5
O	wt%	6.88
N	wt%	1.25
S	wt%	2.51
Ash	wt%	9.7
Moisture	wt%	11.12

4.3 Steady-State Simulation Results

4.3.1 Implementation in the ROM

The ROM was used to simulate the steady-state performance of the gasifier and syngas cooler of the GE-Bechtel Reference IGCC Plant. Figure 4-2 shows the dimensions and characteristics of the reactor network model (RNM) for the 2700 tpd gasifier. The most important features of the RNM are that (a) it does not employ a CCZ (coal combustion zone, or first stage) and (b) it considers external recirculation from the JEZ, through the ERZ, back to the IRZ and to the front of the JEZ. The stream from the CCZ to the IRZ is not used in simulating the GE gasifier because it is a one-stage design. External recirculation is considered as there is a sudden expansion at the gasifier inlet. Internal recirculation is also considered as swirling annular streams are used to stabilize the flame. Since kinetic data is not known for the coal to be simulated, extrinsic kinetic data for Coal M, as developed by Kajitani [7] and used by Watanabe [8] is used here. Refer to Section 3.4 for more information on the kinetic data used in these simulations.

220
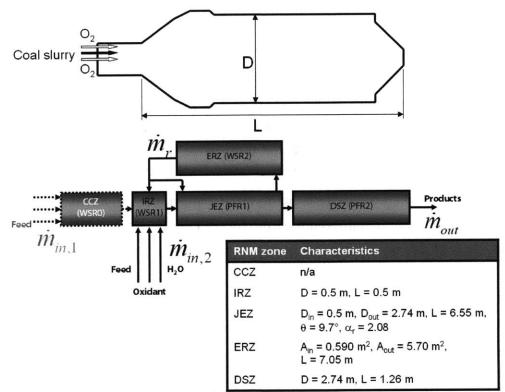
Figure 4-2: Reactor Network Model for GE gasifier in Reference Plant

4.3.2 Steady-State Base Case

The base case for gasifier operation was determined by running the ROM with the data from Table 4-1 and Table 4-2 as inputs. In addition to the above inputs, 2512 kg/hr of fluxant, modeled as CaO (calcium oxide), is added to the gasifier via the particle injection stream. Fluxant is added to reduce slag viscosity to acceptable levels and its use in this base case is discussed in Section 4.3.2.2. The RNM shown in Figure 4-2 was used to simulate the performance of the gasifier shown in Figure 4-1.

The next sections describe the results of ROM simulation of steady-state gasifier operation. Specific results that are discussed include temperature and gas-phase species profiles for the gasifier and radiant syngas cooler, and slag behavior profiles for the gasifier. Additional profile predictions, similar to those presented in Chapter 3, are not shown for the full-scale GE gasifier. The reason for this is that they are virtually identical in form to the additional profile predictions for the slightly smaller Cool Water pilot-scale gasifier, which are shown in Section 3.7.4.

221

4.3.2.1 Temperature and Species Predictions

The temperature profiles predicted by the ROM for the gasifier and RSC in the Reference Plant are shown in Figure 4-3 and Figure 4-4, respectively. The first point to note is that the gasifier temperature profile shown in Figure 4-3 is very similar in shape to that for the 1000 tpd GE gasifier used for validation in Chapter 3. This is to be expected as the 2700 tpd gasifier is merely the same design scaled-up. The maximum predicted refractory face temperature is about 1600 °C, far below the refractory failure temperature of 1800 °C. The maximum external temperature of 180 °C is far below the maximum allowable temperature of 287 °C.

Figure 4-3 shows that the syngas is predicted to leave the gasifier at about 1306 °C, slightly higher than the design temperature of the Cool Water gasifier. In Section 3.2 of the NETL report, the stated gasifier design exit temperature is 1316 °C. This discrepancy between the NETL and ROM temperatures is explained by the use of fluxant in the ROM. The addition of fluxant (and its heat capacity) causes the temperature in the gasifier to drop. The ROM was used to simulate the base case with no fluxant injection and the gasifier exit temperature was found to be 1314 °C, closer to 1316 °C. In this case however, slag exit viscosity was unacceptably high. This is addressed in detail in Section 4.3.2.2.

The significant flattening of the temperature profile indicates that chemical reactions are predicted to cease in the first half of the gasifier. It is not clear whether this is the case in reality, as there are no internal measurements with which to compare the ROM predictions. Exit carbon conversion is predicted to be 99.6%, which is too high regardless of conditions inside the gasifier. This figure is higher than any of those predicted by the ROM for the Cool Water gasifier primarily because of the higher temperatures in the Reference Plant due to its lower inlet H_2O:C ratio. The high temperature causes faster heterogeneous reactions, meaning less time is available for carbon to become trapped in the slag layer, which appears to be the most important mechanism for reducing conversion efficiency. The lack of known kinetic data for the coal in question and an accurate submodel for particle migration to the gasifier wall means conversion is predicted

to be 99.6% or more for all Reference Plant simulations. This is acknowledged to be an inaccuracy with the ROM.
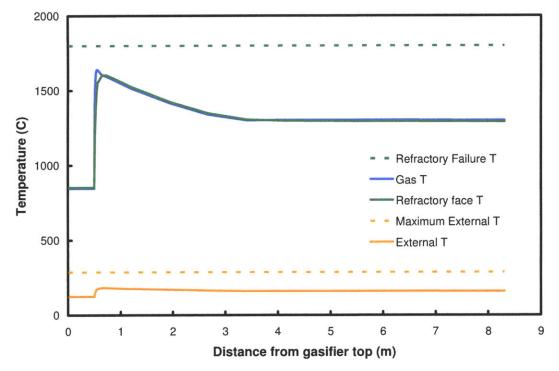
Figure 4-3: Temperature profiles for GE gasifier in Reference Plant

Figure 4-4 shows that the ROM predicts the syngas to leave the RSC at 818 °C. The stated RSC design exit temperature is 816 °C, according to Section 3.2 of the NETL report. However, the flow sheet summarized in Exhibit 3-33 in the same report states that gas leaves the RSC at 593 °C (1100 °F). There is no explanation given in the NETL report as to the origin of this discrepancy. Under no realistic conditions could the ROM achieve an RSC exit temperature of 593 °C for the Reference Plant. Since the ROM base case prediction of 818 °C is so close to the stated design exit temperature of 816 °C, the value shown in Exhibit 3-33 of the NETL report is assumed to be in error.

As previously stated, the temperature of water added to the quench cooler is not given in the NETL report, so the ROM was used to determine it. Therefore, the quenched gas temperature cannot be considered fully predictive. However, the ROM accurately predicts the flow rate of liquid water leaving the quench cooler

with slag (262800 kg/hr predicted by ROM vs. 260852 kg/hr given in the NETL report). The energy balance for the quench cooler is therefore assumed to be accurate for the ROM.
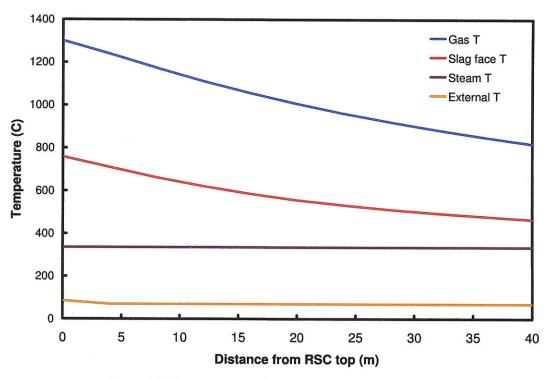
Figure 4-4: Temperature profiles for RSC in Reference Plant

Figure 4-5 and Figure 4-6 show gas composition profiles predicted by the ROM for the gasifier and RSC. Figure 4-5 shows rapid consumption of O_2 primarily by volatiles oxidation, but also by limited char oxidation. Slower char gasification reactions then consume CO_2 and H_2O and produce CO and H_2. As stated above, chemical reactions are predicted to cease in the first half of the gasifier. It is unclear if this is the case in reality or not.

Figure 4-6 shows that the rapid drop in temperature in the RSC (illustrated in Figure 4-4) causes the water-gas shift reaction to convert CO and H_2O to H_2 and CO_2. The broken lines show the equilibrium gas composition at the RSC exit temperature. The ROM predicts that as gas temperature continues to drop, gas phase kinetics halt the shift long before equilibrium is reached.
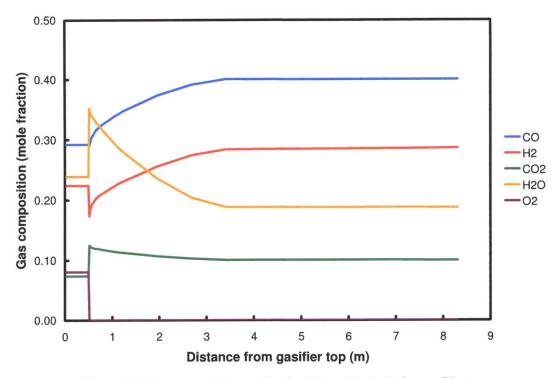
Figure 4-5: Gas composition profiles for GE gasifier in Reference Plant
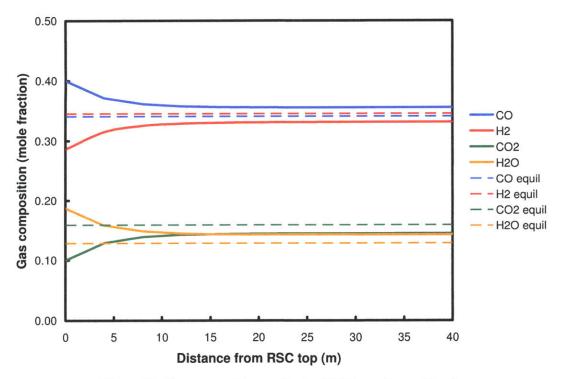
Figure 4-6: Gas composition profiles for RSC in Reference Plant

225

Figure 4-7 and Figure 4-8 show the profiles for nitrogenous and sulfurous gas phase species. Although the nitrogen pollutant submodel tracks the formation N_2O, NO_2 and HCN, they are not present in any meaningful quantities and so are neglected in Figure 4-7. The predicted trends of nitrogen species formation are expected for oxygen-blown gasification [9]: NH_3 evolves from the particle and is converted gradually to N_2. NO is only present in miniscule quantities in the volatiles oxidation region. Figure 4-8 shows expected sulfur pollutant formation behavior. SO_2 is formed in the volatiles oxidation region and is converted to H_2S. H_2S also evolves during char conversion, while COS is produced in smaller quantities.
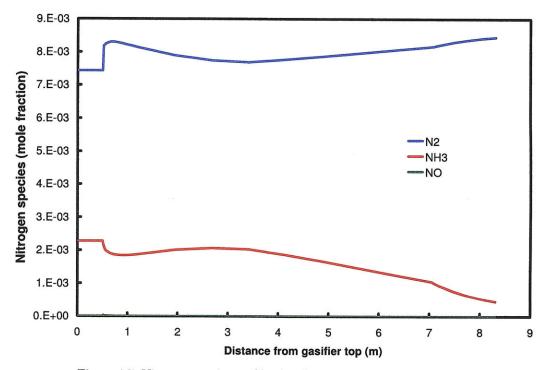
Figure 4-7: Nitrogen species profiles for GE gasifier in Reference Plant
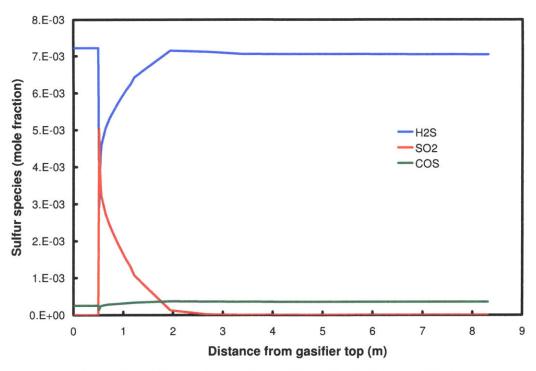
Figure 4-8: Sulfur species profiles for GE gasifier in Reference Plant

4.3.2.2 The Effect of Fluxant and Slag Behavior Predictions

As stated above, the ROM simulation of the Reference Plant uses the input flow rates and conditions specified in Table 4-1, with the addition of a 2512 kg/hr input stream of fluxant, which is modeled as 100% CaO (calcium oxide)[1]. The reasoning for this is explained in this section.

The slag submodel used in the ROM, which is described in Chapter 2, calculates slag viscosity as a function of local slag temperature and slag composition [10, 11]. Therefore the initial composition of coal-ash is required for the submodel. The NETL report does not specify the mass fraction of the various metal-oxides in the coal-ash, so a literature review was performed to identify the dominant components of Illinois No. 6 coal-ash. The results of this literature review are presented in Figure 4-9. The reviewed literature cited in this work is listed in references [12-16]. For all of the cases reviewed, six metal oxides account for at least 92% of coal-ash composition: SiO_2 (silicon dioxide) 44-55%, Fe_2O_3 (iron oxide) 17-21%, Al_2O_3

---

[1] Limestone ($CaCO_3$) and/or dolomite ($CaMg(CO_3)_2$) are typical fluxants. For the purpose of calculating the viscosity of molten limestone and dolomite, virtually all models use CaO as a surrogate [11].

(aluminum oxide) 14-21%, CaO (calcium oxide) 4-8%, SO_3 (sulfur trioxide) 5-7% (where recorded), and K_2O (potassium oxide) 2-3%. The ash composition given in McCollor et al's work [12] is used in the slag submodel for the ROM.
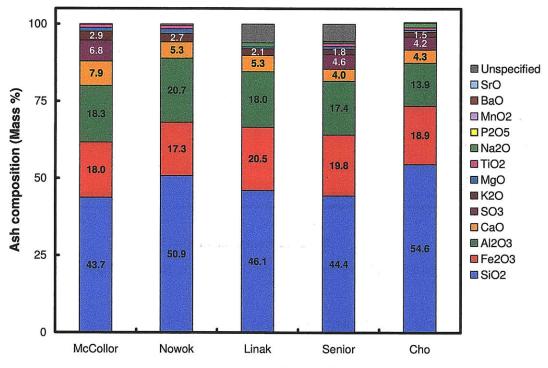
Figure 4-9: Composition of Illinois No. 6 coal-ash

As previously stated, ROM simulation of the Reference Plant without the addition of fluxant results in excessively high slag viscosity at the gasifier exit. For effective slagging operation and slag removal, the maximum allowable slag viscosity is 25 Pa.s (250 poise) [17, 18]. In up-flow gasifiers, for example the Shell and MHI designs, slag removal takes place directly below the injection ports and oxidation zone, meaning slag leaving the gasifier does so at very high temperatures. For down-flow designs, such as the GE gasifier, slag removal takes place at the end of the gasification zone, where temperatures are relatively low. For these types of gasifiers it is therefore extremely important to ensure adequately low slag viscosity.

Figure 4-10 shows ROM predictions for slag temperature and viscosity in the Reference Plant gasifier. The highest temperature, lowest viscosity point for each curve (in the bottom-right) corresponds to the slag condition near the inlet of the gasifier, where temperatures are highest due to volatiles oxidation. The lowest

temperature, highest viscosity point of each curve (on the left) corresponds to the slag condition at the gasifier exit, where temperatures are lowest due to gasification reactions and heat loss. Following any curve from high temperature and low viscosity to low temperature and high viscosity allows one to view the temperature-viscosity history of slag in the gasifier.

The different curves in Figure 4-10 correspond to different flow rates of fluxant and therefore different mass fractions of CaO in slag. The top curve ($T_{slag,exit}$=1314 °C) shows the slag temperature-viscosity history when no fluxant is used. This exit temperature is very close to that given in the NETL report (1316 °C), but results in a slag exit viscosity of 139 Pa.s, far in excess of the maximum allowable viscosity. Increasing the mass fraction of CaO in the slag (i.e. increasing the flow rate of fluxant) has two effects: (1) slag exit viscosity decreases due to the glass-modifying effect of CaO (see Chapter 2), and (2) slag exit temperature decreases slightly due to the additional heat capacity provided by the fluxant and due to increased heat loss because of reduced slag thickness.

Figure 4-10 shows that slag exit viscosity is brought down to an acceptable value at a CaO mass fraction of 25%. This finding is supported by the work of Song et al [17], who found optimal slag viscosity at a CaO mass fraction of 30%. The results of ROM simulation indicate that increasing CaO fraction beyond 25% yields diminishing returns. With these findings in mind all steady-state and dynamic ROM simulations of the Reference Plant employ a fluxant flow rate such that slag CaO mass fraction is maintained at 25%.
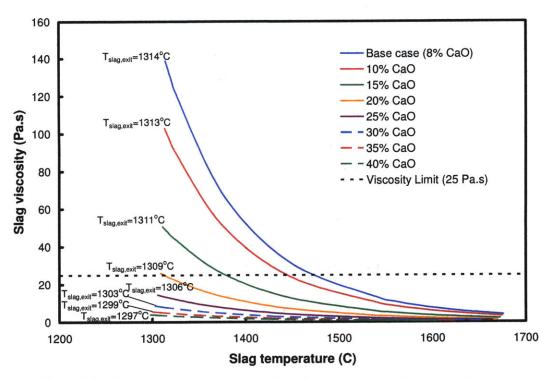
Figure 4-10: Temperature-viscosity curves for Illinois No. 6 slag with fluxant addition

Figure 4-11 shows the ROM predictions for slag viscosity (Pa.s), mean velocity (mm/s), thickness (mm) and mass flow rate (kg/s) along the wall of the gasifier. These four results are displayed on the same plot to show the interactions between them. The CaO fraction in the slag is maintained at 25% by injecting 2512 kg/hr of fluxant. The position-viscosity curve in Figure 4-11 corresponds to the 25% CaO temperature-viscosity curve in Figure 4-10. Mass flow rate increases linearly along the wall as the ROM assumes a uniform flux of particles to the slag layer. Slag layer thickness and mean velocity across the thickness of the slag layer also increases along the length of the wall.

Now that a base case simulation of Reference plant gasifier and syngas cooler performance has been established, the ROM can be used, again in steady-state, to establish realistic initial, intermediate and final states for dynamic simulations. These states are described in the next section.
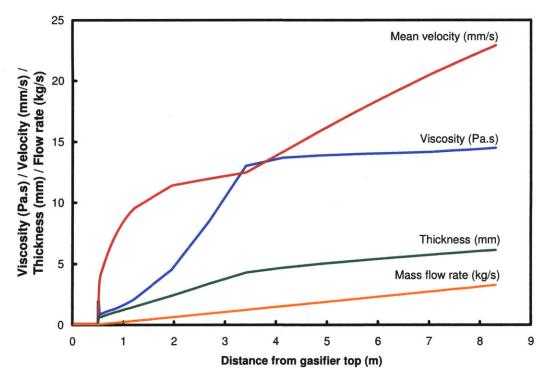
Figure 4-11: Slag viscosity, velocity, thickness and mass flow rate profiles for GE gasifier in Reference Plant

4.3.3 Initial, Intermediate and Final States for Dynamic Simulations

Six gasifier operations have been identified for dynamic ROM simulation. They are identified and described in Table 4-3. The cases were chosen for their importance to IGCC and polygeneration systems. They are described in further detail in the following sections.

Table 4-3: Gasifier operations for dynamic ROM simulation

Case	Title	Description
1	Removal of Fluxant	Inlet flow rate of fluxant is decreased to zero linearly over the course of one hour. System is allowed to reach equilibrium over the following eight hours.
2	Load Following	Inlet flow rates are decreased to half their original values linearly over the course of one hour. System is allowed to reach equilibrium over the following eight hours.
3	Feed Switching	Feedstock is fully switched from Illinois No. 6 to low-sulfur Utah bituminous coal linearly over the course of one hour. Other inlet streams are varied linearly to maintain inlet O_2:C ratio, H_2O:solids ratio, slag viscosity, and RSC and quench exit temperatures. System is allowed to reach equilibrium over the following eight hours.
4	Coal-Petroleum Coke Co-firing	Feedstock is switched linearly over the course of one hour from Illinois No. 6 to a 70:30 blend (by mass) of coal and petroleum coke. Other inlet streams are varied linearly to maintain inlet O_2:C ratio, H_2O:solids ratio, slag viscosity, and RSC and quench exit temperatures. System is allowed to reach equilibrium over the following eight hours.
5	Coal-Biomass Co-firing	Feedstock is switched linearly over the course of one hour from Illinois No. 6 to a 70:30 blend (by mass) of coal and straw. Other inlet streams are varied linearly to maintain inlet O_2:C ratio, H_2O:solids ratio, slag viscosity, full tar oxidation, and RSC and quench exit temperatures. System is allowed to reach equilibrium over the following eight hours.
6	Gasifier Cold Start[1]	Initial condition: The system starts at atmospheric pressure and temperature. The composition everywhere in the gasifier and cooler is that of atmospheric air.
6a		Natural gas preheat: Holding system pressure constant, inlet flow rates of CH_4 and air are ignited and increased linearly over the course of one hour, such that the maximum heating rate of the refractory face does not exceed design specifications. The system is allowed to reach an intermediate equilibrium state such that the refractory temperature near the burner allows auto-ignition of coal.
6b		Switch to coal-water slurry and oxygen feeds: Holding system pressure constant, inlet flow rates of CH_4 and air are decreased linearly over the course of one hour. Inlet flow rates of coal-water slurry and oxygen are then increased linearly over the course of the subsequent hour.
6c		System pressurization: Inlet flow rates of coal-water slurry and oxygen, and system pressure are increased linearly over time such that the maximum heating rate of the refractory face does not exceed design specifications. System is allowed to reach its steady-state operation.

---

[1] Gasifier cold start procedures were explained to the author on a visit to the Eastman Chemical gasification facility in Kingsport, Tennessee during the summer of 2009.

4.3.3.1 Case 1: Removal of Fluxant

As described in previous sections, fluxant can be used to improve the viscosity characteristics of slag. There is no operational reason why fluxant would be removed from the gasifier when the feedstock requires it. Therefore, Case 1 is intended to simulate an unplanned incident, such as a blockage or failure in the fluxant feeding system.

4.3.3.2 Case 2: Load Following

Load following is very important for IGCC plants. Despite the fact that IGCC plants are likely to be deployed primarily as baseload generating units, it is nevertheless important for plants to be able to shed or increase load over a reasonably short time-scale. Case 2 assumes the IGCC must reduce its output by 50% over the course of one hour. Since the ROM does not model the entire IGCC plant, the flow of syngas heating value from the gasifier (measured in units of MW_{th}) is used as a surrogate for plant power output.

4.3.3.3 Case 3: Feed Switching

Due to the highly inhomogeneous nature of coal in general, gasifiers should be able to switch from one coal feed to another over a reasonably short time-scale. Coal of the same seam but from different mines can have a wide variation of gasification characteristics. Case 3 assumes the feedstock is fully switched from high-sulfur Illinois No. 6 to low-sulfur Utah bituminous coal from the Blind Canyon mine over the course of one hour. Important properties of this coal are shown in Table 4-4.

Table 4-4: Important properties of feedstocks used in dynamic ROM simulation

	Illinois No. 6 bituminous coal	Utah Blind Canyon bituminous coal	Straw	Petroleum coke
References	[4, 12]	[19]	[20]	[21, 22]
HHV (kJ/kg)	27,113	27,064[1]	19,000	33,690[1]
Proximate analysis (wt%)				
Fixed carbon	44.19	39.13	12.48	83.32
Volatile matter	34.99	39.71	73.90	11.08
Ash	9.70	12.74	5.42	0.49
Moisture	11.12	8.43	8.20	5.11
Ultimate analysis (wt%)				
C	63.75	63.75	43.70	83.50
H	4.50	4.82	5.32	3.57
O	6.88	8.61	36.83	0.00
N	1.25	1.22	0.46	1.45
S	2.51	0.44	0.07	5.84
Ash	9.70	12.74	5.42	0.49
Moisture	11.12	8.43	8.20	5.11
Ash composition (wt% of ash)				
SiO_2	43.7	61.12	31.4	25.0
Al_2O_3	18.3	15.29	3.9	7.8
Fe_2O_3	18.0	2.90	1.8	10.2
TiO_2	1.0	0.87	0.2	-
P_2O_5	0.2	-	5.1	-
CaO	7.9	7.44	10.0	10.1
MgO	1.2	2.59	3.7	-
Na_2O	0.0	2.50	0.6	-
K_2O	2.9	1.30	22.4	1.2
SO_3	6.8	4.02	-	-
MnO_2	-	-	0.1	-
BaO	-	-	-	-
SrO	-	-	-	-
V_2O_5	-	-	-	46.0
Unspecified	-	1.97	20.8	-

4.3.3.4 Cases 4 & 5: Coal-Petroleum Coke and Coal-Biomass Co-firing

Cases 4 and 5 are similar in that they involve altering the overall feed composition entering the gasifier. These cases assume the feedstock is switched from coal only to a 70:30 blend (by mass) of coal-petroleum coke (petcoke) (Case 4) and coal-biomass (in the form of straw) (Case 5). Overall syngas heating value flow rates will change for these two cases due to the different feedstock heating values. Refer to Table 4-4 for important properties of the co-fired feeds. In Cases 4 and 5 the overall slag behavior changes due to altered feed composition. Note the higher fractions of CaO in both biomass and petroleum coke ash. Petroleum coke ash also has very high levels of V_2O_5 (vanadium(v) oxide), which is corrosive to chromium-oxide-based refractory bricks [26]. Fluxant flow rates must therefore be adjusted to

---

[1] Calculated in ROM.

234

account for this. An additional complication in Case 5 is the high fraction of volatile matter in biomass (74% in Table 4-4), which leads to increased tar production during devolatilization. Additional O_2 must therefore be supplied in Case 5 to oxidize this tar. Petroleum coke has very high sulfur concentrations, which will require downstream cleaning.

4.3.3.5 Case 6: Gasifier Cold Start

Cold-starting the gasifier involves bringing it from atmospheric pressure and temperature to operational pressure (56 bar) and temperature (1200-1700 °C). It is a complex procedure and is selected as a dynamic simulation case to demonstrate the flexibility and utility of the ROM. Cold start typically involves the following steps: refractory preheat, switch to coal-water slurry, system pressurization, and system approach to steady-state. The entire cold start process for a commercial-scale entrained flow gasifier takes 2-3 days.

Gaseous or liquid fuel is used to raise the temperature of the refractory face near the injectors to 900-1000 °C, to ensure auto-ignition of coal. The Eastman Chemical gasification facility in Kingsport, Tennessee uses a proprietary alcohol-based sulfur-free liquid fuel for preheat.[1] Sulfur-free fuel is essential since the gas cleanup equipment downstream of the gasifier does not operate during gasifier startup. The ROM models the preheat fuel as pure CH_4 (methane). The feed rates of fuel and air are set so that (1) the mixture burns slightly lean, and (2) the maximum heating rate experienced by the refractory face is less than 10-20 °C/min (600-1200 °C/hr). This is roughly the range of maximum heating rates for chromium-oxide-based refractory bricks found by Korshunov and Bas'yas [23]. Exceeding this limit causes cracking due to uneven thermal expansion in the brick.

Once the refractory face temperature near the injector has reached the desired temperature, the flows of preheat fuel and air are significantly reduced over the course of one hour. Over the next hour, the flows of preheat fuel and air are further reduced to zero and the flows of coal-water slurry and oxygen are started. The high refractory temperatures heat the incoming particles leading to

---

[1] Eastman Chemical's sulfur-free startup technology has been licensed to the Hydrogen Energy California (HECA) project. HECA is a joint venture between BP Alternative Energy and Rio Tinto to build a 250 MW_e coal and petcoke-fired IGCC plant with CCS in Kern County, California [24].

devolatilization, volatiles oxidation and char conversion. Since the pressure inside the gasifier is still around 1 bar, flow rates of reactants are initially kept low.

Once the stability of the coal flame has been ensured, feed rates and pressure are increased in the gasifier. Again, these must be increased so that the maximum heating rate experienced by the refractory face is less than 10-20 °C/min. Upon reaching full flow and pressure conditions, the system is allowed to come to steady-state. For the ROM simulation of Case 6, the final state is the base case of operation of the Reference Plant.

4.3.3.6 Initial, Intermediate and Final States

The ROM was used in steady-state to determine the input parameters required in order to reach the initial, intermediate and final states to be used in dynamic simulations. Table 4-5 shows the inputs required for the initial, intermediate and final states determined by the ROM. The initial states for Cases 1-5 are the base case established for the Reference Plant, described in previous sections. The initial state for Case 6 is atmospheric pressure, temperature and air composition everywhere in the system. The table also shows the required rates of change for each of the inputs. For example, in Case 1, the only dynamic input is the flow rate of fluxant, which decreases from 2512 kg/hr to 1 kg/hr over one hour. Therefore the rate of change of fluxant flow rate for Case 1 is -2511 kg/hr/hr.

After dynamic changes are made to the inputs, the system is allowed to equilibrate, or reach a new steady state of operation. For Cases 1-5, the time allowed for system equilibration is 8 hours. As is seen in the next section, virtually all transients extinguished after 8 hours. The system equilibration times for Case 6 are discussed in Section 4.4.6.

The column titled "Considerations" in Table 4-5 specifies the important simulation outputs or performance targets that must be adhered to in order for the ROM to predict realistic gasifier performance. An example of a consideration is the fact that maximum slag viscosity must be limited to 25 Pa.s for all cases. This means that fluxant flow must be adjusted accordingly. Another important consideration is the quenched gas temperature. Therefore the flow rate of quench water must be adjusted to account for the input flow rates to the gasifier. For Case 4 (coal-

biomass co-firing) an important consideration is the full oxidation of devolatilized tar.

In cases where certain input flow rates are to be dynamically reduced to zero (Cases 1 and 3) the ROM does not actually allow them to reach zero, as this may cause errors in the solution. Therefore, flow rates are reduced to 1 kg/hr, which is sufficiently small as to be insignificant. For Case 6, the initial flow rate of solid feed, which should be zero, is actually 10 kg/hr in the ROM. This was determined to be the lowest particle flow rate that maintains solution stability. Note that 10 kg/hr represents 0.1% of the total flow rate entering the gasifier in the initial state.

In Case 6, and specifically 6a, CH_4 is used to preheat the gasifier. For the purpose of ROM simulation, CH_4 is considered part of the "Oxidant Feed". This is because the ROM is currently configured to only allow solids in the feedstock streams. However, since the gaseous species mole fractions for the oxidant feed must be specified, and since CH_4 is a tracked gaseous specie, it can easily be included in the oxidant feed. The maximum flow rates of CH_4 and air used in preheating are 440 kg/hr (684 Nm^3/hr) and 9560 kg/hr (8243 Nm^3/hr).

Now that initial, intermediate and final states as well as rates of change of input flow rates and properties have been established for dynamic gasifier operation, the ROM can be used to simulate the dynamic performance of the gasifier and syngas cooling system for the six cases described in this section. The next section discusses the results of dynamic simulation.

Table 4-5: Test matrix for dynamic ROM simulations

Case	Dynamic inputs	Units	Initial values	Final values	Time for change (hrs)	Rate of change (units/hr)	Considerations
1	Fluxant feed	kg/hr	2512	1	1	-2511	Fluxant flow
2	Solid feed 1	kg/hr	113586	56793	1	-56793	Flow rates, slag viscosity
	Fluxant feed	kg/hr	2512	1256		-1256	
	Oxidant feed	kg/hr	95078	47539		-47539	
	H_2O feed	kg/hr	46661	23331		-23331	
	Quench H_2O	kg/hr	323059	161530		-161530	
3	Solid feed 1	kg/hr	113586	1	1	-113585	O_2:C ratio, H_2O:solid ratio, MW_{th}, slag viscosity, quench gas T
	Solid feed 2	kg/hr	0	111803		111803	
	Fluxant feed	kg/hr	2512	2560		48	
	Oxidant feed	kg/hr	95078	93369		-1709	
	H_2O feed	kg/hr	46661	45615		-1046	
4	Solid feed 1	kg/hr	113586	79510	1	-34076	Feed ratio, O_2:C ratio, H_2O:solid ratio, slag viscosity, quench gas T, tar oxidation
	Solid feed 2	kg/hr	0	34076		34076	
	Fluxant feed	kg/hr	2512	1350		-1162	
	Oxidant feed	kg/hr	95078	89000		-6078	
5	Solid feed 1	kg/hr	113586	79510	1	-34076	Feed ratio, O_2:C ratio, H_2O:solid ratio, slag viscosity, quench gas T
	Solid feed 2	kg/hr	0	34076		34076	
	Fluxant feed	kg/hr	2512	1630		-882	
	Oxidant feed	kg/hr	95078	101000		5922	
6							
6a	Solid feed 1	kg/hr	10	10	1	0	Quench gas T, refractory T, refractory heating rate
	Fluxant feed	kg/hr	0	0		0	
	Oxidant feed	kg/hr	10000	10000		0	
	H_2O feed	kg/hr	1	1		0	
	Ox. Comp.						
	Ar		0.0093	0.0086		-7.20E-04	
	CH_4		0.0000	0.0773		7.73E-02	
	N_2		0.7809	0.7207		-6.02E-02	
	O_2		0.2095	0.1933		-1.61E-02	
	Pressure	bar	1	1		0	
	CWS temp.	°C	27	61		33.8	
	O_2 temp.	°C	27	97		69.8	
	Quench H_2O	kg/hr	5769	5769		0	
6b	Solid feed 1	kg/hr	10	2028	1	2018	Inlet flow rates, slag viscosity. Note that oxidant feed is first reduced to 1697 kg/hr over one hour. The other dynamic changes are made subsequent to this.
	Fluxant feed	kg/hr	0	49		49	
	Oxidant feed	kg/hr	10000	1697		-8303	
	H_2O feed	kg/hr	1	833		832	
	Ox. Comp.						
	Ar		0.0086	0.0320		2.33E-02	
	CH_4		0.0773	0.0010		-7.63E-02	
	N_2		0.7207	0.0180		-7.03E-01	
	O_2		0.1933	0.9491		7.56E-01	
6c	Solid feed 1	kg/hr	2028	113586	5	22312	Pressure, inlet flow rates, refractory heating rate, slag viscosity
	Fluxant feed	kg/hr	49	2512		493	
	Oxidant feed	kg/hr	1697	95078		18676	
	H_2O feed	kg/hr	833	46661		9166	
	Quench H_2O	kg/hr	5769	323059		63458	
	Pressure	bar	1	56		11	

238

4.3.4 Summary

The ROM has been used to simulate the steady-state operation of a 2700 tpd (metric-tonne-per-day) GE full-scale gasifier as part of the GE-Bechtel Reference IGCC Plant. One such 630 MW_e plant is currently under construction by Duke Energy in Edwardsport, Indiana. The GE gasifier is down-flow, slurry-fed, O_2-blown, axially-fired, one-stage, refractory-lined, slagging, and radiant- and quench-cooled. Gasifier dimensions were not provided but these have been constructed using information from a number of sources detailed above. No kinetic parameters were provided for the feedstocks, so lumped extrinsic (mass-based) parameters, similar to those used for MHI validation, were used. No experimental data is available for a full-scale GE gasifier, but NETL simulated overall IGCC plant performance using a detailed process flowsheet model. Where possible, the results of NETL's flowsheet model are used in the place of experimental validation results. Additionally, since the ROM has been validated for simulation of a 1000 tpd pilot-scale GE gasifier (the Cool Water gasifier), reasonable ROM accuracy is assumed.

Simulation results show full-scale gasifier performance very similar to that of the pilot-scale Cool Water gasifier. Comparison of predicted gasifier temperature profiles (Figure 3-64 and Figure 4-3) and predicted composition profiles (Figure 3-69 and Figure 4-5) for the two gasifiers illustrates this fact. Figure 4-6 shows that the ROM predicts syngas leaves the radiant cooler in a non-chemical-equilibrium state. This is caused by low temperatures freezing the water-gas shift reaction. Important pollutant species are predicted to be NH_3 and H_2S, with smaller amounts of COS present. Figure 4-7 and Figure 4-8 show exit concentrations of NO_x and SO_x are predicted to be negligible. This finding agrees with gasifier operational experience.

The ROM has also been used to predict the steady-state behavior of slag on the gasifier walls. Recall that the ROM is incapable of predicting realistic flow of particles to the gasifier walls. Instead, a simplified uniform flux of particles is assumed. Figure 4-10 indicates that unless fluxant (limestone modeled as CaO) is used, slag leaves the gasifier with an unacceptably high viscosity. This could lead to slag-freezing and blockage. A fluxant flow rate of 2512 kg/hr (compared to 113586 kg/hr of feedstock) is predicted to guarantee slag exit viscosity below the

limit of 25 Pa.s (250 poise). This causes a slight reduction in exit temperature, which is not accounted for in any other gasifier models.

Finally, the ROM has been used in steady-state mode to establish realistic initial, intermediate and final states for dynamic simulations, which are discussed in the next section. Table 4-5 shows these important states. Steady-state simulation established final states for Cases 1-5, which include dynamic fluxant removal, dynamic load following, dynamic feed-switching, and dynamic co-firing with petcoke and biomass. Initial and intermediate states for Case 6 (dynamic gasifier cold start) have also been determined by steady-state simulation.

Note that the steady-state simulations presented in this section were all performed in a matter of 1-5 minutes on a desktop personal computer. CFD simulations of similar systems are known to take 1-5 days to reach a converged solution, depending on the treatment of turbulence.

4.4 Dynamic Simulation Results

The results of dynamic ROM simulations are presented as history plots of the following: important temperatures in the gasifier and syngas cooling system, quenched syngas composition (on a dry basis), syngas production (or flow rate of syngas heating value in MW_{th}), and slag behavior at the gasifier exit, including viscosity, velocity, thickness and mass flow rate. The positions at which these simulation outputs are recorded are shown in Figure 4-12. Slag behavior is only recorded at the gasifier exit because that is where the slag is removed from the gasifier and the lowest temperatures in the gasifier are found there. So if slag viscosity is adequate at the gasifier exit, it is assumed to be adequate elsewhere in the gasifier. For each case, slag viscosity, velocity, thickness and mass flow rate are shown on the same plot to show the interactions between them.

All dynamic simulations were run at their initial state for one hour of simulated time. After one hour, the dynamic changes are imposed on the simulation. For Cases 1-5, the dynamic changes last for one hour. The system is then allowed to approach a new equilibrium over the next eight hours. The total simulated time for Cases 1-5 is always 10 hours. For all of the history plots presented for Cases 1-5, the area between the dashed lines indicates the period over which dynamic

240

changes are made to the simulation. Case 6 is discussed separately in Section 4.4.6.

History plots of carbon conversion are generally not shown as the ROM predicts carbon conversion greater than 99.6% in virtually all cases. This is discussed in detail in Section 4.3.2.1. History plots of pollutant mole fractions are presented for the cases that entail fuel-switching or co-firing, i.e. Cases 3-5, and also for Case 6.

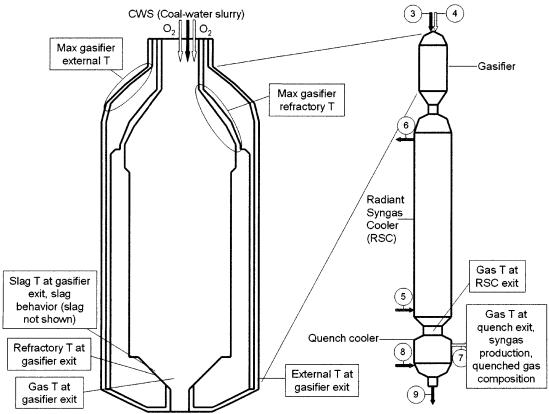Figure 4-12: Recording positions for important dynamic ROM simulation outputs

4.4.1 Case 1: Removal of Fluxant

The results of dynamic ROM simulation for Case 1, removal of fluxant, are shown in Figure 4-13 to Figure 4-16. Figure 4-13 shows the temperature history of the system. There are slight increases in gasifier temperatures due to reduced heat capacity and thicker slag layer caused by fluxant removal.

Figure 4-14 shows quenched gas composition history. Gas composition changes slightly due to small temperature changes in the gasifier, which are carried on to the RSC. Higher temperature allows the water-gas shift (WGS) reaction in the RSC to proceed further before ceasing, meaning more H_2 and CO_2 are produced. If the WGS was not kinetically-limited in the RSC, the opposite effect would be observed; less H_2 and CO_2 would be produced, as determined by the equilibrium constant of the WGS. Changes in syngas composition are seen to be highly responsive to dynamic system changes. There is very little further change after the fluxant flow stops.

Figure 4-15 shows the syngas production history of the system. There is virtually no change in the flow of syngas heating value from the quench cooler. Despite the fact that Figure 4-14 shows there is a shift from CO to H_2, the molar higher heating values of these species are very similar (285.9 kJ/mol for H_2 compared to 282.9 kJ/mol for CO), meaning that the overall heating value of syngas is largely unaffected.

Figure 4-16 shows the slag behavior history for the gasifier. Since Case 1 involves the elimination of fluxant, slag behavior changes drastically during the simulation. Reducing the fluxant flow from 2512 kg/hr to zero decreases the CaO mass fraction in slag from 25% to 8%. This increases the viscosity from 25 Pa.s to 139 Pa.s. This increased viscosity reduces the mass flow rate of slag, leading to accumulation. Slag mean velocity drops and layer thickness increases. All other dynamic simulations (Cases 2-6) entail the adjustment of the fluxant feed rate with the intention of keeping slag viscosity below 25 Pa.s.
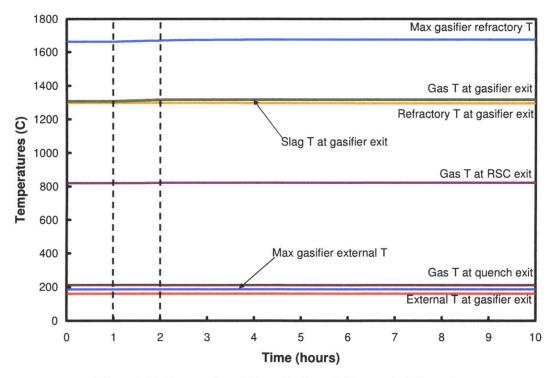
Figure 4-13: Temperature history for Case 1: Removal of Fluxant
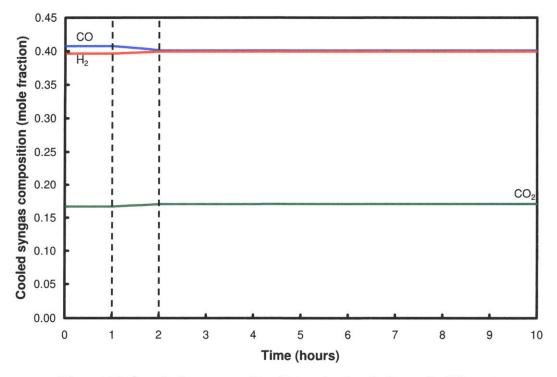

Figure 4-14: Quenched gas composition history for Case 1: Removal of Fluxant
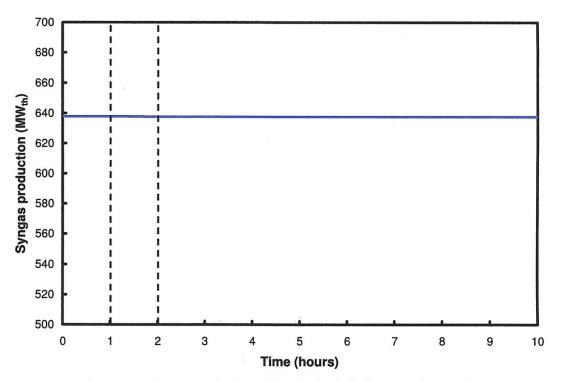
243

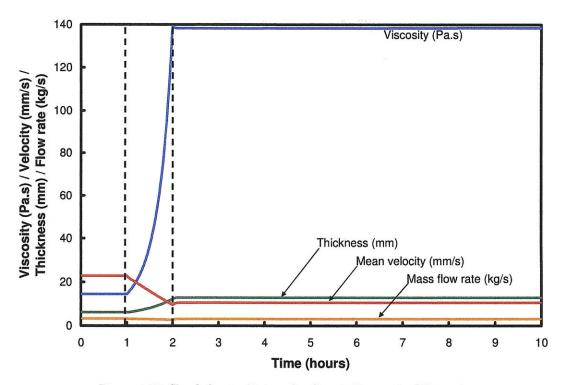Figure 4-15: Syngas production history for Case 1: Removal of Fluxant

Figure 4-16: Slag behavior history for Case 1: Removal of Fluxant

244

4.4.2 Case 2: Load Following

The results of dynamic ROM simulation for Case 2, load following, are shown in Figure 4-17 to Figure 4-20. Figure 4-17 shows the temperature history of the system. As the flow of all inlet streams into the gasifier are reduced to half their initial values, only slight decreases in gasifier temperatures are detected. This is expected as less thermal energy is released per unit gasifier volume at 50% capacity compared to 100% capacity. The most noticeable temperature change is that of gas at the RSC exit. Because of longer residence time in the RSC at 50% capacity, there is more heat loss to the cooling water in the RSC. The knock-on effect on quenched gas temperature is minimal.

Figure 4-18 shows quenched gas composition history. The slight change in composition is due to the fact that at 50% gasifier capacity, the WGS reaction freezes at an earlier point in the RSC. Therefore, less H_2 and CO_2 are produced. Changes in syngas composition are again seen to be highly responsive to dynamic system changes.

Figure 4-19 shows the syngas production history of the system. As expected there is a substantial drop in syngas production. It is interesting to note that syngas production is highly responsive to dynamic changes to the system. There is no discernable lag between input and output. This could have implications for how IGCC power plants are viewed with respect to their response to changing electrical demand. IGCC plants are currently thought to have poor load-following abilities [25]. Figure 4-19 suggests that the gasifier and syngas cooling system are not to blame for this. Since a majority of the other components in an IGCC plant are similar to those used in natural gas combined cycle (NGCC) plants, it is possible that gasification-based systems are more flexible than previously thought. This finding also has implications to gasification-based polygeneration plants, where gasifiers are used to supply syngas to a number of different chemical processes.

Figure 4-20 shows the slag behavior history for the gasifier. Despite the fact that fluxant flow is maintained such that slag CaO mass fraction is 25%, slag viscosity is seen to rise slightly. This is due to the slightly lower temperatures inside the gasifier due to its operation at 50%. Less thermal energy is provided per unit gasifier volume in this case than the base case. Slag mass flow rate drops sharply as expected, due to reduced slag deposition. Slag layer thickness also decreases,

but this is mitigated by the increase in viscosity, which tends to increase accumulation and thickness.
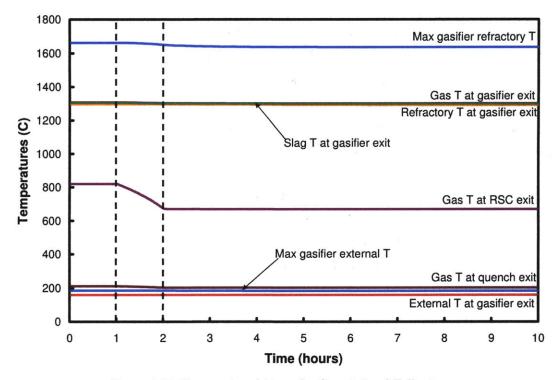
Figure 4-17: Temperature history for Case 2: Load Following
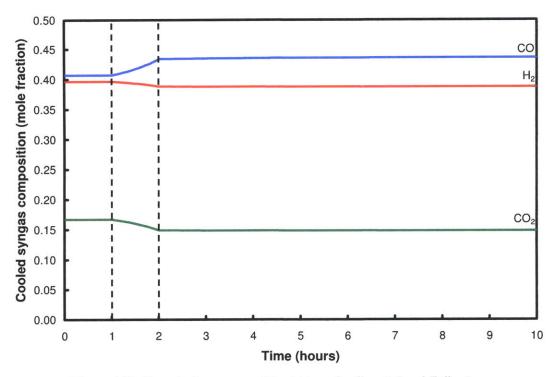
Figure 4-18: Quenched gas composition history for Case 2: Load Following
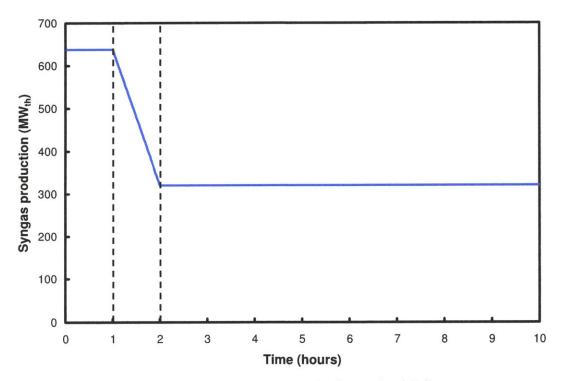
Figure 4-19: Syngas production history for Case 2: Load Following
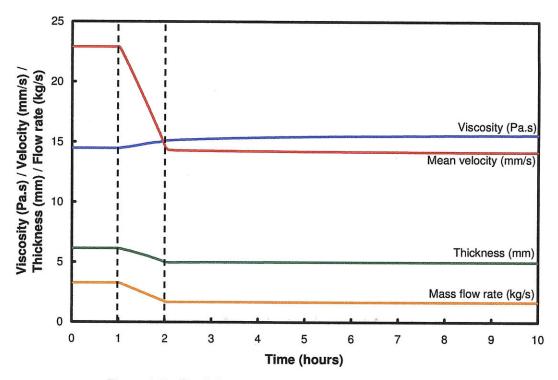
Figure 4-20: Slag behavior history for Case 2: Load Following

4.4.3 Case 3: Feed Switching

The results of dynamic ROM simulation for Case 3, feed switching, are shown in Figure 4-21 to Figure 4-24. Figure 4-21 shows the temperature history of the system. There is virtually no change in system temperatures. This is because the final state for Case 3 was chosen such that the values for inlet O_2:C, H_2O:solid and syngas production were identical to their initial state values. This was intended to simulate the realistic switch-over of feedstock while maintaining the same output. Since there was no change in syngas heating value flow rate, a history plot of syngas production (in MW_{th}) is not shown for Case 3.

Figure 4-22 shows quenched gas composition history. The syngas composition change is relatively small for the same reason the temperatures changes are small; the final state of the simulation was chosen to given the same outputs. The changes that are noticed in Figure 4-22 are due to differences in coal moisture content, which changes the system stoichiometry and temperatures very slightly.

Figure 4-23 shows the slag behavior history for the gasifier. Slag viscosity exhibits unexpected behavior during the dynamic period. A possible explanation for this behavior is that, although the CaO fraction of the slag is kept at 25%, viscosity depends on more than just CaO content. The complex nature of the slag viscosity submodel, described in Chapter 2, and the presence of glass formers, glass modifiers (of which CaO is one) and amphoterics is likely to play a role. SiO_2 (silicon dioxide) mass fraction is explicitly stated as being important to the submodel.

Figure 4-24 shows the nitrogen and sulfur species history at the gasifier exit. There is no real difference in nitrogen species mole fraction for the case. As expected, sulfur pollutants decrease drastically upon switching from high-sulfur (2.51%) to low-sulfur (0.44%) feeds. The difference in sulfur pollutant formation is roughly equivalent to the ratio of sulfur contents of the two coals. No SO_2 formation is observed in the simulation.
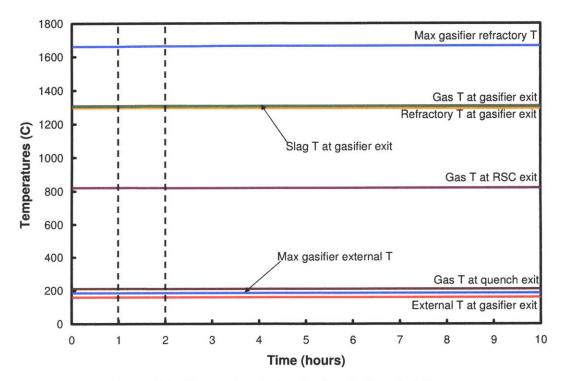
Figure 4-21: Temperature history for Case 3: Feed Switching

249
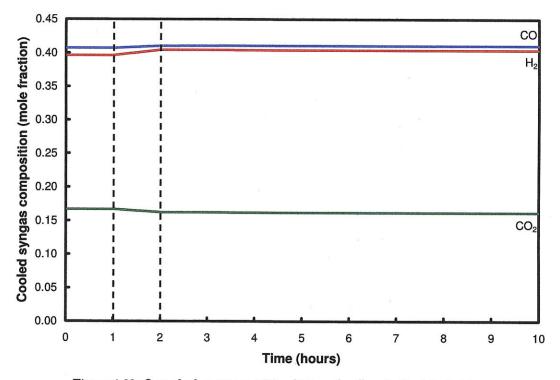
Figure 4-22: Quenched gas composition history for Case 3: Feed Switching
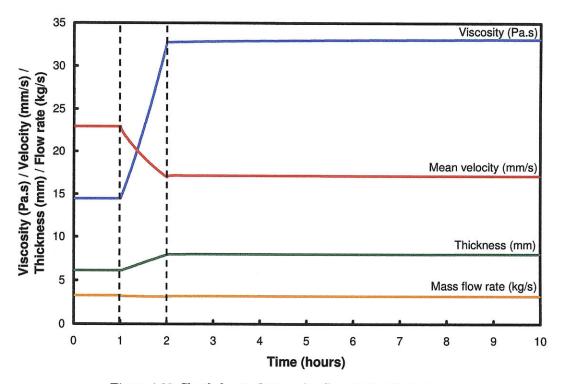
Figure 4-23: Slag behavior history for Case 3: Feed Switching
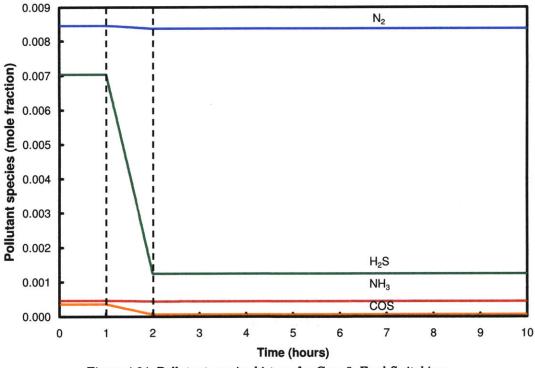
Figure 4-24: Pollutant species history for Case 3: Feed Switching

4.4.4 Case 4: Coal-Petroleum Coke Co-firing

The results of dynamic ROM simulation for Case 4, coal-petcoke co-firing, are shown in Figure 4-25 to Figure 4-29. Figure 4-25 shows the temperature history of the system. There is a noticeable increase in gasifier temperatures due to the addition of petcoke, due primarily to the fact that petcoke has a higher heating and carbon content value than coal. Petcoke's lower ash content, which requires less fluxant, also plays a role in increasing temperature. Again, the temperature changes downstream of the gasifier are less obvious due to the damping effects of the large RSC.

Figure 4-26 shows quenched gas composition history. The compositional changes seen in Figure 4-26 are due to the fact that the stoichiometry in the gasifier for Case 4 is different compared to that for the base case. In Case 4, oxygen flow to the gasifier is increased to maintain inlet O_2:C ratio, while H_2O feed rate is unchanged because the overall flow of solid feedstock into the gasifier does not change. While inlet H_2O:solids ratio does not change, inlet H_2O:C ratio decreases, leading to an increased CO:H_2 ratio in syngas leaving the gasifier. This effect is

strong enough to overcome the effect of increased water-gas shift (WGS) kinetics caused by higher RSC inlet temperature. The very slight rate of change of $CO:H_2$ ratio observed during the equilibration period is caused by the very gradual temperature increase in the gasifier allowing the WGS to proceed slightly further in the RSC.

Figure 4-27 shows the syngas production history of the system. As expected, syngas production increases due to the higher heating value of petcoke compared to coal (33690 kJ/kg vs. 27113 kJ/kg). Again, the gasifier and syngas cooling system is seen to respond to dynamic changes in input very quickly, with virtually no lag.

Figure 4-28 shows the slag behavior history for the gasifier. Similarly to Case 3 (Figure 4-23), slag viscosity behaves in an unexpected matter. The dynamic period sees a rapid increase in viscosity despite increasing slag layer temperatures. As described in the previous section, this behavior could be explained by changes in slag composition having unexpected effects on the complex slag viscosity model. During system equilibration, slag viscosity decreases back to its steady-state value, due to refractory and slag temperature increases. This behavior indicates that while 25% CaO fraction in slag is sufficient to ensure adequately low viscosity at steady-state slag temperature, it is insufficient when slag temperature is in transition.

Figure 4-29 shows the nitrogen and sulfur species history at the gasifier exit. The changes seen in N_2 and NH_3 mole fractions are caused by increased gas temperature inside the gasifier. This increases the rate of conversion of NH_3 to N_2. No HCN, NO or any other nitrogenous species are detected at the gasifier exit. As expected, co-firing with high-sulfur petcoke leads to higher mole fractions of both H_2S and COS, when compared to the base case.

Figure 4-25: Temperature history for Case 4: Coal-Petcoke Co-firing

Figure 4-26: Quenched gas composition history for Case 4: Coal-Petcoke Co-firing

253

Figure 4-27: Syngas production history for Case 4: Coal-Petcoke Co-firing

Figure 4-28: Slag behavior history for Case 4: Coal-Petcoke Co-firing
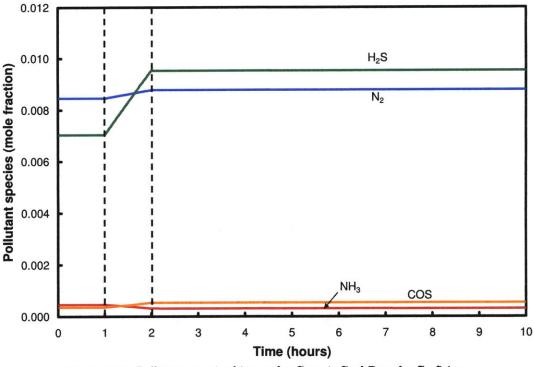
Figure 4-29: Pollutant species history for Case 4: Coal-Petcoke Co-firing

4.4.5 Case 5: Coal-Biomass Co-firing

The results of dynamic ROM simulation for Case 5, coal-biomass (i.e. straw) co-firing, are shown in Figure 4-30 to Figure 4-34. Figure 4-30 shows the temperature history of the system. Similarly to the coal-petcoke case discussed previously, gasifier temperature is seen to rise slightly for coal-straw co-firing, although the peak temperature drops. The primary reason for this general increase is the fact that the inlet O_2:C ratio has to be increased for straw co-firing due to the large amount of volatile matter present in biomass materials, some of which is released as tar during devolatilization. The volatile material fraction of straw is 74% compared to 35% for Illinois No. 6 coal. Inlet O_2:C ratio increases from 1.24 to 1.36 over the course of Case 5.

Figure 4-31 shows quenched gas composition history. The effect of increased inlet O_2:C ratio is illustrated by the higher CO_2 mole fraction after the switch to co-firing. This is the primary reason for the drop in CO mole fraction. A secondary reason is the fact that the higher temperatures lead to increased WGS kinetics in

255

the RSC before its cessation due to low temperatures. This also explains the increase in H_2 mole fraction.

Figure 4-32 shows the syngas production history of the system. As expected, syngas production decreases due to the lower heating value of straw compared to coal (19000 kJ/kg vs. 27113 kJ/kg). Again, the gasifier and syngas cooling system is seen to respond to dynamic changes in input very quickly, with virtually no lag.

Figure 4-33 shows the slag behavior history for the gasifier. The dynamic period sees a rapid decrease in viscosity due to increasing slag layer temperatures. During system equilibration, slag viscosity decreases further to its steady-state value, due to refractory and slag temperature increases.

Figure 4-34 shows the nitrogen and sulfur species history at the gasifier exit. The changes seen in N_2 and NH_3 mole fractions are caused by the fact that straw contains less nitrogen than Illinois No. 6 coal (0.46% vs. 1.25%). No HCN, NO or any other nitrogenous species were detected at the gasifier exit. As expected, co-firing with extremely low-sulfur biomass leads to much lower mole fractions of both H_2S and COS, when compared to the base case.
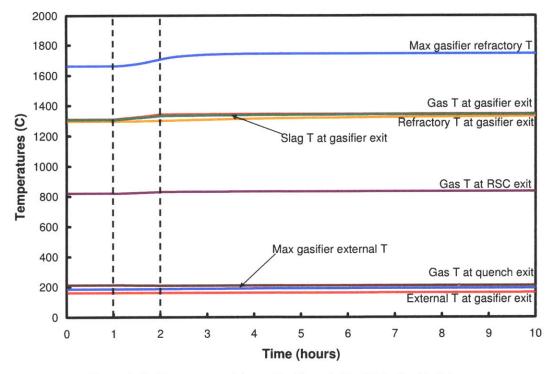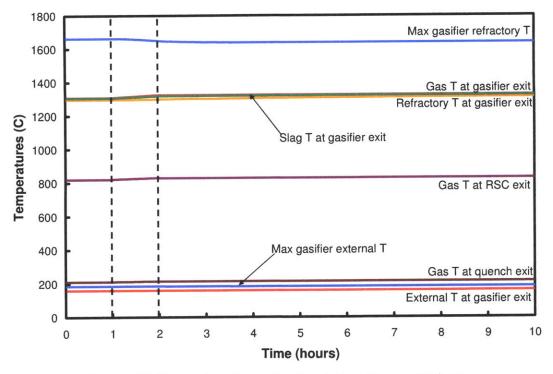
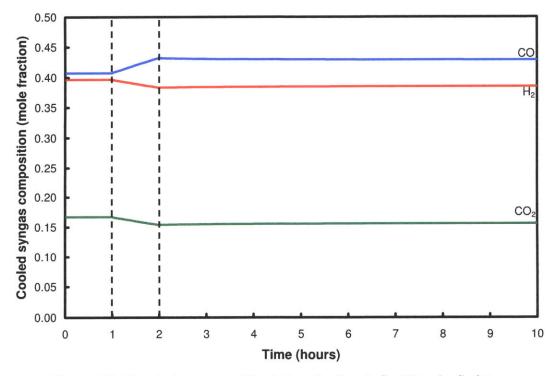Figure 4-30: Temperature history for Case 5: Coal-Biomass Co-firing
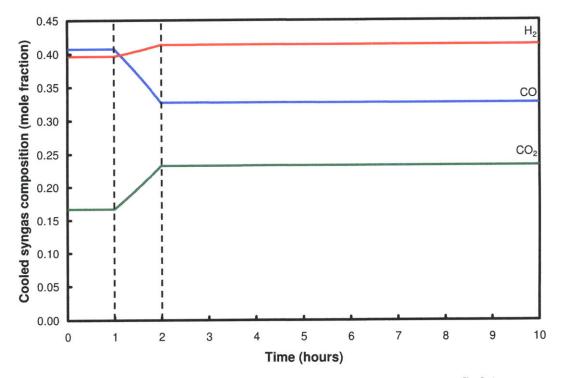
Figure 4-31: Quenched gas composition history for Case 5: Coal-Biomass Co-firing
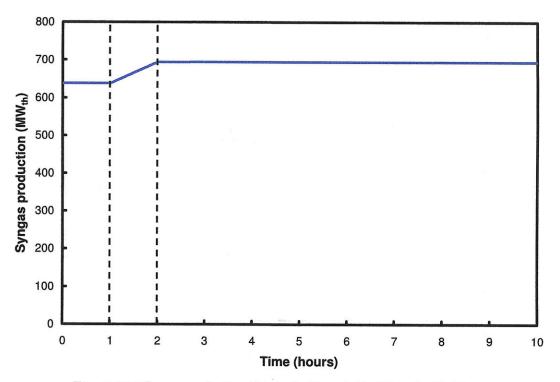
257
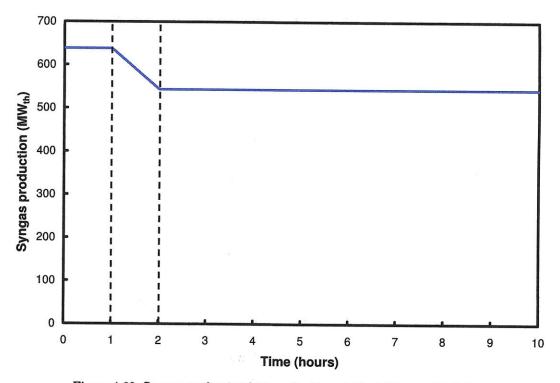
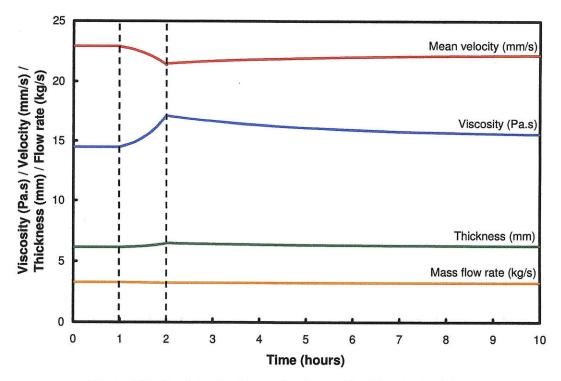Figure 4-32: Syngas production history for Case 5: Coal-Biomass Co-firing
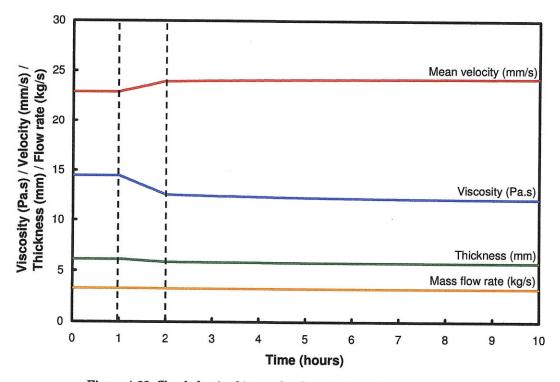
Figure 4-33: Slag behavior history for Case 5: Coal-Biomass Co-firing
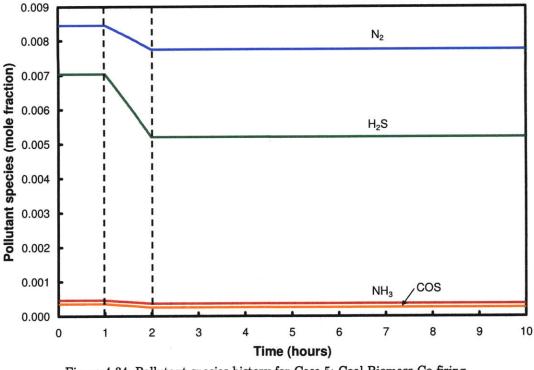
Figure 4-34: Pollutant species history for Case 5: Coal-Biomass Co-firing

4.4.6 Case 6: Gasifier Cold Start
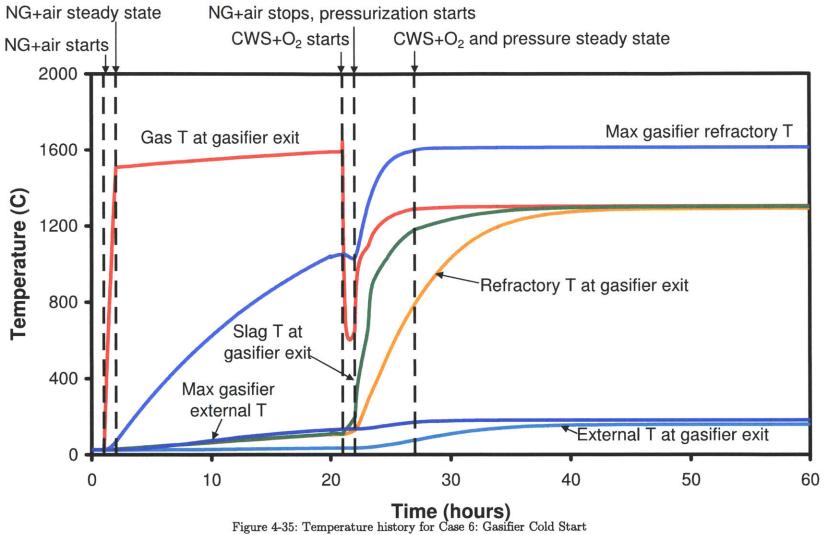
The results of dynamic ROM simulation for Case 6, gasifier cold start, are shown in Figure 4-35 to Figure 4-40. All history plots for Case 6 show the following important time points for the system:

- The time at which CH_4 and air flows for gasifier preheat are started ($t_1 = 1$ hour),

- The time at which CH_4 and air flows reach their steady-state values ($t_2 = 2$ hours),

- The time at which coal-water slurry (CWS) and O_2 flows are started ($t_4 = 21$ hours),

- The time at which (1) CH_4 and air flows reach zero, and (2) pressurization of the system starts ($t_5 = 22$ hours), and

- The time at which (1) CWS and O_2 flows reach their steady-state values (specified by the Reference Plant base case), and (2) pressurization of the system is complete ($t_6 = 27$ hours).

259

An addition important time point, which is not shown on the history plots is the time at which (1) the gasifier refractory wall near the inlets reaches its prescribed temperature, and (2) CH_4 and air flows are initially decreased ($t_3 = 20$ hours). This time point is omitted for reasons of clarity. The time over which CH_4 and air flows are increased ($t_2 - t_1 = 1$ hour) and the time over which system pressurization occurs ($t_6 - t_5 = 5$ hours) are chosen such that the maximum heating rate experienced by the refractory is below 10 °C/min. The ROM predicts that the maximum refractory heating rate occurs during system pressurization and has a value of 5 °C/min.

Figure 4-35 shows the temperature history of the system. Gas temperatures leaving the RSC and quench cooler are omitted for clarity. The ROM predicts rapid heating of the gas inside the gasifier during preheat due to CH_4 oxidation. The refractory brick near the inlet, which will always be the highest-temperature region, heats at a maximum rate of about 1.5 °C/min, which tapers to less than 0.5 °C/min after 18 hours of steady-state preheat. After 18 hours of steady-state system preheat, the refractory at the gasifier inlet has a temperature of 1040 °C. Figure 4-36 shows heating rate histories of refractory near the injector and at the gasifier exit. It is seen that maximum refractory heating rates occur during system pressurization.

Upon switching the gasifier feeds from CH_4-air to CWS-O_2, refractory temperature near the inlet initially drops. This is due to the fact that reduced CH_4 and air flows cause the gas temperature in the gasifier to fall sharply. As the flows of coal-water slurry and oxygen increase, volatiles oxidation and char oxidation increase the heat release to the gasifier walls, leading to temperature increase. This is particularly the case towards the end of the gasifier for two reasons: (1) char oxidation takes place throughout the volume of the gasifier, not just near the injectors, as is the case with CH_4-O_2 oxidation, and (2) the presence of high-temperature, reacting char particles in the gasifier increases emissivity and thermal radiation to the walls. Once system pressurization is complete, all temperatures in the gasifier approach their steady-state values. Fifty to sixty hours after gasifier cold start, the system reaches its operational steady-state. This figure qualitatively agrees with industrial experience of 2-3 days for gasifier cold start.

Figure 4-35: Temperature history for Case 6: Gasifier Cold Start

261
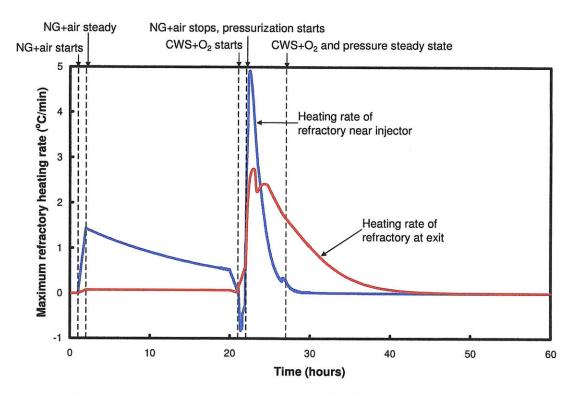
Figure 4-36: Refractory heating rate histories for Case 6: Gasifier Cold Start

Figure 4-37 shows the gasifier exit gas composition history, as opposed to the quenched gas composition history. The reason for this is that it is not clear if the quench cooler would be operational during the initial cold start stages. The x-axis only shows the times around the switch from CH_4-air to CWS-O_2 and system pressurization. Profiles outside this time period are virtually flat. During gasifier preheat, the major species leaving the gasifier are N_2, H_2O and CO_2, with small amounts of O_2 due to the fact that preheat is conducted under fuel-lean conditions. During the switch to CWS and O_2, CO_2 increases due to oxidation of volatiles and char. Char gasification does not commence to any major degree until gas temperature rises due to oxidation. After time t ~ 23 hours the production trends of the main syngas species, CO, H_2, CO_2 and H_2O reverse slightly. This is due to further gas temperature increase, leading to the reverse water-gas shift reaction, i.e. H_2 and CO_2 form H_2O and CO.

262
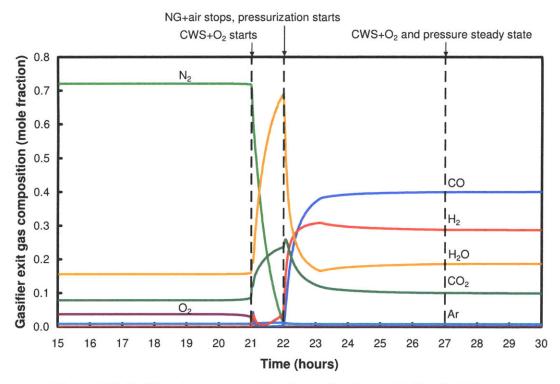
Figure 4-37: Gasifier exit gas composition history for Case 6: Gasifier Cold Start

Figure 4-38 shows the syngas production history of the system. As is the case with all of the dynamic simulations described, syngas production is highly responsive to gasifier input feeds. No output-input time lag is noticed as CWS feed rate increases to its full value at $t_5 = 27$ hours. This again indicates the gasifier's ability to respond quickly to changes in load.
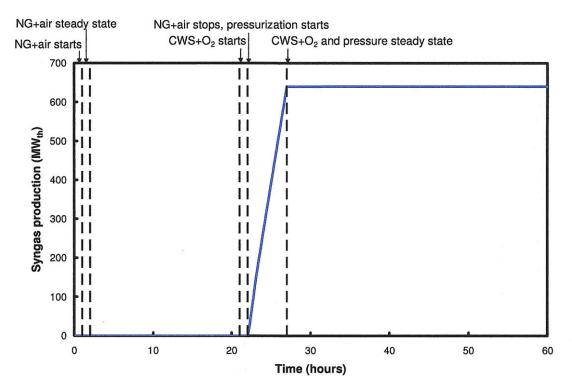
Figure 4-38: Syngas production history for Case 6: Gasifier Cold Start

Figure 4-39 shows the slag behavior history for the gasifier. Note that during preheat, when no solid feed is supplied to the gasifier, uniform slag thickness of 1 mm is assumed. This assumption is made because the ROM requires there to be a non-zero value for slag thickness at all times, and 1 mm thickness ensures simulation stability across the range of operating conditions. Upon the introduction of CWS to the gasifier, Figure 4-39 shows that particle deposition on the walls leads to a rapid increase in slag layer thickness. The instantaneous jump in slag layer thickness from 1 mm to 4 mm seen at 21 hours is explained as follows.

As discussed in previous sections, even during gasifier preheat, when no particles are supposed to be fed to the gasifier, the ROM allows a particle flow rate of 10 kg/hr. This is because when particle volume fraction approaches zero, instabilities appear in the simulation. During preheat, a with particle flow rate of 10 kg/hr, particle concentration is so small that their contributions to most terms in the mass, energy and momentum conservation equations are negligible. There are two important exceptions (1) radiation from particle cloud to wall, and (2) migration of particles to wall and their effect on slag layer thickness.

264

The issue of particle-wall radiation arises because the heat transfer submodel, described in Chapter 2, relies on the assumption that KB > 3, where K is the absorption coefficient of the particle cloud and B is the characteristic dimension of the gasifier. When KB > 3, $K = \pi r_p^2 N_p$ is appropriate; r_p and N_p are the particle radius and number density $(1/m^3)$, respectively. The emissivity of a particle cloud is modeled as $\varepsilon_p = 1 - \exp(-KB)$. At very low particle loadings, such as those required for ROM stability during preheat, use of this radiation model over-predicts the role of radiation. Therefore, the ROM employs a switch that activates the radiation submodel only when KB ~ 3. This means that particles are "invisible" to radiation during preheat but are "revealed" during the switch to CWS and O_2 feeds.

The ROM uses a similar switch when dealing with particle migration to the wall. Since the ROM cannot accurately predict the fluid flow field that causes particles to impact the wall, it assumes a certain fraction of particle mass entering the gasifier (f_{slag}) migrates to the wall in a uniform flux. This is also described in Section 3.3. Despite the low particle concentration required by the ROM during preheat; use of f_{slag} causes unrealistic changes in slag layer thickness. Therefore, f_{slag} is only activated upon the introduction of CWS to the gasifier. This means that particles are "invisible" to slagging during preheat but are "revealed" during the switch to CWS and O_2 feeds. This is the primary cause of the large jump in slag thickness at t = 21 hours. The further increase from 4 mm to 9 mm is caused by increased slagging due to increased particle flow rate.

Concurrent to slag layer buildup, slag temperature increases rapidly, due to improved radiative heat transfer to the wall, char oxidation occurring throughout the gasifier volume, and greater insulation provided by thicker slag. This causes the drastic reduction in slag viscosity seen in Figure 4-39, leading to higher slag velocity and lower slag layer thickness. The slag layer reaches a steady-state viscosity of around 15 Pa.s and thickness of 6 mm.
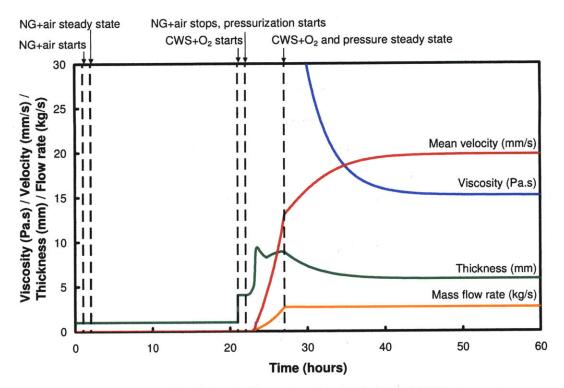
Figure 4-39: Slag behavior history for Case 6: Gasifier Cold Start

Figure 4-40 shows the nitrogen and sulfur species history at the gasifier exit. The x-axis only shows the times around the switch from CH4-air to $CWS-O_2$. Profiles outside this time period are virtually flat. Nitrogen, which is the major gas-phase specie during preheat, decreases in mole fraction drastically during the switch to CWS and O_2. The time for minimum N_2 (and maximum NH_3) coincides with the local minimum of gas temperature. Temperature increases after this point, speeding the conversion of NH_3 to N_2. Sulfur dioxide (SO_2) is the major sulfur specie present during the switch from CH_4-air to $CWS-O_2$. This is due to the O_2-rich (fuel-lean) conditions that exist during this process. The concentration of SO_2 drops precipitously once the system reaches gasification stoichiometry. At this point, H_2S rapidly becomes the primary sulfurous pollutant, with smaller amounts of COS present. Figure 4-40 emphasizes the importance of a sulfur-free preheat fuel (e.g. the Eastman Chemical sulfur-free startup process).
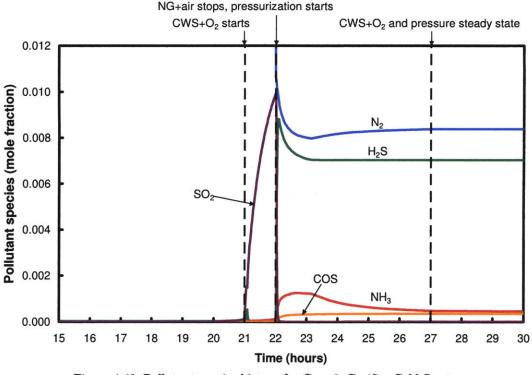
Figure 4-40: Pollutant species history for Case 6: Gasifier Cold Start

4.4.7 Summary

Using realistic initial, intermediate and final states determined in Section 4.3.3, the ROM has been used to simulate the dynamic operation of a 2700 tpd (metric-tonne-per-day) GE full-scale gasifier. To the author's knowledge, this is the first detailed dynamic study of entrained flow gasifier performance. The only previous dynamic study found in the literature does not account for the chemical kinetics of feedstock conversion or slag behavior. Furthermore, there is no publically-available experimental data for dynamic gasifier operation.

Six dynamic cases have been simulated: (1) removal of fluxant, (2) load following, (3) feed switching, (4) coal-petroleum coke co-firing, (5) coal-biomass co-firing, and (6) gasifier cold start. Time histories of temperatures, syngas compositions, syngas production, pollutant concentrations, and slag behavior indicators (i.e. exit viscosity, velocity, thickness and flow rate) are used to visualize predicted dynamic performance. For the first five cases, simulation inputs are changed over the course of 1 hour of simulated time. The system is then allowed to reach a final state over the following eight hours. All dynamic simulations took in the range of

267

15-45 minutes on a desktop personal computer; with the exception of the gasifier cold start case, which took about 6 hours. These simulation times have not been compared to CFD simulations as the author is unaware of any attempt to simulate the dynamic performance of similar systems using CFD-based computer models.

Results for Case 1 show that when fluxant is removed, slag viscosity rises rapidly as expected (see Figure 4-16). Cases 2-5 all vary fluxant flow rate according to feedstock flow rate and ash properties, in order to maintain mass fraction of CaO in slag of around 25%. From steady-state simulations, this is found to give slag exit viscosity of around 15 Pa.s (150 poise). Simulation results for Case 2 indicate that the gasifier responds very quickly to changes in feedstock flow rate (see Figure 4-19). This suggests that the gasifier and syngas cooling system may be better able to load-follow than is currently believed.

Switching from the high-sulfur Illinois No. 6 coal of the base case to low-sulfur Utah Blind Canyon coal leads to a rapid predicted drop in H_2S and COS emissions (see Figure 4-24). While this finding is to be expected, the ROM predicts interesting slag behavior. Despite the fact that CaO mass fraction in slag is maintained at 25% by fluxant flow rate adjustment, Figure 4-23 shows a sharp increase in viscosity. Since no temperature drop is predicted, it is thought likely that changes in SiO_2 mass fraction lead to this behavior. This highlights the complexity of the slag viscosity submodel.

The two co-firing cases involve the blending of a secondary feedstock (petcoke or straw) with the primary feedstock (Illinois No. 6) to a mass percentage of 30%. This leads to an increase in syngas production in the case of coal-petcoke blending (see Figure 4-27) and a decrease in syngas production in the case of coal-straw blending (see Figure 4-32). These changes are due to differences in heating values for petcoke and straw. The syngas production decrease for coal-straw co-firing is exacerbated by the high tar fraction released by straw devolatilization. This requires additional O_2, which leads to increased syngas CO_2 content and lower syngas heating value. Favorable slagging behavior is also seen for the straw co-firing case. This is due to the low ash content of straw as well as the high CaO content of straw ash.

Gasifier cold start is the most demanding dynamic case for the ROM because of the very wide range of temperatures, pressures, gas compositions and particle volume fractions. The ROM predicts rapid heating of the refractory near the injector during gasifier preheat (see Figure 4-35). Heat release is concentrated in this area as CH_4 oxidation occurs extremely rapidly. Upon switching the feeds to coal-water slurry (CWS) and O_2, cooling initially occurs as heat released from the reactions is much lower. However, once system pressurization begins, heat is transferred to the walls in a fairly uniform manner throughout the gasifier. This is due to (a) the fact that char conversion reactions initially occur throughout the reactor, and (b) the presence of a particle cloud in the gasifier drastically increases emissivity. The second point again alludes to the weakness of the radiation submodel in accurately predicting emissivity at low particle volume fraction. Despite this potential error, the ROM predicts compositions of major species and pollutants that are to be expected. Refer to Figure 4-37 and Figure 4-40 for illustrations of this. As is the case for all of the dynamic predictions, slag behavior indicators show the longest response times in the system.

4.5 Chapter Summary

This chapter presented the results of steady-state and dynamic ROM simulation of a full-scale 2700 tpd GE entrained flow gasifier and syngas cooling system. Steady-state operation of the GE-Bechtel Reference IGCC Plant using the input specifications described in the NETL report on baseline fossil energy [5] was chosen as the base case for simulation. The ROM was used in steady-state mode to establish a base case for system operation and to understand the role of fluxant in influencing slag behavior. It was also used to determine realistic input parameters for initial, intermediate and final states of six dynamic cases: (1) removal of fluxant, (2) load following, (3) feed switching, (4) coal-petroleum coke co-firing, (5) coal-biomass co-firing, and (6) gasifier cold start. Dynamic ROM simulation was used to determine the response of the gasifier-syngas cooler system to these dynamic situations. Results show that slag and wall temperature profiles, and slag behavior profiles take the longest times to reach equilibrium. Gas temperatures, syngas composition and syngas production (measured in MW_{th}) equilibrate with very little time lag. The next chapter discusses the results of ROM validation, sensitivity analysis, and steady-state and dynamic simulation in the context of

broad themes and trends observed, and presents proposals for future ROM application.

4.6 References

1. Holt N. IGCC & Gasification for a Changing marketplace. Gasification Technologies Council [GTC]: Gasification Technologies Conference; 2006 Oct.; Washington (DC).
2. Atwell M. "GE and Bechtel Alliance IGCC Reference Plant Update". Gasification Technologies Council [GTC]: Gasification Technologies Conference; 2007 Oct.; San Francisco (CA).
3. White K. GE's Carbon Island. Gasification Technologies Council [GTC]: Gasification Technologies Conference; 2008 Oct.; Washington (DC).
4. National Energy Technology Laboratory [NETL]. Cost and Performance Baseline for Fossil Energy Plants: Volume 1: Bituminous Coal and Natural Gas to Electricity. Revision 1 2007. DOE/NETL-2007/1281
5. Gasification High Performance Refractories Saint-Gobain - [homepage on the Internet]. n.d. [cited 2009 Oct 19]. Available from: http://www.refractories.saint-gobain.com/Gasification.aspx
6. The Babcock and Wilcox Company [B&W]. Steam: its generation and use: Edition 41, 2005. B&W, Barberton (OH).
7. Kajitani S, Hara S, Matsuda H. Gasification rate analysis of coal char with a pressurized drop tube furnace, Fuel 2002; 81: 539-546.
8. Watanabe H, Otaka M. Numerical simulation of coal gasification in entrained flow coal gasifier, Fuel 2006; 85: 1935-1943.
9. Leppalahti J, Koljonen T. Nitrogen evolution from coal, peat and wood gasification: Literature review, Fuel Processing Technology 1995; 43: 1-45.
10. Urbain G, Cambier F, Deletter M, Anseau M R. Viscosity of Silicate Melts, Transactions of the Journal of the British Ceramics Society 1981; 80: 139.
11. Vargas S, Frandsen F J, Dam-Johansen K. Rheological properties of high-temperature melts of coal ashes and other silicates, Progress in Energy and Combustion Science 2001; 27: 237-429.
12. McCollor D P, Zygarlicke C J, Allan S E, Benson S A. Ash Deposit Initiation in a Simulated Fouling Regime, Energy & Fuels 1993; 7: 761-767.
13. Nowok J W. Viscosity and Phase Transformation in Coal Ash Slags near and Below the Temperature of Critical Viscosity, Energy & Fuels 1994; 8: 1324-1336.
14. Linak W P, Wendt J O L. Trace metal transformation mechanisms during coal combustion, Fuel Processing Technology 1994; 39: 173-198.
15. Senior C L, Zeng T, Che J, Ames M R, Sarofim A F, Olmez I, Huggins F E, Shah N, Huffman G P, Kolker A, Mroczkowski S, Palmer C, Finkelman R. Distribution of trace elements in selected pulverized coals as a function of particle size and density, Fuel Processing Technology 2000; 63: 215-241.
16. Cho S-H, Yoo J-I, Turley A T, Miller C A, Linak W P, Wendt J O L, Huggins F E, Gilmour M I. Relationships between composition and pulmonary toxicity of prototype particles from coal combustion and pyrolysis, Proceedings of the Combustion Institute 2009; 32: 2717-2725.
17. Song W, Tang L, Zhu X, Wu Y, Rong Y, Zhu Z, Koyama S. Fusibility and flow properties of coal ash and slag, Fuel 2009 ; 88 : 297-304.
18. Email communication between the author and Mr. Jerry Schlather, Senior Development Associate, Eastman Chemical Company, Kingsport (TN).

19. Sanderson D K, Germane G J. Composition of Combustion Gases and Particles in a Pulverized Coal-Fired Reactor, Energy & Fuels 1993; 7: 910-918.
20. Theis M, Skrifvars B-J, Zevenhoven M, Hupa M, Tran H. Fouling tendency of ash resulting from burning mixtures of biofuels. Part 2: Deposit chemistry, Fuel 2006; 85: 1992-2001.
21. Alvarez-Rodriguez R, Clemente-Jul C, Martin-Rubi J A. Behavior of the elements introduced with the fuels in their distribution and immobilization between the coal-petroleum coke IGCC solid products, Fuel 2007; 86: 2081-2089.
22. Nakano J, Sridhar S, Moss T, Bennett J, Kwong K-S. Crystallization of Synthetic Coal-Petcoke Slag Mixtures Simulating Those Encountered in Entrained Bed Slagging Gasifiers, Energy & Fuels 2009; 23: 4723-4733.
23. Korshunov V S, Bas'yas I P. Determining the maximum possible heating rates of single sided heating of Refractories, Translated from Ogneupory ("Refractories" in Russian) 1971; 4: 51-55.
24. Skinner C. Hydrogen Energy California – Project Update. Gasification Technologies Council [GTC]: Gasification Technologies Conference; 2009 Oct.; Colorado Springs (CO).
25. United States Department of Energy [U.S. DOE]. Gasification Technologies: Gasification Markets and Technologies – Present and Future – An Industry Perspective 2002 July. DOE/FE-0447
26. Bennett J. Field test Results, Phosphate-Modified High Chrome Oxide Refractory for Slagging Gasifiers. Gasification Technologies Council [GTC]: Gasification Technologies Conference; 2007 Oct.; San Francisco (CA).

271

Chapter 5 DISCUSSION OF RESULTS

5.1 Chapter Overview

This chapter presents discussion of the broader trends and themes seen in the results of ROM validation, sensitivity analysis, and steady-state and dynamic gasifier simulation. Specific ROM results, trends and observations are discussed in the context of the reactor network model, particle conversion processes, heat transfer, pollutant formation, slagging behavior and dynamic simulation. Overall ROM accuracy, flexibility, and current and future applicability are also discussed.

5.2 Reactor Network Model

The role of the reactor network model (RNM) in the ROM is to simplify the resolution of the fluid flow field within the gasifier. A properly-defined RNM allows efficient, flexible simulation to an acceptable degree of accuracy. The RNM consists of the components shown Figure 5-1. As previously stated, RNM geometry is determined by the values of five user-defined parameters: IRZ diameter (d_{IRZ}), IRZ length (L_{IRZ}), jet expansion angle (θ), recirculation ratio (α), and the fraction of flow leaving the ERZ to directly enter the JEZ (f_{JEZ}). The values of these parameters for a given gasifier design and operating regime are ideally established through CFD-based simulation of the same system. This is the approach taken by Pedersen et al [2, 3] in developing the original RNM on which the RNM presented here is based.
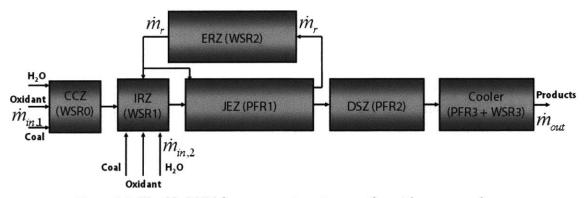

Figure 5-1: Flexible RNM for a one- or two-stage gasifier with syngas cooling

Since CFD simulation results of the gasifier designs under consideration in this work are not available at time of writing, different approaches are taken in estimating RNM parameters. These approaches are described below for each of the parameters in question. In all cases, the methods and parameter values described below will be superseded by values established through detailed CFD-based simulation. The values presented below and used throughout this work may be thought of as temporary in nature.

For axially-fired designs that employ a sudden expansion at the inlet, the diameter of the IRZ (d_{IRZ}) is set equal to the quarl diameter (d_{quarl}), if it is known. This is the approach taken by Pedersen et al. For the BYU gasifier, $d_{quarl} = 0.1$ m, as shown in Figure 3-45. The quarl diameter of the GE gasifier is not known and so is assumed to have a value of 0.5 m. Therefore, $d_{IRZ} = 0.5$ m for the GE gasifier. In the case of gasifiers that do not employ a sudden expansion, such as the CSIRO design, IRZ diameter is equal to gasifier diameter ($d_{IRZ} = d_{gasifier} = 0.07$ m). The same is true of two-stage gasifier designs, such as MHI. Recall that for two-stage gasifiers; the first-stage combustor is modeled using the CCZ (coal combustion zone). Gas and particle flow from the first-stage is assumed to mix with second-stage reactants in the IRZ. So for the MHI, $d_{IRZ} = d_{gasifier} = 0.24$ m. In all designs, the length of the IRZ (L_{IRZ}) is assumed to be equal to its diameter (d_{IRZ}). Again, this is the method proposed by Pedersen et al. and is acknowledged as likely being too simplistic a representation for a wide range of gasifier designs.

The value of the jet expansion angle (θ) chosen for the RNM depends on how d_{IRZ} is evaluated. For designs that do not employ a sudden expansion at the inlet or have two stages, where $d_{IRZ} = d_{gasifier}$, it is apparent that the JEZ cannot expand any further. Otherwise it would expand beyond the walls of the gasifier. Therefore, when $d_{IRZ} = d_{gasifier}$, $\theta = 0°$. This is the case for the MHI and CSIRO designs. For designs that employ a sudden expansion at the inlet, such as the BYU and GE gasifiers, a jet expansion angle of 9.7° is chosen. This is the maximum expansion angle of a turbulent free jet as observed by Pedersen. We acknowledge that this is a very crude method of evaluating jet expansion angle, but in the current absence of information from more detailed CFD-based modeling, this is the method used.

Similarly to jet expansion angle, recirculation ratio (α) is evaluated depending on whether the gasifier in question employs a sudden expansion at the inlet. When no sudden expansion is present or when the gasifier has two stages, such as the MHI and CSIRO designs, recirculation ratio is set to zero. This is because in these cases, the IRZ and JEZ are modeled as cylinders of diameter $d_{IRZ} = d_{JEZ} = d_{gasifier}$. In this configuration, the volume of the ERZ is zero and therefore there is no flow through it. For designs that employ a sudden expansion, such as the BYU and GE designs, $d_{IRZ} < d_{gasifier}$, $\theta = 9.7°$ and therefore $\alpha > 0$. For such cases, α is again evaluated in the same manner as it is in the work of Pedersen. This involves the use of the Thring and Newby method, which states that $\alpha = 0.47(d_{gasifier}/d_c) - 0.5$. In this expression, d_c is the characteristic diameter of the burner and is chosen as $d_c = d_{quarl}$. This expression results in recirculation ratios for the BYU and GE designs of 0.44 and 1.54, respectively.

The method of solution for the final RNM parameter, the fraction of flow leaving the ERZ and flowing directly to the JEZ (f_{JEZ}), is not specified by Pedersen. For designs in which the ERZ is not considered, such as the MHI and CSIRO gasifiers, the value of f_{JEZ} is unimportant since flow entering and leaving the ERZ is zero. For designs in which recirculation ratio is greater than zero, such as the BYU and GE designs, the base case value chosen for f_{JEZ} is zero. Use of non-zero values for f_{JEZ} is explored using sensitivity analysis.

From the discussion above, it is apparent that the structure of the RNM is of major importance to the BYU and GE gasifier designs, as recirculation is likely to be present in the respective fluid flow fields. Therefore all parameters of the RNM must be evaluated in order to accurately model the flow in these gasifiers in a reduced manner. By contrast, the flow fields for the CSIRO gasifier and for the second stage of the MHI gasifier can be reasonably expected to resemble one-dimensional plug flow. This is one possible explanation for the fact that the ROM predicts profiles of temperature, carbon conversion and gas composition with greater accuracy for the MHI and CSIRO gasifiers than for the BYU gasifier. With better understanding of the RNM for the BYU designs, the higher-than-expected temperatures predicted by the ROM, shown in Figure 5-5, may be avoided. Examples of profiles predicted by the ROM for MHI, CSIRO and BYU gasifiers are

shown below in Figure 5-2 to Figure 5-4. Figure 5-2 and Figure 5-3 show close agreement of ROM predictions with experimental results and computer-based modeling performed by others for the MHI and CSIRO gasifiers. Figure 5-4 shows that the ROM predicts the trend of experimentally-recorded gas composition data, but not the exact values.

Recall that the temperature spike (line d-e) seen in the ROM-predicted MHI profiles in Figure 5-2 is due to the fact that no reactions are allowed in the IRZ (seen as the region c-d). Refer to Section 2.6.2 for the full explanation of why this is the case. Since some oxidant is introduced at the second stage injectors and is not allowed to react in the IRZ, it rapidly reacts with volatiles as soon as it reaches the JEZ causing the temperature spike at d-e. As shown in Figure 3-20, decreasing the length of the IRZ decreased the length of line c-d. As IRZ length approaches zero, the ROM-predicted temperature profiles closely match those of the CFD-predicted profiles in the region of the second-stage injectors.

In addition to inaccuracies in the RNM structure, potential reasons for errors seen in the BYU profile predictions in Figure 5-4 include unsuitability of the radiation submodel at the operating conditions encountered in the BYU gasifier, the higher-than-usual volatile matter fraction of the feedstock, the lack of kinetic parameters for the feedstock in question and the fact that only one set of experimental data is available, which could conceivably be flawed in some way. These points are discussed in the sections that follow.

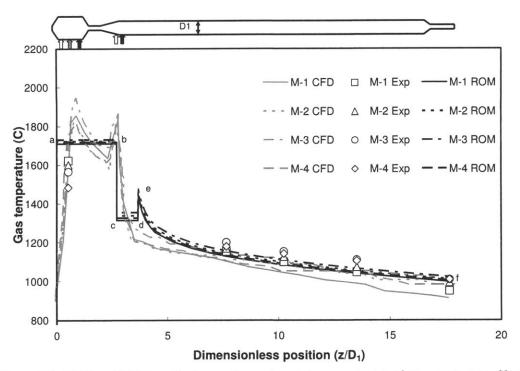Figure 5-2: ROM and CFD predictions and experimental measurement of temperature profiles for Coal M in MHI gasifier
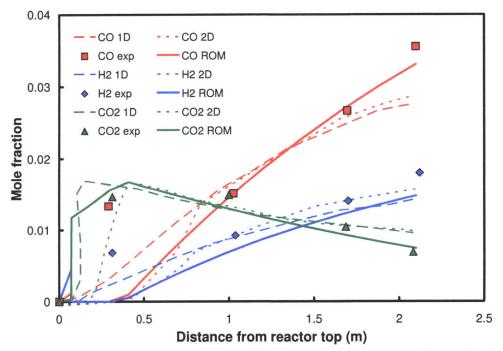

Figure 5-3: ROM prediction and experimental measurement of gas composition profiles for test CRC252 in CSIRO gasifier
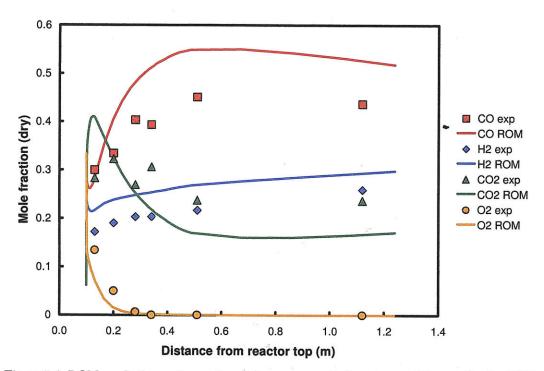
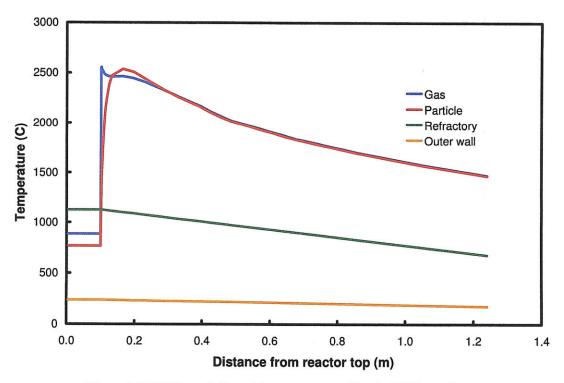Figure 5-4: ROM prediction and experimental measurement of gas composition profiles for BYU gasifier

Figure 5-5: ROM prediction of temperature profiles for BYU gasifier

278

5.3 Particle Conversion Processes

As described in Chapters 1 and 2, particles entering the gasifier first experience rapid heating rates (10^5-10^6 K/s), which leads to drying and devolatilization. These are extremely fast processes, which are usually concluded by the time heterogeneous char reactions begin. Because of extremely high temperatures caused by oxidation (see line a-b in Figure 5-2) and vigorous mixing encountered in the first-stage (combustor) of two-stage gasifiers, all particle conversion processes are assumed to be complete by the time particles leave the CCZ and enter the IRZ. This means that particles leaving the CCZ (first stage) are fully-dried, fully devolatilized, and have undergone char oxidation to as great an extent as CCZ stoichiometry allows. Note that these conditions apply only to the first stage of the MHI gasifier.

For the MHI second stage, and all other gasifiers considered in this work, particle conversion is modeled in a much more detailed and complex manner. The ROM models raw coal particles entering the IRZ as undergoing immediate drying and devolatilization; similar to the MHI first stage. Char conversion reactions, however, are modeled using finite-rate global chemistry, as described in the section on heterogeneous reactions (Section 2.5.4.2). The overall rates of the heterogeneous char reactions, and especially those of the gasification reactions ($C+H_2O$ and $C+CO_2$), are important factors in determining overall reactor size. The plug flow reactors, JEZ and DSZ, that make up the bulk of volume of the RNM allow char conversion via three or four heterogeneous reactions; partial oxidation ($C+\frac{1}{2}O_2$), hydro-gasification ($C+H_2O$), Boudouard reaction ($C+CO_2$), and in some cases methanation ($C+2H_2$). The three latter reactions are known collectively as the gasification reactions. Under entrained flow gasifier conditions, the rate of methanation is typically 1-2 orders of magnitude lower than those of the other gasification reactions. Therefore in virtually all kinetic schemes encountered in the literature, $C+2H_2$ is neglected.

For the systems simulated in this work, heterogeneous kinetic parameters were obtained for the MHI and CSIRO feedstocks only. These expressions were obtained from Kajitani [1] and Hla [7], respectively. For simulation of the BYU and GE systems, Kajitani's expressions were used in the absence of any other data. The parameters provided by Kajitani are extrinsic in nature, meaning that particle

reaction rates are defined per unit mass of particle, leading to rates with units of kg/kg/s or 1/s. Such extrinsic methods do not track particle surface area or consider film diffusion and particle reaction separately. In effect, they lump all heterogeneous-reaction-related phenomena together in one highly-empirical expression. They require less detailed information about the particle compared to intrinsic expressions, but are usually applicable over a smaller range of temperatures, pressures and particle sizes. The parameters for Kajitani's extrinsic expressions are shown in Table 3-5. On the other hand, the expressions given by Hla are intrinsic and therefore track particle surface area evolution. They are applicable only when information on particle structure is available. For this reason, these intrinsic expressions are applied only for the CSIRO validation work. The parameters for Hla's intrinsic expressions are shown in Table 3-9. Note that both Kajitani's and Hla's expressions were developed for gasification at 20 bar (2 MPa).

Figure 5-6, Figure 5-7 and Figure 5-8 show predicted extrinsic reaction rate profiles for the second stage of the MHI gasifier, the BYU gasifier and the GE pilot-scale gasifier, respectively. The general observations for the plots are similar and are listed below:

- If O_2 is present near the injectors, char oxidation has the fastest reaction rate until O_2 is consumed.

- For each gasifier design, the rate of $C+H_2O$ remains consistently 5-10 times greater than that of $C+CO_2$. This stands to reason as the kinetic expressions used to create the three profile plots are the same. However, the gas compositions present in each design are different.

- The rate of $C+O_2$ for the BYU gasifier does not fall as rapidly as it does for the other designs (see Figure 5-7). A possible explanation for this is that the BYU gasifier operates at atmospheric pressure while the others are at 20 bar (MHI) and 42 bar (GE). Recall that the expressions were developed for use at 20 bar.

- The respective rates of all reactions decrease along the lengths of the respective gasifiers due to decreasing gas and particle temperatures. Temperature decreases are caused by heat loss to the walls and by the endothermic gasification reactions.
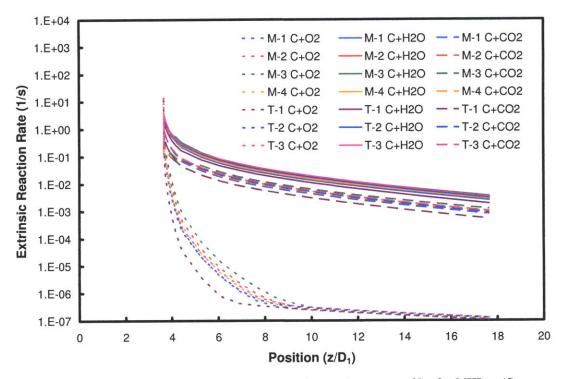
Figure 5-6: ROM-predicted heterogeneous extrinsic reaction rate profiles for MHI gasifier
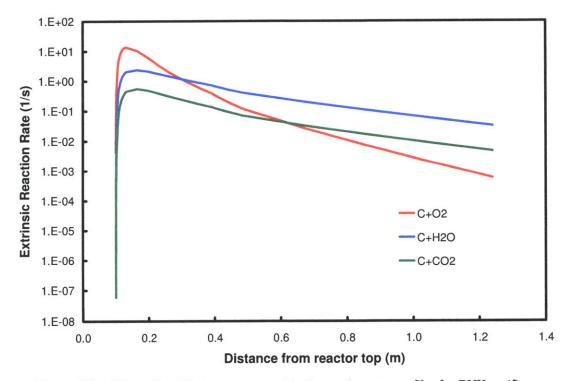
Figure 5-7: ROM-predicted heterogeneous extrinsic reaction rate profiles for BYU gasifier
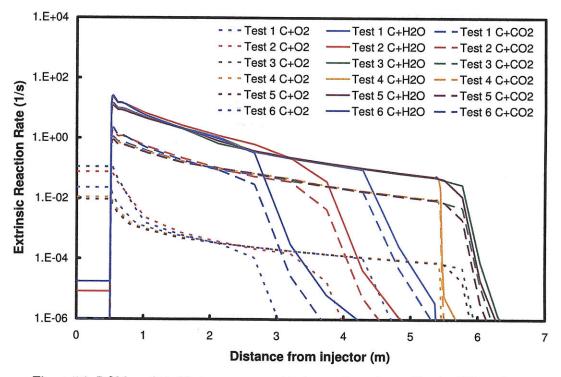
Figure 5-8: ROM-predicted heterogeneous extrinsic reaction rate profiles for GE gasifier

The sudden drops in reaction rates seen in Figure 5-8 are due to the fact that full particle conversion is achieved in simulation of the GE gasifier. As mentioned above, due to the extrinsic nature of the Kajitani expressions, it is not possible to visualize particle surface area and intrinsic reaction rates. Furthermore, due to the lumped nature of the expressions, the controlling processes for each reaction (diffusion or kinetics) are not discernable. As explained below, these are not problems for the CSIRO results.

Figure 5-9 to Figure 5-12 show ROM predictions for particle surface area evolution, intrinsic reaction rates and resistivities due to the film diffusion and pore reaction-diffusion components of heterogeneous reactions. The surface area increases observed in Figure 5-9 are due to particle pore growth during reaction, as modeled by the random pore model (RPM). Subsequent surface area decrease is due to pore coalescence at high particle conversions. Figure 5-10 shows the intrinsic rates of reactions that occur on the surface areas shown in Figure 5-9. Most of the same trends in reaction rates are seen as those observed in Figure 5-6 to Figure 5-8 above; namely that char oxidation rates decrease rapidly once O_2 is consumed, and

that C+H$_2$O reaction rates are consistently greater than those for C+CO$_2$. The rise in reaction rates for coals CRC274 and CRC252 seen in Figure 5-10 is caused by the opening-up of particle pore structure at high conversions, as evidenced by increased effectiveness factors for these coals seen in Figure 3-39.

Figure 5-11 and Figure 5-12 show that while the oxidation reaction is film-diffusion-limited, both gasification reactions are limited by pore diffusion-reaction. High temperatures and high levels of carbon conversion act to reduce resistivity due to pore diffusion-reaction. Resistivities to film diffusion are always in the range 2-4 s/m for all coal types considered, while those for pore diffusion-reaction vary greatly. This is partly due to the fact that while the effectiveness factor method allows one to separate film diffusion from diffusion and reaction within the particle pores, it does not distinguish between these intraparticle phenomena.
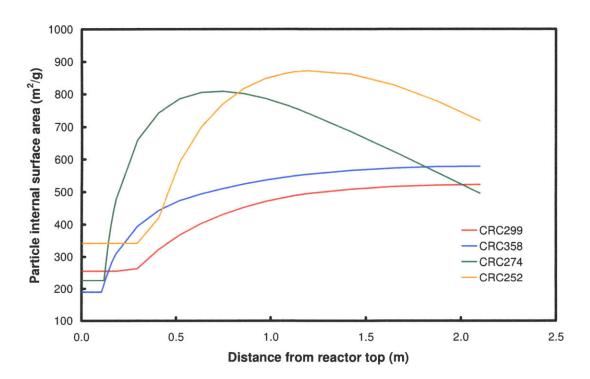
Figure 5-9: ROM-predicted particle internal surface area profiles for CSIRO gasifier

283
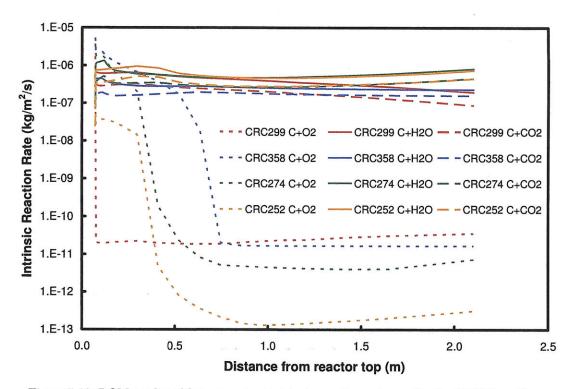
Figure 5-10: ROM-predicted heterogeneous intrinsic reaction rate profiles for CSIRO gasifier
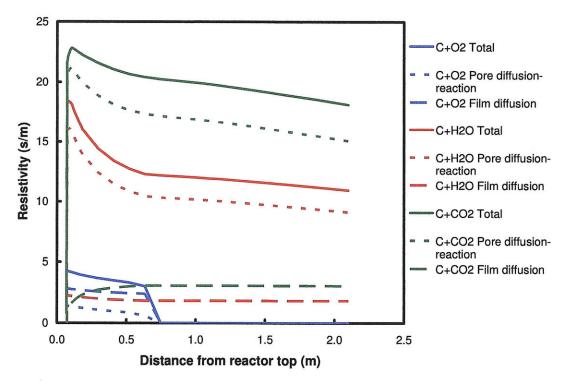
Figure 5-11: ROM-predicted resistivities of film diffusion and pore diffusion-reaction for CSIRO test CRC358
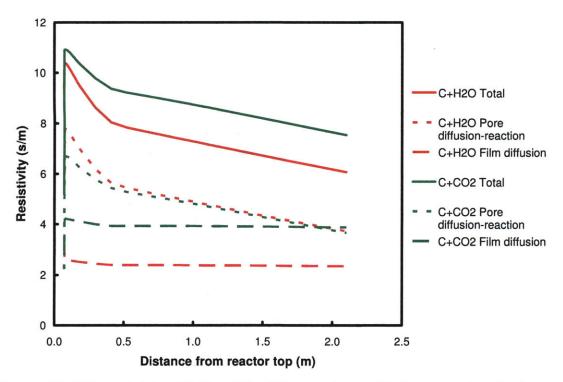
Figure 5-12: ROM-predicted resistivities of film diffusion and pore diffusion-reaction for CSIRO test CRC252

Despite the wealth of information and insight provided by the ROM into char conversion processes, improvements can be made, particularly in the devolatilization submodel. The ROM uses the devolatilization submodel developed by Merrick [8]. This submodel is introduced in Section 2.5.3 and uses the global devolatilization reaction shown below.

$$
\begin{aligned}
C_a H_b O_c N_d S_e \, (\text{daf coal}) \xrightarrow{\;dev\;} &\alpha CO + \beta CO_2 + \chi H_2 + \delta H_2 O + \varepsilon CH_4 + \phi C_2 H_6 \\
&+ \gamma NH_3 + \eta H_2 S + \iota \left(C_n H_o O_p N_q S_r \right)(\text{tar}) \\
&+ \varphi \left(C_i H_j O_k N_l S_m \right)(\text{char})
\end{aligned}
\qquad (\text{Eq. 5-1})
$$

The submodel employs the mass balance shown in Figure 2-5 to determine the mass fractions of the volatile species released. Use of this submodel with the ROM has revealed two potential flaws: (1) HCN (hydrogen cyanide) is not considered in the volatile mass balance, and (2) the assumption of instantaneous devolatilization

285

rate may lead to inaccuracies for high-volatile feedstocks. These two points are addressed in further detail below.

The validation and sensitivity analysis performed for the BYU gasifier in Section 3.6 indicates that HCN should be included as a volatile gas-phase specie. Since the devolatilization model does not allow the release of HCN, the ROM includes a user-defined parameter f_N, which is defined as the mass fraction of devolatilized nitrogen that appears as HCN, as opposed to NH_3. For the conditions encountered in the BYU gasifier, a value of $f_N = 0.3$ was found to adequately reproduce NO and HCN emissions, but not NH_3 emissions. Use of a more accurate devolatilization submodel, which is more predictive of devolatilized NH_3 and HCN mass fractions, could improve ROM pollutant profiles.

Inclusion of rate of volatiles release as part of the devolatilization submodel could also benefit ROM accuracy in predicting BYU gasifier performance. Under normal entrained flow gasifier conditions, at pressures of 20-60 bar, devolatilization occurs extremely rapidly and the assumption of instantaneous appearance of volatiles in the IRZ is valid. However as pressure decreases to that employed in the BYU design (1 bar), this assumption may not be valid. Instantaneous devolatilization in the BYU gasifier, which is immediately followed by volatiles oxidation, could contribute to the extremely high temperature spike predicted in Figure 5-5.

5.4 Heat Transfer

Through sensitivity analysis performed in Chapter 3, heat transfer to, from and through the gasifier walls has been identified as some of the most important processes governing ROM accuracy for all gasifier designs. Temperature boundary conditions, which have been ignored by many previous entrained flow gasifier modeling efforts, are very important to ROM accuracy. At the most basic level, the characteristics of the gasifier wall, such as number of layers, their density, heat capacity, conductivity, thickness, etc., must be established and accurately represented. If wall heating (e.g. CSIRO) or cooling (e.g. BYU) are employed the effects of these on the gasifier wall must be modeled.

Heat transfer inside the gasifier requires knowledge of the radiative properties of the gas-particle flow and of the walls. The heat transfer submodel, described in

286

Section 2.5.6, employs the radiation-as-diffusion (RAD) approximation to model the radiative properties of the particle cloud. For gasifiers in which particle loading is sufficiently high and dimensions are sufficiently large such that the particle cloud can be considered optically thick, the RAD approximation is valid. In such systems, gas-phase radiation is neglected, so that the situation is simplified further. The criterion for the use of the RAD approximation is that KB > 3, where K is the absorption coefficient of the cloud and B is the characteristic dimension of the gasifier [9]. These terms and those for particle cloud emissivity (ε_p) are defined below.

$$K = \pi r_p^2 N_p \qquad \text{(Eq. 5-2)}$$

where

r_p =Particle radius (m)

N_p =Particle number density ($1/m^3$)

$$B = d_{gasifier} = \text{Gasifier diameter (m)} \qquad \text{(Eq. 5-3)}$$

$$\varepsilon_p = 1 - \exp(-KB) \qquad \text{(Eq. 5-4)}$$

The criterion KB > 3 is satisfied at all points inside the GE and MHI gasifiers. This is not the case for the CSIRO gasifier, which has a very narrow diameter and low particle loading, and for the BYU gasifier, which has low particle loading because of its low operating pressure. This introduces errors into the heat transfer calculations, which are suspected to be one of the major causes of the higher-than-expected temperatures predicted near the inlet of the BYU gasifier, seen in Figure 5-5. Errors in temperature prediction for the CSIRO design are not as obvious as the walls are held uniform at 1400 °C. At low particle loading, gas-phase radiation is expected to be of greater relative importance. This means that if the ROM is required to predict wall heat flux at low pressures and low particle loading, radiation for a dispersed particle cloud as well as a gas-phase radiation must be included. No current or future commercial gasification technologies operate or plan to operate under these conditions, so for the purpose of simulating pilot- and commercial-scale gasifiers, the current radiation submodel is adequate.

5.5 Slagging Behavior

Full slagging behavior has been simulated for pilot- and full-scale GE gasifiers only. The reason this has not been done for the lab-scale designs is that it is not clear from the literature how these designs deal with slag. Aspects of slagging operation, such as whether slag is allowed to reach steady-state thickness or if the gasifier is operated for long enough for this happen, are unknown. Therefore, simulations of lab-scale gasifiers simply assume uniform slag layer thickness of 1 mm.

Sensitivity analysis of the GE pilot-scale gasifier shows that slag disposition is one of the most important factors affecting simulation results. Refer to Figure 3-75, Figure 3-76 and Table 3-17 for emphasis of this point. Slagging plays two important roles: (1) particles transfer enthalpy to the gasifier walls, and (2) slag provides thermal insulation at the walls. It is therefore crucial to ROM accuracy that the mechanism and flux by which particles migrate to walls and become trapped in the slag layer are adequately represented. Particle migration to walls is governed by the turbulent flow field in the gasifier [10]. Since the ROM is by design incapable of predicting the turbulent flow field, estimates of particle flux to walls should come from the results of detailed CFD-based simulations. In a manner similar to that used to obtain RNM parameters, CFD-based simulations of identical systems should be used to provide estimates of particle flux to walls as a function of axial position ($\dot{m}'_{slagging}$ (kg/m/s) or $\dot{m}''_{slagging}$ (kg/m^2/s)). These flux terms can easily be incorporated into the ROM as it is currently configured.

Once particles reach the wall, the ROM employs a single-layer slag submodel, which is described in Section 2.5.8. One of the most important physical properties of slag is its viscosity, which is modeled in the ROM using the temperature- and ash-composition-dependent model developed by Urbain [11, 12]. Figure 5-13 shows ROM predictions of the effect of fluxant addition on slag viscosity and temperature in a full-scale GE gasifier. The predicted temperature-viscosity behavior seen in Figure 5-13 has been used to select fluxant flow rates that ensure sufficiently low viscosity for slag removal. The ROM predicts that a full-scale GE gasifier, which gasifies 113586 kg/hr (2700 metric tonnes per day) of coal, requires 2512 kg/hr of fluxant to ensure slag exit viscosity of 14-15 Pa.s (140-150 poise). For a typical Illinois No. 6 bituminous coal, this means that the slag flowing along the gasifier walls has a CaO (calcium oxide) mass fraction of 25% (see the 25% CaO profile in

Figure 5-13). The ROM is the first entrained flow gasifier model, reduced order or detailed, to consider the role that fluxant plays in (1) achieving realistic slag exit viscosity, and (2) affecting the overall heat balance of the gasifier. Note that Figure 5-13 shows slight increase in temperature with increasing fluxant (CaO) loading. The role of slagging in dynamic gasifier operation is included for discussion in the next section.
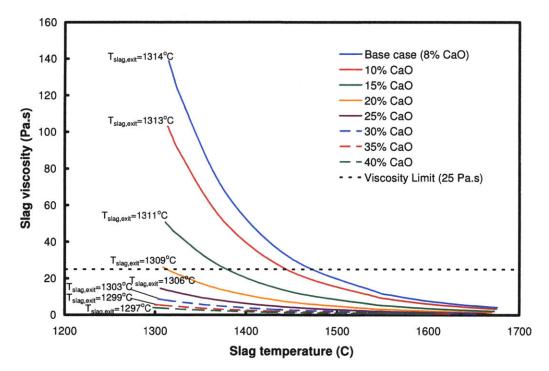
Figure 5-13: ROM-predicted effect of fluxant on slag temperature-viscosity profile for full-scale GE gasifier

5.6 Dynamic Simulation

One of the most valuable attributes of the ROM is its ability to predict dynamic performance of the gasifier. To the author's knowledge, it is the first validated gasifier simulator to have dynamic capability. Six cases of dynamic gasifier operation have been simulated by the ROM. They are: (1) removal of fluxant, (2) load following, (3) feed switching, (4) coal-petroleum coke co-firing, (5) coal-biomass co-firing, and (6) gasifier cold start. Cases 1-5 involve a dynamic change occurring in a linear fashion over the course of one hour of gasifier operation time. The system is then allowed to approach a final steady-state operating condition over eight hours. The gasifier cold start procedure was explained to the author

289

during a visit to the Eastman Chemical plant in Kingsport, Tennessee, which employs two GE gasifiers. Cold start simulation involves three dynamic stages: natural gas preheat of refractory walls from atmospheric temperature to above coal auto-ignition temperature, switch from natural gas-air streams to coal-water slurry-oxygen (CWS-O_2) streams, and system pressurization from atmospheric pressure to full operating pressure.

There is unfortunately no publically-available data with which to validate the dynamic aspects of the model, but the rigorous manner in which the ROM has been constructed hopefully minimizes the errors associated with dynamic simulation. The most important system properties for dynamic simulation are the total heat capacities (mc) for each of the components that make up the gasifier. The heat capacity of each gasifier and syngas cooler component contributes to the value of the internal energy accumulation terms of the energy conservation equations shown in Table 2-2. The mass of each component in the system can be determined from $m = \rho V$. Since densities and heat capacities are generally temperature-dependent, they are evaluated at each component's mean temperature. These components and their volume, density, mass, and specific and total heat capacity values are shown in Table 5-1 below for steady-state base case operation of a full-scale (2700 tpd) GE gasifier.

It is apparent that the largest heat capacities in the gasifier and syngas cooler system are associated with the wall layers (refractory, insulating brick and steel walls) and cooling water (RSC coolant and quench water). Therefore, if the characteristics of these components are well-defined, errors in the dynamic aspects of ROM simulation should be minimized. Geometry, including thicknesses, lengths, volumes and densities of wall layers in the gasifier are known through the methods described in Section 3.7.1. RSC coolant and quench water temperatures, pressures and flow rates are known from the NETL report on the GE-Bechtel Reference Plant, as described in Section 4.2. This means that the geometry of the RSC wall layers, which is largely unknown, is the major source of uncertainty for dynamic simulation. None of the dynamic simulations performed in this work, however, involve major changes to RSC coolant properties. Therefore, for the current set of dynamic simulations, it is likely that uncertainties about RSC geometry do not affect overall solution accuracy.

Table 5-1: Total heat capacities of gasifier and syngas cooler components

Component	Volume	Density	Mass	Average specific heat capacity	Total heat capacity
	m³	kg/m³	kg	kJ/kgK	kJ/K
Gasifier					
Gas	~48.9	~8.5	~416	~1.6	~665
Particles	~0.031	~170	~5.30	~1.5	~7.95
Slag layer	0.219	2700	592	1.5	888
Refractory (firebrick)	47.2	4200	198408	0.9	178567
Insulating brick	22.2	1600	35526	0.9	31973
Steel wall	6.77	7800	52781	0.45	23752
Radiant syngas cooler					
Gas	~236	~10.7	~2519	~1.5	~3778
Particles	~0.150	~160	~24.0	~1.37	~32.9
Slag layer	1.06	2700	2849	1.37	3904
Refractory (firebrick)	195	4200	818598	0.9	736738
Insulating brick	94.5	1600	151158	0.9	136042
Coolant	13.9	570	7951	4.2	33393
Steel wall	28.6	7800	223236	0.45	100465
Quench cooler					
Quench water	6.28	777	4882	4.2	20505
Steel wall	1.63	7800	12703	0.45	5716

Of the dynamic cases simulated, Case 6: Gasifier Cold Start presents the greatest challenge to the ROM. This is because of the range of temperatures (25 to 1700 °C), pressures (1 to 56 bar), gas compositions (ambient air to syngas), and particle flow rates (0 to 113586 kg/hr) encountered during simulation. For these reasons, which are described in more detail in Section 4.4.6, the radiation and slagging submodels have been modified for use at the low particle concentrations found in the early stages of gasifier cold start. As shown by Figure 4-36, at all times during gasifier cold start, maximum refractory heating rates are not allowed to exceed 10 °C/min, which has been found to be the maximum allowable for chromium-oxide-based bricks [13]. The time the ROM predicts for the system to reach a final steady-state operating condition is about 50-60 hours. This agrees qualitatively with the reported time for gasifier cold start at the Eastman Chemical facility at Kingsport, Tennessee.

For all of the dynamic cases, wall layer temperatures and slag behavior indicators take the longest times to reach steady-state. This is explained by the fact that, as shown in Table 5-1, wall layers possess the largest heat capacities in the simulated system. Therefore, these components have the longest thermal response times. Since slag layers are in good thermal communication with refractory, via direct conduction, slag temperatures also have long response times. This affects slag

viscosity, in turn affecting other slag properties, such as slag thickness, which affects thermal resistance provided by the slag. This emphasizes the highly-coupled nature of heat transfer at the walls of slagging gasifiers.

Note that dynamic simulations took in the range of 15-45 minutes on a desktop personal computer, with the exception of the gasifier cold start case (Case 6), which took about 6 hours. These simulation times have not been compared to CFD simulations as the author is unaware of any attempt to simulate the dynamic performance of similar systems using CFD-based computer models.

5.7 Overall ROM Performance

In general, ROM performance may be viewed as satisfactory. Despite potential inaccuracies in current reactor network model (RNM) parameters, and submodels for devolatilization, radiation, pollutant formation and particle-to-wall migration, the ROM has shown itself able to adequately simulate gasifier performance for the wide ranges of gasifier characteristics identified in Section 1.6. These and other characteristics and their ranges are identified below.

- Feedstock throughput: 0.1 tpd for the CSIRO gasifier to 2700 tpd for the full-scale GE gasifier.

- Heterogeneous kinetic data: intrinsic parameters for the CSIRO gasifier, extrinsic parameters for the other designs.

- Flow direction: up-flow for the MHI gasifier, down-flow for the other designs.

- Feedstock delivery: slurry-feed for the GE gasifier, dry-feed for the other designs.

- Injector configuration: opposed/radial for the MHI gasifier, axial for the other designs.

- Oxidant: oxygen-blown for the BYU and GE gasifiers, air-blown for the MHI and CSIRO gasifiers.

- Number of stages: Two stages for the MHI gasifier, one stage for the other designs.

- Wall lining: Membrane-lined combustor and refractory-lined reductor for the MHI gasifier, electrically-heated walls for the CSIRO gasifier, refractory-lined and water-cooled walls for the BYU gasifier, and refractory-lined walls for the GE gasifier.

- Syngas cooling method: Radiant-only, quench-only or radiant-and-quench for the GE gasifier, no cooling for the other designs.

The ROM is the first gasifier model to display such flexibility in the types of systems it can simulate. This is made possible through the use of a simple and flexible one- or two-stage reactor network model, switches to toggle between choices of different gasifier characteristics, conservation equations based, where possible, on fundamental first principles, and highly-detailed submodels for particle properties and evolution, heterogeneous reactions, slagging, heat transfer and other phenomena. The end result is an entrained flow gasifier simulator that is accurate, flexible and computationally efficient.

The goal of rigorous validation for a range of lab-scale gasifiers is to allow the user to have confidence in the accuracy of the ROM for simulation of entrained flow gasifiers of any design. The ROM has been proven to be highly accurate when all required information for feedstock properties, gasifier geometry and operation conditions are available. For the MHI and CSIRO sets of validation data, the ROM is at least as accurate as more detailed and time-consuming CFD simulations. If and when further validation data sets become available for other gasifier designs the ROM is expected to show similar levels of accuracy.

This does not mean, however, that there is no role for CFD-based computer modeling in gasifier simulation. For gasifier designs in which internal and external recirculation is likely to be important, such as the BYU and GE designs discussed in this work, the geometry of the reactor network model is required as a set of user-defined inputs for the ROM. This is also the case for designs in which recirculation is unimportant, but the consequences for these designs are not as obvious. Also, the ROM cannot predict from first principles the flux of solid particles to the gasifier wall due to turbulence, where they may become trapped in the slag layer. Sensitivity analysis for the validation studies revealed the importance of these parameters to simulation results. The provision of values for

293

reactor network model geometry and for particle wall flux are two examples of the role CFD-based computer modeling can play in improving ROM accuracy.

One could envisage a simulation strategy whereby ROM and CFD simulations are built side-by-side for the same gasifier design. This design could be an existing gasifier, a modified design, or a completely novel gasifier. In this strategy, results from CFD simulation are used to construct the reactor network model geometry and provide estimates for particle wall flux for the ROM. The ROM is then used to efficiently and rigorously simulate the performance of a large number of potential gasifier and/or syngas cooler configurations to an acceptable degree of accuracy in a comparatively short time. The results of these ROM simulations are then used to inform decisions about how to allocate computational resources towards further CFD simulations of potentially interesting system configurations. The ROM would also be used to simulate the gasifier performance as a component of an overall IGCC or polygeneration plant. This pooling of resources would have a number of benefits, including: improvement in ROM accuracy, efficient and rigorous examination of a wide range of potential designs, and more efficient allocation of valuable resources for computationally expensive CFD simulations.

The overall goal of such a simulation strategy could be to better understand the fundamental physical and chemical processes in a current gasifier design, to study the effects of design modifications to a current design, or to gain an initial understanding of the processes at work in a completely new design. Regardless of the goal, judicious use of ROM and CFD simulations could drastically reduce the time and expense of building and instrumenting lab-scale and pilot-scale gasifiers in order to study them.

5.8 Chapter Summary

A reduced order model, based on the use of a simplified reactor network model (RNM) and highly detailed submodels for physical, chemical and dynamic processes has been satisfactorily validated for use with a wide range of entrained flow gasifier types. Sensitivity analysis has been used to identify the input parameters and variables most likely to affect ROM simulation results. The ROM is the first validated entrained flow gasifier model capable of detailed simulation of

294

such a range of designs and operating conditions. Use of an RNM significantly reduces computational expense compared to CFD-based simulations.

Action should be taken to improve the accuracy of the ROM. Steps that can increase ROM accuracy and flexibility include: interaction with CFD-based models to improve inputs for RNM geometry and particle-to-wall flux, modification or replacement of the devolatilization and pollutant formation submodels to improve pollutant species and temperature prediction, and modification of the radiation submodel to allow more accurate simulation of very small gasifiers or very low pressure systems.

The results of simulations using intrinsic heterogeneous reaction kinetics and detailed particle structural evolution show the power of the ROM in providing invaluable insights into the processes of importance to char conversion and syngas production. This emphasizes the importance of research currently underway at CCSD in Australia and CANMET in Canada to develop intrinsic reaction rate expressions for a wide range of solid feedstocks. Most of the time, such detailed information is not available, so the ROM is also able to accept lumped (extrinsic) heterogeneous rate parameters.

The ROM has been used to simulate the steady-state and dynamic performance of a full-scale gasifier and syngas cooling system for use in a 630 MW_e IGCC plant. A base case for system performance has been established, including the flow rate of fluxant required to maintain adequately low slag viscosity. This is the first publically-available simulator to show the effect of fluxant use on gasifier performance. Dynamic ROM simulation consists of six cases: (1) removal of fluxant, (2) load following, (3) feed switching, (4) coal-petroleum coke co-firing, (5) coal-biomass co-firing, and (6) gasifier cold start. To the author's knowledge, this represents the first time a validated model has been used to simulate dynamic gasifier performance. We also believe it is the first time gasifier cold start has been simulated.

The best possible use for the ROM is as part of a simulation strategy that includes detailed CFD-based analysis. Detailed simulation incorporating CFD can be used to provide the ROM with RNM and particle-to-wall flux data. The ROM can then be used to simulate a wide range of potential gasifier configurations and/or

operating conditions to reasonable degree of accuracy in a short time. A narrowed-down selection of promising system configurations, as identified by the ROM, can finally be modeled in a detailed fashion using CFD.

5.9 References

1. Kajitani S, Hara S, Matsuda H. Gasification rate analysis of coal char with a pressurized drop tube furnace, Fuel 2002; 81: 539-546.
2. Pedersen L S, Breithauptb P, Dam-Johansen K, Weber R. Residence Time Distibutions in Confined Swirling Flames, Combustion Science and Technology 1997; 127 (1): 251-273.
3. Pedersen L S, Glarborg P, Dam-Johansen K, Hepburn P W, Hesselmann G. A Chemical Engineering Model for Predicting NO Emissions and Burnout from Pulverized Coal Flames, Combustion Science and Technology 1998; 132 (1): 251-314.
4. Beer J M, Chigier N A. Combustion Aerodynamics. London (UK): Applied Science Publishers, Ltd; 1972.
5. National Energy Technology Laboratory [NETL]. Cost and Performance Baseline for Fossil Energy Plants: Volume 1: Bituminous Coal and Natural Gas to Electricity. Revision 1 2007. DOE/NETL-2007/1281
6. Electric Power Research Institute [EPRI]. Cool Water Coal Gasification Program: Final Report. EPRI GS-6806: 1990.
7. Cooperative Research Centre for Coal in Sustainable Development [CCSD]. Gasification Conversion Model - PEFR: Research Report 80 2007 Dec.
8. Merrick D. Mathematical models of the thermal decomposition of coal: 1. The evolution of volatile matter, Fuel 1983; 62: 534-539.
9. Hottel H C, Sarofim A F. Radiative Transfer. New York (NY): McGraw-Hill; 1967.
10. Barta L E, Beer J M, Sarofim A F, Teare J D. Coal Fouling Tendency Model. The Impact of Ash Deposition on Coal Fired Plants, Proc. Engineering Found. Conf.; 1993; Solihull, UK: 177-188.
11. Urbain G, Cambier F, Deletter M, Anseau M R. Viscosity of Silicate Melts, Transactions of the Journal of the British Ceramics Society 1981; 80: 139.
12. Vargas S, Frandsen F J, Dam-Johansen K. Rheological properties of high-temperature melts of coal ashes and other silicates, Progress in Energy and Combustion Science 2001; 27: 237-429.
13. Korshunov V S, Bas'yas I P. Determining the maximum possible heating rates of single sided heating of Refractories, Translated from Ogneupory ("Refractories" in Russian) 1971; 4: 51-55.

Chapter 6 CONCLUSIONS AND FUTURE WORK

6.1 Conclusions

A robust, flexible dynamic reduced order model (ROM) for simulating the performance of entrained flow gasifiers and syngas coolers has been developed in Aspen Custom Modeler. The ROM incorporates a reactor network model (RNM) that approximates the complex fluid flow in the gasifier as a series of idealized chemical reactors, which is capable of modeling the effects of mixing and recirculation within the gasifier. Submodels are employed to model properties of multiple feedstocks, physical and thermodynamic properties, drying and devolatilization, homogeneous and heterogeneous chemical reactions, fluid dynamics, heat transfer, pollutant formation, slag behavior and syngas cooling.

The ROM has been successfully validated for steady-state simulation of four different lab-scale and pilot-scale gasifiers, for which sufficient experimental and/or detailed simulation results are available. The feedstock throughputs of these gasifiers are in the range 0.1-1000 metric tonnes per day. These feedstock throughputs translate to syngas higher heating value outputs of 3 kW_{th} to 240 MW_{th}. Sensitivity analysis has been performed to identify the input and modeling parameters most important to ROM accuracy. The most important modeling parameters are found to be those that determine RNM geometry, particle physical and kinetic properties, and slagging.

The ROM has also been employed to simulate the steady-state and dynamic performance of a full-scale 2700 metric-tonne-per-day entrained flow gasifier and syngas cooler. The design chosen for full-scale simulation is the GE gasifier used in the 630 MW_e GE-Bechtel Reference IGCC Plant. Steady-state simulation establishes a base case of gasifier operation. The ROM crucially allows the user to determine slagging behavior and is extremely useful in selecting gasifier operating conditions, including fluxant flow rates. Steady-state simulation has also been used to determine realistic initial, intermediate and final states for dynamic gasifier simulation. Six dynamic cases have been examined: (1) removal of fluxant, (2) load following, (3) feed switching, (4) coal-petroleum coke co-firing, (5) coal-biomass co-firing, and (6) gasifier cold start. The ability of the ROM to simulate

gasifier performance during cold start, which involves extremely wide ranges of temperature, pressure and composition, highlights its flexibility and stability. The predicted time for gasifier cold start qualitatively agrees with industrial experience.

The ROM is the first experimentally-validated steady-state or dynamic gasifier simulation tool to incorporate the essential submodels listed above. It addresses a pressing commercial need for flexible, accurate and dynamic simulation tools that are capable of being employed over a wide range of gasifier designs and operating conditions, both existing and prospective. A potential high-impact application for the ROM is its use, along with more detailed CFD-based computer models, as part of an overall gasifier simulation strategy. CFD simulations are necessary to provide the values for essential modeling parameters in the ROM, such as RNM geometry and particle wall flux. The ROM can be used to simulate a wide range of designs and operating conditions in order to select the best candidates for more detailed CFD simulation. A further use of the ROM is the ability to simulate gasifier performance within the framework of an overall IGCC or polygeneration plant.

6.2 Future Work

The performance of the ROM can be improved primarily through increasing its accuracy and applicability. The most important step in improving ROM accuracy is to use the results of CFD simulations of the same designs to better model the structure of the reactor network model (RNM). The current work uses RNM geometry developed for similar, but not identical, coal combustion at atmospheric pressure. More accurate RNM geometry would lead to more accurate ROM results. Another important role CFD simulation can play in improving ROM accuracy is to provide estimates of particle flux to gasifier walls. The ROM cannot predict the movement of char or ash particles to the walls, where they may become trapped. This has important implications in predicting carbon conversion and slagging behavior. Specific ROM submodels that should be improved upon include those for devolatilization, pollutant formation and radiation.

Feedstock characterization is of great importance to simulation accuracy and applicability. While ultimate, proximate and ash composition analyses information are relatively easily obtained, feedstock parameters such as high-pressure kinetic

data and surface area evolution are difficult to obtain. This point is discussed frequently in this work, and must be addressed for the ROM to accurately simulate gasification of a wide range of feedstocks. Current research underway by the CCSD group in CSIRO, CANMET and others, which are referenced in Chapter 2, should be closely followed.

The issue of feedstock characterization becomes even more important when materials such as biomass are considered. The term "biomass" is extremely broad and can apply to materials as diverse as wood, offal, agricultural waste, specifically-grown energy crops, etc. There is likely to be huge variability among these materials in terms of composition, particle evolution, devolatilization, heterogeneous kinetics and ash and slag formation. The issue of pollutant formation from nitrogen-rich biomass may also be of importance. It is possible that the gasification characteristics of some biomass feedstocks are so vastly different to those of coal that the ROM may have to be adapted to properly account their simulation.

Geometries and operating conditions for entrained flow gasifier designs other than those already examined are necessary to increase the applicability of the ROM. The only full-scale gasifier for which geometries and operating conditions have been found is the GE design. Designs of interest for further reduced order modeling include Siemens, Shell, ECUST, E-GAS and Rocketdyne. Experimental and/or detailed simulation data for these gasifiers are also necessary for ROM validation.

6.3 Gasifier Instrumentation

One course of action that would be of enormous benefit to reduced order modeling is to build and instrument an experimental-scale pressurized entrained flow gasifier. This would allow ROM validation for any range of experimental conditions used. While the gasifier itself could have any of the characteristics shown in Table 1-2, such as being one- or two-stage, air- or oxygen-blown, up- or down-flow, etc., it should be adequately instrumented to ensure useful data can be obtained for validation. In addition, input feedstocks should be characterized to the greatest degree practicable. Thoughts on gasifier instrumentation and feedstock characterization for the purpose of ROM validation are discussed below.

Raw feedstocks should be characterized in terms of proximate and ultimate analyses on as-received bases, particle diameter, particle density, particle porosity, particle internal surface area. Feedstock high-pressure heterogeneous kinetic data is also extremely important. Where possible intrinsic data similar to that employed for the CSIRO gasifier, should be used. This will enable the tracking of important results such as particle surface area, and resistivities due to film diffusion and pore diffusion-reaction. Initial ash composition should be known in order to use the slag submodel. In order to use the particle properties submodel as currently configured, post-devolatilization particle porosity should also be known.

It is essential that any experimental-scale gasifier be instrumented at various points along its axis. Since results for the BYU gasifier show large differences between internal wall temperature and gas temperature, both should be measured. Temperature probes that extend into the gas flow, as well as thermocouples in the wall, should be used. The probes in the gas flow should be capable of radial adjustment to develop a 2-D or 3-D flow temperature map. Gas composition, include pollutant concentrations, should also be measured at various axial and radial positions in the gasifier. The choice of method for cooling gas samples is unclear. Quenching the gas samples quickly halts all chemical reactions but introduces additional water into the sample. This means that compositions may only be known on a dry basis. On the other hand, cooling the gas samples externally, by using a heat exchanger, maintains original mass but may allow chemical reactions to proceed to some extent.

Particle samples should be taken at various axial and radial points in a manner similar to the CSIRO gasifier. These particles can then be analyzed to determine their composition and hence their level of conversion. Other measurable data includes density, diameter, internal surface area and porosity. The gasifier should operate for long enough periods of time to allow wall slag flow to reach steady-state. This would allow sampling of slag behavior at the gasifier exit. Measurable slag quantities include mass flow rate, temperature, viscosity and composition. The extent to which carbon becomes trapped in the slag layer could be measured in this way.